THE NAVY'S CORPORATE LABORATORY

2005 NRL REVIEW

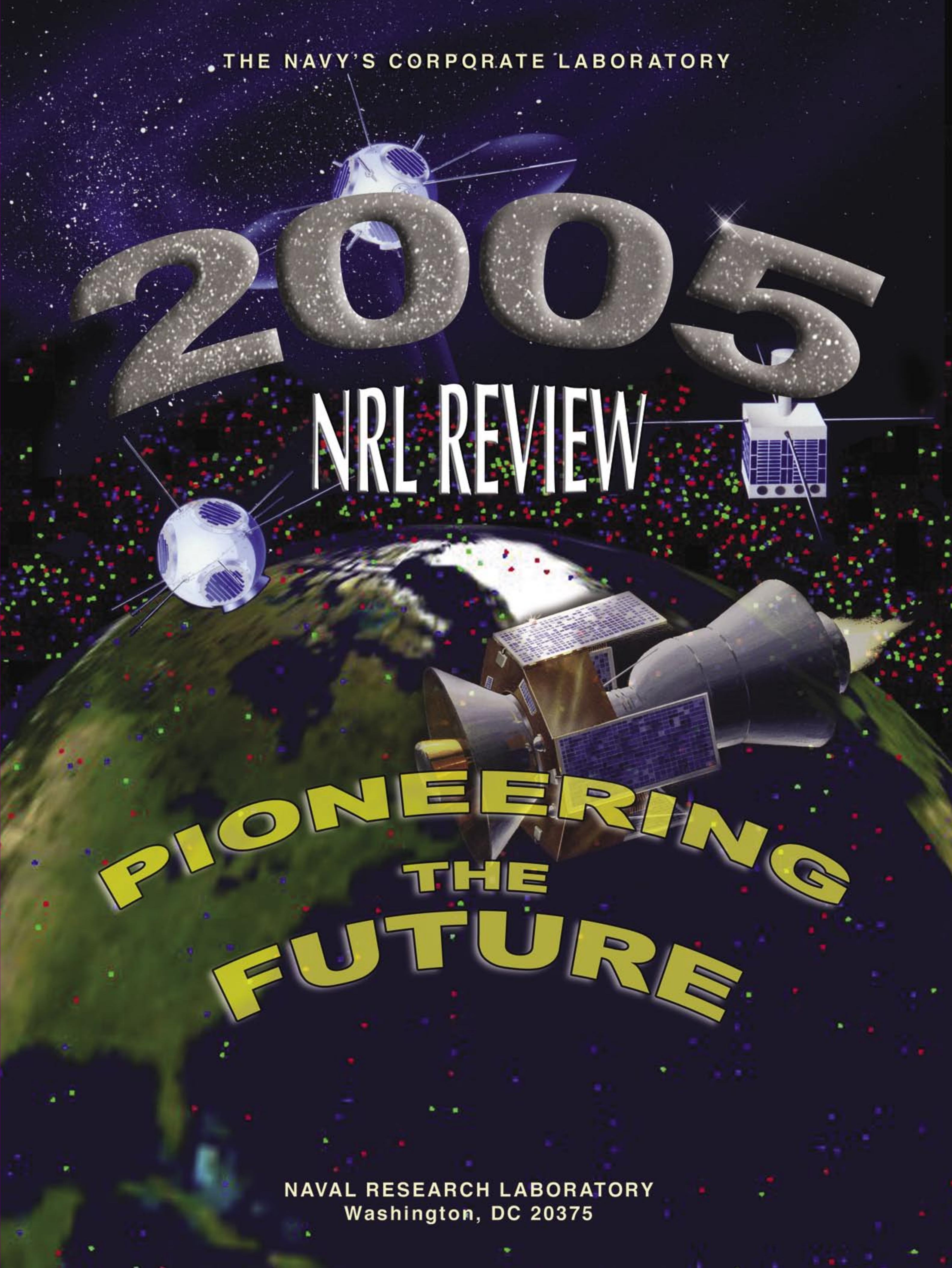

PIONEERING THE FUTURE

NAVAL RESEARCH LABORATORY
Washington, DC 20375

General information on the research described in this NRL Review can be obtained from the Public Affairs Office, Code 1030, (202) 767-2541. Information concerning Technology Transfer is available from the Technology Transfer Office, Code 1004, (202) 767-7230. Sources of information on the various educational programs at NRL are listed in the chapter entitled "Programs for Professional Development."

For additional information about NRL, the Fact Book lists the organizations and key personnel for each division. It contains information about Laboratory funding, programs, and field sites. The Fact Book can be obtained from the Technical Information Services Branch, Code 3430, (202) 404-4963. The web-based NRL Major Facilities publication, which describes each NRL facility in detail, can be accessed at http://www.nrl.navy.mil.

NRL Review Staff

Senior Science Editor
John D. Bultman
Coordinator
Jonna Atkinson
Consultant
Kathy Parrish
Design, Layout, and Graphic Support
Jonna Atkinson and Donna Gloystein
Editorial Assistance
Maureen Long, Saul Oresky, Donna Gloystein,
Kathy Parrish, and Nancy Holly
Historical Update
John D. Bultman
Photographic Production
Gayle Fullerton and Michael Savell

REVIEWED AND APPROVED
NRL/PU/3430--05-481
RN: 05-1226-4037
December 2005

David M. Schubert, Captain, USN
Commanding Officer

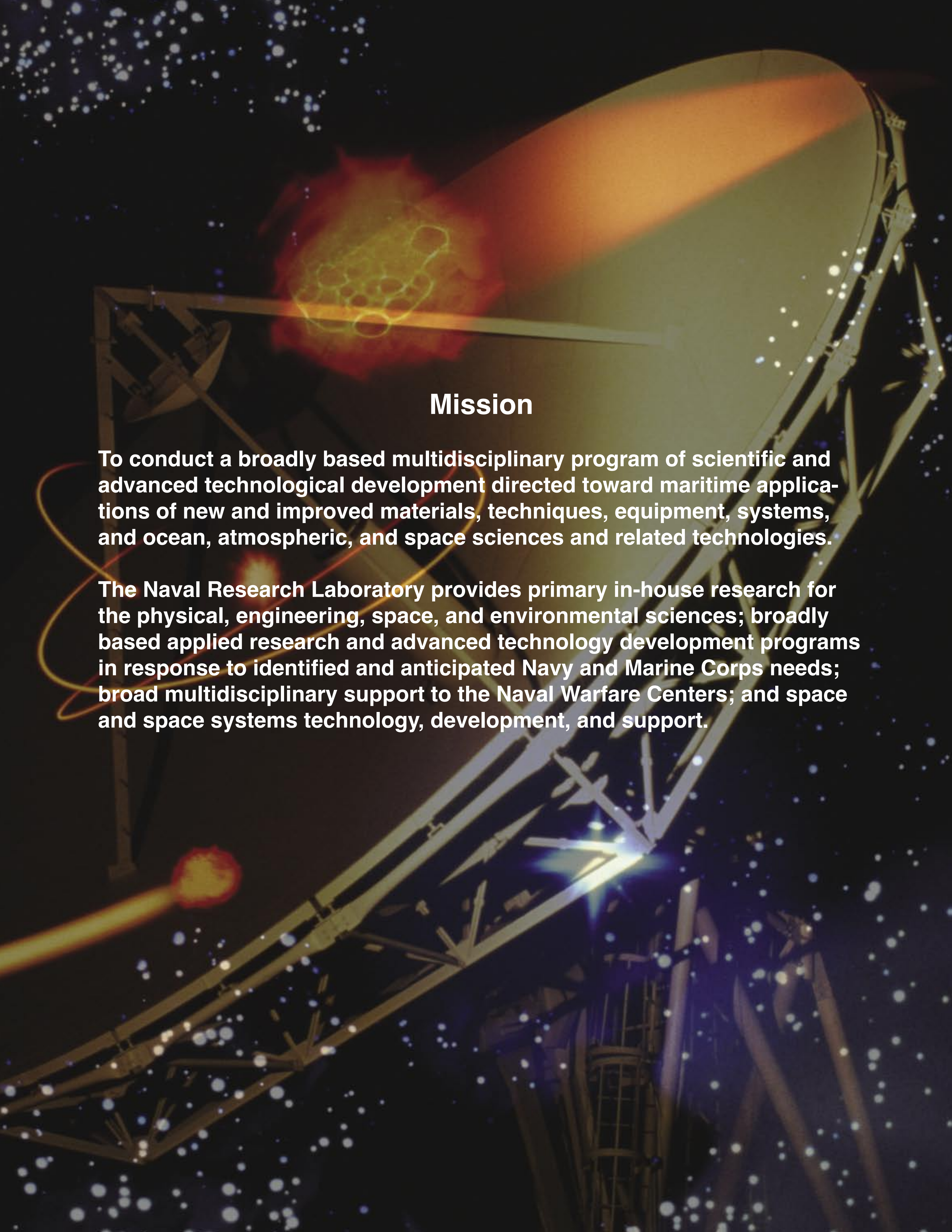

Mission

To conduct a broadly based multidisciplinary program of scientific and advanced technological development directed toward maritime applications of new and improved materials, techniques, equipment, systems, and ocean, atmospheric, and space sciences and related technologies.

The Naval Research Laboratory provides primary in-house research for the physical, engineering, space, and environmental sciences; broadly based applied research and advanced technology development programs in response to identified and anticipated Navy and Marine Corps needs; broad multidisciplinary support to the Naval Warfare Centers; and space and space systems technology, development, and support.

View from the Top

A message from the Captain and the Director of Research

Captain David M. Schubert
USN

Dr. John A. Montgomery
Director of Research

As the saying goes "when the going gets tough, the tough get going." With our nation at war in Afghanistan and Iraq, the ever-present threat of terrorism, and huge financial challenges facing our Navy and Marine Corps as we move from Cold War era legacy equipment to the forces needed in the 21st century, the going is tough, indeed. The scientists at the Naval Research Laboratory are going — full speed ahead into 2005, with new technologies to help our Sailors and Marines face the future.

During the summer of 2004, Chief of Naval Research RADM Jay Cohen approached us with two challenges. The first was short term. "Too many of our Soldiers and Marines are losing arms and legs to terrorist bombers. What can we do to quickly produce flexible, effective arm and leg protection?" Current body armor does an impressive job at protecting the chest and torso, but arm and leg protection is too hot, heavy, and inflexible to be practical in the desert environment of Iraq. Drs. Peter Matic and Graham Hubler of the NRL Materials Division stepped up to the plate. Working with the Army, the Marines, and commercial and university partners, they were able to produce lightweight, flexible arm and leg protection in a matter of months that is now ready to go into production.

RADM Cohen's second challenge was broader and more formidable. "We need technologies to detect, deter, and defeat the broad array of improvised explosive devices (IEDs) that are being used by terrorists in car bombs, suicide vests, and roadside bombs." Working with ONR, the Navy's University Affiliated Research Centers, and the Marine Corps Warfighting Lab, NRL has focused a significant portion of its fundamental research program on technologies to address the IED problem, including possible future use threats using chemical, biological, or radiological attack mechanisms. Our program is looking at the basic physics of energetic materials, including methods to detect explosives at distance, at a number of approaches aimed at controlling when and how explosives are detonated, and at sensors for the broad array of attack mechanisms. Resisting the temptation to immediately grab for low hanging fruit, we are tackling the hard problems that will lead to big payoffs a few years down the road.

On a broader scale, the results of our basic and applied research programs are coming to fruition across the spectrum of Naval needs. To mention just a few examples:

- The first TacSat, built here at NRL, should launch this summer. TacSat-1 is the first of a series of small, inexpensive satellites aimed at giving the nation a much more responsive method of providing space-based capability to our war-fighters.
- Following our success with the Dragon Eye small UAV, which the Marines are flying in Iraq with impressive success, NRL is developing a number of small autonomous, expendable air vehicles for a host of customers and applications.
- The prototype for the Advanced Multi-function RF Concept (AMRFC) is being demonstrated at our Chesapeake Beach facility and shows incredible promise to bring improved electronic warfare, communications, and radar capability to our new generation of ships, all in a single aperture.
- New sensors and analytical techniques for dealing with chemical and biological agents are also coming to fruition, most notably shown this winter in the Silent Guardian project, a joint effort between the Air Force and NRL, which took a newly developed NRL protocol for gene-based pathogen identification (EOS Chip) into full operation for bio-surveillance in the National Capital Region for two months centered on the Presidential inauguration. This effort served to kick off an advanced concept technical demonstration for this approach that will provide bio-surveillance for a number of biological warfare agents and simultaneous multiple diagnoses for upper respiratory pathogens.

Our basic research program, in addition to addressing the IED challenge, contains many innovative technologies that will deliver in the years ahead. Areas that we are particularly excited about include nanoscience, where new sensors and electronics are being developed at the molecular scale; new optical sensors, including hyperspectral, lidar, and IR spectroscopy, which will improve our ability to see into littoral areas; bio-molecular engineering, where new sensors and materials are being produced using biological foundations; alternative fuel sources such as fuel cells, synthetic fuels, and the methane clathrates in the ocean bottom; and innovative and renewable weapon systems such as lasers, microwaves, and rail guns.

The Navy and Marine Corps are in the midst of a time of both great challenge and great opportunity. It is an exciting time to be at the forefront of science and technical innovation. The challenges facing the Naval services are in constant change, and the Naval Research Laboratory will continue to bring forth the technologies that will keep our Sailors and Marines at the top of their game now and for the foreseeable future.

– Captain David M. Schubert
– Dr. John A. Montgomery

reviewcontents

VIEW FROM THE TOP

NRL'S INVOLVED!

THE NAVAL RESEARCH LABORATORY

FEATURED RESEARCH

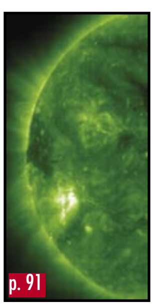

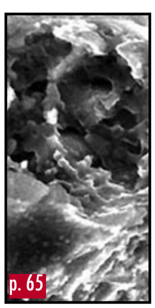

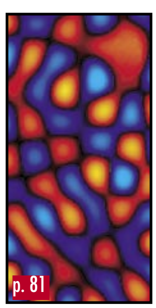

ACOUSTICS

ATMOSPHERIC SCIENCE AND TECHNOLOGY

CHEMICAL/BIOCHEMICAL RESEARCH

ELECTRONICS AND ELECTROMAGNETICS

ENERGETIC PARTICLES, PLASMAS, AND BEAMS

INFORMATION TECHNOLOGY AND COMMUNICATIONS

MATERIALS SCIENCE AND TECHNOLOGY

p. 81

OCEAN AND ATMOSPHERIC SCIENCE AND TECHNOLOGY

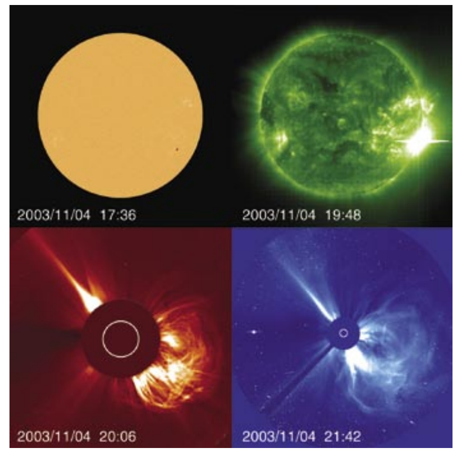

p. 91

OPTICAL SCIENCES

REMOTE SENSING

SIMULATION, COMPUTING, AND MODELING

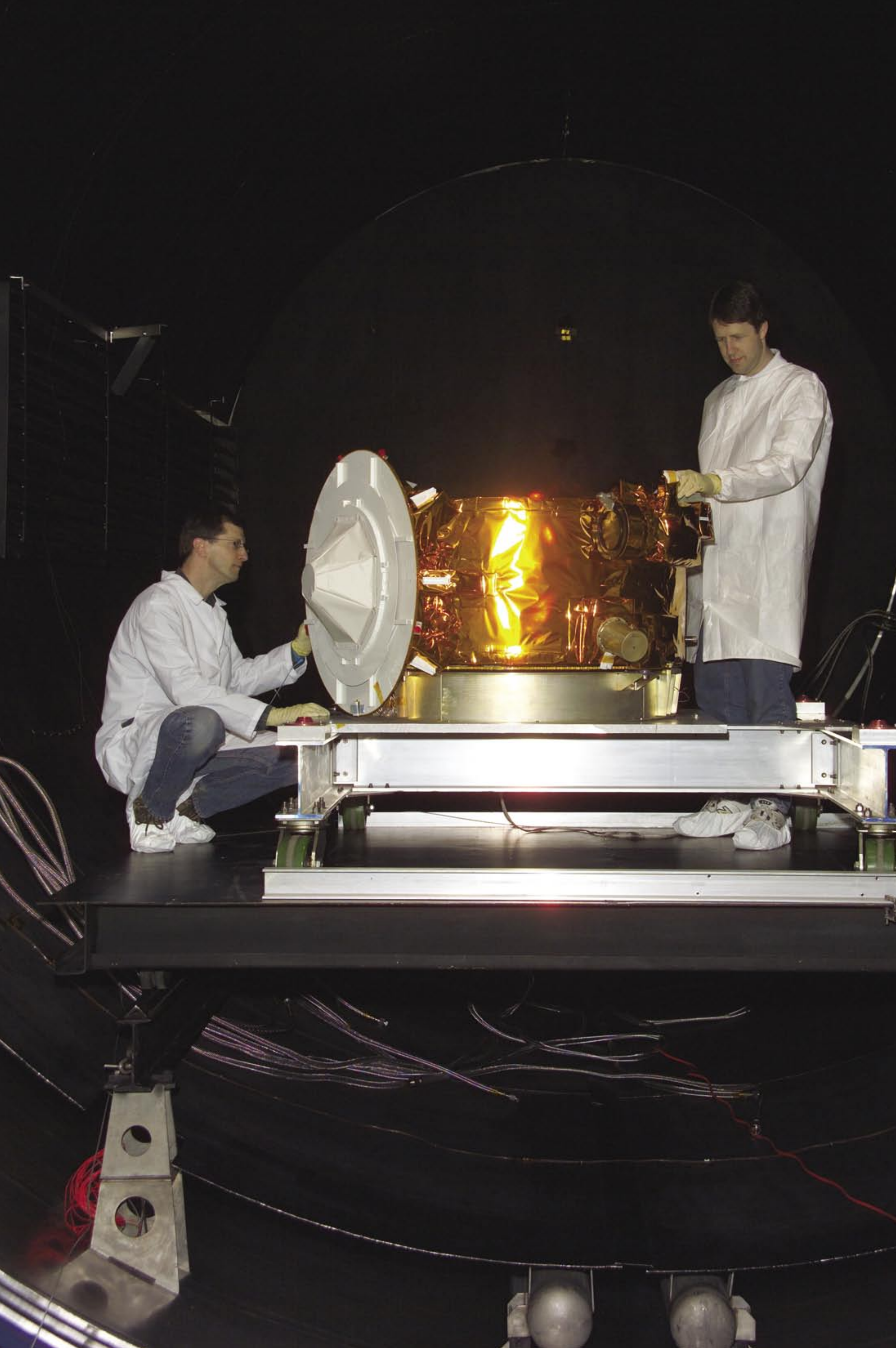

NRL's Involved!

Photo caption: The TacSat 1 satellite, built in 9 months for the Office of Force Transformation, puts its four payloads (two low-resolution cameras and two electronic intelligence sensors) directly under the control of the warfighter via the secret Internet SIPRNET and via a UHF two-way link on military aircraft.

The Naval Research Laboratory

A PIONEER IN SPACE SCIENCE AND TECHNOLOGY

The entry of the United States into the realm of space began when American forces entered Germany in 1945 and captured the huge underground factory for V-2 production at Nordhausen. In a race to beat the Russians to Nordhausen, the Americans won and confiscated about a hundred rockets. The rockets were shipped to the White Sands Missile Range in New Mexico, where the Army set about studying the propulsion system. The first American-launched V-2 flew from White Sands on April 16, 1946. Some 60 launches were carried out—up to the fall of 1952.

Even before the Army began flying the captured German V-2 rockets after World War II, the Naval Research Laboratory (NRL), grasping the opportunities for upper atmosphere research and solar astronomy, convinced the Navy that it should have the lead in the Navy for conducting rocket research. The V-2 Rocket Panel was formed with membership from NRL, APL (Applied Physics Laboratory), California Institute of Technology, Harvard University, University of Michigan, and other organizations to oversee the allocation of space on V-2 rockets for high-altitude research, with NRL's Mr. Ernst Krause as the first chair. The research goals included radio and sound propagation in the atmosphere; properties of the atmosphere, cosmic rays, solar ultraviolet radiation, and various biological investigations.

Using V-2s, NRL's Dr. Richard Tousey's measurements of the Sun's ultraviolet emission in 1946 and Dr. Herbert Friedman's measurements of the Sun's X-ray emission in 1949 began a major space science program at NRL. As an adjunct to the science payloads, NRL engineers photographed the Earth in order to determine the location and orientation of the rocket. This led, in 1954, to an image of a hurricane as it moved inland from the Gulf of Mexico, the first time that a major weather feature was seen from space and a convincing argument that cloud imagery from space could be a valuable tool for meteorologists.

The V-2 program was also the impetus for the emergence of a strong space technology effort at NRL. Almost as soon as the program of V-2 rocket flights began, Krause recognized the limitations of the V-2 and directed one of his staff members, Mr. Milton Rosen, to learn about rockets and develop a new design. This led directly to NRL's Viking rocket that first flew in 1949.

So within a decade of Krause's introduction to German rocketry, NRL had developed a base of rocket science that had formed into two distinct branches: one related to applications, including the development of scientific payloads; the other, the development of rocket technology.

By the mid 1950s, space science and technology had advanced to where the U.S. committed itself to the development and launch of orbiting satellites in support of the International Geophysical Year (IGY) in 1957-1958. NRL was chosen to conduct America's first satellite program, Project Vanguard. This entailed designing, developing, and launching the first three-stage rocket and satellite, as well as developing the Minitrack ground-tracking network to track the satellite. Although the Russians beat the U.S. into space with Sputnik and the Army beat the Navy with Explorer 1 on January 31, 1958, NRL did successfully launch satellites into orbit, beginning in March 1958 and during the IGY. The Vanguard satellite is the oldest man-made object in space and the three-stage rocket technology was the basis for much of today's rocket development. The Vanguard team at NRL was transferred in October 1958 and became the core of the newly established National Aeronautics and Space Administration (NASA).

Herbert Friedman (left) and Richard Tousey used V-2 rockets to establish basic science programs at NRL that continue today.

A sign of the depth and maturity of the NRL space program was the development of rocket and satellite tracking systems using radio interferometric technology. Minitrack led to the Navy Space Surveillance System (NavSpaSur), developed (1958-1964) by NRL on a "crash basis" for the Advanced Research Projects Agency (ARPA) to detect and track such satellites.

So in the second decade of space activities at NRL, scientists and engineers had moved past a pure discovery phase and were developing space applications directed toward resolving major military issues, as demonstrated by the development of NRL's GRAB electronic surveillance satellite, the Nation's first space intelligence asset, which began in 1957. So when a U-2 surveillance aircraft piloted by the Central Intelligence Agency's employee Gary Powers was shot down by a Soviet surface-to-air missile over Sverdlops in the Soviet Union in May 1960, this new space capability was ready to take its place. Within a month of the incident, GRAB was launched into orbit on top of a Thor Able-Star rocket. NRL's early rocket science and technology allowed Mr. Reid Mayo, an electrical engineer working on countermeasures in the Radio Division to conceive GRAB. The name GRAB, Galactic Radiation and Background, was a cover since it revealed nothing about the true nature of the instrument. There was no instrument to measure "galactic radiation and background." But SolRad (Solar Radiation Satellite), an instrument to monitor the Sun's X-ray emission, also flew along with GRAB. By 1960, NRL scientists had been conducting space experiments for more than a decade, so the ruse was effective.

In other pursuits of space science during the 1960s, NRL scientists were successful in competing for instruments on the earliest NASA satellites, the Orbiting Geophysical Observatory and the Orbiting Solar Observatory (OSO). NRL scientists also continued their program of rocket experiments. Of particular note was Friedman's switch to stellar investigations, beginning in 1955 with a survey of the Milky Way for ultraviolet emission from ordinary stars, culminating in the 1960s with noteworthy contributions to the new field of x-ray astronomy.

A substantial point of departure occurred in 1972 when NRL's Dr. George Carruthers' Far Ultraviolet Camera/Spectrograph was carried to the Moon on Apollo 16 and became Earth's first, and to this day the only, Lunar observatory. Skylab became America's first space station in 1973 and contained a suite of solar telescopes, including NRL's SO82A and B, representing a huge advance in the quality of the instruments and the sophistication of the space platform.

NRL was also able to take advantage of space flight opportunities offered by DoD's Space Test Program (STP), which was established in 1960. One of the first and most important of the STP's programs was the development and launch of the NRL Timation (TIMeAndnavigaTION) satellite series, a concept by NRL's Roger Easton, in the 1970s, that led to the demonstration of the Global Positioning System (GPS) principle of navigation. Mr. Easton, one of the young engineers working for NRL at the time, turned around the Minitrack concept and was able to use radio signals from known satellites in space to determine the position of a receiver on Earth. The concept was to become GPS.

Major solar research efforts took place during the 1980s. In 1980, NRL was able to fly a solar coronagraph on an STP-sponsored mission called SolWind. The data from that mission included the first observation of a comet crashing into the Sun. In 1985, an extraordinary research opportunity occurred for NRL when two NRL solar-observing instruments, SUSIM (Solar Ultraviolet Spectral Irradiance Monitor) and the HRTS

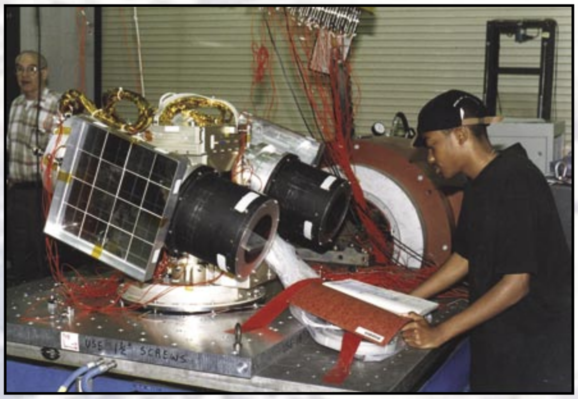

Local students helped develop NRL's GIMI instrument, an ultraviolet telescope flown on the ARGOS satellite.

(High Resolution Telescope and Spectrograph), accompanied by NRL scientist and payload specialist, Dr. John-David Bartoe, flew as part of Spacelab 2 on the Space Shuttle Challenger. The opportunity to pursue space observations allowed NRL to develop into one of the world's leading solar research groups and in a position to compete successfully for the LASCO/EIT (Large Angle and Spectrometric Coronagraph/Extreme ultraviolet Imaging Telescope) instruments flown as part of the SOHO (Solar and Heliospheric Observatory) mission in the 1990s. These instruments have provided, for the first time, a genuine basis for predicting geomagnetic storms on the Earth, which can be highly disruptive of the space and terrestrial power and communications infrastructure, as well as damaging to spacecraft.

NRL scientists currently have responsibility for two major new NASA-supported solar instruments: STEREO (Solar TErrestrial RElations Observatory), in which two satellites will obtain stereoscopic images of the Sun as they drift in opposite directions away from the Earth in orbit around the Sun; and EIS (EUV Imaging Spectrometer), a spectroscopic instrument that will provide spectral images of the Sun's atmosphere with unprecedented speed and resolution.

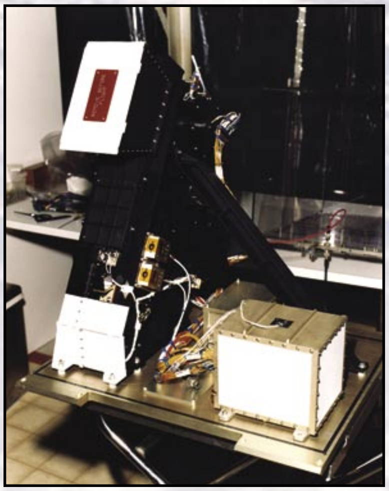

NRL's SSULI instrument on the bench. Copies of this instrument will fly on five DoD weather satellites to provide ionospheric data to military and civilian customers.

NRL scientists have also contributed other space instruments that provide operational data for the warfighter. The SSULI (Special Sensor Ultraviolet Limb Imager) instrument, a direct outgrowth of rocket and satellite experiments, is being flown as part of the Air Force's meteorological satellite, DMSP (Defense Meteorological Satellite Project), and will provide ionospheric data. NRL's space activities in relation to the ionosphere have also provided impetus to the development of an entirely new model of the ionosphere being sponsored by the Office of Naval Research (ONR) and its Air Force equivalent, AFOSR (Air Force Office of Scientific Research). The new model, GAIM (Global Assimilation of Ionospheric Measurements), is physics based and borrows heavily from the weather community in its structure. The model is currently being made operational for DoD and civilian applications by the Air Force Weather Agency with NRL's assistance.

An almost separate tradition of space science at NRL is that associated with remote sensing, which had its start, as noted, in cloud photography from sounding rockets. The most notable success has been in the area of microwave imaging of the Earth for the purpose of gathering information about the oceans and the atmosphere above the oceans, including temperature, winds, and sea ice. The technique was pioneered at NRL and culminated in the launch of the SSM/I (Special Sensor Microwave Imager) on DMSP in 1987. More recently, the NRL-developed WindSat was launched in January 2003 as a joint NOAA (National Oceanographic and Atmospheric Administration), NASA, DoD mission. WindSat (like SSM/I) measures both the intensity and polarization of microwave radiation from the sea surface and allows both wind speed and direction to be measured. NRL scientists also make extensive use of space products from almost every space platform, providing a huge advance in the Navy's ability to sense the environment in its diverse operational areas.

In another area, NRL now has a highly regarded program of middle atmosphere research. This program had its beginning with two highly successful Shuttle-based instruments flown under the DoD's auspices: POAM (Polar Ozone and Aerosol Monitor), which measured ozone, water vapor, and chlorine monoxide (a critical ingredient in stratospheric ozone depletion chemistry) from the Shuttle bay during three flights, and MAHRSI (Middle Atmosphere High Resolution Spectrometer Instrument), on a German satellite, which made global measurements of OH, the hydroxyl ion. POAM led to the development of the ozone sensor for the converged NOAA/DoD satellite system under NRL guidance.

The German SPAS pallet was released from the Space Shuttle to operate as a free flying satellite for a week, then returned to the Shuttle. The SPAS contained a number of instruments to study the upper atmosphere, including NRL's MAHRSI, a high-resolution ultraviolet telescope.

NRL has continued their high level of innovation in space hardware. With the development of the Space Shuttle as the Nation's exclusive basis for carrying payloads into orbit, a means was needed to bring satellites to other than the Shuttle orbit. For this purpose, NRL developed a specialized rocket-powered vehicle that was to be carried by the Shuttle into orbit and continue on its own into other orbits, where it could drop off individual satellites. The vehicle, the SLD (Shuttle Launch Dispenser), never did fly because of the Challenger disaster, but achieved a new life on the Titan rocket with a new name, the TLD (Titan Launch Dispenser), but with the same role.

Being somewhat outside the "establishment" (Air Force, NASA, etc.) has its advantages, which were revealed in the Clementine program, a Missile Defense Agency-sponsored project to fly to the Moon and built under the mantra of the '90s, "faster, better, cheaper." The spacecraft, designated by NRL as the Deep Space Program Satellite Experiment or DSPSE, was indeed developed in little more than a year, something the U.S. had not done for decades, and provided a wealth of new lunar data and the successful development of innovative space technology. The idea of "faster, better, cheaper" is also central to a new approach to military space capability being sponsored by DoD's Office of Force Transformation. The centerpiece of this new program is TacSat (Tactical Satellite), designed to bring tactical capability to the

The Ballistic Missile Defense Organization (BMDO) assigned prime responsibility for the *Clementine* spacecraft design, manufacture, integration, and mission execution to NRL in March 1992. The construction and integration of the spacecraft was completed in 22 months.

warfighter as it is needed and without the decade of development normally associated with operational military satellites. NRL is responsible for the first in this series.

Although not directly tied to DoD's transformation, ONR and NRL have formed a space office with joint ONR and NRL leadership to direct Navy space technology, aided by a cash infusion from ONR. The organization is taking responsibility for the signal intelligence instruments for TacSat 2.

Huge changes are taking place in the Nation's space science and technology. NASA is redirecting its priority to support manned exploration of the solar system; DoD is committed to transform itself as a consequence of the end of the Cold War and the beginning of the war on terror.

There are major thrusts that the Navy should be involved in, one being Maritime Domain Awareness (MDA), as in knowing what is heading to our shores and ports over the ocean. Satellites with a varying array of sensors can be a major contributor to developing and maintaining that picture. The integration and correlation of satellite data with other sources of data is absolutely critical.

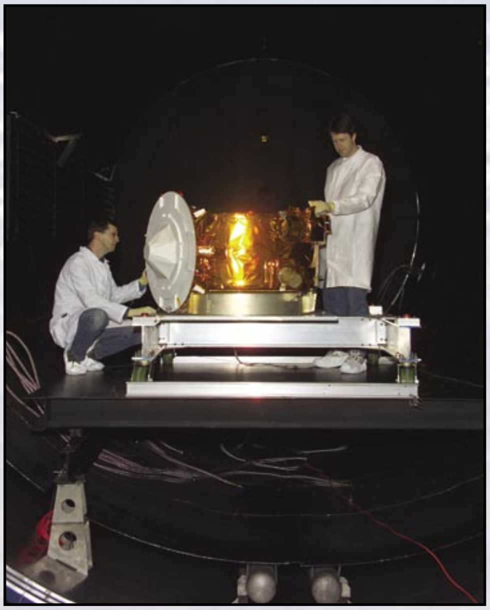

The TacSat-1 satellite, built in 9 months for the Office of Force Transformation, puts its four payloads (two low-resolution cameras and two electronic intelligence sensors) directly under the control of the warfighter via the secret Internet SIPRNET and via a UHF two-way link on military aircraft.

Another important mission is data-exfiltration, where satellites receive data from remote sensors placed in the field. Sensors could be on land, in the water or in the air. The challenge is to design the transmitted links from the sensor to be of low average power and reliable; in some cases, what is called LPI/LPD. Other platforms could be used to exfiltrate data from the remote sensors; aircraft or UAV could, and probably will be used. But if the sensors are spread out over a very large area, like the oceans of the globe, it's hard to see how a constellation of Low Earth Orbit (LEO) satellites could be beat. LEO satellites can cover more area per unit time and do so at a lower operating cost than any other platform.

Another future major area will be robotics in space for purposes of repair, refueling, assembly, orbit changing, and other missions. NRL has made a major investment in facilities and talented researchers to be a leader in this field. There are a number of important and unique missions for space robotics and NRL wants to be a major researcher and participant.

Whatever the future will demand, history has shown for nearly six decades now that NRL is well positioned to provide much of the innovation and leadership needed to effect the necessary changes.

1946 Richard Tousey's first V-2 rocket flight measuring solar ultraviolet radiation.

1949 Herbert Friedman's first V-2 rocket flight measuring solar x-radiation.

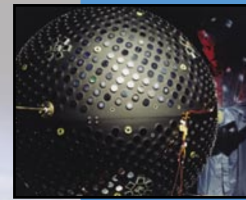

1949 First flight of NRL's Viking rocket, designed to replace the V-2 for scientific missions which required higher altitudes and pointing stability.

1954 Photograph of a hurricane from an Aerobee rocket over the Southwest United States.

1958 Vanguard 1, the world's oldest man-made satellite, achieves orbit on St. Patrick's Day.

1958 The observation of a solar eclipse from sounding rockets flown from the USS *Point Defiance*.

1960 Launch of the GRAB satellite, the United States' first electronic surveillance satellite. NRL's Solrad payload to monitor solar x-radiation was carried on the same satellite.

1961 The first launch in the Low Frequency Trans-Ionospheric (LOFTI) radio satellite series, intended to study the propagation of radio waves through and in the ionosphere.

1967 Launch of the first Timation satellite, which demonstrated NRL's new navigation concept that became GPS.

1971 NRL's Lunar Surface Camera operates on the Moon during the Apollo 16 mission and obtains images of the Earth and of celestial objects.

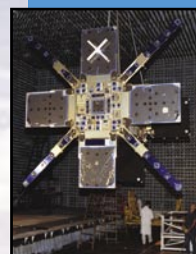

1973 NRL solar spectrometers operate on Skylab, America's first space station.

1976 The first launch of NRL's Multiple Satellite Dispenser (MSD), an upper stage for the Atlas F booster, which carried multiple satellites into precise orbits.

1980 Launch of the Solwind Coronagraph on a DoD satellite to monitor the solar corona and catalog coronal mass ejections.

1983 The first successful launch of the Living Plume Shield II (LIPS II), a demonstration program to prove the capability of direct downlink of tactical data from a low Earth orbiting spacecraft.

1985 NRL scientist John David Bartoe flew on the Space Shuttle as the payload specialist for NRL's High Resolution Telescope Spectrometer for studying the Sun.

1987 The first of NRL's Special Sensor Microwave Imager (SSM/I) was flown on DoD's Defense Meteorological satellite Project (DMSP) to map water vapor and ocean wind speed.

1987 The launch of Living Plume Shield III (LIPS III) provided a test bed for new space power sources.

1990 NASA's Compton Gamma Ray Observatory containing NRL's Oriented Scintillation Spectrometer Experiment (OSSE) put in orbit from the Space Shuttle. It operated for 10 years.

1990 The NRL-developed Titan Launch Dispensers (TLD), a transfer stage for the Titan IV rocket.

1990 The launch of the Low-Power Atmospheric Compensation Experiment (LACE), a spaceborne target with sensors to characterize a laser beam emitted from a ground-based laser site.

1993 NRL's Polar Ozone and Aerosol Monitor (POAM) was launched as part of the French Space Agency SPOT remote sensing satellite.

1994 NRL's Middle Atmosphere High Resolution Spectrometer Instrument (MAHRSI) on the German Space Agency's Shuttle Pallet Atmosphere Satellite (SPAS). The instrument was recovered and flew again in 1997.

1994 The joint DoD-NASA *Clementine* satellite, developed by NRL, was launched to orbit the Moon and conduct deep space experiments.

1995 NRL's Large Area Solar Coronagraph and Extreme Ultraviolet Imaging Telescope (LASCO/EIT) were launched on the joint NASA/ESA mission Solar and Heliospheric Observatory (SOHO) to operate in space. The instruments are still operating.

1999 The ARGOS satellite, launched by DoD, contained five NRL instruments to measure the upper atmosphere, conduct astronomy experiments, and test new technology.

2003 The first in a series of NRL's Special Sensor Ultraviolet Limb Imagers (SSULI) flew on DMSP.

2003 NRL's WindSat was launched on the joint Navy/DoD/NASA Coriolis spacecraft to measure wind speed and direction.

2005 Scheduled launch of TacSat-1 will provide capabilities for cross-platform missions, specific emitter identification, and visible and infrared (IR) imaging.

Nanoscience Research

Open for Business!

FY 05 ushered in a new era for NRL as the recently completed Nanoscience Research Laboratory - (Building 250) – began to host NRL researchers to carry out cutting edge research at the nanometer length scale. The central core of the new building, a 5000 square foot class 100 cleanroom, has been outfitted with the newest tools to permit lithographic fabrication, measurement, and testing of devices. This includes deposition systems for metals and insulators, optical mask aligners, and etching systems. This is supported by chemistry stations and fume hoods for spinning on photo resists, baking, and developing the patterns that ultimately result in small devices and circuits. Additional new equipment includes an electron beam writer for fabricating features down to 10 nanometers; a focused ion beam workstation for 10 nanometer-scale machining of materials; and a scanning electron microscope for inspection of these small-scale devices.

The cleanroom also contains an atomic force microscope, optical microscopes, optical index characterization, scanning stylus surface measurement, a probe station for electronic measurements on finished devices, and a wire bonder to connect the circuits in completed microchips to plug-in carriers.

In addition to the cleanroom facility, Building 250 also contains 5000 square feet of controlled-environment laboratory space, which is available to NRL researchers whose experiments are sufficiently demanding to require this space. There are 12 of these laboratories within the new building. All of them provide shielding from electromagnetic interference and very low floor vibration and acoustic levels. In addition, eight laboratories will control the temperature to within ± 0.5 °C and four to within ± 0.1 °C.

These spaces, after approval by the Director of the Institute for Nanoscience, Dr. R. J. Colton, and by the Director of Research, Dr. J.A. Montgomery, are assigned to a requesting Division for an agreed upon period to house that Division's experimental equipment. The first tenants are the Material Science and Technology Division with its ultra-high resolution transmission electron microscope (TEM); the Acoustics Division with its near-field scanning optical microscope (NSOM); and the Chemistry Division with its ultra-high vacuum, four-probe scanning tunneling microscope (STM) that is installed in one of the ultra-quiet laboratories and its atomic force microscopes (AFM) that are installed in one of the quiet laboratories. Additional applications for space, which are pending, indicate that this highly desirable research space will be fully subscribed.

Dr. Richard Colton, Director, Institute of Nanoscience
nanoscience@nrl.navy.mil — http://nanoscience.nrl.navy.mil

Laboratory

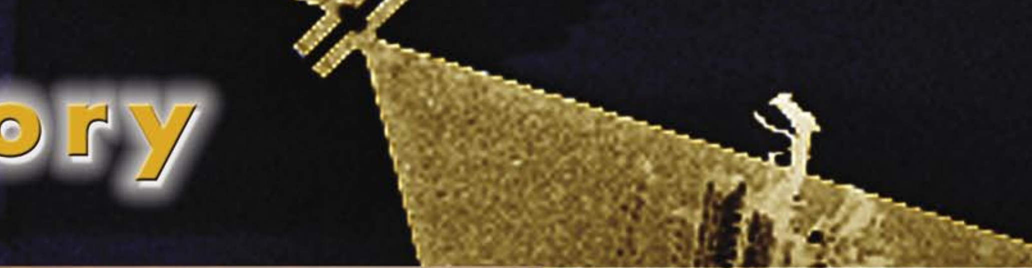

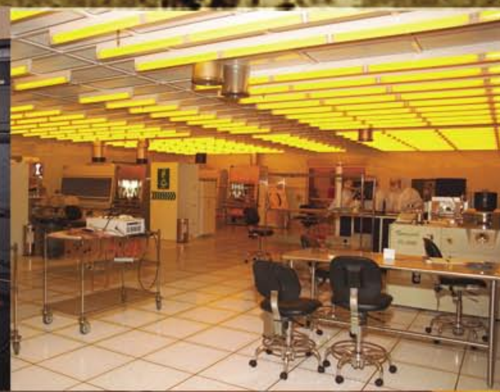

NRL's Technology Transfer Office

Implementing NRL's innovative technologies in products and services to benefit the public…

Members of the Technology Transfer Office

The Year in Review

During FY04, the Technology Transfer Office (TTO) staff was increased by three full-time equivalent. The total number of new licenses executed in FY04 was 13; a three-fold increase over FY03. In addition to the 13 licenses, six new sublicenses and seven license amendments were executed. Total licensing royalties collected were $526,077, a decrease from FY03; however, royalties in FY05 and beyond are forecasted to increase significantly due to the large number of new licenses. The total number of active licenses at the end of FY04 was 36. The total number of CRADAs executed in FY04 was 15, a two-fold increase over FY03. In addition to the new CRADAs, 11 CRADA amendments were executed. The total funds received from new CRADAs was $686,050. The total number of active CRADAs at the end of FY04 was 38.

Major Success Stories

In February 2004, NRL licensed its Biosensor Technology to Seahawk Biosystems Corporation. Seahawk is currently developing a multi-use, multiplexed veterinary diagnostic system. This system is based on NRL's patented Bead Array Counter (BARC) magnetic microarray technology combined with proprietary assay protocols that greatly reduce the incidence of false positives and false negatives. This unique and proven combination of technologies makes Seahawk's system more versatile, sensitive, and specific than other veterinary diagnostic systems currently on the market.

NRL licensed its Biosensor Technology to Seahawk Biosystems Corporation.

Catastrophic dust abatement using NRL-DAS6100 formulation.

Also in February 2004, NRL signed a partially exclusive patent license agreement and Cooperative Research and Development Agreement (CRADA) with CorActive High-Tech Inc. This license focuses on the commercial manufacture and future development of NRL's infrared (IR) fiber technology. This will have a tremendous impact in the area of high laser power delivery systems required to support advanced applications in military, industrial, and medical products.

In March 2004, NRL licensed a smart probe that identifies underground minerals and contaminants with Austin AI, LLC. The technology has the potential to improve the way that mineral exploration, soil contaminant characterization, and petrochemical and chemical processing are done. Austin AI will take the NRL technology and develop the CP-1000 X-ray fluorescence cone penetrometer for commercial applications.

In September 2004, NRL signed a licensing agreement with SoilWorks, LLC for a dust abatement technology that will make it safer for helicopters operating in dusty environments. In addition to its use for creating safe landing pads, the product may be used to abate dust around facilities, such as field hospitals, and around high value, critical equipment. It has many commercial applications as well, such as prevention of soil erosion, dust abatement at construction sites, and dirt road maintenance.

Marketing and Outreach

The NRL Exhibits group's primary objective is to showcase and market NRL technology at technical conferences and trade shows throughout the U.S. The Exhibits group negotiates for booth space, solicits the technical divisions for technologies to showcase and/or demonstrate at the show, prepares marketing materials including pamphlets, flyers, and CDs for selected technologies available for licensing, designs the booth contents, and attends the shows. The Exhibits group's annual schedule includes more than two-dozen shows, representing a cross-section of NRL technologies.

The TTO and Exhibits group regularly publish articles related to technology transfer and the marketing of NRL technology in Labstracts, the NRL bi-weekly publication that is distributed to NRL employees and retirees.

The TTO has initiated contact with local, regional, and national organizations to assist in the marketing of NRL technology. Partnership Intermediaries such as TechLink, OLETC, and the University of Pittsburgh are assisting NRL in finding potential licensing and CRADA partners.

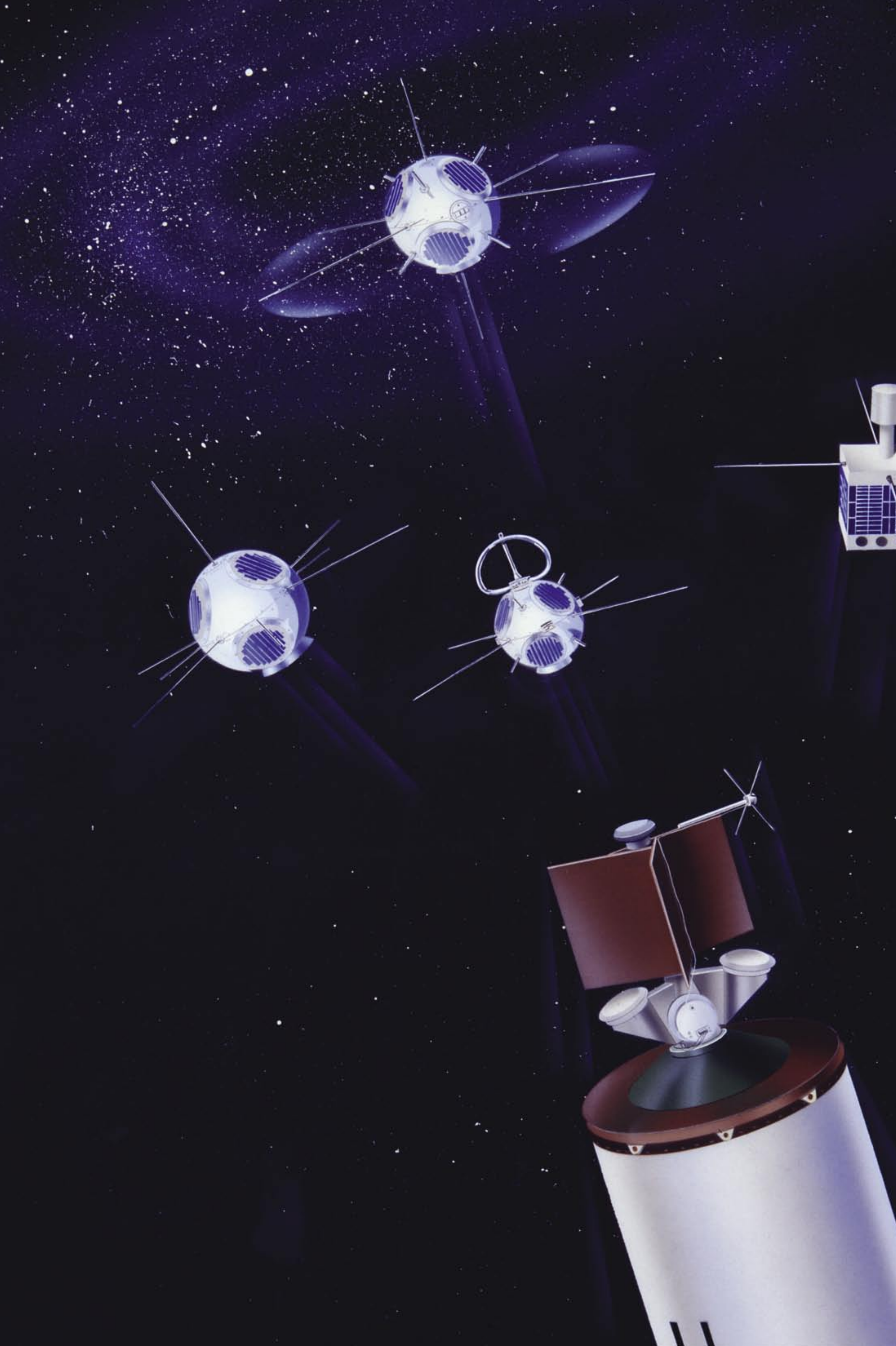

The Naval Research Laboratory

Photo caption: The artist's conception shows the planned "buckshot" release of four of this mission's five satellites. Unfortunately, the 1962 launch aboard a Thor Able-Star rocket failed, a common occurrence in those early years.

NRL — OUR HERITAGE

Today, when government and science seem inextricably linked, when virtually no one questions the dependence of national defense on the excellence of national technical capabilities, it is noteworthy that in-house defense research is relatively new in our Nation's history. The Naval Research Laboratory (NRL), the first modern research institution created within the United States Navy, began operations in 1923.

Thomas Edison's Vision: The first step came in May 1915, a time when Americans were deeply worried about the great European war. Thomas Edison, when asked by a *New York Times* correspondent to comment on the conflict, argued that the Nation should look to science. "The Government," he proposed in a published interview, "should maintain a great research laboratory....In this could be developed...all the technique of military and naval progression without any vast expense." Secretary of the Navy Josephus Daniels seized the opportunity created by Edison's public comments to enlist Edison's support. He agreed to serve as the head of a new body of civilian experts—the Naval Consulting Board—to advise the Navy on science and technology. The Board's most ambitious plan was the creation of a modern research facility for the Navy. Congress allocated $1.5 million for the institution in 1916, but wartime delays and disagreements within the Naval Consulting Board postponed construction until 1920.

The Laboratory's two original divisions—Radio and Sound—pioneered in the fields of high-frequency radio and underwater sound propagation. They produced communications equipment, direction-finding devices, sonar sets, and perhaps most significant of all, the first practical radar equipment built in this country. They also performed basic research, participating, for example, in the discovery and early exploration of the ionosphere. Moreover, the Laboratory was able to work gradually toward its goal of becoming a broadly based research facility. By the beginning of World War II, five new divisions had been added: Physical Optics, Chemistry, Metallurgy, Mechanics and Electricity, and Internal Communications.

The War Years and Growth: Total employment at the Laboratory jumped from 396 in 1941 to 4400 in 1946, expenditures from $1.7 million to $13.7 million, the number of buildings from 23 to 67, and the number of projects from 200 to about 900. During WWII, scientific activities necessarily were concentrated almost entirely on applied research. New electronics equipment—radio, radar, sonar—was developed. Countermeasures were devised. New lubricants were produced, as were antifouling paints, luminous identification tapes, and a sea marker to help save survivors of disasters at sea. A thermal diffusion process was conceived and used to supply some of the ^{235}U isotope needed for one of the first atomic bombs. Also, many new devices that developed from booming wartime industry were type tested and then certified as reliable for the Fleet.

NRL Reorganizes for Peace: Because of the major scientific accomplishments of the war years, the United States emerged into the postwar era determined to consolidate its wartime gains in science and technology and to preserve the working relationship between its armed forces and the scientific community. While the Navy was establishing its Office of Naval Research (ONR) as a liaison with and supporter of basic and applied scientific research, it was also encouraging NRL to broaden its scope and become, in effect, its corporate research laboratory. There was a transfer of NRL to the administrative oversight of ONR and a parallel shift of the Laboratory's research emphasis to one of long-range basic and applied investigation in a broad range of the physical sciences.

However, rapid expansion during the war had left NRL improperly structured to address long-term Navy requirements. One major task—neither easily nor rapidly accomplished—was that of reshaping and coordinating research. This was achieved by transforming a group of largely autonomous scientific divisions into a unified institution with a clear mission and a fully coordinated research program. The first attempt at reorganization vested power in an executive committee composed of all the division superintendents.

This committee was impracticably large, so in 1949, a civilian director of research was named and given full authority over the program. Positions for associate directors were added in 1954.

The Breadth of NRL: During the years since the war, the areas of study at the Laboratory have included basic research concerning the Navy's environments of Earth, sea, sky, and space. Investigations have ranged widely—from monitoring the Sun's behavior, to analyzing marine atmospheric conditions, to measuring parameters of the deep oceans. Detection and communication capabilities have benefitted by research that has exploited new portions of the electromagnetic spectrum, extended ranges to outer space, and provided a means of transferring information reliably and securely, even through massive jamming. Submarine habitability, lubricants, shipbuilding materials, firefighting, and the study of sound in the sea have remained steadfast concerns, to which have been added recent explorations within the fields of virtual reality, superconductivity, and biomolecular science and engineering.

The Laboratory has pioneered naval research into space—from atmospheric probes with captured V-2 rockets, through direction of the Vanguard project (America's first satellite program), to inventing and developing the first satellite prototypes of the Global Positioning System. Today, NRL is the Navy's lead laboratory in space systems research, fire research, tactical electronic warfare, microelectronic devices, and artificial intelligence.

The consolidation in 1992 of NRL and the Naval Oceanographic and Atmospheric Research Laboratory, with centers at Bay St. Louis, Mississippi, and Monterey, California, added critical new strengths to the Laboratory. NRL now is additionally the lead Navy center for research in ocean and atmospheric sciences, with special strengths in physical oceanography, marine geosciences, ocean acoustics, marine meteorology, and remote oceanic and atmospheric sensing. The expanded Laboratory is focusing its research efforts on new Navy strategic interests and needs in the post-Cold War world. Although not abandoning its interests in blue-water operations and research, the Navy is also focusing on defending American interests in the world's littoral regions. NRL scientists and engineers are working to give the Navy the special knowledge and capabilities it needs to operate in these waters.

2004 IN REVIEW

In the year just past, the scientific community at NRL has conducted innovative research across a wide spectrum of technical areas in addition to that reported elsewhere in this *NRL Review*, and part of this scientific effort is reflected in the following material.

Communications: A problem of recurring importance within the operational Navy is one of general communication. In this area, NRL designed and implemented the first instance of the Global Information Grid Evaluation Facility (GIG-EF), which consisted of interconnecting all-optical networks in the Washington area to MIT Lincoln Laboratory, and across the U.S. using commercial services. Advanced network monitoring tools were developed and deployed. The first Internet working event spanned all of the Services and a number of organizations.

A new signal collection capability was sought by the Office of Naval Intelligence (ONI) in 1999. A quick response system based on NRL analog technology was provided and given the name Cluster Pennant. This system was improved upon by NRL, culminating in the first Advanced Cluster Pennant (ACP) receiver system, which was transitioned to the Fleet as part of the carry-on Cluster Snoop ES system, the first unit being installed in a U.S. submarine in May 2004. Two modified versions of this system were also provided to Fleet Air Reconnaissance Squadron One.

Under the Universal Communications Interface Module (UCIM) project, NRL is applying its advanced C^4I technologies in the development of a universal, integrated, net-centric C^4I architecture for future Marine Corps and Naval systems, and is also developing a set of universal, scalable, production-ready hardware and software modules that implement this architecture, accomplishing net centric integration of voice, data, and video functions within and across the battlespace. UCIM enables operator access to and control of all communications, RF cosite, computers, C^2 applications, sensors, and gateway assets in the system of systems UCIM network.

Nanotechnology: In the advanced area of nanotechnology, a new electronic material composed of an interconnecting network of single-wall carbon nanotubes (SWNTS) has been developed. Single-wall carbon nanotubes are cylinders of C atoms with a wall thickness of one atomic layer, a diameter of one nanometer, and a length of about one micron. This new material, a carbon nanotube network (CNN), is electrically continuous over macroscopic dimensions and can be fabricated into devices using conventional microprocessing technology. The CNN retains the interesting electronic and sensor properties of individual SWNTs. CNNs have application as the transducer for low power chemical sensor arrays and as active semiconductors for electronics flexible substrates.

Nanotechnology also promises to revolutionize biomaterial research involving protein-nanomaterial composites. A system consisting of Rhodamine Red® (RR) fluorophore labeled *E. Coli* maltose binding protein (MBP) coordinated to the surface of a 555 nm emitting quantum dot (QD) was used as a maltose sensor, and variants of the MPB were made to alter the location of the RR attachment. Fluorescence resonance energy transfer studies were performed to determine the distance from each of six unique dye acceptor locations to the center of the energy-donating QD. Critically important is a fundamental understanding of how proteins or bioreceptors interact with inorganic nanomaterials. The approach used here provides a generalized strategy for determining the orientation of a protein on a QD or other spherical nanoparticle.

Radar: During 2004, the Advanced Multifunction Radio Frequency Concept (AMRFC) test-bed development was completed with all major goals accomplished and demonstrated. The goal of the AMRFC Test-Bed Program was to design, build, and test a proof-of-principle system that would allow the integration of many RF functions including radar, communications, and electronic warfare (EW), utilizing a common set of broadband array apertures. The success of this program is critical to the Navy's goal of minimizing the total number of topside antennas on future Navy vessels in an affordable way. To accomplish this task a large, broadly based, Navy-Industry team was formed, led by NRL as the system integrator. It involved several divisions at NRL (Radar, Tactical Electronic Warfare, Information Technology, Optical Sciences, and Space Systems Development), other Navy laboratories (NSWC Dahlgren and NAWC Patuxent River), and numerous major contractors (Northrop Grumman, Lockheed Martin, Raytheon, and General Dynamic-AIS). This first-of-its-kind general purpose RF antenna system has recently demonstrated the following simultaneous functionality: two satellite downlinks (one commercial link, one military link), one full-duplex Tactical Common Data Link (TCDL) from remote air or sea platforms, one navigation radar function, five electronic attack engagements, an electronic surveillance function, and an internal calibration function. Never before have these different classes of RF functions been integrated into a common set of antennas, RF and processing equipment, and real-time control software, much less demonstrated *simultaneously* under real-world conditions in a relevant environment.

Materials/Chemistry: In the area of materials/chemistry, NRL researchers have devised a lightweight, metal-coated microsphere pigment consisting of metal-coated spheres containing a phase change solid/liquid that is capable of both absorbing and reflecting large amounts of thermal energy. The pigment can be incorporated into construction materials or insulation by a relatively low-temperature electroless metal deposition process for coating ultra-thin metallic films onto commercially available encapsulated phase change materials to regulate the temperature of commercial/residential buildings.

NRL research has also enhanced trace detection of illicit materials such as explosives, chemical agents, biological agents, and narcotics. To improve detection limits, a preconcentrator can be used to collect and concentrate an analyte sample over time. A novel analyte preconcentrator, the Cascade Avalanche Sorbent Plate Array (CASPAR), has been developed to enhance trace detection of the illicit materials which is superior to currently available equipment designed for the detection of such materials. CASPAR provides a novel micromachined preconcentrator design that dramatically changes the characteristic performance of preconcentrators.

As a new energy treasure-trove, gas hydrates to be found in world coastal waters and the Arctic permafrost has initiated an NRL methane hydrate program. Gas hydrates (clathrates), estimated to exceed by two to three times the current fossil fuel reserves, may be the next source of clean global energy and are recognized as such by many nations. These hydrates form when water and methane, as a biogenic byproduct during decomposition of organic matter, lie within a specific pressure-temperature regime (≤ 6 °C and ≥ 550 m), remain in the ocean sediment as an ice-like solid. One m^3 of hydrate contains 0.8 m^3 of water and about 164 m^3 of methane. An environmental extra: combustion of methane produces considerably less CO_2 than coal or oil and thus mitigates global warming.

High Energy Beams: With regard to the use of high energy propagation, the Navy has a primary interest in a laser-based, directed energy weapons system. However, the maritime environment is particularly challenging for the propagation of high energy laser because of its relatively high water vapor and aerosol concentration. A number of interrelated physical processes affect and limit the amount of laser energy that can be delivered to a target. To deal with this problem, NRL has developed HELCAP, a High Energy Laser Code for Atmospheric Propagation, a 3-D space + time computer simulation that models all of these physical processes. HELCAP represents the most comprehensive and advanced description of high energy laser pulse propagation in air.

NRL has investigated an alternative approach to high power, solid-state lasers by attempting to reduce the heat generated in yttrium lasers. Fluorescent cooling inside the laser was used to offset the detrimental laser heating. This was accomplished by radiating the excess power away as light, thereby reducing heat generation by more than 100 fold. Reduced heat loads allow higher powers without loss of beam quality or increased complexity. By maintaining overall efficiency while reducing the thermal load, this experimental yttrium laser points the way to revolutionary power and brightness.

Modern radar systems also require reliable high power, solid-state transmitters to extend their radar operational range. For III-N high electron mobility transistors such as aluminum-gallium-nitride/gallium nitride, degradation of the dc, transient, and microwave characteristics are often seen after relatively short service time. To correct this problem, a passivation method involving exposure to a low power NH_3 plasma prior to deposition of a silicon nitride passivation layer has been incorporated into the device fabrication process. This reduces the degradation of the electrical properties caused by extended dc bias or microwave power operation. Devices fabricated using the NH_3 pretreatment show minimal trapping effects after extended dc bias operation and reduction in the microwave power output degradation rate by at least a factor of 100.

Marine Research: Significant advances in the area of observing, measuring, understanding, and predicting the maritime environment were achieved by NRL. NRL's airborne hyperspectral optical sensor, real-time processing and compressing algorithms, and data fusion technologies have opened a broad front for future Naval capabilities as well as being transitioned to industry through industrial CRADAs with NRL.

NRL developed an instrumented field platform, which along with an aircraft-mounted set of laser and other sensors precisely measures the ocean wave spectra, wind speed, and surface currents. Using these sensors and platforms, a series of high resolution, precise field experiments were accomplished and followed by careful physical analysis. The purpose of these developments and experiments was to resolve a long-standing dilemma as to understanding the ocean drag coefficient for derived wind stress from wind speed. This dilemma appears to be resolved. The new understanding requires one to take into account the wavelength of the ocean waves as being a critical parameter in depicting the ocean surface roughness from which one calculates wind stress.

A very high resolution (1-m) circulation model under development for coastal areas and shallow embayments was tested in an operational area (Um Qsar, Iraq). The results forecasting depth-averaged currents in shallow embayments were shown to be greatly affected when shoreline inundation was included. Therefore, for such models, the nature of the underlying bottom (e.g., sand, mud, and rock) in addition to the actual ocean physics (e.g., tides and currents) must be taken into account. A new tool using motion imagery of the nearshore region (beach to just off shore) was developed and is able to estimate both surf wave conditions and bathymetry. The applications for this go beyond DoD to the coastal civil engineering community.

High-resolution tactical weather models and observations are a continuing need for a broad range of Navy and DoD operations. NRL continues to upgrade its Coupled Ocean and Atmosphere Prediciton system (COAMPS®) and enhance ability and utility of NASA, DoD, and other satellite sensors for observing and predicting weather conditions. NRL's excellence in this area was recognized by NRL being a recipient of a NASA Group Achievement Award "in recognition of establishing a Near Real Time Processing and Delivery System providing Earth Observing System (EOS) products to operational agencies."

Field experiments designed to evaluate deoxygenation of natural seawater as a corrosion control measure for protecting seawater ballast tanks demonstrated decreased corrosion in hypoxic seawater, however the experiments also demonstrate the difficulty of maintaining hypoxic seawater and the impracticality of using deoxygenation as a corrosion control measure for unprotected carbon steel ballast tanks.

And as a replacement for battery power, the BUG (Benthic Unattended Generator) is a fuel-like power generator that produces electrical power by oxidizing fuels (produced by naturally occurring microbial processes) at an anode embedded in marine sediment and passing the generated current through an external circuit to the cathode where the reduction of oxidants (O_2, etc., which are present in marine water) occurs. BUG could be used as a power source to replace batteries needed to drive a range of oceanographic instruments.

Techniques to estimate acoustic uncertainty will be required by the next generation of tactical decision aids to determine error bounds on performance predictions. To this end, an analytic technique was developed for transferring oceanographic and bottom uncertainty into acoustic uncertainty under simplified (adiabatic) assumptions concerning the effects of environmental perturbations on acoustic propagation. Full-wave models were used to quantify coupling effects and simultaneously evaluate the full transfer of uncertainty. The transfer of environmental measurement uncertainty to model prediction uncertainty was demonstrated.

Inner/Outer Space: The growth of space-based technologies has made Navy operations (communications, navigation, radiation hazard to satellites and astronauts) increasingly vulnerable to variable Sun emissions. Consequently, there is a need to determine the mechanism for the giant eruptions of the Sun's atmosphere known as coronal mass ejections (CMEs). A theoretical "breakout" model was prepared for the physical origins of CMEs, and a simulation of the complete evolution of a CME as predicted by the model showed that breakout reproduces all the major observed features of CMEs.

There are continuing requirements from NOGAPS weather forecast users for an increase in the skill of numerical weather prediction guidance over longer time, and a new demand for analysis and prediction in the stratosphere and mesosphere for missile defense, high altitude air vehicles, and nonproliferation enforcement. To address this need, various new components to the NOGAPS model have been developed, implemented, and successfully evaluated. Added components include a new vertical structure and new parameterization schemes for model physics and chemistry. Multiyear simulations using climatological boundary conditions have also been performed. The evolution of chemical tracers is well reproduced by the prognostic chemistry routines, and the distribution of gravity wave drag from the orographic, convective, and spectral parameterization schemes correspond well with observed data.

Attention was also paid to more remote space-based phenomena. Starburst galaxies form many massive stars, and these stars are thought to end their lives on short astronomical time scales in huge explosions called supernovae. From the observations of the far infrared dust emission and mid-infrared plasma emission, the massive star formation rate can be calculated and should equal the supernova rate if every massive star produced a supernova. But measures of supernova rate come up lacking. Using an NRL-designed infrared camera on a U.S. Naval Observatory telescope, NRL scientists discovered the third supernova of 2004. This particular supernova was several times fainter at optical wavelengths than expected, which is just the sort of supernova that the NRL program is designed to detect.

In order to use robotic manipulators in the vicinity of a target vehicle or a servicing or construction worksite, algorithms are needed to determine the best trajectory for the robot arm to take in order to accomplish the mission goals. A new optimal trajectory planning algorithm, called Limited-Horizon Planning, has been developed to address this need. Simulation results indicate that the algorithm returns trajectories that are near the quality of transitional optimal trajectory planners, but require approximately two orders of magnitude less computation time to calculate.

NRL TODAY

ORGANIZATION AND ADMINISTRATION

The Naval Research Laboratory is a field command under the Chief of Naval Research, who reports to the Secretary of the Navy via the Assistant Secretary of the Navy for Research, Development and Acquisition.

Heading the Laboratory with joint responsibilities are CAPT David M. Schubert, USN, Commanding Officer, and Dr. John A. Montgomery, Director of Research. Line authority passes from the Commanding Officer and the Director of Research to three Associate Directors of Research, the Director of the Naval Center for Space Technology, and the Associate

Director for Business Operations. Research divisions are organized under the following functional directorates:

- Systems
- Materials Science and Component Technology
- Ocean and Atmospheric Science and Technology
- Naval Center for Space Technology.

NRL operates as a Navy Working Capital Fund (NWCF). All costs, including overhead, are charged to various research projects. Funding in FY04 came from the Chief of Naval Research, the Naval Systems Commands, and other Navy sources; government agencies, such as the U.S. Air Force, the Defense Advanced Research Projects Agency, the Department of Energy, and the National Aeronautics and Space Administration; and several nongovernment activities.

PERSONNEL DEVELOPMENT

At the end of FY04, NRL employed 2810 persons—35 officers, 84 enlisted, and 2691 civilians. In the research staff, there are 819 employees with doctorate degrees, 342 with masters degrees, and 474 with bachelors degrees. The support staff assists the research staff by providing administrative, computer-aided design, machining, fabrication, electronic construction, publication and imaging, personnel development, information retrieval, large mainframe computer support, and contracting and supply management services.

Opportunities for higher education and other professional training for NRL employees are available through several programs offered by the Employee Relations Branch. These programs provide for graduate work leading to advanced degrees, advanced training, college course work, short courses, continuing education, and career counseling. Graduate students, in certain cases, may use their NRL research for thesis material.

For non-NRL employees, several postdoctoral research programs exist. There are also agreements with several universities for student opportunities under the Student Career Experience Program (formerly known as Cooperative Education), as well as summer and part-time employment programs. Summer and interchange programs for college faculty members, professional consultants, and employees of other government agencies are also available.

For more information, see the *NRL Review* chapter, “Programs for Professional Development.”

NRL has active chapters of Women in Science and Engineering, Sigma Xi, Toastmasters International, and the Federal Executive and Professional Association. Three computer clubs meet regularly—NRL Microcomputer User’s Group, NeXT, and Sun NRL Users Group. An amateur radio club, a drama group (the Showboaters), and several sports clubs are also active. NRL has a Recreation Club that provides sports leagues and swim, whirlpool bath, gymnasium, and weight-room facilities. The Recreation Club offers classes in martial arts, aerobics, swimming, and water walking.

The Community Outreach Program traditionally has used its extensive resources to foster programs that provide benefits to students and other community citizens. Volunteer employees assist with and judge science fairs, give lectures, and serve as tutors, mentors, coaches, and classroom resource teachers. The program sponsors African American History Month art and essay contests for local schools, student tours of NRL, an annual holiday party for neighborhood children in December, and a book donation program for both students and teachers. Through the Community Outreach Program, NRL has active partnerships with four District of Columbia public schools.

NRL has an active, growing credit union. Since its creation in 1946, NRL Federal Credit Union (NRLFCU) has grown to about $350 million in assets and serves about 23,000 NRL employees, contractors, select employee groups, and their families. NRLFCU is a leader in providing innovative financial services such as a dynamic home page and online access (Internet home banking) with free bill payer. Focusing on its mission of *Trusted Partners for Life*, NRLFCU offers a wide array of no-fee services plus financial education and assistance. NRLFCU is a full-service financial institution offering various savings programs, creative lending services, and mortage programs. NRLFCU

Guests met with the NRL Federal Credit Union Mascot, the Cash Hound, during the annual “Take Our Children to Work” program.

also offers full-service investment and brokerage services. For information about membership or any financial services, call (301) 839-8400 or click on www.nrlfcu.org.

Public transportation to NRL is provided by Metrobus. Metrorail service is three miles away.

SCIENTIFIC FACILITIES

In addition to its Washington, D.C., campus of about 130 acres and 85 main buildings, NRL maintains 11 other research sites, including a vessel for fire research and a Flight Support Detachment. The many diverse scientific and technological research and support facilities are described in the following paragraphs.

RESEARCH FACILITIES

Institute for Nanoscience

The revolutionary opportunities available in nanoscience/nanotechnology have led to a National Nanotechnology Initiative. NRL has been a major contributor to the science of nanostructures and is making a commitment to expand that effort. The NRL Institute for Nanoscience has been established with a $10 million annual budget in core research funds. The mission of the Institute for Nanoscience is to conduct highly innovative, interdisciplinary research at the intersections of the fields of materials, electronics, and biology in the nanometer-size domain. The Institute will exploit the broad multidisciplinary character of the Naval Research Laboratory to bring together scientists with disparate training and backgrounds to pursue common goals at the intersection of their respective fields at this length scale. The objective of the Institute's programs is to provide the Navy and DoD with scientific leadership in this complex, emerging area and to identify opportunities for advances in future Defense technology.

Its current research program emphasizes multidisciplinary, cross-division efforts in nanoassembly, nanochemistry, nanophotonics, nanoelectronics, and nanomechanics.

Radar

NRL has gained worldwide renown as the "birthplace of radar" and, for a half-century, has maintained its reputation as a leading center for radar-related research and development. A number of facilities managed by NRL's Radar Division continue to contribute to this reputation.

A widely used major facility is the Compact Antenna Range (operated jointly with the Space Systems Development Department) for antenna design and development, as well as radar cross-section measurements. The range is capable of simulating farfield conditions from 1 to 110 GHz, with a quiet zone of approximately 7 ft in diameter and 8 ft in length. Instrumentation covers from 1 to 95 GHz. Another strong division capability is in the Computational Electromagnetics (CEM) Facility, which has capabilities for complex electromagnetic modeling, including radar target and antenna structures. The Radar Signature Calculation Facility within this group produces detailed computations of radar cross sections of various targets, primarily ships. The CEM facility includes multiple-CPU supercomputers that are also used to design phased array radar antennas. There is tremendous synergism between the CEM group and the Compact Range Facility. This provides the ability to design in the CEM environment, test in the compact range, and have immediate feedback between the theoretical and experimental aspects to shorten the development cycle for new designs.

In connection with airborne radar, the division operates a supercomputer-based Radar Imaging Facility and an inverse synthetic aperture radar (ISAR) deployed either in the air, on the ground, or aboard ship for radar-imaging data collection. A P-3 aircraft equipped with the AN/APS-145 radar and cooperative engagement capability is also available for mounting experiments.

The AMRFC testbed, located at NRL's CBD, was developed as a proof of principle demonstration system that is capable of simultaneously transmitting and receiving multiple beams from common transmit and receive array antennas for radar, electronic warfare, and communications. These RF functions are controlled by common resource allocation manager (RAM) software over a real-time control network. New RF functionality may be readily added to the testbed as required for further demonstrations.

In connection with ship-based radar, the division operates the Radar Test Bed Facility at the Chesapeake Bay Detachment (CBD), Randle Cliffs, Maryland. Represented are radars for long-range air search and surface search functions. The CBD facility also features the newly developed W-band Advanced Radar for Low Observable Control (WARLOC). This high-power coherent millimeter wave radar operating at 94 GHz is now fully operational. The transmitter is capable of producing 10 kW of average power with a variety of waveforms suitable for precision tracking and imaging of targets at long range. Waveforms with a bandwidth of 600 MHz can be transmitted at full power. A 6-ft cassegrain antenna is mounted on a precision pedestal and achieves 62 dB of gain.

The Advanced Multifunction RF Concept (AMRFC) testbed is a new installation at CBD, operated by the Radar Division, but with joint participation of several other NRL divisions as well. The goal of the AMRFC program is to demonstrate the integration of many sorts of shipboard RF functions, including radar, electronic warfare (EW), and communications, utilizing a common set of broadband array antennas, signal and data processing, signal generation, and display hardware. The testbed consists of separate active transmit and receive arrays that operate over the 6 to 18 GHz band (nominally). Current functionality of the testbed includes a multimode navigation/surface surveillance Doppler radar, multiple communication links (line-of-sight and satellite), and passive and active EW capabilities. Testbed electronics are housed in seven converted 20-ft shipping containers, or trailers. The arrays are mounted on a 15-degree tilt-back in the ends of two of the trailers overlooking the Chesapeake Bay, emulating a possible shipboard installation.

The division also operates the microwave microscope, a high-resolution (2-cm) capability for investigating backscatter from both surface and volumetric clutter. The division provides direct technical support and has direct access to data from the AN/TPS-71, the Navy's relocatable over-the-horizon radars. Concepts and engineering developments in connection with target identification are explored by using an experimental Cooperative Aircraft Identification system.

Information Technology

The Information Technology Division (ITD) is at the forefront of DoD research and development in artificial intelligence, telecommunications, net-centric distributed computing, human-computer interaction, information security and assurance, parallel supercomputing, and computer science.

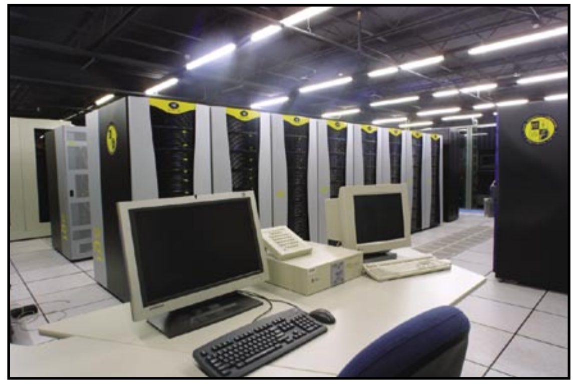

The 256-processor Silicon Graphics Altix 3000 with 1 terabyte of RAM (the first production unit in the world with this capability). It was brought online in the third quarter FY04.

The division maintains local-area computer networks to support its research, and it hosts testbeds for advanced high performance optical network research. These networks make hundreds of high performance computers across DoD available to local and remote users. The ITD research networks connect internal NRL networks via high-speed links to the NASA Science Internet (NSI); to OC-12c (622 Mbps) on DREN/S-DREN; to OC48c on DREN and S-DREN to HPCMP sites; and to OC192c and all optical wavelengths across ATDnet and BoSSNET to form the DoD's Global Information Grid Evaluation Facility (GIG-EF) internetworking facility. GIG-EF provides wavelengths for DoD end-to-end demonstration, system engineering, and experimentation. GIG-EF provides a coalition of early adopters the key test validation infrastructure for transforming the DoD to network-centric IPv6/MPLS convergence for future use by the services, NASA, and Intelligence and Coalition partners.

The ATDnet and BoSSNET also provide the core of an extended all-optical network that supports advanced signaling, routing, and switching research with transparent wavelengths. Major collaborators include the National Security Agency, the Defense Information Systems Agency, the Defense Advanced Research Projects Agency, the Defense Intelligence Agency, the National Aeronautics and Space Agency, the Mid-Atlantic Crossroads (MAX), and the Massachusetts Institute of Technology/Lincoln Laboratory. Optical research includes introduction and testing of new network protocols that emphasize low latency and wave-division multiplexing, greatly increased network capacity for both aggregate and single flows, and the evolution of all-optical networks with direct switching and tuning at the optical layer.

Research of high-end computational assets and networks results in close association with ONR/Naval S&T applications' communities that demand these leading-edge capabilities. This has allowed ITD to achieve significant results in a number of areas. Current efforts include raising the state-of-the-art in motion imagery with progressive scan high-definition sensors and displays where 1 to 10 Gbps data streams are used to handle raw output to disk-based archives. The Motion Imagery Laboratory (MIL) continues exploitation of imagery to provide a flexible, immersive visualization environment for experiments in the convergence of progressive motion imagery; high performance distributed computing; large distributed, federated, scalable petabyte datasets; and dynamic wavelength networking that allow the end user to be enveloped in the data presentation immersively, with a capability for real-time manipulation and fusion.

The Defense Research and Engineering Network (DREN) is a high-speed Continental U.S. (CONUS) network that connects the four High Performance Computing Modernization Program (HPCMP) Major Shared Resource Centers (MSRCs), and the 16 Distributed Centers (DCs), as well as a number of service user organizations that use HPCMP resources.

As one of the HPCMP DC sites, ITD's Center for Computational Science (CCS) supports a range of shared resources, including large memory parallel supercomputers, SAN archives, and high performance networks. Current systems include an SGI Altix 3000 Scalable Linux Supercomputer with Intel Itanium 2 processors (384 Madison) and 1.25 terabytes of shared memory, an SGI Onyx 3400 IR4, and an Onyx4 visualization capability. The Altix supercomputer extends NRL-SGI's first successful attempt to pioneer the use of Linux as the basis of a single scalable shared memory (SHMEM) image supercomputer. A pioneering Multi-Threaded Architecture (MTA) from Cray Systems complements the mix. The Cray MTA is a 44-processor system with 160 gigabytes of flat memory, capable of executing across 128 concurrent threads on each processor. The CCS has approximately 30 terabytes of nearline shared rotating disk and robotic storage for fileserving and archiving that holds 500 terabytes and is capable of multipetabyte scale. The Center manages the NRL local area NICEnet, a fully switched infrastructure based on ATM and gigabit ethernet backbones. The goal of the Center is to provide digital transparency of information resources with security across the information assured infrastructure from globally available archives, to computational engines, to autonomous networks that bring resources together at 10 Gbps directly to desktops of the most demanding researchers. NICEnet provides external connections to other Federal networks and to the Internet.

Division facilities include an Information Security Engineering Laboratory, a Robotics Laboratory, an Immersive Simulation Laboratory, an Audio Laboratory, and a high-data-rate multimedia satellite transmission facility.

The Integrated Communications Testing (ICT) Laboratory houses research facilities for multiple projects. Its primary role is to serve as a platform for researching, testing, and evaluating new protocols and technologies for high-speed terrestrial networks. At the present time, it is heavily used for experimenting with networking technologies that benefit the Joint Forces Command (JFCOM) Modeling and Simulation (M&S) community. It houses a large base of networking equipment that can be used to reproduce large nationwide networks or small specialized networks. The ICT Lab also contains equipment capable of injecting "real-world" conditions into test environments. The test equipment ranges from commercial-grade equipment to specialized software tools developed at NRL. The ICT Lab is connected into the NRL networking infrastructure such that connections across the DREN and other nationwide networks are possible to facilitate collaborative efforts with other DoD/government facilities. Protocol testing of network cryptographic equipment is routinely done in the ICT Lab in conjunction with other affiliated facilities. By using its large base of equipment and rapidly configurable nature, the ICT Lab also serves as a debugging environment for many other projects such as JTF WARNET, Fleet Battle Experiments, and Dragon Warrior. These projects, once proven in the laboratory, are deployed at reduced risk to their execution schedule. The Mobile and Dynamic Networking Laboratory supports development and evaluation of next-generation communication technologies for mobile and dynamic wireless data networks. The research focus of this facility is in challenging network technology areas relevant to military systems operating in dynamic and wireless environments. The Laboratory provides for large-scale network simulation, real-time network emulation, and tools to support live field tests of wireless, mobile networks. The facility has provided support for a variety of ongoing NRL, ONR, and DARPA-sponsored projects including cooperative international research in support of coalition networks.

The General Electronics Environmental Test Facility includes automated electronic test equipment and instrumentation, a phase noise measurement system, a noise figure measurement system, precision spectrum analyzers, wide-band signal generators, a 40-cubic-foot environmental chamber, and an electromagnetic interference (EMI) test chamber located off-site. A variety of additional test equipment including signal generators, signal analysis, stimulation and response measurement equipment, is employed in the performance validation of electronic equipment. This facility provides resources for testing the performance and function of electronic equipment under conditions that represent the environment that the equipment could experience during the deployment to and installation in a Naval ship or Marine Corps tactical environment. Several laboratories are available to test electronic equipment to validate the performance under the conditions described in MIL-PRF-28800F. The test conditions defined in MIL-PRF-28800F are designed to replicate the variety of environmental conditions that test equipment could experience when deployed to the Fleet.

The Naval Cryptographic Technology Laboratory provides a secure environment to perform research and develop prototype programmable cryptographic technologies for Navy and DoD applications. The Laboratory also allows for development of certifiable Communications Security (COMSEC)/Information Security (INFOSEC) products, including programmable cryptographic devices, cryptographic applications, and high assurance guards.

The Naval Key Management Laboratory provides a secure environment to conduct research and develop advanced electronic key management and networked key distribution technologies for the Navy and DoD. This Laboratory, in conjunction with ITD's Naval Cryptographic Technology Laboratory, serves as a testbed for testing new key management components and key delivery protocols developed for the Electronic Key Management System (EKMS) and the modernized Key Management Infrastructure (KMI).

The Fleet Information Systems Security Technology Laboratory (FISSTL) provides unique facilities for NRL research into Navy information technology network security. From architectural design, review, and prototyping, to component evaluation and integration, the FISSTL ensures secure capability and availability of Navy network-centric information operations.

The Virtual Reality (VR) Laboratory provides the facilities and enables NRL scientists to examine virtual reality in a variety of scientific investigations. Research areas include shipboard firefighting, simulation-based design, command and control, and situation awareness for dismounted warfighters.

Current VR technologies available include desktop VR systems, head-mounted displays (HMDs), the Responsive Workbench, and the surround-screen Immersive Room. The Responsive Workbench is an interactive 3-D tabletop environment that displays computer-generated stereographic images on the workbench surface for use in battlespace situation awareness, simulation-based design, and other applications. The surround-screen Immersive Room is a multiuser, high-resolution 3-D visual and audio environment that projects computer-generated images onto three walls and the floor, to create an immersive, large-scale, shared virtual environment.

In addition, the VR Laboratory has a suite of augmented reality hardware available. These technologies include wearable computers, optical see-through displays, vision-and non-vision-based tracking hardware, as well as Global Positioning System (GPS) and inertial sensors.

ITD has the facilities to support a range of motion-based research, from vestibular to ship motion. A one-person, three-degrees-of-freedom platform for vestibular research has been procured recently for NRL-DC.

A second motion-based platform is located at NRL-CBD. The ship motion simulator (SMS), owned and operated by NRL since 1943, has been modified to accommodate four to five experimenters and subjects. The integrated SMS system is designed to evaluate the impact of shipboard motion (pitch and roll) on human performance.

Optical Sciences

The Optical Sciences Division has a broad program of basic and applied research in optics and electro-optics. Areas of concentration include infrared materials and fibers, organic electro-optics, optical signal and information processing, fiber-optic sensors, surveillance and reconnaissance, integrated optical devices, and laser development.

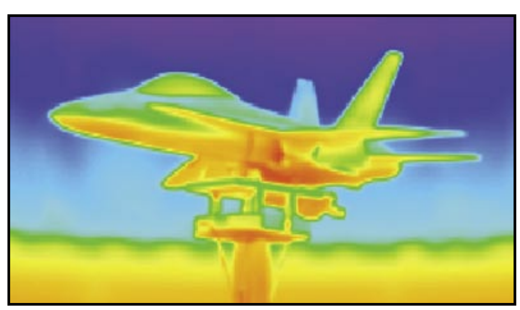

Thermal infrared image of a model of an F/A-18 aircraft while in NRL infrared range.

The division occupies some of the most modern optical facilities in the country. This includes an Ultralow-loss, Fiber-Optic Waveguide Facility using high-temperature infrared glass technology. There is also a Focal-Plane Evaluation Facility to measure the optical and electrical characteristics of infrared focal-plane arrays being developed for advanced Navy sensors. The IR Missile-Seeker Evaluation Facility performs open-loop measurements of the susceptibilities of IR tracking sensors to optical countermeasures. The Large-Optic, High-Precision Tracker system is used for atmospheric transmission and target signature measurements. The Infrared Test Chamber is an ultradry test chamber used to measure the IR signatures of new surface treatments, scale models, and components used for signature control on ships, aircraft, and missiles. A UHV multichamber deposition apparatus for fabrication of electro-optical devices is interfaced to a surface analysis chamber equipped with UPS, XPS, AFM, and STM. Other scanning probe facilities are equipped with Atomic Force and Magnetic Force Microscopes.

There are several fiber-optic sensor facilities with fiber splicers, an acoustic test cell, a three-axis magnetic sensor test cell, equipment for evaluating optical fiber coatings, and various computers for concept analysis. The Digital Processing Facility is used to collect, process, analyze, and manipulate infrared data and imagery from several sources. The Emittance Measurements Facility performs measurements of directional hemispherical reflectance. An extensive set of laboratories exists to develop and test new laser and nonlinear frequency conversion concepts and to evaluate nondestructive test and evaluation techniques.

Mobile Ground Control Station (GCS) for unmanned vehicle research. The Mobile GCS is used for data analysis and provides communication and control to the unmanned vehicles during field experimentation. The photos show a typical field set-up and an internal view of the equipment van.

Electronic Warfare

The scope of the Tactical Electronic Warfare (TEW) Division's program for electronic warfare (EW) research and development covers the entire electromagnetic spectrum. The program includes basic technology research and advanced developments and their applicability to producing EW products. The range of ongoing activities includes components, techniques, and subsystems development as well as system conceptualization, design, and effectiveness evaluation. The focus of the research activities extends across the entire breadth of the battlespace. These activities emphasize providing the methods and means to counter enemy hostile actions—from the beginning, when enemy forces are being mobilized for an attack, through to the final stages of the engagement. In conducting this program, the TEW Division has an extensive array of special research and development laboratories, anechoic chambers, and modern computer systems for modeling and simulation work. Dedicated field sites and an NP-3D EW flying laboratory allow for the conduct of field experiments and operational trials. This assembly of scientists, engineers, and specialized facilities also supports the innovative use of all Fleet defensive and offensive EW resources now available to operational forces through the Naval Fleet/Force Technology Innovation Office.

Laboratory for Structure of Matter

This laboratory investigates the atomic arrangements in materials to improve them or facilitate the development of new substances. Various diffraction methodologies are used to make these investigations. Subjects of interest include the structural and functional aspects of energy conversion, ion transport, device materials, and physiologically active substances such as drugs, antibiotics, and antiviral agents. Theoretical chemistry calculations are used to complement the structural research. A real-time graphics system aids in modeling and molecular dynamics studies. The facilities include three X-ray diffraction units, two being state-of-the-art facilities, and an atomic force microscope.

Chemistry

NRL has been a major center for chemical research in support of naval operational requirements since the late 1920s. The Chemistry Division continues this tradition. It is pursuing a broad spectrum of basic and applied research programs focusing on

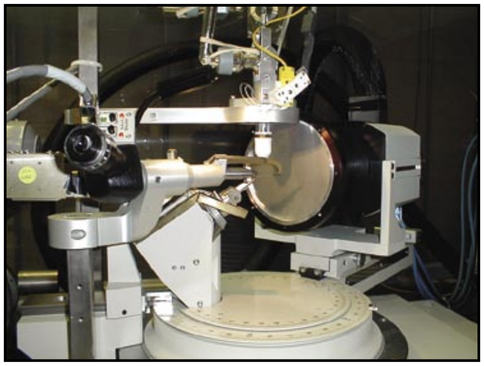

SMART 6000 CCD X-ray detector, which detects the X-ray scattering pattern of interest, is shown mounted on a platform goniometer. The scattering patterns are used to determine the geometric arrangements of molecules in their crystallographic form.

controlled energy release (fuels, fire, combustion, countermeasure decoys, explosives), surface chemistry (corrosion, adhesion, tribology, adsorbents, film growth/etch), advanced materials (high-strength/low-weight structures, drag reduction, damping, polymers, thin films, nanostructures), and advanced detection techniques (environment, chemical/biological, surveillance). Facilities for research include the following:

Chemical Analysis Facilities, with a wide range of modern photonic/electronic, magnetic- and ionic-based spectroscopic/microscope techniques for bulk and surface analysis;

Synchrotron Radiation Facility, with intense, monochromatic X-ray photon beams tunable from 10 eV to 12 KeV available from four beam lines developed by NRL at the National Synchrotron Light Source at the Brookhaven National Laboratory. Environmental target chambers span a pressure range from 10^{-12} to 10^{5} atm and temperatures from 10 to 1500 K;

Nanometer Measurement/Manipulation Facility, which includes fabrication and characterization capability based on scanning tunneling microscopy/spectroscopy, atomic force microscopy, and related techniques;

Materials Synthesis/Property Measurement Facility, with special emphasis on polymers, surface-film processing, and directed self assembly;

Fire Research Facilities, ranging from laboratory combustion chemistry to a 10^4 ft^3 fire-research chamber (Fire I) and the 475-ft ex-USS *Shadwell* (LSD-15) advanced fire research ship;

Commensurate support has been devoted to survivorability of the new classes of ships, DDX, LUN21, LPD17, and LHA(R); and

Marine Corrosion Test Facility, located on Fleming Key at Key West, Florida, offers an ocean-air environment and clean, unpolluted, flowing seawater for studies of environmental effects on materials. Equipment is available for experiments involving weathering, general corrosion, fouling, and electrochemical phenomena as well as coatings, cathodic protection devices, and other means to combat environmental degradation.

Materials Science and Technology

The Materials Science and Technology Division at NRL conducts materials research using seven major division facilities.

Femtosecond laser system for ultrafast dynamics; nonlinear mixing techniques are used to generate femtosecond pulses over a wid
include photochemistry and vibrational energy dynamics of ions in solution and in reverse micelles.

The *Magnetoelectronics Fabrication Facility* consists of a Class 1000 clean room facility equipped with tools for lithographic construction of magnetoelectronic and spintronic devices. It provides pattern definition, metallization, dielectric layer deposition, and both reactive and Ar^+ ion etching of wafers and small pieces.

The *Electrical, Magnetic, and Optical Measurement Facility* is comprised of several complementary instruments that allow for the magnetic, electrical, optical and heat capacity characterization of materials and devices. SQUID and vibrating sample magnetometry are used to determine important properties of superconducting, paramagnetic, diamagnetic, and ferromagnetic materials. The transport properties of materials, namely the temperature and magnetic field-dependent resistivity combined with heat-capacity measurements, allow for a fundamental physical understanding of electronic properties.

The *Materials Processing Facility* includes apparatuses for powder production by fluid atomization, thermal evaporation, arc erosion, and a physical vapor deposition system designed to produce and coat submicron powders, in situ. Facilities to process powder into bulk specimens by hot and cold isostatic pressing permit a variety of consolidation possibilities. Isothermal heat treatment facility and quenching dilatometer permit alloy synthesis and single crystal growth. Bulk alloys can be prepared by induction melting, while rapid solidified metals of thin cross section can be made by splat quenching and melt spinning. Ceramic and ceramic-matrix composites processing facilities include a wide variety of conventional, controlled atmospheric furnaces, hot presses, ball milling apparatus and particle size determination, and sol-gel and organometallic coating processing capabilities.

The *Mechanical Characterization Facility* consists of various testing systems, many with automated computer control and data acquisition, for determining the mechanical response of materials under controlled loading/deformation and environmental conditions. Basic capabilities include quasistatic tensile and fracture testing, dynamic storage and loss moduli as a function of frequency and temperature, cyclic fatigue crack growth and corrosion fatigue testing, and stress-corrosion cracking testing.

The *Thin-Film Materials Synthesis and Processing Facility* provides users a wide variety of techniques for growth and processing of thin films (thickness 1 μm or less). Sputter deposition offers a versatile method of depositing metallic and dielectric films and is a primary tool of this facility. Thermal evaporation of metals is implemented in both high-vacuum and ultrahigh vacuum systems. Pulsed laser deposition (PLD) with temperature-variable stage temperature and controlled atmosphere allows growth of oxides. Electrolytic deposition offers efficient growth of gold and silver films. Laser direct write—both ablation and deposition—provide unique methods for imposing CAD-defined features via ablation of a substrate film and ablative mass transfer to a substrate.

The *3-MV Tandem Pelletron Accelerator Facility* uses two "pelletron" charging chains to produce a terminal voltage up to 3 MV in the accelerator. Negative ions are injected at 10 to 70 keV, accelerated up to the terminal where they undergo collisions with a stripper gas or a carbon stripper foil and lose electrons, then are accelerated as positive ions back to ground potential. Protons can be accelerated up to 6 MeV, He up to 9 MeV, and highly stripped Au (+12) up to 39 MeV. The lower limit of beam energy is about 400 keV. On the analysis beam line, the sample of interest is located

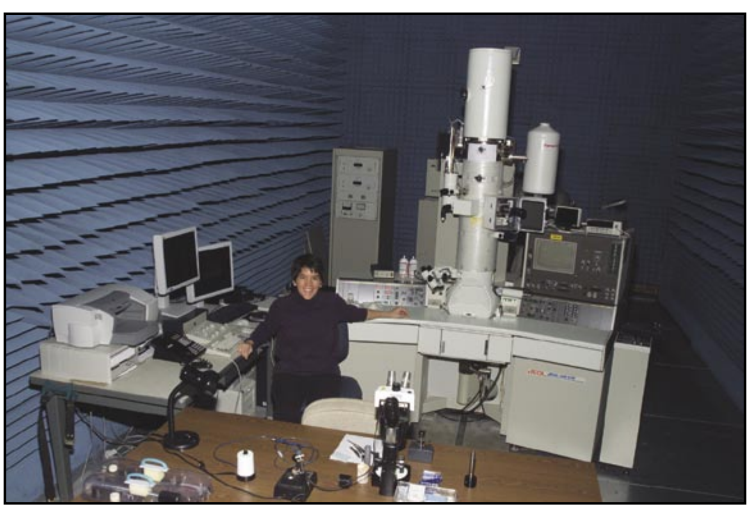

The high-resolution transmission electron microscope allows visualization and quantitative analysis of the sub-nanometer-scale structure and composition of new materials.

at the end of the beam line, and a signal generated by scattering of incident high-energy ions indicates the composition of the sample. Incident high-energy ions can also be used to damage the surface of a sample of interest, or to introduce a dopant.

The *Micro-Nano Structure Characterization Facility* is capable of performing transmission electron microscopy, scanning transmission electron microscopy, ARTEM, electron energy loss spectroscopy, Z-contrast imaging, and spectral imaging through the use of a JEOL 2010F Transmission Electron Microscope, a Phillips CM30 Transmission Electron Microscope, and a Leo Scanning Electron Microscope. Other standard microstructure characterization instruments are also available.

Laboratory for Computational Physics and Fluid Dynamics

The Laboratory for Computational Physics and Fluid Dynamics (LCP&FD) maintains a very powerful collection of computer systems applied to a broad collection of work. There is currently a total of 120 parallel SGI processors, 512 clustered x86 processors, and several other support systems. In addition, there are over 50 Macintoshes in the group, most of which are capable of large calculations both indendently and in parallel ad hoc clusters.

The SGI computer systems comprise a 64 processor Itanium 2 processor SGI Altix, a 12 Itanium 2 processor SGI Altix, a 28 R12K processor Origin 3800, an 8 processor R14K processor Origin, and an 8 R12K processor Origin 2000. There are two 256 x86 processor clusters well coupled with Myrinet high-speed switched interconnect.

Each system has on the order of 200 gigabytes of disk space for storage during a simulation, and at least 512 megabytes of memory per processor. All unclassified systems share a common disk space for home directories as well as almost 250 gigabytes of AFS space, which can be used from any AFS-capable system throughout the allowed Internet.

The AFS capability also allows access to other storage systems including NRL's multiresident AFS (MRAFS) system, which automatically handles archival to a multi-terabyte tape archival system.

Plasma Physics

The Plasma Physics Division is the major center for in-house Navy and DoD plasma physics research. The division conducts a broad experimental and theoretical program in basic and applied research in plasma physics, which includes laboratory and space plasmas, pulsed-power sources, plasma discharges, intense electron and ion beams and photon sources, atomic physics, laser physics, advanced spectral diagnostics, plasma processing, nonlinear dynamics and chaos, and numerical simulations. The facilities include an extremely high-power laser—Pharos III—for the laboratory simulation of space plasmas and nuclear weapons effects studies and two short-pulse high-intensity lasers—the Table-Top Terawatt (T^3) laser and the new Ti:Sapphire Femtosecond Laser (TFL)—to study intense laser-plasma, laser-electron beam, and laser-matter interactions. The division also has an 11-m^3 space chamber capable of reproducing the near-Earth space plasma environment and a Large Area Plasma Processing System (LAPPS) facility to study material modification such as surface polymerization or ion implantation. The division has developed a variety of pulsed-power sources to generate intense electron and ion beams, powerful discharges, and various types of radiation. The largest of these pulsers—GAMBLE II—is used to study the production of megampere electron and ion beams and to produce very hot, high-density plasmas. Other

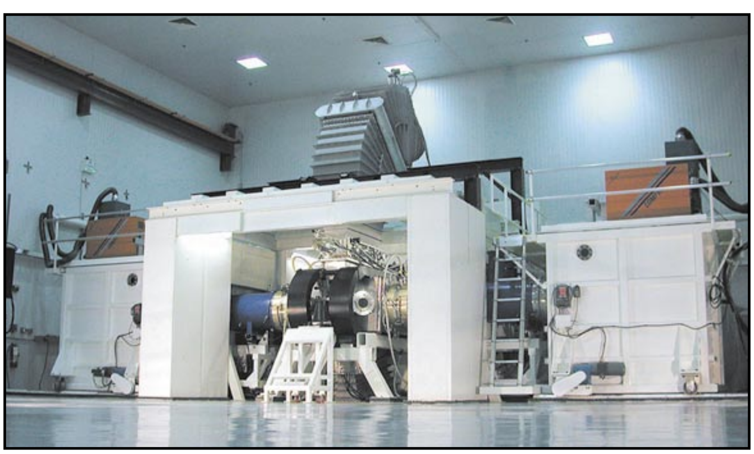

The NRL Electra system is used to develop high-energy high-repetition-rate KrF laser technology. The Electra 30-cm aperture electron-beam-pumped amplifier is shown in the photograph. A portion of the recirculating system that cools the laser gas can be seen at the top. This amplifier is capable of a 5 Hz repetition rate and is expected to produce more than 500 J of laser light per pulse.

generators are used to produce particle beams that are injected into magnetic fields and/or cavities to generate intense microwave pulses. A large array of high-frequency microwave sources (2.45, 35, and 83 GHz) are available to conduct research on microwave processing of advanced ceramic materials. In particular, the division added a 15-kW, continuous wave, 83 GHz gyrotron to its facility for research on high-frequency microwave processing of materials. The Russian-made gyrotron produces a focused, high-intensity millimeter-wave beam ($10^3 – 10^5$ W/cm^2) that has unique capabilities for rapid, selective heating of a wide range of nonmetallic materials. The new gyrotron-based system will be used to investigate the application of such beams to important areas of material processing, including coating of materials, soldering and brazing, and treatment of ceramics, semiconductors, and polymers.

A major 3 kJ KrF laser facility (Nike) opened in June 1995. This facility is made up of 56 laser beams and is single-pulsed (4-ns pulse). This facility provides intense radiation for studying inertial confinement fusion (ICF) target heating at short wavelengths (0.25 μm) and high-pressure physics.

Electronics Science and Technology

The Electronics Science and Technology Division conducts a multidisciplinary basic and applied research program to exploit the creation/discovery/invention of new enabling materials, components, and techniques in electronics. In-house efforts include research and development in solid-state electronics; electronic materials including growth, theory, and characterization of semiconductors, heterostructures, and superconductors; surface and interface science; microwave and millimeter-wave components and techniques; microelectronic device research and fabrication; nanoelectronics science and technologies; vacuum electronics; power electronics; device and process modeling and simulation; and cryoelectronics.

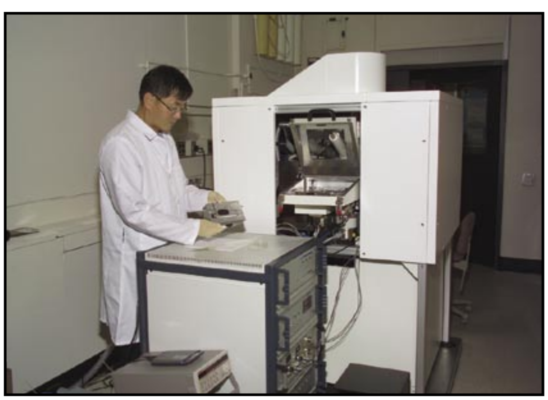

Electronics Science and Technology Division's ultrahigh-resoluton electron beam lithography and metrology system.

In addition to specific equipment and facilities to support individual science and technology programs, the division operates the Compound Semiconductor Processing Facility (CSPF), the Laboratory for Advanced Materials Synthesis (LAMS), the Epicenter, the Vacuum Electronics Fabrication Facility (VEFF), the Ultrafast Laser Facility (ULF), the Wafer Bonding Facility (WBF), and the Space Solar Cell Characterization Facility (SSCCF).

The CSPF is dedicated to processing compound semiconductor devices and circuits, to providing micro- and nanofabrication processing support, and to selectively serve the hands-on fabrication needs of individual division and NRL scientists. The LAMS uses metallorganic chemical vapor deposition to synthesize a wide range of thin films, particularly wide bandgap semiconductors such as GaN and related alloys. The Epicenter (a joint activity of the Electronics Science and Technology, Materials Science and Technology, Optical Sciences, and Chemistry Divisions) is dedicated to the growth of multilayer nanostructures by molecular beam epitaxy (MBE). Current research involves the growth and etching of conventional III-V semiconductors, ferromagnetic semiconductor materials, 6.1 Å III-V semiconductors, magnetic materials, and II-VI semiconductors. The structures grown in this facility are analyzed via in situ scanning tunneling microscopy and angle-resolved electron spectroscopy. The Ultrafast Laser Laboratory is optimized for the characterization of photophysical and photochemical processes in materials on a timescale of tens of femtoseconds. It includes a synchronously pumped dye laser system for simulating the effects of charge deposited in semiconductors characteristic of space radiation. The Wafer Bonding Facility is a Class 100 clean room facility for conducting research on the fabrication of high-voltage wafer-bonded power devices and the development of novel high-performance wafer-bonded substrates for epitaxial growth of both narrow bandgap and wide bandgap material layers. The Power Device Characterization Facility characterizes the performance and reliability of silicon and SiC power devices. The SSCCF studies the effect of particle irradiation on new and emerging solar cell technologies for space applications. The VEFF provides electrical and mechanical design, fabrication, assembly, modification, and repair, as well as processing services for vacuum electronic devices.

Bio/Molecular Science and Engineering

The Center for Bio/Molecular Science and Engineering conducts research and development using biotechnological approaches to support the Navy, DoD, and the nation at-large. Studies are currently underway to investigate biomaterial development (for electronic and structural applications), environmental quality (including pollution cleanup and control), and chemical/biological warfare defense. Other program areas of interest include optical biosensors, nanoscale manipulations, genomics and proteomics, controlled sustained release, bio/molecular and cellular arrays, surface modification and patterning, energy harvesting, viral particles as scaffolds, advanced materials from self-assembly, and liquid-crystal-based electro-optic materials.

The staff of the Center is an interdisciplinary team with expertise in bio- and surface chemistry, biophysics, genetic engineering, cell biology, advanced organic synthesis, solid-state and theoretical physics, and electronics and materials engineering. In addition, the Center has collaborations throughout the Laboratory, with other government laboratories, at universities, and in industry.

The Center occupies laboratories and offices in Buildings 30 and 42. These modern facilities include general laboratories for research in chemistry, biochemistry, molecular biology, and physics. Specialized areas include a 600-ft^2 Class-1000 clean room, an advanced electron microscope facility, and a scanning probe microscope laboratory. Instrument rooms provide access to a variety of spectrophotometers and other equipment used in biochemical or physical analyses of biomaterials. Additional laboratories accommodate an X-ray diffraction instrument, a liquid crystal fabrication facility, and equipment for advanced electronics, microarrays, and biosensor programs. The Center has added a plastic microfabrication facility, which enables fabrication of microfluidic and micro-optical systems in polymers, and a state-of-the-art LC-MS for molecular characterization.

Acoustics

The Acoustics Division has three integrated structural acoustic facilities—two pools (including one with a sandy bottom) and a large in-air, semi-anechoic laboratory—that support research in submarine target characteristics for antisubmarine warfare, submarine acoustic design and quieting, sensors for hull-mounted sonars, mine detection and identification, torpedo quieting, and interior noise control in air platforms and submarines. Scaled submarine structures, real mines, sensors on hull simulators, underwater buried objects, torpedoes, aircraft fuselages, and space payload launch fairings and containers can all be examined with advanced nearfield holographic and scanning 3-D laser vibrometer systems to measure nearfield, farfield, and interior sound fields as well as the physics of the sound-structure-fluid interactions.

The division operates state-of-the-art laboratories equipped to study the structural dynamics and performance of high-Q oscillators and other micro-mechanical systems. A number of laser Doppler vibrometers, including a super-resolution nearfield scanning optical microscope (NSOM), permit spatial mapping of the complex vibratory motion down to resolutions of 100 nm. The laboratories include the ability to measure the mechanical and electrical properties of the micro-oscillators, and of thin films applied to them, down to 370 mK.

The division operates a portable, ocean-deployable synthetic aperture acoustic measurement system. The primary elements are sources and receivers attached to a robotic carriage that can be positioned precisely at any point along a 100-meter rail using an encoder feedback system. A separate source tower enables

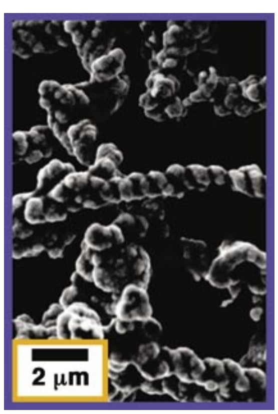

Metallic Cu spiral/helical nanostructures prepared via selective electroless metallization of a phospholipid microtubule template.

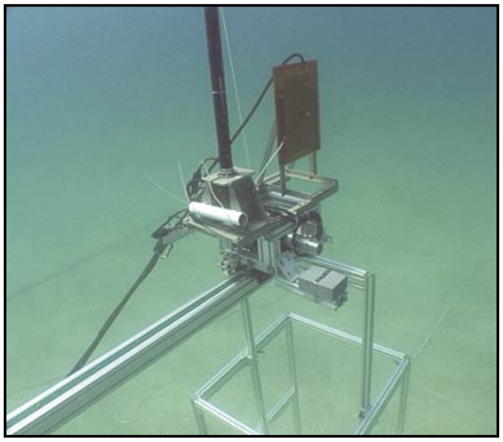

The 100-meter underwater rail-based synthetic aperture acoustic measurement system. Sources and receivers can be attached to a robotic carrier (shown here at one end of the rail). The carriage is shown in a monostatic configuration with integrated broadband projector (rectangle) and vertical receiver array (black cylinder).

bistatic scattering data collection. Bidirectional control and data transfers are made over a dedicated RF link to a surface platform. This facility supports the collection of high quality, scattering cross sections of mines, and the associated clutter necessary for the implementation of new broadband MCM technologies on UUVs.

The Acoustics Division Salt Water Tank Facility is designed to provide a controlled environment for studying a variety of complex ocean processes under saline conditions, especially the study of the acoustics of bubbly media. Instrumentation includes acoustic sources, amplifiers, hydrophones, environmental sensors, a digital holographic imaging system, high-speed digital cameras, and a LabVIEW-based data acquisition system.

The division operates several sound sources for the generation and reception of sound in at-sea experiments. Sound sources include three XF-4 units, one ITC 2077 source that can be operated while being towed by a ship, two battery-operated organ-pipe sources that can project single tones from offboard moorings, and a towable, directional source array for active sonar studies consisting of 10 individually controllable elements, at frequencies 2.5 to 5 kHz. In addition, the division has several battery-operated rubidium-clock-controlled, programmable sound source moorings that can transmit sounds having arbitrary waveforms.

The division has a 64-channel broadband source-receiver array with time-reversal mirror functionality. Projects involving scanning focused acoustic fields and phase conjugation for multistatic sonar will utilize the new array to test and study time reversal methods. The transducers for the array are 6-in. spheres that operate from 500 to 3500 Hz.

The Acoustics Division performs research to relate acoustic array gain variability to fluid dynamic variability and bottom-heterogeneity in the littorals. The measurements are made with an autonomous acoustic data acquisition suite. Three independent autonomous 32-channel vertical arrays and a 465-m 96-channel horizontal array receive and store 24-bit data at a 4 kHz sample rate for 22 days. The acoustic sources operate at 300 and 500 Hz center band with ±10% bandwidth and generate programmable waveforms at 50% duty cycle for 22 days. As presently configured, the systems will operate to water depths of 500 m. The division also has unique, self-recording digital acquisition buoy systems (DABS) that are used to obtain multichannel (up to 128) acoustic data in the 10 Hz to 5 kHz regime. These systems provide up to 250 gigabytes of data on a single 15-in. reel of 1-in. tape.

The Acoustics Division has a radio-controlled buoy system with underwater receive arrays to collect acoustic and oceanic data, unattended, for periods of up to one month. The system can currently handle 64 channels of acoustic data (distributed on one or two arrays), and can implement onboard signal processing prior to data transmission. The system contains a high-speed line-of-sight data link utilizing a GPS-linked directional antenna. A low-speed command and control link is available to remotely control buoy functions and array settings.

The division conducts research addressing the channel capacity of multinode underwater acoustic communications networks. The research is conducted in the 1 to 10 kHz and 10 to 20 kHz frequency band using four 8-channel acoustic communications data acquisition systems or modems, which can be moored or towed.

A narrow beam 200 and 350 kHz acoustic backscattering (flow visualization) system is used to study fine structure, internal wave, and larger scale fluid dynamic perturbation of the density and sound speed field in the ocean. It consists of a deck-mounted towing assembly, power amplifiers, and a real-time display and digital data acquisition system. A 25 kW radar system is used in conjunction with the flow visualization system to record the surface expression of internal waves.

The division operates high-frequency (up to 600 kHz) acoustic measurement systems to obtain scattering, target strength, and propagation data using bottom-moored instrumentation towers and a high-speed, remotely operated vehicle. These data are used to simulate the performance of weapons and mine countermeasure sonars.

The Tactical Oceanography Simulation Laboratory (TOSL) is a modeling and simulation architecture consisting of a set of tools for processing climatology and real-time environmental data and applying energy propagation models to those data. TOSL features a high performance computational capability to provide calculations in support of training, war games, operations rehearsal, and other distributed simulation functions. TOSL is coupled via Ethernet and SIPRNET with the Tactical Oceanography Wide Area Network (TOWAN) repository of environmental data, which allows full participation in a distributed simulation environment.

Remote Sensing

The Remote Sensing Division conducts a program of basic research, science, and applications to develop new concepts for sensors and imaging systems for objects and targets on Earth, in the near-Earth environment, and in deep space. The research, both theoretical and experimental, leads to discovery and understanding of the basic physical principles and mechanisms that give rise to background environmental emissions and targets of interest and to absorption and emission mechanisms of the intervening medium. Accomplishing this research requires the development of sensor systems technology. The developmental effort includes active and passive sensor systems used for study and analysis of the physical characteristics of phenomena that evolve from naturally occurring background radiation, such as that caused by the Earth's atmosphere and oceans, and man-made or induced phenomena, such as ship/submarine hydrodynamic effects. The research includes theory, laboratory, and field experiments leading to ground-based, airborne, or space systems for use in remote sensing, astrometry, astrophysics, surveillance, nonacoustic ASW, meteorological/oceanographic support systems for the operational Navy, and the environmental/global climate change initiatives. Special emphasis is given to developing space-based platforms and exploiting existing space systems.

The Remote Sensing Division conducts airborne hyperspectral data collections for characterization of the environment. Hyperspectral data are series of pictures, taken simultaneously, of a scene at many different wavelengths (colors). The sensors are built and calibrated in-house, although they rely heavily on commercial off-the-shelf elements. The most recent sensor was specifically designed for use over ocean areas. It covers the 400 to 1000-nm wavelength range with 128 different wavelengths (channels). The sensor consists of a standard video camera lens, a grating spectrograph, and a 1024 × 1024 pixel charge-coupled device (CCD). The spectrograph and CCD are specially designed to achieve high sensitivity in the blue end of the spectrum to optimize water-penetrating measurements. This makes possible measurements such as the determination of the ocean bottom type (coral, sea grass, sand, rock, etc.) to water depths of as much as 20 m (in clear water) and the identification of material in the water column (phytoplankton, sediments, colored dissolved organic matter, etc.). The sensor is very compact and can be flown at heights of 8000 to 10,000 ft, simply "looking" out of a hole in the bottom of the airplane. At ground speeds of 90 kts, the data can still be collected digitally and stored on computer. They are then processed in a ground system operating on a standard personal computer.

Proper interpretation of the hyperspectral data requires calibration of the sensor. This means both radiometric and spectral calibration. The latter plays a critical role in the successful correction of the data for atmospheric effects. The Remote Sensing Division operates an Optical Calibration Facility to perform these calibrations. NIST radiometric standards are transferred to a large integrating sphere. The integrating sphere has 10 precisely controlled quartz-halogen lamps to enable linearity measurements. A set of gas emission standards provides wavelength calibration. As a result, the complete process of data collection through data analysis can be handled in-house.

To validate the results of airborne hyperspectral sensing and to support interpretation of the physical processes they reveal, the Remote Sensing Division has developed a Profiling Optics Package. This system measures the inherent optical properties of water (absorption, attenuation, and scattering) in the 400 to 700-nm range, and collects water samples for various laboratory measurements. The package was built around a Seabird Rosette frame and includes a WETLabs Histar meter to measure water absorption and attenuation at 103 wavelengths; an unfiltered

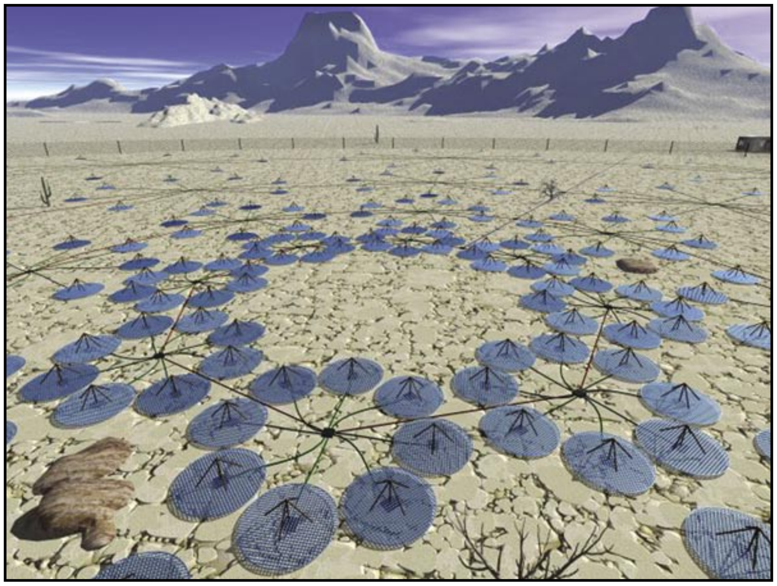

Artist concept of the future Low Frequency Radio Array (LOFAR) telescope.

The Navy Prototype Optical Interferometer (NPOI) is used for both operational astrometry and for development of distributed aperture imaging techniques.

WETLabs ac9 meter to measure water absorption and attenuation at nine wavelengths; a filtered WETLabs ac9 meter to measure colored dissolved organic matter (CDOM) absorption and attenuation at nine wavelengths; a HOBILabs Hydroscat to measure backscattering of water in six wavelengths; a WETLabs WetStar fluorometer to measure stimulated fluorescence of chlorophyll; a Seabird CTD to measure conductivity (salinity), temperature, and depth; and eight sample bottles to collect up to 20 liters of water. Data from each sensor are collected and archived inside a WETLabs Super MODAPS instrument. They are then transmitted to the surface via an armored sea cable, where they are stored on a computer disk. The package has a maximum depth rating of 300 meters, although it is usually operated in coastal waters of less than 50 meters.

The Navy Prototype Optical Interferometer (NPOI), a major facility of the Remote Sensing Division, is actually two collocated instruments for making high-angular-resolution optical measurements of stars. Light from widely separated individual siderostats is combined simultaneously to synthesize the angular resolution of a telescope tens to hundreds of meters in diameter. Four siderostats are placed in an array with extremely accurate metrology to enable very-high-precision measurements of stellar positions (wide-angle astrometry). These measurements are used by the U.S. Naval Observatory to refine the celestial reference frame, determine Earth rotation parameters, and thus satisfy Navy requirements for precise time and navigation data. They also provide determinations of basic astrophysical parameters, such as stellar masses and diameters. Additional relocatable siderostats can be placed out to distances of 250 m from the array center and used to construct very-high-resolution images of stars. These images provide fundamental astrophysical information on stellar structure and activity. When complete, the NPOI will be the most advanced high-resolution imaging optical interferometer in the world.

To validate numerical and theoretical efforts ongoing within the Remote Sensing Division, extensive hierarchical-coupled experiments are carried out in the Free-Surface Hydrodynamics Laboratory. This laboratory is used to study free-surface turbulence interactions, wave-generation phenomena, jet-flow phenomena, vorticity dynamics, and free-surface/surfactant interactions. Emphasis is placed on those processes that determine the fluxes of heat, mass, and momentum across the air-sea interface. State-of-the-art diagnostic tools are available, such as Langmuir film balance to measure the properties of surface films, hot-wire and laser-Doppler anemometry, and the new quantitative flow techniques of laser speckle, particle tracking, and particle image velocimetry. The laboratory is also equipped with an IR camera with a 20×10^{-3} K resolution. These experimental diagnostic techniques use high-powered lasers, high-tolerance optical lenses, and extensive ultra-high-resolution video-imaging hardware and PC-based computerized systems. Further computational assets consist of powerful graphical computer work stations, the NRL Connection Machine, and other off-site Cray supercomputer systems.

The Airborne Polarimetric Microwave Imaging Radiometer (APMIR) is a state-of-the-art multichannel microwave radiometer system being designed and built by the Remote Sensing Division. APMIR is being developed in response to the emerging need for extensive airborne calibration and validation of spaceborne remote sensing assets: the SSMIS, WindSat, and CMIS spaceborne microwave imaging systems. APMIR will cover five frequency bands: 5-7, 10.7, 18.7/19.35, 22.23/23.8, and 37.0 GHz. Frequency agility allows for frequency matching to each of the spaceborne systems of interest. The 10.7, 18.7/19.35, and 37.0 GHz channels are fully polarimetric, and will thus measure the ocean surface wind speed and direction. The 5 to 7 GHz channel simultaneously observes several frequencies, providing sensitivity to sea surface temperature; the means to separate rain effects from surface effects; and protection from radio frequency interference (RFI). The 22.23/23.8 GHz channels respond to the atmospheric water vapor in the column below the aircraft, while the 18.7/19.35 and 37.0 GHz channels are sensitive to both ocean surface and cloud parameters. The APMIR system will be mounted in the bomb bay of the NRL P-3 aircraft and flown at altitudes ranging from 500 to 25,000 ft over the ocean.

Oceanography

The Oceanography Division is the major center for in-house Navy research and development in oceanography. It is known nationally and internationally for its unique combination of theoretical, numerical, experimental, and remotely sensed approaches to oceanographic problems. The division modeling focus is on a truly integrated global-to-coastal modeling strategy, from deep water up to the coast including straits, harbors, bays, and inlets. This requires emphasis on both ocean circulation and wave/surf prediction, with additional emphasis on coupling the ocean models to biological, optical, and sediment models. This modeling is conducted on the Navy's and

DoD's most powerful vector and parallel-processing machines. To study the results of this intense modeling effort, the division operates a number of highly sophisticated graphic systems to visualize ocean and coastal dynamic processes. The seagoing experimental programs of the division range worldwide. Unique measurement systems include a wave measurement system to acquire in situ spatial properties of water waves; a salinity mapper that acquires images of spatial and temporal sea surface salinity variabilities in littoral regions; an integrated absorption cavity, optical profiler system, and towed optical hyperspectral array for studying ocean optical characteristics; and self-contained bottom-mounted upward-looking acoustic Doppler current profilers for measuring ocean variability. Specifically, NRL is working jointly with NATO Undersea Research Center (NURC) for development and deployment of the SEPTR instrument. This is a trawl-resistant, bottom-mounted ADCP system that includes a pop-up profiling float for real-time observation and reporting.

In the laboratory, the Division operates an environmental scanning electron microscope for detailed studies of biocorrosion in naval materials. The Division's remote sensing capabilities include the ability to analyze and process multi/hyperspectral, IR, SAR, and other satellite data sources. The division is a national leader in the development and analysis of Sea WiFS data for oceanographic processes and naval applications in littoral areas.

SEPTR is the prototype of a trawl-resistant, bottom-mounted ADCP system that includes a pop-up profiling float for real-time observation and reporting. After a successful test in the Adriatic Sea in May 2003, SEPTR is being winched aboard NURC's research vessel *Alliance*. NRL and NURC continue a cooperative agreement for engineering development of SEPTR and for deployment of several in a real-time environmental assessment system.

Marine Geosciences

The Marine Geosciences Division is the major Navy in-house center for research and development in marine geology, geophysics, geodesy, geoacoustics, geotechnology, and geospatial information and systems. The division has unique suites of instrumentation and facilities to support laboratory and field experimental programs.

The instrumentation used in the field experiments is deployable from ships, remotely operated and unmanned vehicles, and airborne platforms and by divers. Instrumentation includes an integrated airborne geophysical sensor suite with gravity, magnetic, and sea/ice/land topographic profiling sensors, all based on cm-level KGPS aircraft positioning. Seafloor and subseafloor measurements use the Deep-Towed Acoustic Geophysical System (DTAGS—220 to 1000 Hz); chirp sub-bottom profiler; high-resolution sidescan sonars (100 and 500 kHz); the Acoustic Seafloor Characterization System (ASCS-15, 30, and 50 kHz); an optically pumped marine magnetometer; several gravimeters; the In Situ Sediment Acoustic Measurement System (ISSAMS); underwater stereo photography; and nearshore video imaging systems. ISSAMS has specialized probes that measure acoustic compressional and shearwave velocities and attenuation, sediment shear strength, and electrical conductivity in surficial marine sediments.

Five instrumented, 8-ft-long, 2220-lb, minelike cylinders are used to gather impact burial data (one system) and scour and sand wave burial data (four systems) for validation of mine burial prediction models.

Laboratory facilities include sediment physical, geotechnical, and geoacoustic properties and sediment core laboratories. The Electron Microscopy Facility is the focal point for research in microscale biological, chemical, and geological processes. The key instrumentation includes a 300 kVa transmission electron microscope with environmental cell. The environmental cell allows hydrated and gaseous experiments.

A high-resolution industrial CT scanner is a recent addition to the laboratory. It will be used for investigating volumetric heterogeneity of sediments.

The Moving Map Composer Facility is used to design and write mission-specific map coverages for F/A-18 and AV-8B tactical aircraft onto militarized optical disks. The National Geospatial-Intelligence Agency also uses this state-of-the-art computer facility to update the compressed aeronautical chart library on CD for distribution. The Geospatial Information Data

Base (GIDB) capability provides Internet access to the Digital Nautical Chart data, mapping data, imagery, and other data types such as video and pictures. This development tool can be used for planning, training, and operations.

Marine Meteorology

The Marine Meteorology Division is located in Monterey, California. NRL-Monterey (NRL-MRY) serves the Navy's needs for basic and applied research in atmospheric sciences and develops meteorological analysis and prediction systems and other products to support global and tactical operations.

NRL-MRY is collocated with Fleet Numerical Meteorology and Oceanography Center (FNMOC), the Navy's operational center of expertise in numerical weather prediction (NWP) and satellite data products. NRL-MRY's Atmospheric Prediction System Development Laboratory has direct connectivity to the FNMOC internal network, which provides NRL-MRY with efficient access to a variety of classified and unclassified computer resources and databases to support development and transition of operational analysis and prediction systems. In addition, interfaces to the Defense Research and Engineering Network provide access to the DoD High Performance Computing resources, which can be accessed directly from any office in the Atmospheric Research Laboratory via a recently upgraded network that offers gigabit/second speed to the office capability. NWP and aerosol prediction system development is further supported by the in-house Daley Supercomputer Resource Center, which currently includes an SGI Origin 2000 128-processor supercomputer and a 44-processor LINUX cluster. These computers are supported by a 28-terabyte Storage Area Network, which enables the division to save observational and model output data to support research in atmospheric processes and development of improved numerical prediction systems for Fleet operations around the globe.

The Mobile Atmospheric Aerosol and Radiation Characterization Observatory (MAARCO) can be deployed in areas with limited facilities, even onboard ship, to gather data to support research on atmospheric aerosols, gases, and radiation. In August 2004, MAARCO was used in a field experiment in the United Arab Emirates.

A state-of-the-art Satellite Data Processing Laboratory allows local collection of real-time NOAA geostationary data (imagery and sounder data from GOES-E and GOES-W) and supports real-time data feeds via FNMOC and the Air Force Weather Agency for the remaining three geostationary satellites and a number of polar orbiting satellites (3 from NOAA, 4 from the Defense Meteorological Satellite Program, and 5 from NASA—Tera, Aqua, TRMM, SEAWifs, and QuikScat). All together, NRL-MRY processes data from 22 low-earth orbiting sensors and uses these data along with geostationary satellite data to conduct research and develop multisensor, multiplatform products for a variety of DoD operations, from monitoring and analyzing tropical cyclone intensity in support of the Joint Typhoon Warning Center to providing dust enhancement imagery in support of strike warfare operations in Southwest Asia. These products are typically transitioned to FNMOC or to one of the Navy's regional METOC centers, which use their local FMQ-17 to process satellite data using algorithms developed by NRL for data display on the TeraScan system. The Satellite Data Processing Laboratory is supported by the 24-terabyte Bergen Data Center, which has a hierarchical storage management capability to provide archival and easy retrieval or research data sets. The Bergen Data Center also provides support for the data that is archived as part of the Master Environmental Library.

NRL-MRY's Classified Satellite/Radar Data Processing Facility, consistent with the FORCEnet vision, hosts classified computer systems for receiving, processing, and storing classified and unclassified satellite, radar, and observational data and development of applications using those data. This facility has a 10-node LINUX cluster for high performance computing, two LINUX workstations for data processing, a LINUX database workstation and two desktop computers, along with a 128 Kb SIPRNET connection in a shielded workspace. This facility provides the environment for the classified high-resolution data integration and fusion technology development using through-the-sensor data collected from shipboard weather radars and direct broadcast low-earth orbiting meteorological satellite sensors to generate products for direct dissemination to the tactical decision-makers.

To support the division's growing program in aerosol research and aerosol prediction system development, NRL-MRY has designed and built the Mobile Atmospheric Aerosol and Radiation Characterization Observatory (MAARCO). MAARCO is a modified 20-ft × 8-ft climate controlled container that contains an integrated suite of meteorological, aerosol, gas, and radiation instruments, with space maintained for guest instrumentation. The radiation suite includes an AERONET Sun Photometer, solar and IR radiometers, a Total Sky Imager, and a Micro-pulse Lidar. A 3-wavelength Nephelometer; Aerodynamic Particle Size, total suspended particulates (TSP) filter sampler; tapered-element oscillating microbalance (TEOM) sampler; SO2 and Ozone monitors; and a Micro-Orifice Uniform Deposit Impactor (MOUDI) sampler complete the aerosol and gas suite. Meteorological data are provided by a weather station and a Rawinsonde system. MAARCO can be easily deployed in areas with limited facilities, thereby enabling research on atmospheric aerosols, gases, and radiation in areas of key interest, including remote areas, overseas locales, and onboard ships.

In addition to computational and instrumented facilities, NRL-MRY's research program is supported by an on-site library, which maintains current and past copies of most of the U.S. and many of the international journals dedicated to the atmospheric, oceanographic, and computational sciences, as well as a number of reference books and hundreds of scientific texts in the mathematical, physical, and earth sciences. The library also serves as a repository for technical publications from a number of national and international institutions engaged in atmospheric and oceanographic research, including technical reports from the laboratories that preceded NRL at the Monterey site. The Monterey library also maintains historical and current copies of the graduate theses and dissertations written by students in meteorology and oceanography at the Naval Postgraduate School.

Space Science

The Space Science Division conducts and supports a number of space experiments in the areas of upper atmospheric, solar, and astronomical research aboard NASA, DoD, and other government agency space platforms. Division scientists are involved in major research thrusts that include remote sensing of the upper and middle atmospheres, studies of the solar atmosphere, and astronomical radiation ranging from the ultraviolet through gamma rays and high-energy particles. In support of this work, the division maintains facilities to design, construct, assemble, and calibrate space experiments. A network of computers, workstations, image-processing hardware, and special processors is used to analyze and interpret space data. The division's space science data acquisition and analysis efforts include: data analyses of the Oriented Scintillation Spectrometer Experiment (OSSE) for NASA's Compton Observatory; observation of the Sun's interaction with the Earth's upper atmosphere through the Solar Ultraviolet Spectral Irradiance Monitor (SUSIM) experiment in support of NASA's Upper Atmosphere Research Satellite (UARS); observation and analysis of solar flares using the Bragg Crystal Spectrometer (BCS) on the Japanese Yohkoh space mission; and observation and analysis of the evolution and structure of the solar corona from the disk to 0.14 AU. This latter effort involves acquiring and analyzing data from the Large-Angle Spectrometric Coronagraph (LASCO) and the Extreme Ultraviolet Imaging Telescope (EIT) on the Solar Heliospheric Observatory satellite. In each of these missions, NRL maintains a complete database of spacecraft observations and control over acquisition of data from new observations. These data are available to qualified investigators at DoD and civilian agencies. In addition, the division has a sounding rocket program that affords the possibility of obtaining specific data of high interest and of testing new instrument concepts. These include the general area of high-resolution solar and stellar spectroscopy, extreme ultraviolet imagery of the Sun, and high-resolution, ultraviolet spectral-imaging of the Sun.

Division scientists have developed and maintain physical models in support of their research, including Mass Spectrometer and Incoherent Scatter Radar (MSIS), the standard model for the density of the upper atmosphere; Global Assimilation of Ionospheric Measurement (GAIM), a physics-based model of the ionosphere; Navy Operational Global Atmospheric Prediction System (NOGAPS-HI), a model to extend weather modeling into the upper atmosphere; Cosmic Ray Effects on Micro Electronics (CRÈME), the standard model of the effect of energetic solar particles and cosmic rays; and many others.

The division is currently developing a number of new space instruments, including: Sun Earth Connection Coronal and Heliospheric Investigation (SECCHI), the coronagraph and solar disk imagers for NASA's STEREO mission; Extreme Ultraviolet Imaging Spectrometer (EIS), the extreme ultraviolet imaging spectrometer for Japan's SOLAR-B mission;

Gamma Ray Large Area Space Telescope (GLAST), a high energy gamma ray detector for NASA; Spatial Heterodyne Imager for Mesopheric Radicals (SHIMMER), a Michelson interferometer for upper atmospheric research for a DoD mission; and Tether Physics and Survivability Experiment (TiPS), ultraviolet spectrometers for upper atmospheric research for Taiwan's COSMIC program.

Optical calibration facilities, including clean rooms, are maintained to support these activities. These calibration facilities are routinely used by outside groups to support their own calibration requirements.

Space Technology

In its role as a center of excellence for space systems research, the Naval Center for Space Technology (NCST) designs, builds, analyzes, tests, and operates spacecraft and identifies and conducts promising research to improve spacecraft and their support systems. NCST facilities that support this work include large and small anechoic radio frequency chambers, clean rooms, shock and vibration facilities, an acoustic reverberation chamber, large and small thermal/vacuum test chambers, a spacecraft robotics engineering and control system interaction laboratory, satellite command and control ground stations, a fuels test facility, and modal analysis test facilities. Also, the Center maintains and operates a number of electrical and electronic development laboratories and fabrication facilities for radio frequency equipment, spacecraft power systems, telemetry, and command and control systems, and includes an electromagnetic interference-electromagnetic compatibility test chamber. NCST has a facility for long-term testing of satellite clock time/frequency standards under thermal/vacuum conditions linked to the Naval Observatory; a 5-m optical bench laser laboratory; and an electro-optical communication research laboratory to conduct research in support of the development of space systems.

RESEARCH SUPPORT FACILITIES

Exhibits/Multimedia Office

This office designs and develops full-sized and portable displays and posters for technical conferences and symposia, briefings on Capitol Hill, at DoD installations, Laboratory special events, and public events. The NRL booth at trade shows and technical conferences provides a platform for scientists and engineers to market research projects and also enhances NRL's technology transfer efforts.

The Exhibits Office also designs and develops static displays for buildings, i.e., wall arrangements, division research highlights, and award panels and cases. The static displays found in Buildings 72, 43, 226, 28, 222, and Quarters A are maintained by the Exhibits Office. Other available services to the researcher and Lab management are: assistance in presentation development including research, writing, layout, design, photo/video archival searches, and finalized vugraph/computer presentation products; and acting as a translator between the researcher and

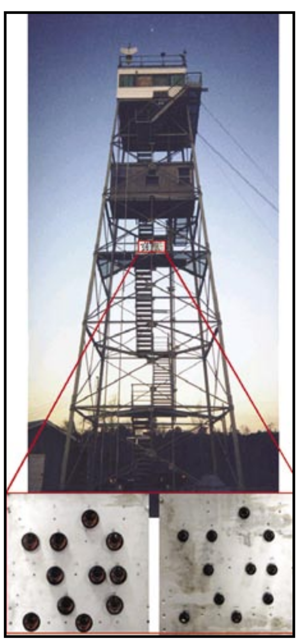

Retro-reflectors on NRL's Tilghman Island tower on the eastern shore of the Chesapeake Bay. These retro-reflectors and a transceiver at NRL's Chesapeake Bay Detachment are used to test long-range free-space laser communication links in a maritime environment. Laser communication links at data rates up to 2.5 Gbps have been successfully demonstrated over this 32-km test range.

the artist to assist researchers in developing the artist's concept that visually explains their research concept.

The Exhibits Office produces, directs, and develops multimedia products (CD-ROMs, videos, and films) to enhance exhibits at trade shows and to directly support Laboratory presentation capabilities needed for briefings to existing sponsors, potential sponsors, Congressional representatives, and for recruitment and special events. The most recent "A Tour of NRL" has won four international awards: the Crystal, the Gold Aurora, and two Bronze Tellys.

Technical Information Services

The Technical Information Services Branch combines publications, graphics, photographic, multimedia, and video services into an integrated organization. Publication services include writing, editing, composition, publications consultation and production, and printing management. Quick turnaround digital black-and-white and color copying/printing services are provided. The primary focus is to use digital publishing technology to produce scientific and technical reports that can be used for either print or Web. Graphic support includes technical and scientific illustrations, computer graphics, design services, photographic composites, display panels, sign making, and framing. The NovaJet Pro 600e and HP Designjet 5500ps printers offer exceptional color print quality up to 600 dpi. They produce large-format indoor and outdoor posters and signs with 48 inches being the limitation on one side. Lamination and mounting are available. Photographic services include digital still camera coverage for data documentation, both at NRL and in the field. Photographic images are captured with state-of-the-art digital cameras and can be printed on a variety of digital media. Photofinishing services provide automatic and custom printing from digital files on a new digital minilab. Quick-service color prints are also available. Video services include producing video reports of scientific and technical programs. Digital video editing equipment is available to support video production and produce QuickTime movies.

Administrative Services

The Administrative Services Branch is responsible for collecting and preserving the documents that comprise NRL's corporate memory. Archival documents include personal papers and correspondence, laboratory notebooks, and work project files—documents that are appraised for their historical or informational

Technical Information Services' new Noritsu digital minilab can produce low-cost photographic prints, ranging in size up to 12 x 18 inches.

value and considered to be permanently valuable. The Branch provides records management services, training, and support for the maintenance of active records, including electronic records, as an important information resource. The Branch is responsible for processing NRL's incoming and outgoing correspondence and provides training and support on correct correspondence formats and practices. The Branch is responsible for NRL's Forms and Reports Management Programs (including designing electronic forms and maintaining a website for Lab-wide use of electronic forms), compiles and publishes the NRL Code Directory and Organizational Index, and is responsible for providing NRL postal mail services for first class and accountable mail and for mail pickup and delivery throughout NRL. The Branch also provides NRL Locator Service.

Mail clerks sort and prepare mail to be delivered throughout the Laboratory.

Ruth H. Hooker Research Library

The Ruth H. Hooker Research Library offers a full range of traditional and digital services to enhance and support the research program of the Naval Research Laboratory. Traditional library services include an extensive technical report, book, and journal collection dating back to the 1800s, housed within a physical facility configured for study and research, staffed with subject specialists and information professionals. To enhance traditional services, the NRL library has developed and is continuing to enhance the NRL Digital Library. The Digital Library currently provides desktop access to thousands of journals, books, and reference sources at NRL-DC, NRL-Stennis, NRL-Monterey, and the Office of Naval Research.

The NRL Research Library collections are focused to specifically support the research areas at NRL, including physics, chemistry, oceanography, meteorology, and space sciences. The collections include 150,000 books and journal volumes, 3,000 current journal subscriptions, and nearly 2 million technical reports in paper, microfiche, or digital format (classified and unclassified). Services include reference assistance in using the collections and locating information from external sources; mediated literature searches of several hundred online databases, including classified databases, to produce on-demand subject bibliographies; circulation of materials from the collection including classified literature up to the Secret level; interlibrary loan to obtain needed items from other scientific and research libraries or from commercial document providers; ordering all journals for office retention; and user education and outreach to help researchers improve productivity through effective use of the physical library and the rapidly growing Digital Library resources available through InfoWeb, TORPEDO *Ultra*, and the World Wide Web. The "portal" to the NRL Digital Library is called InfoWeb, which is located at http://infoweb.nrl.navy.mil, and provides desktop access to all of the online resources licensed through the NRL library. A key Digital Library service is TORPEDO *Ultra*, which serves as a digital archive for thousands of licensed journals and technical reports with over 3.5 million items currently available.

FIELD STATIONS

NRL has acquired or made arrangements over the years to use a number of major sites and facilities for research. The largest facility is located at the Stennis Space Center (NRL-SSC), in Bay St. Louis, Mississippi. Others include a facility at the Naval Postgraduate School in Monterey, California (NRL-MRY), and the Chesapeake Bay Detachment (CBD) in Maryland. Additional sites are located in Maryland, Virginia, Alabama, and Florida.

Scientific Development Squadron One (VXS-1)

On 13 December 2004, the Naval Research Laboratory Flight Support Detachment was transformed into one of the Navy's newest commands—Scientific Development Squadron One (VXS-1). As VXS-1, the new command will continue its mission as the Naval Research Laboratory's aviation component as an Echelon III command reporting to the Commanding Officer, Naval Research Laboratory. Located at the Naval Air Station Patuxent River, Lexington Park, Maryland, VXS-1 is currently manned by 16 officers, 66 enlisted personnel, and 12 civilians. The squadron is responsible for the maintenance, employment, and security of four uniquely configured P-3 Orion turboprop research aircraft. The assigned aircrew are tasked with conducting numerous single-aircraft deployments around the world in support of a wide range of scientific research projects.

During this past year, the Flight Support Detachment provided flight support for diverse research programs including: the Bow Echo and Mesoscale

TORPEDO *Ultra*, one of the Web-based services available through the NRL Research Library.

Convective Vortices Experiment (BAMEX), the Airborne Geographical Sensor Suite (AGSS), the Global Netcentric Surveillance and Targeting project (GUNCOAST), and the airborne part of Navy's Cooperative Engagement Capability (CEC), just to name a few. The squadron's flight safety record spans more than 40 years and includes over 62,000 mishap-free flight hours.

Chesapeake Bay Detachment (CBD)

CBD occupies a 168-acre site at Randall Cliffs, Maryland, and provides facilities and support services for research in radar, electronic warfare, optical devices, materials, communications, and fire research. A ship-motion simulator (SMS) is used to test and evaluate radar, satellite communications, and line-of-sight RF communications systems under dynamic conditions (various sea states). The SMS can handle up to 12,000 lb of electronic systems. A roll motion of up to 30 deg (15 deg to port and 15 deg to starboard) can be applied to this axis. The pitch axis has a fixed motion of 10 deg (5 deg to stern and 5 deg to bow). Periods along both axes, pitch and roll, are variable—from a slow 32-s to a brisk 4-s rate. Variable azimuth motion can also be added to the pitch and roll action. Synchronized positioning information (×1 and ×36) is available for each of the three axes of the SMS.

Because of its location high above the western shore of the Chesapeake Bay, unique experiments can be performed in conjunction with the Tilghman Island site, 16 km across the bay from CBD. Some of these experiments include low clutter and generally low-background radar measurements. By using CBD's support vessels, experiments are performed that involve dispensing chaff over water and radar target characterizations of aircraft and ships. Basic research is also conducted in radar antenna properties, testing of radar remote-sensing concepts, use of radar to sense ocean waves, and laser propagation. CBD also hosts facilities of the Navy Technology Center for Safety and Survivability, which conducts fire research on simulated carrier, surface, and submarine platforms.

Stennis Space Center (NRL-SSC)

The NRL Detachment at Stennis Space Center, Mississippi (NRL-SSC) consists of NRL's Oceanography Division and portions of the Acoustics and Marine Geosciences Divisions. NRL-SSC, a tenant activity at NASA's John C. Stennis Space Center (SSC), is located in the southwest corner of Mississippi, about 50 miles northeast of New Orleans,

CAPT Schubert, RADM Cohen, and CDR Salitsky flank new logo of VXS-1 Squadron after Establishment Ceremony, Pax River NAS.

Louisiana, and 20 miles from the Mississippi Gulf Coast. Other Navy tenants at SSC include the Naval Meteorology and Oceanography Command, the Naval Oceanographic Office, the Navy Small Craft Instruction and Training Center, the Special Boat Team-Twenty-two, and the Human Resources Service Center South East. Other Federal and State agencies at SSC involved in marine-related science and technology are the National Coastal Data Development Center, the National Data Buoy Center, the U.S. Geological Survey, the Environmental Protection Agency's Gulf of Mexico Program and Environmental Chemistry Laboratory, the Center for Higher Learning, University of Southern Mississippi, and Mississippi State University.

The Naval Meteorology and Oceanography Command and the Naval Oceanographic Office are major operational users of the oceanographic, acoustic, and geosciences technology developed by NRL researchers. The Naval Oceanographic Office operates the Major Shared Resource Center (MSRC), one of the nation's High Performance Computing Centers, which provides operational support to the warfighter and access to NRL for ocean and atmospheric science and technology.

The Acoustics, Marine Geosciences, and Oceanography Divisions occupy more than 175,000 ft^2 of research, computation, laboratory, administrative, and warehouse space. Facilities include the dual-use analysis center, sediment core laboratory, transmission electron microscope, moving-map composer facility, underwater navigation control laboratory, computed tomography scanning laboratory, visualization laboratory, ocean color data receipt and processing facility, environmental microscopy facility, maintenance and calibration systems, environmental modeling and simulation high-speed network, and numerous laboratories for acoustic geosciences and oceanographic computation, instrumentation, analysis, and testing. Special areas are available for constructing, staging, refurbishing, and storing sea-going equipment.

Marine Meteorology Division (NRL-MRY)

NRL's Marine Meteorology Division (NRL-MRY) is located in Monterey, California, on the grounds of the Naval Postgraduate School (NPS) Annex, which is about a mile from the NPS main campus. The NRL facility is collocated with the Navy's operational Fleet Numerical Meteorology and Oceanography Center (FNMOC) and with a NOAA National Weather Service Forecast Office (NWSFO). The NPS Annex campus, which covers approximately five acres, comprises four primary buildings—one occupied exclusively by NOAA, one that houses both the NRL and FNMOC supercomputer/operational facilities, and two large buildings containing office space, computer laboratories, and conference facilities that are shared by FNMOC and NRL-MRY personnel. The site also provides two modular office buildings, warehouse space, and recreational facilities. NRL-MRY occupies approximately 30,000 ft^2 in shared buildings. This includes not only office and meeting space, but also a small library, the Daley Supercomputer Resource Center, the Bergen Data Center, the Geostationary Satellite/Radar Processing Facility, and space for the hardware supporting the Navy Integrated Tactical Environmental System (NITES), the Coupled Ocean/Atmosphere Mesoscale Prediction System-On Scene (COAMPS-OS™), the Master Environmental Laboratory, and the Division's SIPRNET connection.

NRL-MRY is dedicated to advancing fundamental scientific understanding of the atmosphere, including the air-sea interface, and to applying those scientific discoveries in the development of innovative objective weather prediction systems. FNMOC is the Navy's central facility for the production and distribution of numerical weather prediction and satellite products in support of Navy operations around the globe, as well as to other defense-related activities. Fleet Numerical and the Navy's regional METOC Centers are the primary customers for the numerical weather prediction and satellite product systems that are developed by NRL-MRY. This collocation of the scientific developer with the operational customer offers advantages for the successful implementation of new systems and system upgrades, and for the rapid infusion of new research results from the community at large. NRL-MRY has direct access to FNMOC's large classified supercomputers and other systems. This allows advanced development to take place using the real-time on-site global atmospheric and oceanographic databases. Collocation also offers the opportunity for FNMOC scientists to team with NRL-MRY scientists during the transition and implementation process, and NRL-MRY scientists remain readily available for consultation on any future problems that arise.

NRL-MRY benefits from the opportunities provided by NPS for continuing education and collaborative research with the Meteorology and Oceanography Departments, while NPS utilizes the expertise of NRL scientists as guest lecturers and thesis committee members. NRL-MRY also maintains collaborative relationships with a number of the 25 local organizations that make up the Monterey Bay Crescent Ocean Research Consortium, which coordinates and promotes research, education, and outreach activities using the Monterey Bay as a natural laboratory.

Midway Research Center

The Midway Research Center (MRC) is located on a 162-acre site in Stafford County, Virginia. Located adjacent to the Quantico Marine Corps' Combat Development Command, the MRC has 16,000 ft^2 of operations and administration area. Instruments include three precision 18.5-m-diameter parabolic antennas housed in 100-ft radomes, a fast-tracking 1-m telescope currently used for satellite laser ranging, and a transportable 16-in. telescope capable of passive optical tracking and laser communications. The MRC, under the auspices of the Naval Center for Space Technology, provides NRL with state-of-the-art facilities dedicated solely to space-related applications in naval communications, navigation, and basic research.

Research Platforms

Mobile research platforms contribute greatly to NRL's research. These include six P-3 Orion turboprop aircraft and one ship, the ex-USS *Shadwell* (LSD-15), berthed in Mobile Bay, Alabama. The ex-USS *Shadwell* is used for research on aboard-ship fire-suppression techniques.

LOOKING AHEAD

To provide preeminent research for tomorrow's Navy, NRL must maintain and upgrade its scientific and technological equipment to keep it at the forefront of modern research facilities. The physical plant to house this equipment must also be state of the art. NRL has embarked on a Corporate Facilities Plan to accomplish these goals. This plan and future facility plans are described below.

THE CORPORATE FACILITIES INVESTMENT PLAN (CFIP)

The CFIP is a capital investment plan that uses both Congressionally approved military construction (MILCON) and Laboratory overhead funds to provide modern, up-to-date laboratory facilities for NRL. Past MILCON projects have included the Electro-Optics Building at NRL-DC, the Ocean Acoustics Research Laboratory at NRL-SSC, and the Nanoscience Research Laboratory at NRL-DC. Future MILCON projects include an Autonomous Vehicles Research Building in the FY07 time frame.

To complement these efforts, overhead funds have been used to renovate and upgrade laboratory and support areas in several existing buildings. Modern laboratory facilities have recently been provided for the Center for Bio/Molecular Science and Engineering, the Materials Science and Technology Division, the Remote Sensing Division, the Acoustics Division, the Information Technology Division, and the Radar Division.

In parallel with efforts to upgrade laboratory buildings to the most modern standards, those buildings that were built during World War II and do not lend themselves to renovation are being demolished. This will provide space for the construction of future MILCON buildings, and it will also reduce the Laboratory's overhead costs.

Institute for Nanoscience

The manipulation and measurement of materials with nanometer dimensions is very difficult. One must be able to reliably and precisely locate structures of nanometer dimensions in much larger areas. Furthermore, the measurement of nanostructure properties is difficult simply because not many atoms/molecules are present. Vibrations and thermal/humidity/pressure fluctuations in the environment can cause major problems in positioning a tool. Good signal-to-noise ratios require electromagnetic and acoustic interference-free environments. Airborne contamination can readily cover a nanostructure. A new Nanoscience Research building has been constructed that controls these sources of "noise"; it became available for use in January 2004. There are 5000 ft^2 of Class 100 clean room for device fabrication; 4000 ft^2 of "quiet" space with temperature controlled to 0.5 °C, acoustic isolation at the NC35 standard (35 dB at 1 kHz), floor vibration isolation to <150 μm/s rms 10 to 100 Hz and <0.3 m0e magnetic noise at 60 Hz. There are also 1000 ft^2 of "ultra-quiet" space with temperature controlled to 0.1 °C and acoustic isolation at the NC25 standard (25 dB at 1 kHz).

Ruth H. Hooker Research Library

The Ruth H. Hooker Research Library has encouraged "Innovation for Research" for many years, exemplified by the first-of-its-kind systems such as InfoNet, InfoWeb, and TORPEDO *Ultra*. These custom systems, combined with the licensing of online resources for all NRL sites, have dramatically increased the resources available at the desktop and changed the research process. Over the next several years, the NRL Research Library plans to continue to expand desktop access to include all current and historical journal and conference proceedings that are relevant to NRL research. The NRL Library is also capturing a complete record of research results (journal articles, conference proceedings, books, etc.) of all Laboratory researchers, both a bibliographic citation and a copy of the physical artifact, for use with annual reviews and higher level summaries of productivity. Finally, the NRL Library is evolving all services to a more reliable and intuitive infrastructure that is focused on the needs of NRL researchers and engineers.

Information Technology

The Information Technology Division's Center for Computational Science (CCS) operates scalable, massively parallel Global Shared Memory (GSM) computer systems, including a 128-processor SGI Altix with cache-coherent Non-Uniform Memory Access (ccNUMA) architecture. Resources include an experimental multithreaded architecture (MTA) high-performance computer with 40 processors. Recent additions for FY04 include a 256-processor SGI Altix, based on the leading-edge Intel IA64 architecture.

The Motion Imagery Lab in the Center for Computational Science. This resource brings together extremely high resolution global images in progressive scan combined with high performance distributed databases, computing, and networking support of decision-making tools for the warfighter.

Altix is particularly interesting as it is the first HPC machine to run a single system image across more than 128 processors using a commercially available LINUX operating system (Red Hat). These systems comprise the Distributed Center (DC) at NRL whose hardware is funded by the DoD High Performance Computing Modernization Program (HPCMP). The systems are used in the innovative exploration and evaluation of massively parallel processing (MPP) technology for solving significant militarily relevant problems relating to computational and information science. The systems allow leading-edge research in support of heterogeneous parallel processing applications by the Navy and DoD science and technology communities.

Chemistry

Force Protection/Homeland Defense (FP/HD) has been a focus of the Chemistry Division since September 11, 2001, especially in the development of improved detection techniques for chemical, biological, and explosive threats. In conjunction with technologies contributed by other divisions, Chemistry Division staff will be major contributors to the definition and development of new technology systems. In a parallel and complementary multidivisional program, the Chemistry Division will be a major contributor to the NRL Nanoscience Research Institute. Nanoscience complements FP/HD in that nanoscience is expected to provide dramatic improvements to chemical/biological detection, protection, and neutralization. Chemistry will approach the nanoscale from the bottom-up—building smaller atoms and molecules into nanostructures with new properties and developing the directed assembly of nanostructures into hierarchical systems. The new NRL Nanoscience building is linked directly into the Chemistry building to provide both controlled access and auxiliary space for work not requiring a "low noise" environment.

Plasma Physics

The Plasma Physics Division has established a new Electromagnetic Gun Laboratory to study barrel materials science issues associated with an electric gun for a future all-electric warship. The laboratory will house a 6-m-long railgun, a 10 to 16 MJ capacitive energy storage bank, and solid-state switching hardware capable of driving up to 2 MA current in a barrel. The interface between the sliding projectile and the rails will be studied by a multidivision research team in an effort to design a high performance and long-lived electric gun barrel.

Electronics Science and Technology

The Electronics Science and Technology Division has expanded the capabilities of the Compound Semiconductor Processing Facility (CSPF) to include inductively coupled plasma etching and specialty electron beam nanowriting necessary for nanoelectronic material and device research. Expansion in silicon carbide (SiC) technology for advanced power electronic devices will also be addressed. The Silicon Carbide Processing Laboratory (SCPL) and the Advanced Silicon Carbide Epitaxy Laboratory

(ASCEL) will be established in 2005 to serve the needs of the Division's power electronics materials and devices research activities.

Acoustics

NRL's Salt Water Tank Facility is designed to provide a controlled environment for studying complex bubble-related processes found in the ocean. It is an experimental pool facility for studies of underwater acoustics, fluid dynamics, and air-sea interface environmental topics under saline conditions. This facility is currently being used to study the acoustics of bubbly media, including bubble entrainment and ambient noise generation, scattering from bubbly structures, and propagation through bubbly media. Future studies include the interaction of bubbles with turbulent fluid flows, bubble coalescence and dissolution, effects of surfactants and contaminants, and bubble-related gas exchange across the air-sea interface.

The Division operates state-of-the-art laboratories now resident in NRL's new Nanoscience Building. These new capabilities, dedicated to the study of the behavior of electromechanical systems confined to the near atomic scale (< 100 nm), are referred to as the "Nanomechanics Laboratory" and the "Low Temperature Near-field Scanning Optical Microscopy (NSOM) Laboratory." These laboratories allow temperature/size scaling experiments involving the broadband (~3 GHz) linear and non-linear dynamics of individual Nanoelectromechanical Systems (NEMS) devices and artificial crystal arrays formed from nanomechanical unit cells.

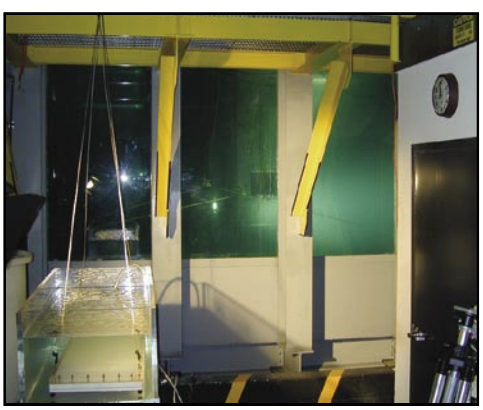

The Acoustic Division's Salt Water Tank Facility is designed for studying underwater acoustics in controlled, saline environments. Currently, this facility is being used to make measurements of sound propagation through bubble clouds.

Remote Sensing

The Remote Sensing Division has developed and installed 74 MHz receivers on the National Radio Astronomy Observatory's (NRAO) Very Large Array (VLA), thereby producing the world's highest angular resolution and most sensitive astronomical interferometric array operating below 150 MHz. In contrast to the VLA's maximum baseline of 35 km, all previous astronomical interferometers operating below 150 MHz had baselines less than 5 km because ionospheric structure had been thought to impose phase variations that would corrupt the interferometric imaging. Work in the Remote Sensing Division has shown that radio astronomical techniques can now remove the ionospheric phase variations and extend interferometer baselines to arbitrary lengths. In its first year of operation, the NRL/NRAO 74 MHz system has been used for a variety of innovative observations with encouraging initial results in solar system, Galactic, and extragalactic astrophysics. The success of the NRL/NRAO 74 MHz system indicates that it is possible to open a new high-resolution, high-sensitivity astronomical window by going to an even larger, more sensitive system. The Remote Sensing Division, in collaboration with the Netherlands Foundation for Research in Astronomy, is currently designing a follow-on instrument, the Low Frequency Array (LOFAR). LOFAR will be a fully electronic, broadband array operating in the 15 to 150 MHz range, with a collecting area of 1 square km at 15 MHz and a maximum baseline of 500-km resolution and sensitivity over the state of the art.

The Remote Sensing Division is also developing other new facilities-class sensors including the Navy Ultrawideband Synthetic Aperture Radar (NUSAR). NUSAR is a fully capable high-resolution (less than 1-m impulse response) synthetic aperture radar system made to be operated from light aircraft. It is fully polarimetric and can operate as an along-track interferometer. Its frequency range will be expandable, and ultimately it will operate from VHF to X-band.

Ocean Research Laboratory

NRL's Ocean Research Laboratory is a 52,000 ft^2 building that houses the Oceanography Division of the Ocean and Atmospheric Science and Technology Directorate. The building contains office space, oceanographic laboratories, staging areas, a small machine shop, electronic and secure laboratories, and visualization and computing facilities for research and development in ocean science and remote sensing.

Marine Geosciences

The Marine Geosciences Division has greatly enhanced the capabilities and quality of seafloor sediment fabric analyses through completion of installation and staff training for its High-Resolution Industrial CT Scanner. The CT Scanner is a powerful tool for investigating volumetric heterogeneity of materials. By using X rays at energies from 10 to 225 kV and 0-1 mA, the scanner can image single- or multi-phase media with resolving power as fine as 10-μm voxel size with the microfocus system. The system is capable of rendering and storing real-time radiographic images, reconstructing the images in three dimensions, and processing the images to fit a wide range of project applications.

Vacuum Ultraviolet Space Instrument Test Facility

The Space Science Division facilities include an ultraclean solar instrument test facility in Building A-13 on the main NRL campus. The facility is designed to satisfy the rigorous contamination requirements of state-of-the-art solar spaceflight instruments. The facility has a 400-ft^2 Class 10 clean room and a large Solar Coronagraph Optical Test Chamber (SCOTCH). This completely dry-pumped, 550-ft^3 vacuum chamber is maintained at synchrotron levels of cleanliness. Solar instrumentation up to 1 m in diameter and 5 m in length can be physically accommodated in the chamber. The instrument's optical performance is probed and calibrated with a variety of visible and XUV sources mounted on the chamber's 11-m beamline. The optical testing and characterization of the Large-Angle Spectrometric Coronagraph (LASCO) instrument for the European Space Agency's Solar Heliospheric Observatory satellite were conducted in this chamber. Coronagraph stray-light characterization was carried out by mounting a set of baffles in the main beamline, illuminating the instrument with a simulated solar beam, and measuring the residual radiation. A stray light background measurement of 10^{-12} was successfully measured in the LASCO C3 channel. Coronagraph calibration was carried out by installing back-illuminated calibrated opals in front of the instrument entrance aperture. Instrument polarization properties were analyzed by using a variety of polarizers installed in a wheel located between the opal and the instrument. The wheel was remotely controlled from outside the chamber. Instrument Mueller matrices were verified with a 12-in. diameter, two-plate partial polarizer. Calibration and focus of XUV solar instrumentation are accomplished by exposing the instrument to an XUV windowless collimator at the end of the tank. The facility also has a small thermal bake/vacuum test chamber used for vacuum conditioning and thermal testing of spaceflight components and subassemblies. Both the SCOTCH and the small test chamber are instrumented with temperature-controlled quartz-crystal monitors and residual gas analyzers for real-time, quantitative measurements of volatile contamination.

REHABILITATION OF SCIENTIFIC FACILITIES

Specialized facilities are being installed or upgraded in several of the research and support divisions.

Flight Support Detachment

NRL's Flight Support Detachment (FSD) has continued to improve both capabilities and diversity among its aircraft platforms. Aircraft 153442 has undergone extensive modifications with Lockheed Martin to install a "rotodome" antenna and full AEW radar system. The aircraft is currently supporting the Navy's Theater Air Defense programs and providing a testbed for advanced EW radar research. Additionally, all aircraft have completed extensive bomb-bay design improvements that will allow the aircraft to carry more diverse scientific payloads. These upgrades and modifications will ensure that NRL will have the finest airborne research capabilities well into this century.

Information Technology

The Information Technology Division continues to transition stable technology from high performance network testbed activities into the NRL local area network. This effort includes support of ATM technology at stream rates of 2.5 Gbps (OC48) across the enterprise with demonstrations and technology integration to allow first use of 10 Gbps single streams and higher. The current computing architectures and the SGI Altix and Cray MTA are continuously undergoing upgrade and evaluation of both hardware and software. The NRL Center for Computational Science (CCS) works closely with the DoD HPC community and the HPC vendors to provide insight, balance, and value-added capabilities within the massively parallel processing (MPP) testbed infrastructure.

Personnel who work in the Integrated Communications Testing (ICT) Laboratory have extensive knowledge of multiprotocol interactions and are poised to help in future Navy/DoD network research, evaluation, and integration efforts. The ICT facility will be involved in future work providing a transition between high performance fiber-optic technologies and tactical networking.

Plasma Physics

A single-shot, short-pulse (400 fs), high-intensity Table-Top Terawatt (T^3) laser has been recently upgraded for operation with two independently timed beams one with up to 15 TW and 3×10^{19} W/cm^2, and the other up to 2 TW for intense laser-matter interaction studies, including particle acceleration. A new 10 Hz ultrashort-pulse (40 fs), Ti:Sapphire Femtosecond Laser (TFL) system is now operational at 1 TW. These lasers comprise a facility to do fundamental physics experiments in intense laser-plasma interactions, intense laser-electron beam interactions, and intense laser-matter interactions.

The division has built two large electron-beam-pumped krypton-fluoride (KrF) laser systems that have applications to both fusion energy and defense. Nike is a large 5 kJ system used for studies of laser-target interaction, while the Electra system is developing the next-generation efficient and reliable technologies needed to progress from the laboratory to commercial laser-fusion energy. Electra has a goal of a laser output of 700 J at 5 Hz. Larger KrF systems that would be needed for a fusion driver are being designed based on experience with these systems.

The Plasma Physics Division will be bringing on line the new Mercury pulsed-power generator in FY04. The facility is located in renovated space in Building 256. Mercury is an inductively isolated, voltage-adder device that will be capable of producing a 6-MV, 360-kA, 50-ns electrical power pulse for driving electron beam and ion beam diodes. The new facility will support ongoing radiographic source development for the Department of Energy and nuclear weapons effects simulation for the Defense Threat Reduction Agency.

Electronics Science and Technology

The Electronics Science and Technology Division has embarked on upgrading and expanding capabilities in solar-cell characterization and power-electronics materials growth and device fabrication. The solar-cell laboratory has been rehabilitated in Building 208 with a wide range of new measurement capabilities up to one sun, air mass zero (AM0) illumination. Key equipment includes a Spectrolab solar simulator and a TS Space systems simulator with three independently controllable light zones. To address needs in the division's power electronics programs, the Silicon Carbide Processing Laboratory (SCPL) and the Advanced Silicon Carbide Epitaxy Laboratory (ASCEL) will be created in 2005 through a rehabilitation of existing space, existing equipment, and the installation of a new epitaxial reactor.

Featured Research

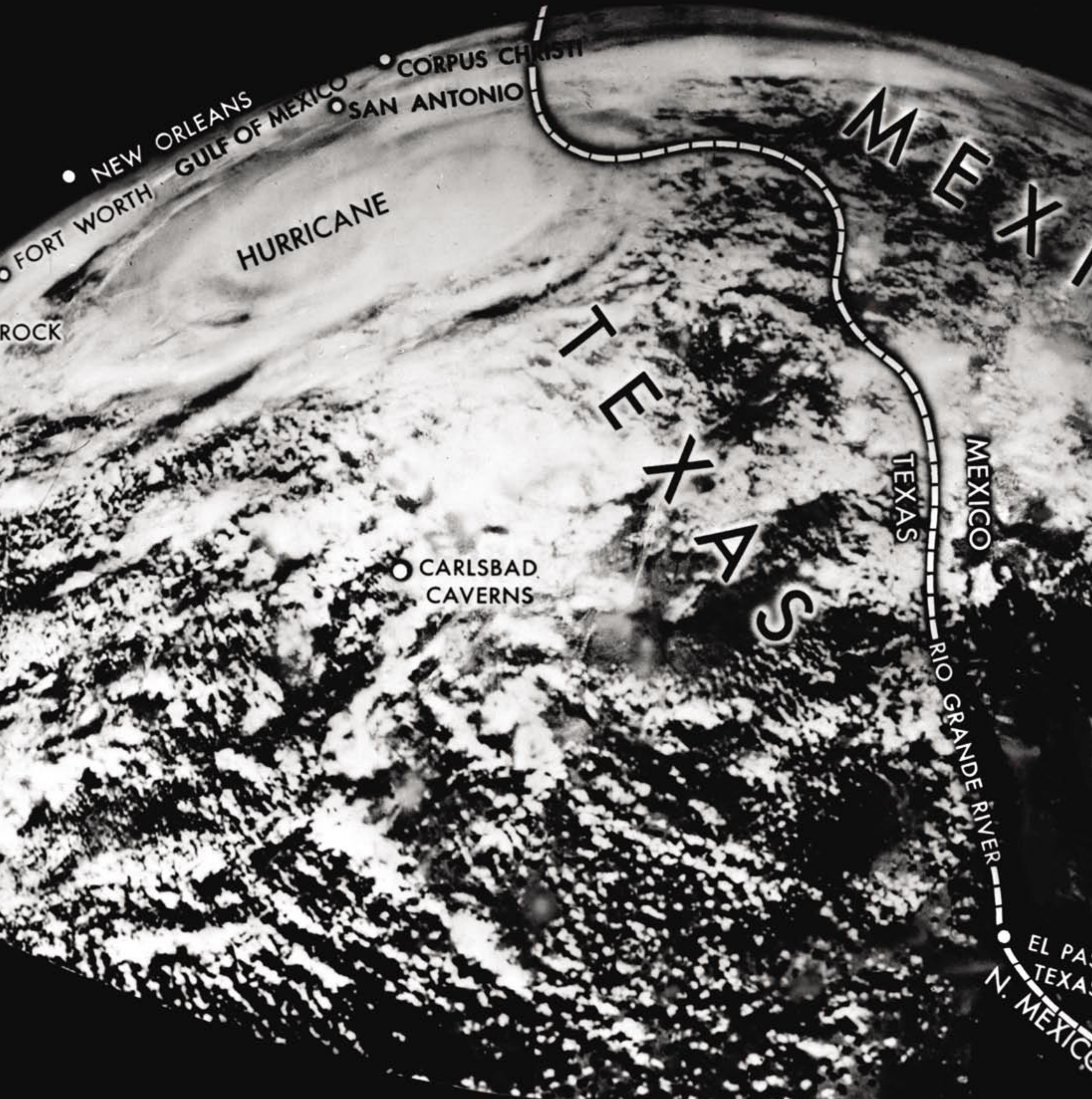

Photo caption: Image of a weather system captured from an NRL rocket experiment on October 5, 1954. Images of this sort were instrumental in established space cloud imagery as a tool to assist weather forecasters.

Microelectronic Array for Stimulation of Retinal Tissue

D. Scribner,[1] L. Johnson,[4] P. Skeath,[4] R. Klein,[4] F.K. Perkins,[2] L. Wasserman,[4] W. Bassett,[4] D. Ilg,[4] J. Peele,[1] J. Friebele,[1] J.G. Howard,[1] W. Freeman,[5] W. Krebs,[3] and A. Taylor[1]
[1]*Optical Sciences Division*
[2]*Electronics Science and Technology Division*
[3]*Military Support Division*
[4]*SFA, Inc.*
[5]*Smart Logic, Inc.*

PROJECT BACKGROUND AND GOALS

The development of a high-resolution retinal prosthesis device at the Naval Research Laboratory (NRL) was first discussed in the late 1990s. At that time, NRL researchers and Office of Naval Research (ONR) Science Officers were studying the topic: "Image Processing: What Can We Learn from the Retina?" It had long been recognized that the retina must perform remarkable image processing functions, yet neuroscientists had only a limited understanding of the systemic mechanisms. ONR felt that studying retinal mechanisms could provide valuable inspiration for new algorithms and low-power analog designs for microelectronic circuitry in future electro-optical imaging arrays.

Although "smart focal plane arrays" had been of great interest to the electro-optical community, traditional digital image processing was far too power-hungry to integrate into a focal plane array. Analog ("retina-like") processing might provide new methods that would allow computationally intensive algorithms to be performed in parallel while dissipating only small amounts of power.

ONR had also been discussing related topics with the Wilmer Ophthalmological Institute of Johns Hopkins University (JHU). The JHU team was not only interested in retinal processing mechanisms, but was performing some interesting experiments that were aimed at demonstrating the feasibility of a retinal prosthesis—namely, electrically stimulating retinal cells and analyzing the perceived effects in blind human subjects.

It was this overlapping mutual interest in the retina that led NRL researchers to propose the use of advanced DoD technologies for a revolutionary new neural-electronic interface for both a retinal prosthesis and for advanced retinal studies.

At the same time, a new DARPA program was soliciting proposals for the development and demonstration of innovative tissue-based biosensors that would be a key component in DARPA's programs in Biological Warfare Defense. Of particular interest was the capability to rapidly detect and predict physiological consequences of biological and chemical agents, both known and unknown. DARPA foresaw the need for new techniques to create an effective and massively parallel interface between microelectronic arrays and neural cells.

In response to this DARPA program, NRL proposed to design and fabricate a miniaturized, high-resolution human retinal stimulator device to be used in conjunction with the Johns Hopkins University program. The device would create a neural-electronic interface between a high-resolution array of 3,200 microelectrodes and a retinal surface. The proposal was unique because a microelectronic interface to neural tissue with 3,200 independent electrodes was unprecedented. It supported the DARPA program because it would provide detailed information about microelectronic interfaces at a cellular level.

Development of a Test Device for Acute Experiment

The development of an implantable retinal prosthesis for chronic use is a complex undertaking. Such a device would require wireless operation; it must meet stringent biocompatibility requirements; and it must have a lifetime of several decades. A logical first step is to make a test device that can be used in very short, acute experiments to prove the feasibility of a high-resolution device. In the early 1990s, the Johns Hopkins group performed human experiments with a single electrode used to electrically stimulate the retina. Since that time, a number of research groups have begun to develop technologies that support retinal prostheses.

A review article in the journal *Science* details this field of research.[1] Currently most conceptual designs for retinal prostheses are attempting to provide only the most rudimentary vision. Furthermore, these technologies are not scalable to higher resolution. The NRL retinal device seeks to remedy these problems.

The remainder of this paper describes the program at NRL for designing, fabricating, and testing a high-density electrode array that would be suitable for acute tests with human subjects. This will lead to clinical tests to begin in 2005 by a surgical team in an operating room environment. The experiment would last approximately one hour. The highly trained patient would be conscious and receive high-resolution, intra-ocular retinal stimulation in the form of a series of image sequences and describe his or her perceptions.

Figure 1 shows the NRL test device as it will be positioned against the retina during the surgical experiment. Note that a small cable passes through an incision in the sclera, allowing a direct means of powering the device and inputting image data. Figure 2 shows the device architecture and the corresponding retinal anatomy with regard to the device placement. Note that the outermost layer of the retina consists of photoreceptors. Proceeding from the photoreceptors inward toward the center of the eye, the layers of the sensory retina are the bipolar, amacrine, horizontal, and the ganglion cells. The axons of the ganglion cells form a radial pattern across the retina and converge to form the optic nerve. Photoreceptor loss from diseases such as retinitis pigmentosa and age-related macular degeneration are the leading causes of blindness in the developing world, affecting approximately 30 million people. There are no known restorative therapies. Nevertheless, even in advanced stages of these degenerative diseases, the inner retinal layers remain viable for long periods of time. By stimulating these remaining functional retinal layers, it may be possible to restore visual perception.

The basic operation of a retinal prosthesis device is straightforward in theory. Visual images can be produced in the brain by electrical stimulation of retinal cells (which substitutes for optical stimulation) so as to provide a one-to-one mapping to areas in the visual cortex. A layer of retinal cells, such as a ganglion cell layer, can be stimulated using an adjacent microelectronic array that inputs electrical impulses. The axons of the stimulated ganglion cells then transmit the image through the optic nerve to cells in the visual cortex to create the perception of an image. This is in place of the normal photo-transduction process that occurs in a healthy retina.[2]

Advanced DoD Technologies for Neural-Electronic Interfaces

To meet the above-mentioned specifications, the NRL program leveraged advanced DoD technologies by (1) modifying infrared focal plane array (IRFPA) microelectronic multiplexer technology and (2) creating microwire glass electrode arrays using microchannel plate glass as the starting material. Microchannel plate glass is used in image intensifier tubes like those in night vision goggles. It is produced by a unique process that involves bundling optical fibers to produce thin wafers of glass (with all the hollow channels extending straight through the glass wafer). Microchannel sizes are typically 5 μm diameters, and the density of the microchannels is approximately 20,000 per square millimeter. At NRL, the hollow channels are filled by electroplating, which creates microwires. Then, one surface of the glass is ground and polished to a spherical shape consistent with the radius of curvature of the inside of the retina.

A primary function of the device is to multiplex image data from the incoming analog video to the individual unit cells. The IRFPA community has been developing similar integrated circuits over the past 15 years. Microwire glass is hybridized to the multiplexer using indium bump bonds—again, this is similar to hybridization techniques used in IRFPAs. The image is serially input onto the multiplexer via a very narrow, flexible microcable. The electrical connection to the silicon multiplexer is made such that nothing is protruding above the spherical curved envelope defined by the polished microwire glass surface and, therefore, protects the retina from damage.

MICROELECTRONIC MULTIPLEXER

The multiplexer capability is of major importance because it allows the operation of all 3,200 unit cells with only 10 leads connected to the outside world. Directly connecting individual leads to all 3,200 unit cells would make for a very thick cable and make it highly impractical to route the image data through the eye wall. A proposed future version of the device could be wireless.

Microelectronic Multiplexer Description and Layout

The floor plan of the multiplexer is shown in Fig. 3(a). The NRL device was fabricated using a 1.2 μm design-rule process. The core area of the multiplexer

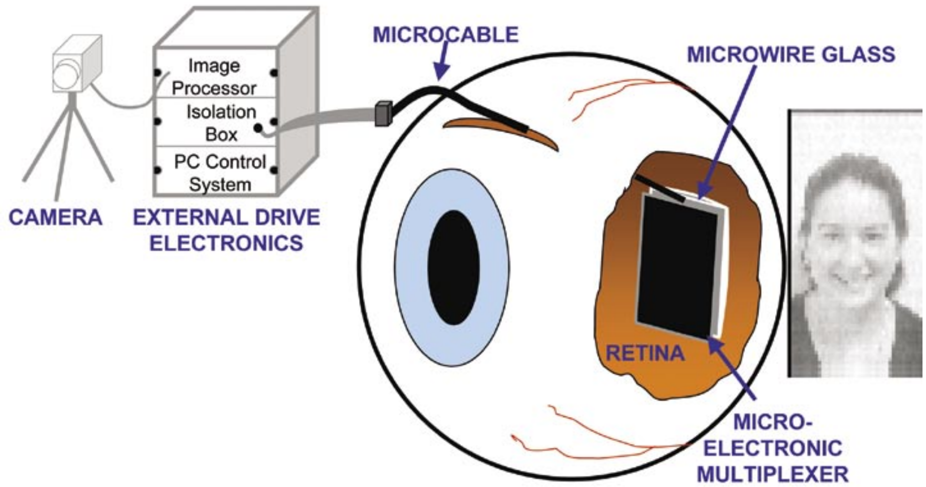

FIGURE 1
Retinal prosthesis test system, illustrating the device positioned against the retina during a one-hour surgical experiment. To provide basic visual function that is sufficient to treat common types of blindness (enough pixels for facial recognition or to read text), an extremely thin microcable passes through an incision in the eye wall, allowing a direct means of powering the device and inputting image data. The image to the right represents the image quality achievable with the 80 x 40 device. A future retinal prosthesis system, now in the planning stage, would be wireless – no microcable required – and backside illuminated.

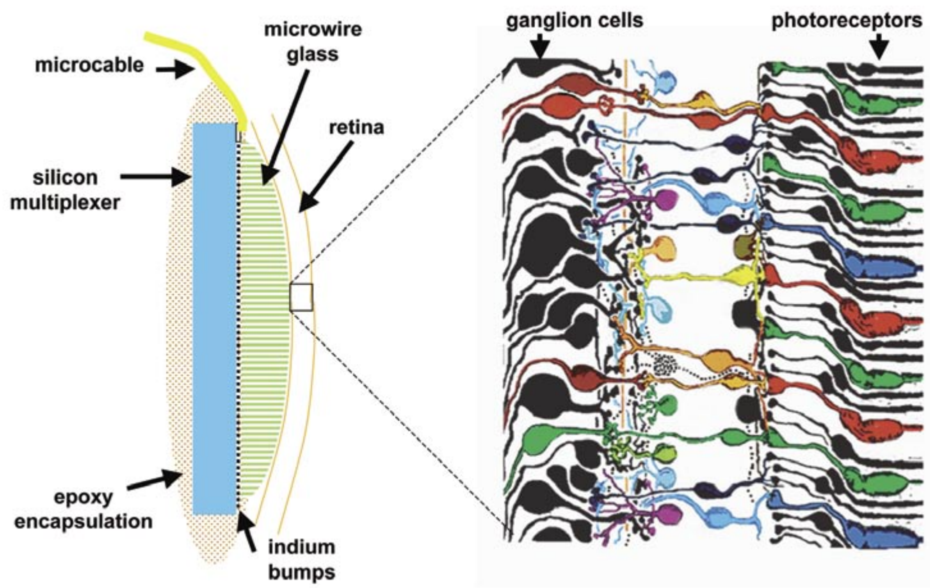

FIGURE 2
Device architecture and the corresponding retinal anatomy with regard to device placement. Note that the outermost layer of the retina consists of photoreceptors and the ends of the microwire glass are positioned in close proximity to the ganglion cell layer of the retina.

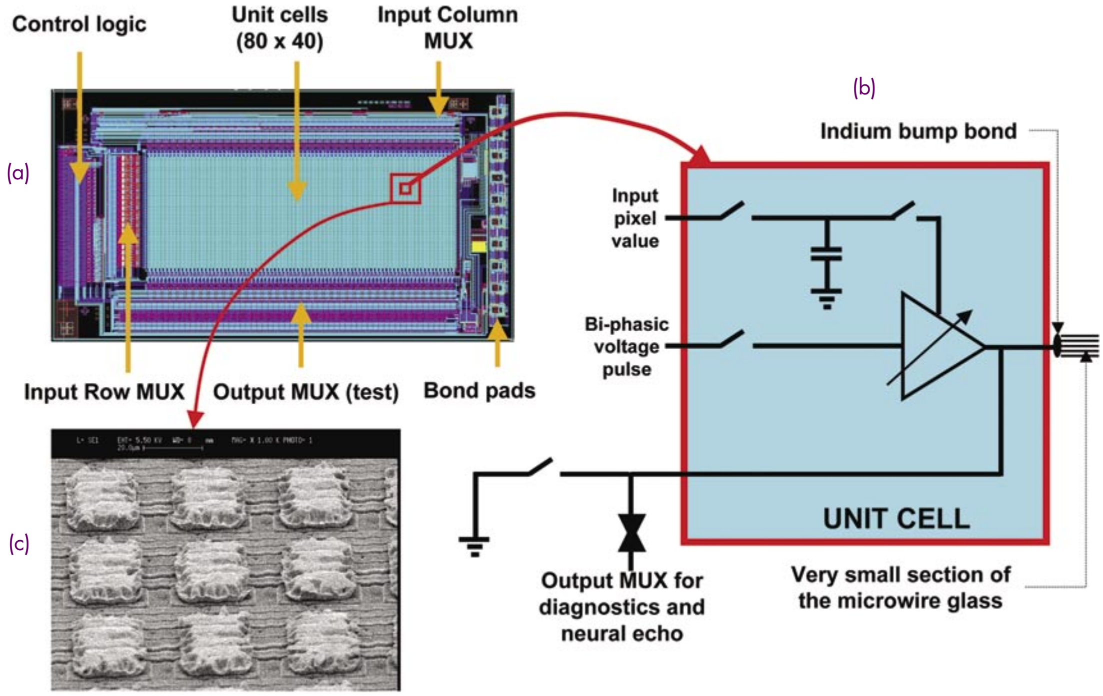

FIGURE 3
The microelectronic multiplexer floor plan is shown in (a) and a simplified schematic of the electronics in each unit cell (pixel) is shown in (b). Each unit cell has its own charge storage capacitor and a transconductance amplifier. The storage capacitors control the brightness of all 3,200 pixels within each frame. In (c), a scanning electron microscope (SEM) image of nine indium "bumps" is shown. There is one indium bump for each unit cell. Microwires on the flat side of the microwire glass will be pushed into all the bumps, connecting approximately 20 microwires to the output of each transconductance amplifier in the array. The opposite ends of those microwires will become the microelectrodes that send electrical stimulation into the retina.

is the 2D array of 80 by 40 unit cells that stimulates adjacent retinal tissue. Each unit cell is 50 by 36 μm. Although the device discussed here for use in retinal prostheses will perform demultiplexing operations, for simplicity, it will be referred to as a multiplexer.

Each unit cell has a charge storage capacitor and a transconductance amplifier as shown in Fig. 3(a). The multiplexer performs a number of important functions that are defined by its internal digital logic. The basic operation involves three steps that are performed in a sequential order and then continuously repeated at rates of up to 60 frames per second (fps). During the first step, an image frame is loaded pixel-by-pixel into corresponding unit cells. Each unit cell samples the input analog video in a raster scan format and stores the pixel value as electronic charge on an integrated circuit capacitor. A full field image can be synchronized with the RS-170 television format (30 fps consisting of two fields per frame); this allows the use of the multiplexer with standard video equipment. If standard video speeds are not required, then the frame rate can be arbitrarily changed. However, the input image will need to be timed accordingly and the device will no longer be RS-170 compatible. After all the unit cells have been loaded with the pixel values for the current frame, the second step is to send a biphasic pulse to the transconductance amplifier in each unit cell, which in turn is modulated in proportion to the pixel value stored in each unit cell.

An important feature of the multiplexer is that each unit cell stores individual pixel values and then uses them to modulate the biphasic pulse that is input to the retinal tissue through the microwire glass. The biphasic pulse and the image data are both generated off-chip. This allows for greater flexibility during human testing as any image sequence can be input and combined with any shape of biphasic pulse.

The design also includes an output multiplexer as indicated in Fig. 3(a). Its purpose is for diagnostic testing and performance monitoring during experiments. Although actual stimulation current being driven into retinal tissue will be closely monitored, an image displayed from the output multiplexer is very useful for verifying proper operation. During testing it allows the system operator to essentially view the same image that the patient "sees." In fact, it is possible to perform a type of extracellular recording by operating the multiplexer during quiescent periods between frames to monitor "neural echoes," the firing of retinal neurons in response to stimuli.

Indium Bump Deposition

After the multiplexers are fabricated at the silicon foundry, indium bumps are deposited to provide an electrical interconnection between the multiplexer and the microwire glass. A scanning electron microscope (SEM) image of a few indium bumps is shown in Fig. 3(c). Each indium bump is 30 by 20 μm in area and approximately 6 μm in height. The indium bump deposition is achieved by evaporation of indium into the openings of a photoresist layer on the multiplexer and then lifting off the photoresist.

MICROWIRE GLASS ELECTRODE ARRAY

Template

Production of microwire glass begins with microchannel plate glass, which serves as a kind of template in which microwires are formed. Microchannel plate glass is used in image intensifier tubes like those in night vision goggles. An SEM image of the front surface of a microchannel glass plate is shown in Fig. 4(a); these empty microchannels extend through the entire thickness of the glass plate. Microchannel plate glass has approximately two million microchannels per square centimeter!

Specific requirements for microwire glass are that the microwires be small enough so that 20 or more microwires can be connected to each unit cell or pixel. This provides redundancy as well as greatly simplifying the alignment process when the electrode array is joined ("hybridized") to the silicon multiplexer.

Three types of commercially available microchannel plates have been tested: borosilicate (similar to pyrex), soda-lime (similar to window glass), and lead glass (similar to crystal wine glasses). Tests on these candidate glasses have shown that nerve cells can be cultured on the borosilicate and soda lime glasses, but they do not survive long on the leaded glass. Susceptibility of the glass to cracking (during electroplating, polishing, or saw-cutting) is also a very important consideration. Resistance of the glass and metal to etching or leaching during extended immersion in saline solution is critical.

Microwire Formation

The hollow microchannels are filled with a metal to create a high-density array of microwires. Microwire glass is fabricated at NRL by electroplating nickel through the entire thickness of the microchannel plate glass, as shown in Fig. 4(b). The actual plating process involves current flowing through the microchannels to the backside contact. This forces the metal deposition to take place only in the microchannels, filling the microchannels with nickel and forming the microwires.

Completely electroplating metal through a microchannel plate with a thickness of 1 millimeter can take considerable time—generally one week. To expedite the processing, multiple plating baths were configured that could be operated simultaneously, but independently of each other. Each plating bath contained an 800 ml glass beaker, and up to six of these beakers were placed on a sealed 15-position stirring plate submerged in an isothermal tank. Nickel plating was performed at a 39 °C bath temperature. The plating solution in each beaker was continually stirred via magnetic bar. Bath control based on a reference electrode potential is performed by a potentiostat programmed in LabVIEW software, which also performed related data logging tasks.

Considering the huge number of microchannels in a piece of microchannel plate, nickel plating in the microchannels generally progressed with remarkable uniformity under the right conditions. When the plating was halted about halfway through the microchannel plate, cleaving the microchannel plate revealed solid microwires of nearly the same length in essentially every microchannel.

Shaping and Finishing the Microwire Glass

The resulting composite material, "microwire glass," is then cut very precisely to a size slightly larger than the central core area of the multiplexer IC chip, which contains the 80 by 40 unit cells or pixels. The core area (where electrical stimulation occurs) is 1.5 mm by 4 mm, and the microwire glass is cut to a size of 2 mm by 4.5 mm to ensure coverage of the pixel array.

Next, one side is ground and polished to obtain a smooth, curved surface that conforms to the curvature of the retina inside the eye. The microwire glass sample is polished with a series of CeO grits down to 0.5 μm. After the microwire glass sample has been sufficiently curve-polished, it is demounted and cleaned, and the

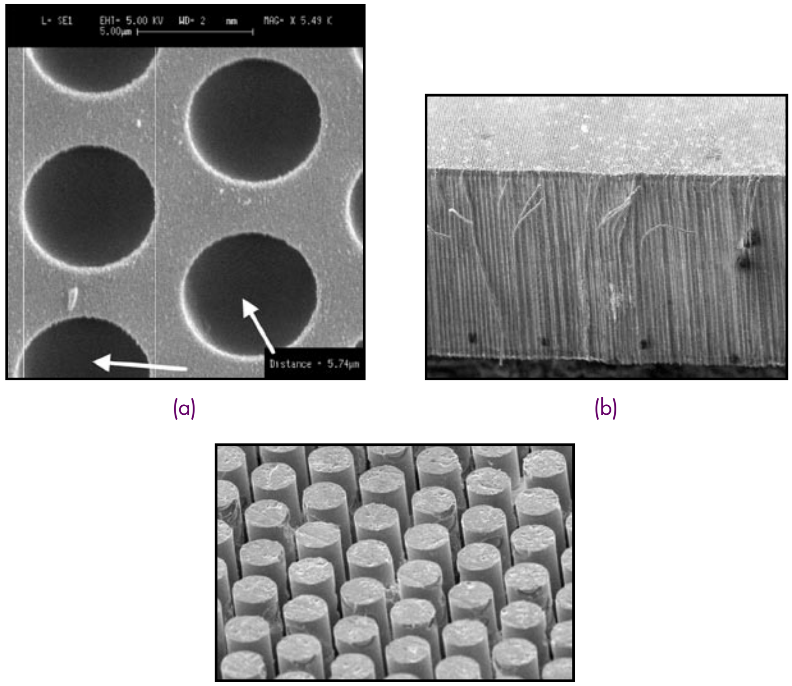

(a) (b)

(c)

FIGURE 4
Various stages of microwire glass fabrication: (a) an SEM of the microchannel plate starting material — typical channel diameters are 5 μm with center-to-center spacings of 8 μm; (b) SEM of a cleaved edge of a nickel-filled sample — channel lengths can be plated up to one millimeter; (c) SEM view of top surface showing microwires protruding from the glass after etch-back.

curvature is checked. The radius of curvature is nominally 12.7 mm to provide a conformal fit against the inside of the retina. This allows positioning of all the microwire tips in very close proximity to the retinal tissue, minimizing the power needed to achieve retinal stimulation and also maximizing spatial resolution. The other side of the microwire glass is left flat for connection to the flat silicon multiplexer.

The entire piece of microwire glass is then placed in a hydrofluoric (HF) acid solution to chemically etch-back the glass (5 to 30 μm of glass are typically removed). This creates protruding microwires on both the curved and flat sides as shown in Fig. 4(c).

Finally, the protruding microwires on the curved side are clad with a thin layer of gold using another electroplating process. Those protruding gold-clad tips of the microwires, on the curved surface, form the microelectrode array.

DEVICE ASSEMBLY AND ENCAPSULATION

The novel design of the NRL stimulator required a number of new device miniaturization and integration methods. Assembling a complete device, like that shown in Fig. 2, involves a sequence of steps as shown in Fig. 5. First, the microwire glass piece is hybridized to the microelectronic multiplexer. Second, the microelectronic multiplexer is directly connected to a polyimide microcable via a novel ribbon bonding method. Third, the device is encapsulated with a biocompatible epoxy.

Hybridization of Microwire Glass to the Multiplexer

Hybridizing the microwire glass to the multiplexer is accomplished by pressing the microwire glass onto the indium bumps. The difficulty arises in that the top surface of the microwire glass is curved and the bottom surface that mates with the chip is flat. The flat bottom surface must maintain parallelism with the chip surface. The microwire glass is somewhat fragile, so compression must be uniform across the curved surface.

Considering the high pressure required to hybridize the two pieces, we have designed and constructed a hydraulic system that produces uniform and adjustable compression over the curved surface of the glass while also keeping accurate alignment of the two components being hybridized.

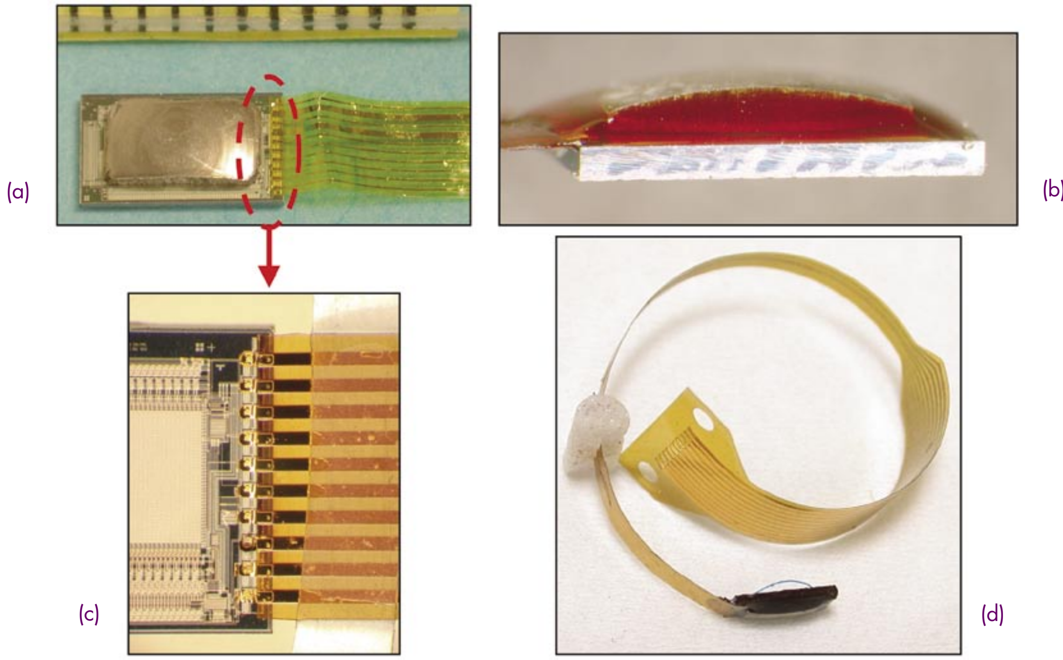

FIGURE 5
A number of steps are required to complete a fully assembled device: (a), the microwire glass piece is hybridized to the microelectronic multiplexer and the polyimide microcable is ultrasonically bonded to the 10 electrical bond pads as shown in (b). The device is then encapsulated with a biocompatible epoxy that also wicks between the microwire glass and multiplexer (c). A fully assembled device is shown in (d).

Pressures of up to 1,000 psi can be applied uniformly across the surface of the glass with the system. This presses the microwires (on the flat side of the microwire glass) into the indium bumps on the multiplexer. The microwires on the curved side of the microwire glass are held by a highly flexible latex layer, so no distortion or bending of the microwires will occur during hybridization.

Ultrasonic Bonding of Microcables to the Multiplexer

The microcable serves as the connection to the multiplexer and passes through the sclera as shown in Fig. 1. The microcable must be both flexible and tough. There are 10 electrical lines within the microcable to carry power and signals to and from the multiplexer chip. The microcable is a laminate made of two outer layers of polyimide with gold electrical traces between them. The total thickness of the microcable is 25 μm.

The microcable is fabricated such that bare gold traces extend beyond the polyimide. These short gold "ribbons" can be ultrasonically bonded directly to the bond pads on the multiplexer as shown in Fig. 5(b). After ultrasonic bonding, a small amount of the nonconducting epoxy is added to reinforce the connection. At the other end, the microcable is clamped to the minicable with a small printed circuit board that becomes a custom part of a commercially available connector.

Encapsulation and Plasma Etching

To protect the microelectronic multiplexer from the damaging saline environment of the eye, a Class IV biocompatible epoxy (Epotek™ 353ND) is used as a sealant. In addition to being safe for implantation, the 353ND nonconducting epoxy has a very low viscosity (25,000 to 35,000 cPs, at 23 °C). The low viscosity enables the epoxy to wick between the microwire glass and the multiplexer as well as in the ~3 μm spaces between the microwires. This ensures a good seal to exclude saline from contacting the multiplexer as well as stabilize the device. The low viscosity requires a mold to form the epoxy around the device. The Teflon™ mold resists adhering to the epoxy after the 30-min epoxy cure at 125 °C.

DEVICE OPERATION AND LABORATORY TESTING

The device is operated by a set of external electronics consisting of drive electronics (multiplexer biases, timing signals, and image I/O data) and an isolation box as shown in Fig. 1. There is also provision for image processing to precondition images before stimulating the retina—this is based on knowledge of retinal processing but is not covered in this paper.

Instrumentation and Ancillary Electronics

The drive electronics are composed of a PC and two customized I/O boards that control and monitor the device. Being a PC-based system makes the operation more user-friendly for clinical trials outside of NRL. Input images that are sent to the device may be either live images from a camcorder or a digitally stored image sequence. Standard video images from a camcorder may be sent to the device after being digitized by a CODEC on the PC card. Alternately, an image sequence, digitally stored on the PC, may be used as input to the device. The digital images and synchronous timing signals are sent to the device from the PC through an isolation box such that the system meets all Food and Drug Administration (FDA) electrical safety requirements.

Isolation Box

This is a critical safety device that is needed to eliminate any possibility of electrical shock. It contains an extreme isolation power supply and a printed circuit board. It electrically isolates the device from the outside world, provides dc biases and timing signals, and passes image input and output video. The timing signals and video are isolated using optocouplers. The isolation box can adjust the gain and offset of all signals with control potentiometers mounted on its front panel.

Laboratory Measurements

There are two primary operating modes that the multiplexer sequences through during each image frame: 1) "Write" image into unit cells (while charge equilibrating); and 2) Stimulate and "read" from the output multiplexer. Characterizing the device performance involves measuring the electrical current output into tissue (a saline bath acts as an equivalent medium) as a function of pixel value and biphasic pulse amplitude. The device is capable of producing currents of more than 1 μA per electrode with no electrode damage in preliminary saline testing. The level of electrical current that can be generated by each unit cell is shown in Fig. 6. The measured performance very closely matched design predictions. During laboratory testing, the device survived many hours of saline testing, indicating that the device should easily withstand one-hour clinical tests. The signal-to-noise ratio of individual pixels is estimated to be on the order of 100:1. Images recorded from the device output multiplexer were of good quality as shown in Fig. 1.

CLINICAL TRIALS AND COMMERCIALIZATION

Preclinical trials were performed by a surgical team at the MedStar Research Institute and Washington National Eye Center under separate DARPA funding to evaluate the NRL device, to develop surgical techniques (based on standard intraocular surgical methods and materials), and to study related issues pertaining to safety and biocompatibility.

The initial findings by the MedStar team were that acute surgical experiments with the NRL device, while challenging, are technically feasible for human experi-

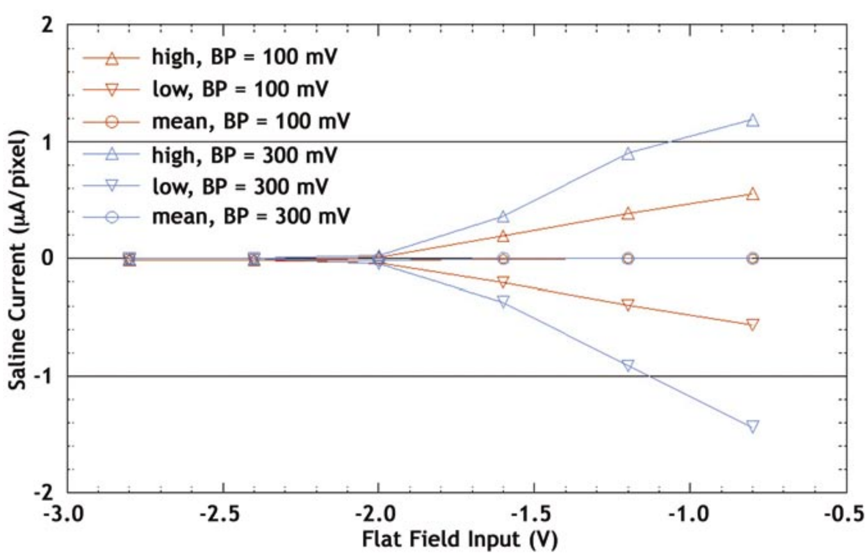

FIGURE 6
Plot of the level of electrical current that can be generated by each unit cell as a function of pixel value and biphasic pulse (BP) amplitude.

ments. More specifically, future human experiments should not result in any eye damage (even in the case of blind patients) while significantly advancing the state of knowledge of visual perception, neural-electronic interfaces, and related image preprocessing.

The NRL device is a unique system for demonstrating a high-resolution retinal prosthesis, but was conceived as a pathfinder for wireless implementations of the same technology. Regarding commercialization, negotiations for licensing agreements and cooperative partnerships are currently under discussion between the NRL Technology Transfer Office and biomedical companies.

ACKNOWLEDGMENTS

This program was funded by the DARPA NeoVision Program managed by Dr. L. Buckley with previous support from ONR Code 342, Dr. J. Davis. The unit cell circuitry was originally designed at NRL with the assistance of Fritz Kub and Eric Justh, while the detailed layout of the complete multiplexer was performed by Raytheon RIO Corporation in Santa Barbara, California, with design reuse of their SB-221 ROIC. Additional support was also received from NRL's Advanced Neural Electronic Interfaces 6.1 base program.

[Sponsored by DARPA and ONR]

References

[1] E. Zrenner, "Will Retinal Implants Restore Vision?" *Science* **295** (5557), 1022-1025 (2002).

[2] E. Margalit, M. Maia, J.D. Weiland, R.J. Greenberg, G.Y. Fujii, G. Torres, D.V. Piyathaisere, T.M. O'Hearn, W. Liu, G. Lazzi, G. Dagnelie, D.A. Scribner, E. de Juan, Jr., and M.S. Humayun, "Retinal Prosthesis for the Blind," *Survey of Ophthalmology* **47**(4):335-356 (2002). ★

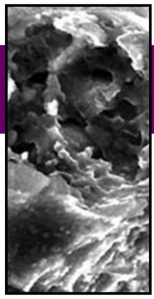

Clues to Stellar Evolution from Microscopy of Star Dust

R.M. Stroud
Materials Science and Technology Division

INTRODUCTION

Micron-sized dust grains that formed in stars older than the Sun can be found in the matrices of some meteorites.[1] Analysis of the structure and composition of this star dust in the transmission electron microscope (TEM) provides important constraints to stellar condensation models and spectroscopic stellar observations. Additional benefits of these presolar grain studies include the development of techniques for the micromanipulation of critical dust samples and a better understanding of the materials stability in extreme environments.

BACKGROUND

New solar systems form from the dusty residue of older stars. Most of the dust that was the raw material for the formation of our solar system was heavily processed in the early solar nebula. A few grains escaped heavy processing, and retain the isotopic, chemical, and structural record of their presolar origin (Fig. 1). By analyzing the structure of the presolar grains, we are able to infer the environmental conditions of the circumstellar space in which the dust condensed. Thus, microscopy studies of presolar grains provide data for direct constraint of stellar evolution models and for interpretation of spectroscopic measurements of stellar envelopes. Furthermore, presolar grains are test cases for studying the formation and survival of materials in extreme environments, including highly oxidizing atmospheres and heavy radiation fluxes.

GRAIN IDENTIFICATION

Presolar grains are trace constituents of primitive meteorites and can be identified as presolar on the basis of isotopic signatures that deviate from solar values by 100% to 1000% (Fig. 2). Such large variations from solar values can only be explained in terms of nuclear reactions occurring within the parent stars. In comparison, physical and chemical fractionation processes, which explain most of the isotope variations within terrestrial materials, produce variations two to three orders of magnitude lower, i.e., approximately 1% or lower variation from solar values.

To isolate presolar grains from the host meteorite, researchers use physical crushing, acid dissolution treatments or both to obtain a grain residue, then disperse the residue on a sample mount and measure the grain isotopes by secondary ion mass spectrometry (SIMS). The isotope measurements for the NRL presolar grain studies are performed by collaborators at the Carnegie Institution of Washington, Washington, DC; Laboratory for Space Sciences, Washington University in St. Louis; and the Max Planck Institute for Chemistry, Mainz, Germany.

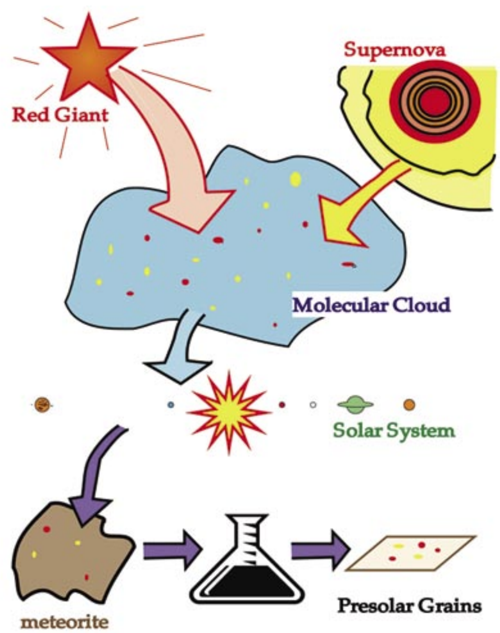

FIGURE 1
Schematic of presolar grain history. Presolar grains formed in the outflows of red giant stars and supernovae. The dust from many stars condensed into a molecular cloud that formed the solar nebula. In the early solar nebula, most material was isotopically homogenized, but the presolar grains escaped this processing and are preserved in asteroids and meteorites. We isolate the presolar grains by acid dissolution or other laboratory processing of meteorites. (Figure courtesy of Dr. Larry Nittler.)

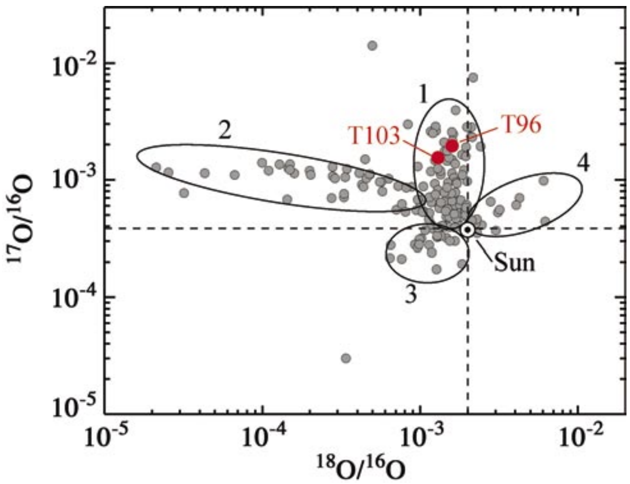

FIGURE 2
Oxygen isotope plot of presolar Al_2O_3 grains. The grains fall into four groups representing four distinct types of progenitor stars. The labels T103 and T96 indicate the isotope values for two grains that we examined in the TEM. (Figure courtesy of Dr. Larry Nittler.)

MICROMANIPULATION OF MICRON-SIZED DUST

After isotopic characterization, the grains must be extracted from the mounts and thinned to electron transparency. This simple sounding task is extremely challenging due to the size of the grains (0.3 to 2 μm), and because the individual isotopically significant grains are surrounded by thousands of isotopically normal (solar) grains. In order to solve this microscopic needle-in-a-haystack problem at NRL, we have adapted focused ion beam (FIB) lift-out techniques traditionally applied to site-specific defect analysis in semiconductor devices (Fig. 3). Using an FIB workstation, we deposit a protective Pt mask (1 μm wide, 10 μm long, and 1 μm high) on the grain of interest. This creates a large enough "handle" that we can manipulate the grain. Next, we use the approximately 10-nm Ga^+ beam to sputter excess material from the grain, creating an electron transparent slice less than 100 nm thick. After cutting the sides and bottom of the slice free using the Ga^+ beam, we take the grain to an optical microscope. There we use a glass needle mounted on a micromanipulator to move the FIB-prepared slice from the SIMS mount to a TEM support grid. This technique for extraction of individual micron-to-submicron grains is not limited to presolar grain analysis, but broadly applicable to the forensic analysis of dust and materials failure analysis, and will be an important use of the newly arrived dual-beam FIB system in the Institute for Nanoscience. A major advantage of this particle-handling technique is that it permits coordinated analyses of the same particles using multiple techniques, e.g., isotope and structure determination.

TRANSMISSION ELECTRON MICROSCOPY

To determine the structure and composition of the grains, we take advantage of the state-of-the-art TEM facilities at NRL, including the new energy-filtered high-resolution TEM housed in the Institute for Nanoscience, which will replace the temporary JEOL 2010F facility in early 2005. For greater flexibility in tilt angle for diffraction analysis, the Philips CM30, housed in the Materials Science and Technology Division, is also used.

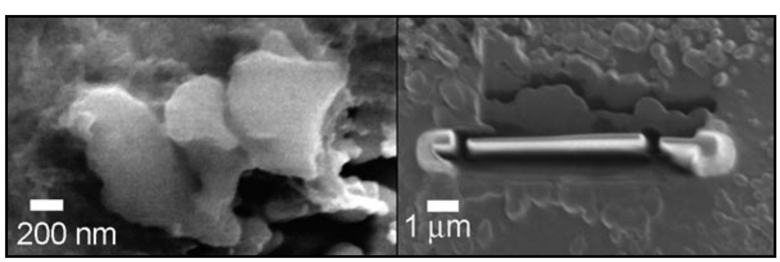

(a) (b)

FIGURE 3
(a) Secondary electron image of a presolar oxide grain. (b) Secondary electron image of a focused-ion-beam-prepared thin section of the grain ready for lift-out.

RESULTS

To date, we have investigated four different kinds of presolar grains: Al_2O_3 grains from O-rich asymptotic giant branch (AGB) stars, SiC from C-rich AGB stars, SiC from type-II supernovae, and silicates from O-rich AGB stars. The information to be gained from the grains depends on the grain composition and structure, as well as the stellar origin. The most refractory, radiation hard materials, i.e., Al_2O_3 and SiC, primarily provide information about the circumstellar environments in which the dust condensed. The less refractory silicates are likely to reflect both the condensation environment and the alteration processes by which dust is converted from molecular clouds to the solar nebula to rocky materials, i.e., asteroids, planets, and planetesimals.

PRESOLAR AL_2O_3

Aluminum oxide is a cosmically important phase because many equilibrium thermodynamic calculations predict it to be the first solid phase to condense in O-rich AGB stars. However, the formation of solid Al_2O_3 is kinetically inhibited because Al_2O_3 molecules are rare in the gas phase, and there is a 30-yr debate in the astrophysical community over whether other oxide phases, such as TiO_2, form first. Furthermore, it has typically been assumed that when Al_2O_3 condenses, it takes the stable corundum (α-Al_2O_3) structure, despite the established laboratory synthesis of many metastable structures close in free energy.

A parallel debate in the observational astronomy community concerns the identification of broad and narrow features at 12.5 μm in the infrared spectra of some AGB stars. Some astronomers have attributed these features to amorphous and corundum forms of Al_2O_3, while others have argued for assignment to spinel or polymerized silicate phases.

Our research helps resolve both of these controversies by providing data from direct laboratory study of the star dust in question (Fig. 4). Our TEM studies of two presolar aluminum oxides show that at a minimum, both corundum (Fig. 5) and amorphous forms of Al_2O_3 form in O-rich AGB stars, without prior formation of any seed phases such as TiO_2. Our data also indicate that Ti could be important in determining the structure, as we find detectable levels of Ti in the corundum grain, and not in the amorphous grain. The results of this study appeared in the September 3, 2004 issue of *Science*.[2]

SiC FROM C-RICH AGB STARS

One of the mysteries of presolar SiC is how it survives the highly oxidizing, O-rich plasma of the early solar system, without sublimation of the C to form CO gas. On Earth, SiC is extremely rare except as a synthetic material, but it is a large fraction of the dust produced by C-rich AGB stars. The structure of AGB SiC extracted from meteorites by acid treatments has been well studied by NRL staff scientist Dr. Tyrone Daulton, Code 7431.[3] However, the acid treatments drastically alter the grain surfaces, and remove all the surrounding meteoritic material, including any protective surface coatings (Fig. 6). Our FIB-based sample micromanipulation techniques allow us to extract thin sections of SiC grains located in situ in the host meteorite, or as physical separates, without the use of acids, thus preserving the grain context and surface.

The TEM results from the "pristine" (i.e., not acid exposed) AGB SiC shows that the SiC can indeed survive the early solar nebula without the formation of a protective oxide layer. The grain shapes range from heavily faceted to well-rounded (Fig. 7). The surrounding meteoritic materials show no orientation or compositional relationship to the enclosed SiC grains. This indicates that the accretion of the SiC

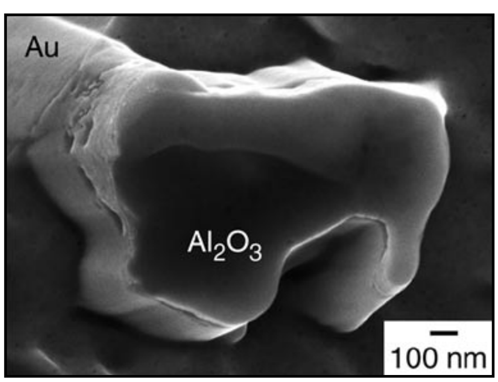

FIGURE 4
Scanning electron micrograph of a presolar Al_2O_3 grain.

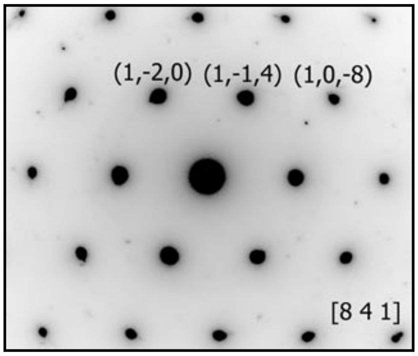

FIGURE 5
Electron diffraction pattern of a presolar Al_2O_3 grain. The indexing of the pattern confirms that the grain has the corundum crystal structure.

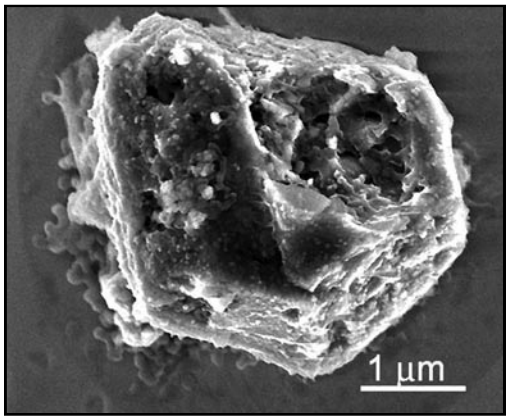

FIGURE 6
Scanning electron micrograph of an acid-treated presolar SiC grain.

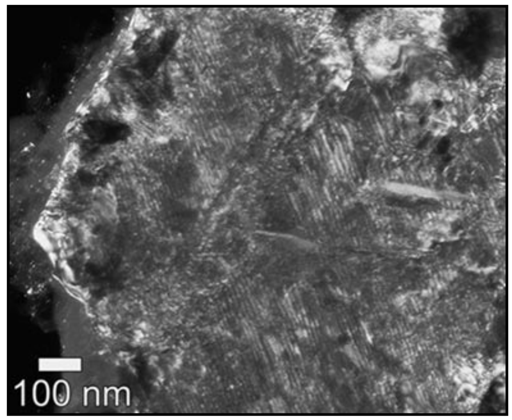

FIGURE 7
Transmission electron micrograph of an in situ presolar SiC grain.

dust onto the asteroid parent body occurred at a great enough distance from the center of the solar nebula (> 2 a.u.) that the ambient temperature was < 900 K. A surprise find in the SiC grains was an interior Ru-bearing subgrain in one SiC and many 100-nm graphite subgrains in another SiC. The occurrence of these subgrains was not observed in the acid-treated grains, possibly because the acid treatment removes subgrains, but should aid in the study of C-rich AGB star atmospheres.

SUPERNOVA SiC

Type-II supernovae are among the most extreme environments known. They are literally the rapid explosion of astronomical-sized nuclear reactors, initiated by the collapse and reexpansion of the core of massive stars (> 8 × solar mass), after they become too Fe-rich to support continued nuclear fusion. During the supernova event, most of the mass of the star is ejected in the form of jets of gas and dust. These events are the largest production source of the elements heavier than He in the galaxy. The isotope ratios of grains from supernovae are even more different from the solar materials than even the pre-solar AGB stars. One class of supernova SiC is known as the "X grains" due to the "eXtreme" isotope values. Prior to our study, it was not clear whether the supernova origin of the X grains was reflected in the structure of the grains as well as in the isotopes. In other words, do the highly nonequilibirum condensation conditions and high radiation fluxes leave specific signatures on the crystal structure? Our TEM study of two X grains provides an affirmative answer. Unlike the AGB SiC grains that are all essentially single crystals of approximately 1 µm in diameter with varying levels of defects, the X grains are agglomerates of many smaller crystallites. We have observed both a dense aggregate of 10-nm crystallites and a porous aggregate of 100-nm crystallites. In addition, the dense aggregate shows evidence of directional recrystallization of the grains due to both radiation and physical shock, two events characteristic of supernovae (Fig. 8).

AGB SILICATES

Silicate minerals constitute the greatest fraction of the dust that condenses around O-rich AGB stars, but

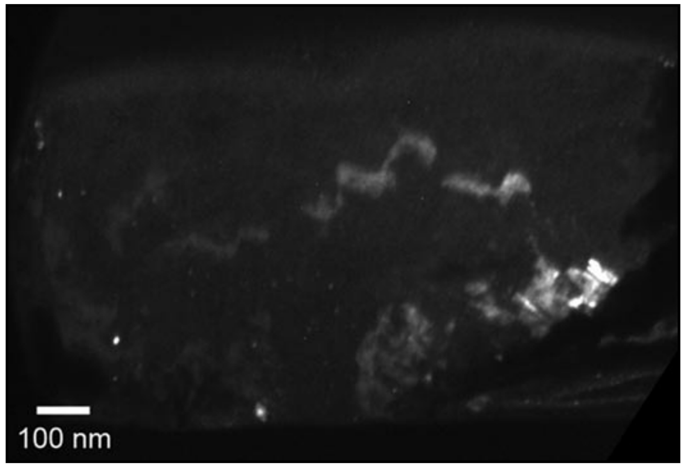

FIGURE 8
Dark-field transmission electron micrograph of a supernova SiC grain. The white "smoke trail" that crosses the grain highlights oriented recrystallization due to a radiation event.

presolar silicates have been the hardest of the presolar grains to identify. The biggest difficulties have been (1) that the host meteorites are primarily made up of silicate minerals with a solar, rather than presolar origin, so that thousands of individual isotope measurements must be made to locate a single presolar grain, and (2) that the spatial resolution of the SIMS instruments has only recently reached the submicron range required to measure these grains individually.

We have examined the structure of one presolar silicate (Fig. 9), and it was revealed to be glassy, with a composition not corresponding to a known mineral stoichiometry. This immediately raises the issue of whether this grain condensed as a nonstoichiometric amorphous grain, or was structurally and chemically altered in the trajectory from stellar condensate to meteorite inclusion. Solar silicate minerals are known to have experienced varying degrees of thermal and aqueous alteration due to the processing that occurred during and after accretion of the individual grain onto the meteorite parent body (asteroid). At some point, heavy alteration would completely erase the presolar isotopic signature, but low levels of structural and compositional alteration might preserve a distinctly nonsolar isotope composition. By comparing the isotope signatures with the structural and compositional data from more presolar silicate grains, we aim to learn about (a) the dust that was the biggest fraction of the materials that went into the initial formation of our solar system, and (b) the processes that converted those raw materials from dust to larger bodies.

SUMMARY

The microscopy of star dust is a mixture of extraterrestrial materials science and astronomy in the laboratory. We literally have samples of star dust that we can experimentally trace to stars of specific class and composition in order to better understand the stars themselves and the formation of our own solar

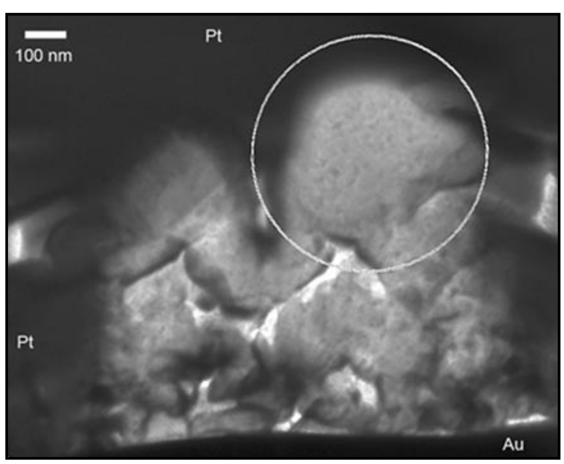

FIGURE 9
Transmission electron micrograph of a presolar silicate grain.

system. The tools, e.g., the high-resolution analytical transmission electron microscope and focused ion beam workstation, that we use for these analyses are more conventionally applied to the development of materials for new electronic devices. The same fundamental laws of nature apply to materials that condense inside a laboratory vacuum chamber as in circumstellar space. By putting presolar grains under the electron microscope, we are helping to answer some of the big picture questions that have long challenged astronomers, i.e., how does stellar material get recycled from old stars to new stars. In addition, we are building a knowledge base about the long-term survival of electronic insulators (Al_2O_3) and conductors (SiC) in space, and determining protocols to handle submicron grains for parallel analytical studies. This is a prime example of the synergistic relationship between cutting-edge research in seemingly unrelated fields, and the unexpected collateral benefits of interdisciplinary basic research.

ACKNOWLEDGMENTS

Financial support for this work is provided by the Office of Naval Research through the NRL 6.1 Core program and from the NASA Office of Space Sciences Cosmochemistry Program. Many thanks to my colleagues and collaborators, including Dr. Larry Nittler, Dr. Conel Alexander, Dr. Peter Hoppe, Dr. Tom Bernatowicz, Dr. Ernst Zinner, and Ann Nguyen.

[Sponsored by ONR/NRL 6.1 and NASA]

References

[1] L.R. Nittler, "Presolar Stardust in Meteorites: Recent Advances and Scientific Frontiers," *Earth and Planetary Science Letters* **209**, 259-273 (2003).

[2] R.M. Stroud, L.R. Nittler, and C.M.O'D. Alexander, "Polymorphism in Al_2O_3 Presolar Grains from Asymptotic Giant Branch Stars," *Science* **305**, 1455 (2004).

[3] T.L. Daulton, T.J. Bernatowicz, R.S. Lewis, S. Messenger, F.J. Stadermann, and S. Amari, "Polytype Distribution of Circumstellar Silicon Carbide: Microstructural Characterization by Transmission Electron Microscopy," *Geochimica et Cosmochimica Acta* **67**(24), 4743-4767 (2003). ★

Using Light to Prepare and Probe an Electron Spin in a Quantum Dot

A.S. Bracker, D. Gammon, E.A. Stinaff, M.E. Ware, J.G. Tischler, D. Park, A. Shabaev, and A.L. Efros
Electronics Science and Technology Division

INTRODUCTION

Electrical charge is the fundamental physical quantity that makes modern electronic devices possible. However, recent advances in nanofabrication and materials physics have created the opportunity to use electron spin for next-generation devices. Spin is a quantum mechanical property with great potential to bring about entirely new technologies for computing, communications, and encryption. All of these applications require the ability to prepare electrons in specific spin states and to measure those states following a sequence of operations. We have recently demonstrated optical pumping and measurement of individual electron spins in quantum dots (QDs).[1] Circularly polarized laser light excites a specific spin state of the dot. We achieve spin-selective detection through the energy and magnetic field response of subsequent luminescence, which reveals clear signatures of our prior spin state preparation. These results lay the groundwork for using individual semiconductor electron spins as addressable logic elements for quantum information processing and quantum communication.

COHERENT SEMICONDUCTOR SPINTRONICS

Transmitting and processing information are essential to the success of military and intelligence operations, and the security of that information is naturally of prime importance. A fundamentally new class of optoelectronic devices that exploit quantum mechanical phase could enable a revolution in communications, encryption, and data processing. In a solid-state device, electron spin is a natural choice for the carrier of quantum phase, because we can leverage established materials and device technologies that already use electrons as charge carriers. “Spintronics” is a broad interdisciplinary research field that seeks to exploit this spin degree of freedom. While the invention of the transistor started a revolution in solid-state electronics by providing an elegant means to manipulate electrical charge, spintronics is expected to open still broader frontiers for electronics and optoelectronics.

Spin is an inherently quantum mechanical property, yet we often visualize it as if it were a classical angular momentum with the electron rotating about an axis. We usually depict the spin as a vector pointing along its rotation axis (Fig. 1). An arbitrary classical angular momentum is a vector that can point in any direction, while the analogous state of a quantum mechanical spin is a coherent sum $a|\uparrow\rangle + b|\downarrow\rangle$ of two basis states, spin up $|\uparrow\rangle$ and spin down $|\downarrow\rangle$, with some relative phase described by the coefficients a and b. Spin is therefore a two-level system, and some forms of spintronics approach spin as an additional binary degree of freedom. However, arbitrary superposition states have character of both “up” and “down.” In coherent spintronics, we take advantage of these quantum superposition states, which provide a great advantage as a form of information. While electrical charge readily provides a binary form of logic (i.e., a charged or uncharged bit), each spin quantum bit or “qubit” provides a continuum of states, and the degree to which we can use this information is determined by how precisely we can write or read the coefficients a and b that describe the superposition. By entangling a collection of many such spins, the information processing power increases greatly.

Quantum communication may be best achieved with photons of light or other electromagnetic waves, because they readily propagate over long distances, and their polarization states are robust to environmental perturbations. Indeed, basic quantum communication hardware is already available commercially, with information carried over hundreds of meters by the polarization state of light in an optical fiber. Someday, these approaches will be extended to longer distances through the use of optical repeaters and perhaps adapted to free-space transmission over much longer distances, including satellite communication.

While pure optics may be an excellent approach for communication, quantum information processing and storage are better achieved with electrons or holes

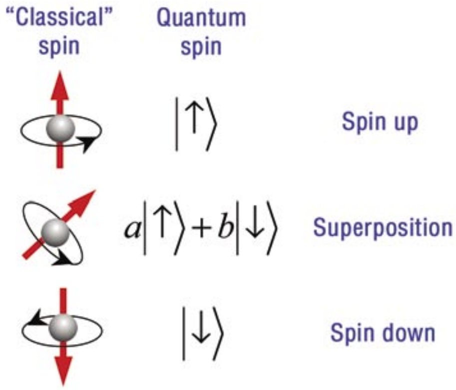

FIGURE 1
Schematic depiction of classical angular momentum with different projections and analogous quantum mechanical spin wavefunctions.

in a solid material, just as conventional electronics and logic are today. A complete communications and data processing system must therefore incorporate a hybrid technology that combines photonic and electronic spin qubits, and it must provide a way to convert between them. The research that we describe in this article addresses materials science and basic spin physics that can enable solid-state electronics based on spin coherence. Optical techniques are central to our work, as the ability to prepare and measure individual spins is critical for coupling spin-based electronics with communication.

SEMICONDUCTOR QUANTUM DOTS

Just as conventional logic circuits consist of ordered networks of transistors, one must likewise specify the spatial position, energies, and mutual interactions of electron spins in a multispin circuit. We use semiconductor QDs for this purpose. QDs are very small particles of crystalline material with discrete energy levels that correspond to confined orbital states of electrons in the QD. A typical QD in our research program consists of 10^4 to 10^5 atoms of a III-V compound semiconductor such as InAs, which is embedded within a host material of larger bandgap such as GaAs or AlGaAs. We can control their energy levels by modifying their composition, size, and shape. Advanced crystal growth and nanofabrication techniques offer ways to position QDs into ordered arrangements.

We fabricate QDs by molecular beam epitaxy (MBE), an ultrahigh vacuum technique for growing extremely pure semiconductor crystals from elemental precursors. Our QD fabrication was carried out in the NRL Epicenter, an MBE facility in Building 208 that is staffed by scientists and engineers from four NRL divisions. The facility contains four MBE machines for growth of III-V and II-VI compound semiconductors and magnetic materials, material processing capabilities, scanning probe microscopy, and surface spectroscopy.

Our work on spin preparation and measurement involves two types of QDs. The first type consists of a thin planar GaAs quantum well sandwiched between AlGaAs barriers (Fig. 2(a)). Although the GaAs layer is nominally two-dimensional, with confinement in the growth direction, the interfaces between GaAs and AlGaAs have roughness on the scale of one or two atomic layers. This roughness is sufficient to confine electrons within the plane of the quantum well, thereby producing a QD. The second type of QD is formed through Stranski-Krastanov self-assembly (Fig. 2(b)). Here, a material such as InAs is grown on a flat substrate surface of GaAs, which has a smaller lattice constant. When the growth first starts, a very thin planar "wetting layer" forms, but only a few atomic layers of planar InAs can be grown before a critical threshold is reached. When the strain between the two materials becomes too great, most of the wetting layer coalesces into small solid droplets of InAs. These QDs are shaped like domes or pyramids, 10 to 50 nm wide and 3 to 6 nm high. For many of our samples, the newly formed dots are buried under a capping layer of GaAs or other materials. Figure 2(c) shows a typical plan-view atomic force microscope image of these dots (taken without the capping layer).

In order to controllably insert a single electron into each QD, we embed the QD layer in the insulating region of a Schottky diode heterostructure (Fig. 2(d)). This structure consists of an insulating GaAs layer grown by MBE on a heavily doped GaAs substrate and buffer layer. With a metal layer evaporated on the surface and wire contacts to the front and back of the sample, we apply an electric field across the insulating layer that contains the QDs. Figure 2(e) shows a heterostructure band-edge diagram. At low or forward bias (dark blue), the electric field is small, and the discrete energy levels of the QD lie below the Fermi sea of electrons, so that the dots each contain

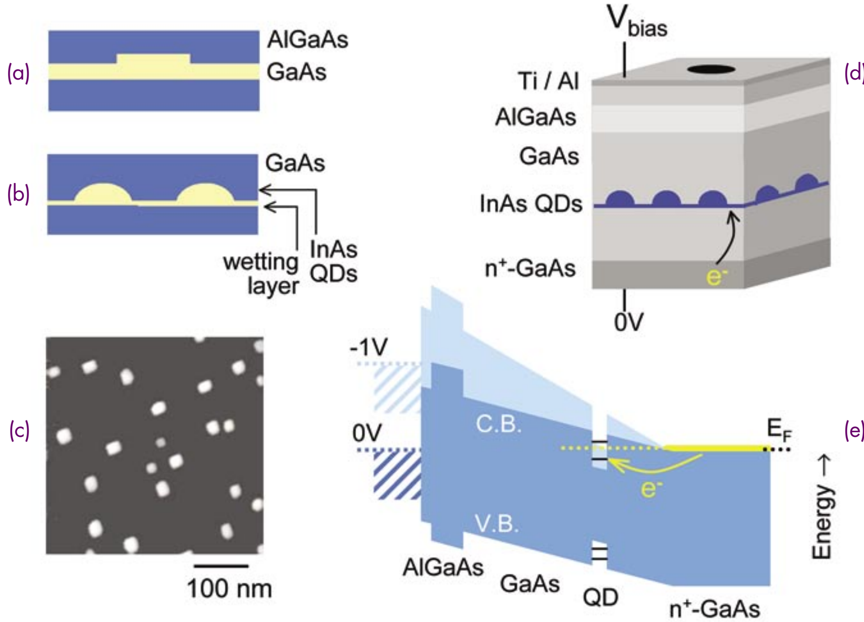

FIGURE 2
(a) Schematic side view of QDs formed by interface roughness in a GaAs/AlGaAs quantum well. (b) Schematic side view of Stranski-Krastanov self-assembled QDs and two-dimensional wetting layer, embedded in GaAs. (c) Plan-view atomic force microscope image of self-assembled QDs. (d) Schematic structure of InAs QD Schottky diode for tuning the charge state of QDs. (e) Conduction and valence band-edge profile of InAs QD Schottky diode for two typical biases.

one or more electrons. In reverse bias (light blue), the electric field increases, and electrons are driven out of the QDs. As we will show below, the small size of each QD allows electrons to be injected one at a time.

OPTICAL SPECTROSCOPY OF CHARGED QUANTUM DOTS

Photoluminescence (PL) spectroscopy is a powerful method for examining the energy levels and spin properties of electrons in QDs. In this technique, we excite a QD sample with a laser, which creates electron-hole pairs (e^--h^+) in the material (Fig. 3(a)). An electron-hole pair (exciton) confined in a QD will eventually relax to the lowest unfilled energy level of the dot, where it can recombine and emit a photon. The energies of these luminescence photons, which we disperse in a grating spectrometer, provide information on the energy level structure of the QD. Figure 3(b) shows a typical PL spectrum obtained when the laser is focused to a 50-μm spot on the sample, illuminating thousands of QDs. Because these QDs all have slightly different energies, the spectrum is inhomogeneously broadened. Nevertheless, we can resolve a discrete energy level structure with a progression of S-, P-, D-, and F-like orbital states, confirming that we have three-dimensional atom-like quantum confinement in these QDs.

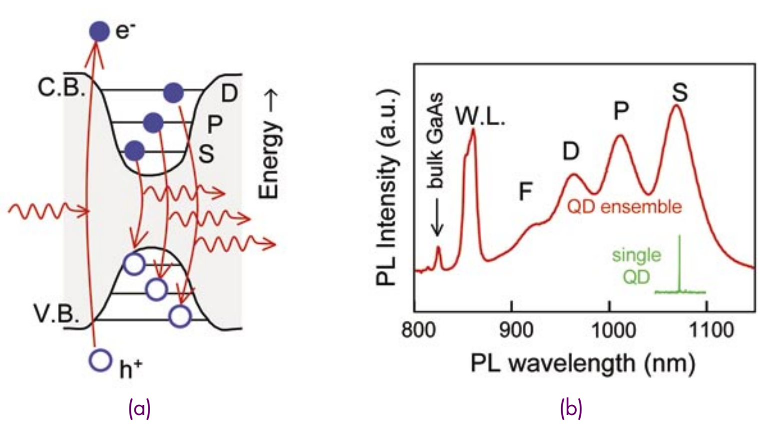

FIGURE 3
(a) Band-edge profile, level structure, and optical transitions (absorption and PL) in a neutral QD. Electrons are solid circles, and holes are open circles. (b) PL spectrum of a QD ensemble showing inhomogeneously broadened atomic-like level structure (red curve) and a single QD spectrum (green).

The inhomogeneous broadening in this spectrum obscures many details that would be clear if the peaks were much sharper. We get around this problem by using the powerful techniques of single-QD spectroscopy, which were developed at NRL and other institutions in the mid 1990s. With electron beam lithography and liftoff techniques, we fabricate a metal mask containing an array of tiny apertures, some as small as 200 nm, on the sample surface (Fig. 4(a)). Each aperture contains a small number of QDs and sometimes only one, so that if we point the laser beam at the aperture, we measure PL from only those QDs (Fig. 4(b)). The green curve in Fig. 3(b) illustrates the power of this technique, where a single, very sharp spectral peak from one QD inside an aperture is shown below the much broader ensemble spectrum.

By combining single-dot spectroscopy with bias-controlled charging in a diode heterostructure, we see a much richer picture of the energy level structure and charge states of the QD. Figure 5(a) is an intensity contour plot that shows how the PL spectrum of an InAs QD evolves as we vary the bias across the diode. A vertical slice through this graph would correspond to single PL spectrum, and each colored band in the two-dimensional plot represents the evolution of a particular spectral peak with bias. Each PL peak corresponds to an exciton (electron-hole pair) recombining in the presence of one or more additional electrons or holes. Figure 5(b) depicts the possibilities. Going from left to right in Fig. 5(b), or from negative to zero bias in Fig. 5(a), we see excitons with increasing negative charge: first an extra hole (X^+), then a neutral exciton (X^0), then an extra electron (X^-), and finally two extra electrons (X^{2-}). When the diode is unbiased (0V), the QD and the wetting layer are filled with electrons, and the single QD PL spectrum at the right of the figure is smeared out. Each charge complex has a distinct PL energy, because the addition of new charge changes the net Coulomb energy (attraction or repulsion). These Coulomb shifts and the wide energy spacings of the orbital levels (Fig. 3(b)) provide energy discrimination that allows us to control the charge state in the QD.

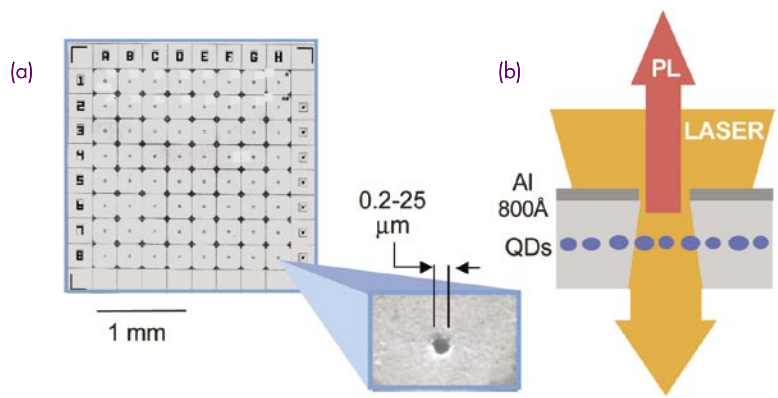

FIGURE 4
(a) Image of an aluminum aperture mask on a GaAs QD sample used for single QD spectroscopy. (b) Cross-sectional schematic of laser excitation and PL of a small number of QDs through a submicron aperture.

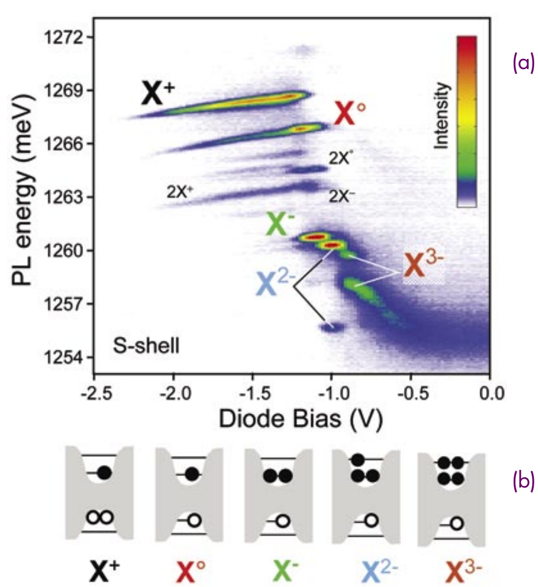

FIGURE 5
(a) PL intensity map as a function of PL energy and diode bias. PL features from various charge states of excitons (X symbols) and biexcitons (2X symbols) are labeled accordingly. (b) Electron and hole configurations for the various excitons as labeled in (a).

Finally, we note that the pairs of peaks for X^{2-} and X^{3-} can be attributed to exchange interactions, while biexciton peaks (e.g., $2X^-$ and $2X^+$) appear due to the fairly high laser intensities used in this work.

SPIN SPECTROSCOPY AND OPTICAL PUMPING

We consider the spin properties of a QD containing a single electron in a confined conduction band level. This simple system serves as a model for a semiconductor spin qubit. The two degenerate spin states of this electron (up and down) are depicted with arrows at the bottom of the level diagram of Fig. 6. The optically excited state of this electron is the three-particle negative "trion" (X^-), which consists of the original electron, plus an additional exciton. The electrons in the trion are paired with opposite spins in a singlet state; therefore, they do not contribute to the overall spin of the trion. Instead, the spin of the trion is determined by whether the unpaired hole spin points up or down. The trion is an important focus of our work, because it can be used as an optically addressable intermediate state for initializing, rotating, and reading out the ground-state electron spin.

As shown in Fig. 7(a), our starting point for spin spectroscopy is a technique called optical orientation. In optical orientation, a photon of circularly polarized light is absorbed by a QD, where it is converted into a polarized electron-hole pair, with the hole spin "up" and the electron spin "down." Through subsequent relaxation, this polarization may transfer to other spin degrees of freedom such as the electron that was initially in the QD. This process is known as "optical pumping," in analogy with a similar process from the field of atomic physics. Optically pumped electron spin can persist long after recombination of excitons is over, providing the type of spin memory that is needed for storage and processing of information. Optical pumping may provide a way to initialize spins prior to quantum logic operations. After exciting a QD sample with right-circularly polarized light to initiate optical orientation, we measure the degree of circular polarization "memory" in the PL. This polarization memory reveals the electron and hole spin dynamics that are caused by optical excitation and relaxation, including the possibility of optical pumping.

Figures 7(b) and 7(c) show the PL and PL polarization memory as a function of diode bias for a GaAs QD. We see distinctive behavior for all three types of excitons, but here we focus on the remarkable properties of X^-. In particular, its polarization memory has a negative value between 4 V and 4.3 V bias. A negative polarization memory implies that the PL emitted from the QD has the opposite helicity from the laser beam that excited the sample in the first place. This effect can be seen in an even more striking way if we measure the raw PL polarization directly as a function of the laser polarization (Fig. 7(d)). We can vary the laser polarization continuously from left circular to right circular and back, including intermediate linear and elliptical polarizations. When we do this, we see that the X^- raw PL polarization changes in the opposite sense from the laser polarization, while for X^0 and X^+ it changes in the same sense. We show next that this behavior is a consequence of optical pumping of the original QD electron spin.

Optical pumping of electron spins should occur more readily at higher laser intensities, where it can dominate competing processes. Under modest laser intensity, the polarization memory of X^- is negative only near the bias value of 4 V, but it becomes positive at higher bias, due to competing processes related to electron injection (Fig. 7(c) and Fig. 8(a) (blue)). However, if we increase the laser intensity by a factor of 15, the PL polarization becomes negative for all

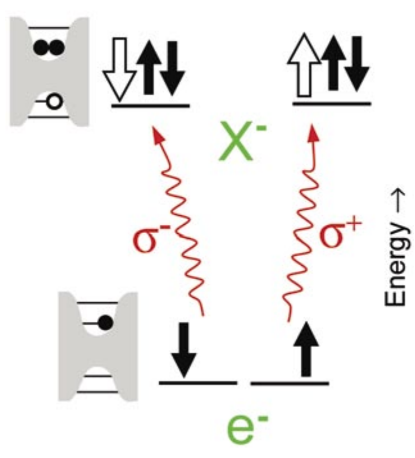

FIGURE 6
Total energy diagram showing spin configurations of a ground state electron (e^-) and its optically excited state (negative trion). Open and filled arrows represent hole and electron spins, respectively. Optical transitions are achieved with right (σ^+) and left (σ^-) circularly polarized light.

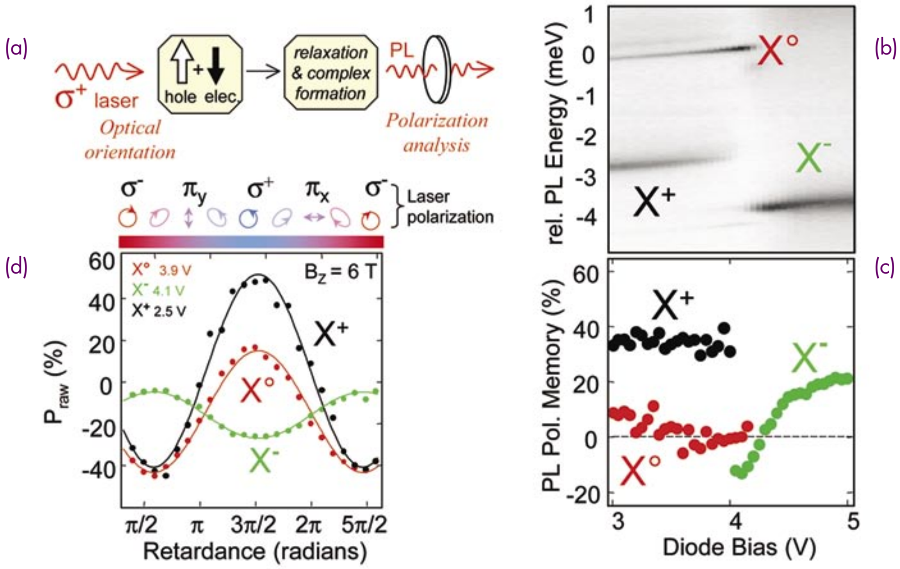

FIGURE 7

(a) Schematic of an optical orientation experiment. (b) PL intensity map for a GaAs QD as a function of PL energy and diode bias. (c) Circular polarization memory for the same features as in (b). (d) Raw PL polarization as a function of laser polarization.

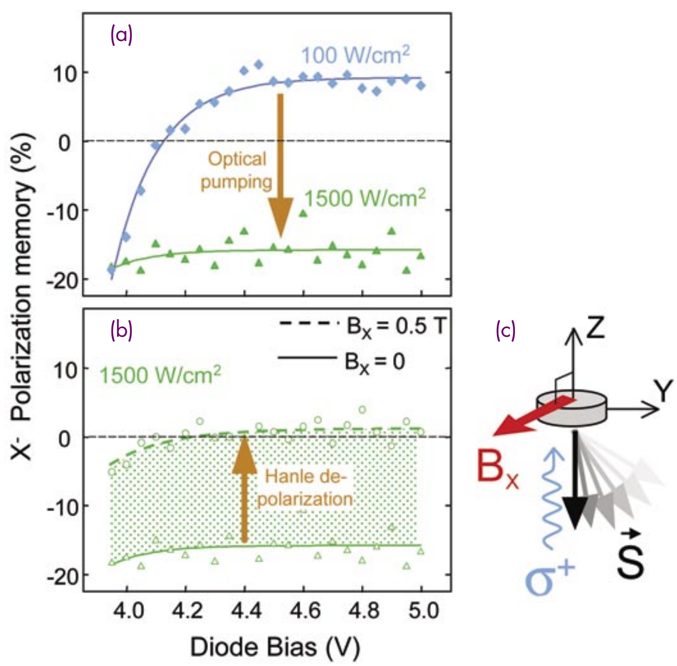

FIGURE 8

(a) Polarization memory of negative trion (X^-) for two laser excitation intensities. (b) Elimination of negative polarization memory for X^- through Hanle depolarization of optically pumped electrons. (c) Geometry of Hanle effect: optically pumped electrons are initially oriented parallel to Z axis, but are depolarized by precession about transverse magnetic field B_X.

values of the bias (Fig. 8(a) (green)). This behavior is suggestive of optical pumping becoming more efficient than the high-bias competing process. The second piece of evidence comes from the Hanle effect. In the Hanle effect, the sample is placed in a small transverse magnetic field, where electron spins will precess around the field axis (Fig. 8(c)). If the magnetic field is high enough, this precession will erase the spin polarization that is caused by optical pumping. Indeed, application of a small magnetic field causes the negative polarization to disappear (Fig. 8(b), upper curve), proving that the negative polarization is caused by optical pumping.

SUMMARY

We have used polarized laser light to optically pump an electron spin in an individual semiconductor quantum dot. We detect this prepared spin state through an unusual negative spin memory that is imprinted on the luminescence polarization of a charged exciton. These processes represent very basic forms of electron spin read and write operations. The critical aspect of this research is the ability to fabricate charge-tunable quantum dots that can be injected with a single electron and measured individually using microphotoluminescence spectroscopy. Together with new nanofabrication methods and coherent optical spin control, these advances should enable a new generation of spin-based electronics, providing capabilities in computation and secure communication that are not achievable with existing technologies.

[Sponsored by ONR, DARPA, SPINS/QuIST, ARDA/NSA/ARO]

Reference

[1] A.S. Bracker, E.A. Stinaff, D. Gammon, M.E. Ware, J.G. Tischler, A. Shabaev, A.L. Efros, D. Park, D. Gershoni, V.L. Korenev, and I.A. Merkulov, "Optical Pumping of the Electronic and Nuclear Spin in Single Charge-tunable Quantum Dots," *Phys. Rev. Lett.* **94**, 047402 (2005).

★

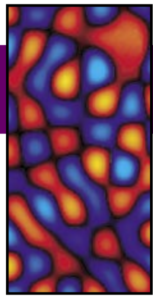

Fault Detection and Localization Using Laser-Measured Surface Vibration

J.A. Bucaro, J.F. Vignola, and A.J. Romano
Acoustics Division

INTRODUCTION

Structural health monitoring techniques have become increasingly important to the Navy of the 21st century whose strategy is to emphasize advanced designs and new material technologies in its modern high performance structures while utilizing existing aging structures beyond their planned lifetimes. At the same time, the Navy would like to reduce manning levels on Naval platforms, reduce time in repair and total ownership costs, and increase survivability. Among other things, these trends have driven the need for the development of reliable, automated, structural health assessment methodologies. In response to this need, we have been addressing the feasibility of structural acoustic techniques for monitoring the mechanical condition of structures.

The focus of our structural acoustic development efforts thus far can be summarized by the following question: Given sufficient but readily accessible displacement information over the surface of a vibrating structure, can we develop and implement corresponding *local* inversion algorithms for mapping material parameter variations, detecting and localizing flaws (such as cracks, voids, and delaminations), and uncovering the depth profiles of such?

In this article, we present the details of the structural acoustic approach to fault monitoring, describe various "inversion" algorithms for extracting the fault information, show the results of numerical feasibility studies, discuss the associated measurement technologies, and then present applied studies we have carried out using this methodology. These include both laboratory-based studies on simple structures and spin-off work we have done on art-laden walls at the U.S. Capitol building.

THE STRUCTURAL ACOUSTIC APPROACH

Mechanical fault monitoring using the dynamic response of a structure excited by externally applied forces is not new. For the most part, traditional methods involve some application of modal analysis techniques that typically extract changes in resonance frequencies and/or associated mode shapes. One drawback of such modal approaches results from the fact that local changes in a structure caused by a fault often produce only very small changes in these global modal parameters whereas unavoidable environmental changes can have a large impact on these measured characteristics. In addition, even when modal analysis is used successfully to indicate a structural problem, localization of the detected flaw is in general difficult.

Our focus has been to develop techniques that not only use the traditional mechanical dynamic response but also are able to detect and characterize *local* changes in the structural dynamics caused by the presence of a fault. Figure 1 illustrates this methodology, which uses measurements of surface displacement associated with vibration of the structure caused by externally applied forces. These forces can be created simply by a local actuator in direct contact with the structure or in some cases by an incident airborne acoustic wave. The measured normal surface displacements $u_z(x, y)$ are then inverted *locally* by using various mathematically optimized algorithms in order to obtain a desired material parameter—for example, the elastic modulus—whose spatial variation then serves to detect and localize the fault. We choose to rely on *surface* displacements because these are readily accessible for all materials and for most structures using existing scanned sensor technologies, such as laser Doppler vibrometry. There are techniques capable of interior displacement measurements, including magnetic resonance elastography (MRE) and various optical scattering methods, but these can be applied only to a restricted set of materials—those with high proton spin density for MRE and those that are optically transparent for the latter.

INVERSION ALGORITHM EXAMPLES

To a large extent, the power of the fault detection techniques pursued here depends on the successful development of a compatible set of inversion algorithms that can operate efficiently and in the presence

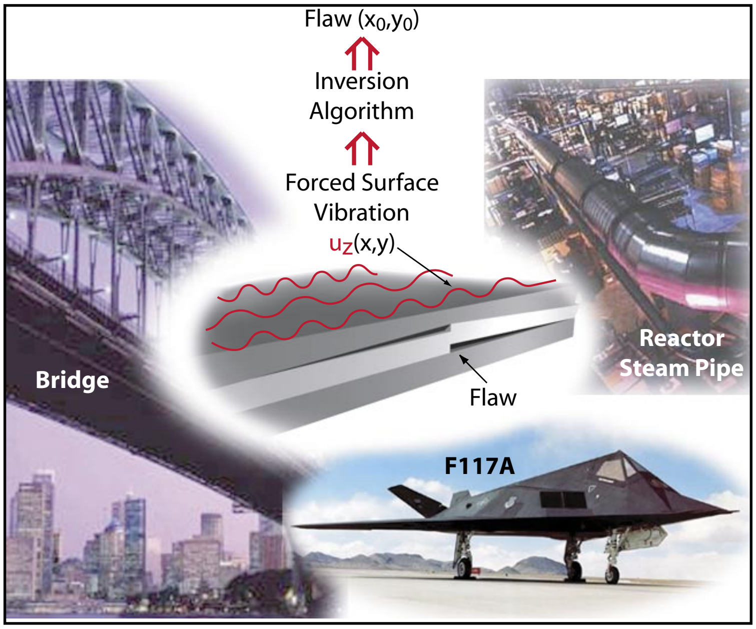

FIGURE 1
Depiction of the structural acoustic fault monitoring methodology applied to a variety of structures. Surface displacements are monitored over the area of interest due to structural vibrations induced either by an applied shaker or an acoustic source. The displacements measured over the surface are algorithmically inverted to produce a map of a desired material parameter that serves to detect and locate the flaw.

of noise on the scanned surface displacements of the vibrating structure to produce a meaningful map of some fault-sensitive mechanical parameter. Below we discuss four such algorithms with which we have had various degrees of success.

Direct Inversion

In the direct inversion approach,[1] we seek to invert the equations of motion for the structure. For the vibration of general elastic media at frequency ω, the fundamental equation is given as

$$\sigma_{ij,j}\,[\vec{u}] + \rho\,\omega^2 u_i = f_i, \tag{1}$$

where σ_{ij} is the stress, the subscript j denotes the partial derivative with respect to co-ordinates x_j, $\vec{u}$ is the displacement, ρ the density, and $\vec{f}$ the applied force used to vibrate the structure. Without detailing the mathematics here, in locations away from the applied force, a variational form of the above equation is constructed through multiplication by a smoothly varying "virtual" function having specifically designed boundary conditions and insertion of the relevant relationship between stress and strain. The resulting equation is then inverted to obtain an effective elastic modulus in terms of the measurable displacements $\vec{u}$. For the case of a plate structure of thickness h, Young's modulus E, and Poisson ratio υ, the inversion results in the relatively simple relationship

$$M(E, \upsilon, \rho, h) = \omega^2 G(u_z), \tag{2}$$

where M is the *local* plate stiffness/(ρh) and G is an integral function over the surface whose integrand depends upon the measured $u_z(x, y)$ and which by design contains no spatial derivatives of u beyond the first. We will show later that this latter property, which results from introduction of the virtual functions, is important because of its ability to greatly reduce the effects of spatially dependent noise on the inversion result. The simple application of Eq. (2) on the measured displacements can thus provide *local* mechanical information involving E, υ, ρ, and h.

Generalized Force Mapping

In contrast to direct inversion, the generalized force mapping technique[1] uses the *known* values of the elastic moduli, density, and thickness together with the measured displacement $u_z(x, y)$ across the surface to compute the left-hand side of Eq. (1). Away from the applied force, a non-zero result here as a function of position identifies a *generalized* force that now exists in the plate as a consequence of the presence of the flaw. The appearance of these forces together with their position then serve to detect and locate the fault. In principal, the details of the derived force could be used to further characterize the fault, although we have not yet exploited this possibility.

ω-*k* Mapping

In ω - k mapping,[2] a two dimensional temporal and spatial FFT is performed on the measured displacement data thus providing a frequency (ω) - wavenumber (k) representation of the elastic vibration. These transforms are spatially windowed to provide *local* information. For elastic wave propagation, this format displays characteristic "dispersion" curves indicating the elastic wave types present (e.g., compressive, shear, and flexural) and the frequency dependent velocities. Local differences in these curves from those observed or expected in unflawed structures indicate variations in wave types or in their speeds that are directly related to material parameter variations associated with the development of flaws. This Fourier acoustic technique has been particularly successful when applied to delamination effects in layered structures. In such cases, slow flexural waves excited in the detached layer present their unmistakable $\sqrt{\omega}$ dispersion curves in distinct contrast to the nearly vertical lines of the faster waves traveling in the uncompromised, adhered structure.

Dot Product/Cross Correlation

In the dot product/cross correlation approach, the frequency spectra of the displacements at each data location are viewed as a multicomponent vector. Using this perspective, a vector dot product is performed between spectral data obtained at two separated locations; and with one of these points fixed, the resultant projection is mapped onto the surface. This approach highlights local differences in spectra providing a good indication of material parameter fluctuation across the structure.

NUMERICAL DEMONSTRATION

An effective way to illustrate the workings of an inverse algorithm and to evaluate its expected performance is through numerical simulation. We focus discussion of our numerical studies on the case of a solid homogeneous metal plate with and without an internal inclusion near its upper left-hand corner. In the context of fault monitoring applications, plate results are more general than one might first think in that many structures can be addressed at some level as a collection of platelike elements. A finite-element structural dynamics code is used to compute the dynamic displacements $u_z(x, y, \omega)$ on a rectangular grid with a spacing much less than the fault size. In an actual system, it is the parameter u that would be monitored over the structure's surface and then used as an input to an inversion algorithm.

We consider the more typical case in which the displacement data itself does not directly reveal the presence of the flaw. For such a case, Fig. 2 shows the results of applying three inversion algorithms to displacement "data" obtained at 20 kHz in steel plates 60 × 30 × 2.54 cm, one having a 2 × 1 × 1.5-cm inclusion, whose Young's modulus is 0.05 that of the plate.

Figure 2(a) shows the displacement "data" for both the homogeneous plate and the plate with the inclusion. Clearly, there does not appear to be any definitive indication of the location of the flaw in the displacement data itself. Figure 2(b) shows the result of applying the variational inversion algorithm specified by Eq. (2). In both plates, the somewhat regular modal pattern seen throughout the elastic modulus map is an artifact of the inversion algorithm operating on the zero displacement levels (i.e., $u_z = 0$) that exist at the nodal lines of a mode. This particular inversion algorithm is not properly conditioned to handle these zero levels. We have shown that this modal structure in the elastic moduli maps can be eliminated by using broadband data so that the nodal lines for any particular mode do not lead to zero displacement levels anywhere across the plate. One method we have developed to accomplish this is called the |VV*| algorithm, which sums, at each spatial point and over each frequency component in the band, the absolute square of the magnitude of the measured normal velocity. (Note that the velocity is the time derivative of the displacement u.) We show an example of how the algorithm is used |VV*| later when we discuss experimental results.

Ignoring these nodal line artifacts, one can clearly see the rectangular flaw in the upper left-hand corner of the modulus map. Further, the color map gives the correct value for the ratio of the bending modulus $Eh^2/(12(1 - \upsilon^2))$ of the flawed region vs the homogeneous region (0.3), a parameter that can be used to further characterize the fault. To demonstrate the importance of developing the "variational" formulation of the inversion algorithm, we apply a simpler flexural inversion algorithm to the displacement data and show the results in Fig. 2(c). As can be seen, in addition to the pattern associated with the nodal lines, there exists a finer scaled pattern as well. This is an artifact of this algorithm associated with the presence of high-order (up to the fourth) spatial derivatives operating on the discretized (and therefore "noisy") displacement data generated by the finite-element calculations. As discussed previously, this effect is all but eliminated when applying the variational inversion algorithm (Eq. (2)) because in the expression for G, the higher order derivatives operate on the smooth, noiseless virtual functions unlike the simpler inversion algorithm where they instead operate directly on the "measured" data $u_z(x, y,)$.

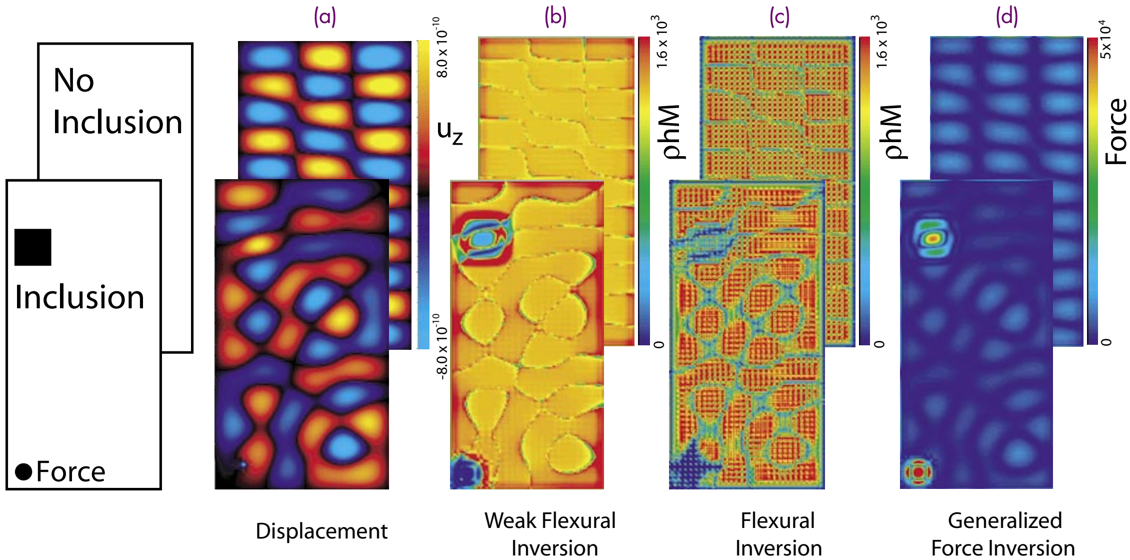

FIGURE 2
Results of a finite-element-based numerical study to detect and locate an internal inclusion in a steel plate. The upper and lower rows are for the cases of the homogeneous plate and the flawed plate respectively. Column (a) displays the "measured" surface displacements. The next three columns show the results for applying three different inversion algorithms to the surface displacements, (b) variational flexural inversion designated by Eq. (2), (c) flexural inversion, and (d) generalized force inversion.

Next we consider application of the generalized force mapping algorithm wherein we assume known values for the elastic plate parameters, computing the left-hand side of a variational form of Eq. (1) using these and the measured displacement data. Non-zero values indicate internal forces in the structure associated with the inclusion. Figure 2(d) shows the results for the homogeneous plate (upper figure) and for the plate with the inclusion (lower figure). As can be seen, the generalized force map does clearly detect and locate the inclusion (and of course the applied force as well). Compared to the elastic moduli inversion algorithms, this algorithm is not so affected by the presence of nodal lines.

APPLIED STUDIES

Laboratory Studies

Experimental studies conducted in the laboratory indeed confirm the efficacy of implementing structural acoustic fault detection methodologies. In addition, the experiments have been used to develop practical implementations of these concepts wherein we have addressed shaker and acoustic speaker methods for mechanically exciting the structure; acquisition of broadband, surface-scanned displacement data; and the performance of the inversion algorithms in real structures.

We have implemented two techniques for acquiring the surface displacement data. The first is a commonly used technique employing a scanning laser Doppler vibrometer (SLDV). In addition to special laboratory designed devices, there are commercially available SLDV systems that are ideal for this function, some of which have software allowing versatility in choosing spatial sampling intervals as well as specific surface sampling paths. Typically, the analog output of the SLDV is band-passed filtered and stored digitally for the postprocessing by which we implement the inversion algorithms. A second less well-known surface displacement measurement technique uses a miniature scanning acoustic microphone to sample the evanescent sound *pressure* field emanating from the vibrating structure. Using the principles of nearfield acoustic holography (NAH),[2] we have taken the measured pressure fields and back-projected them onto the structure's surface, converting them to spatial displacement information, i.e., $u_z(x,y)$.

Using these actuation and displacement measurement techniques, we have studied and successfully demonstrated our structural acoustic fault detection methods on a number of relatively simple laboratory structures. These include metal plates with flaws, lap joints with varying degrees of attachment, and thin, stiffened panels with segments of frame detachment.

An illustrative and important example of these studies is that carried out on frame-stiffened plates and composite panels. Our interest here is related to composite airframe structures and the need to detect and locate areas where problems are developing along the frame/skin bond. Figure 3(a) shows the ribbed side of a stiffened plate, and Fig. 3(b) shows the underside of the plate showing the location of the detached frame segment (red rectangle). Figure 3(c) shows an SLDV-measured displacement scan made on the topside of the plate, and Fig. 3(d) shows the result of operating the variational inversion algorithm on these data. In this latter map, dark blue vertical lines successfully track the locations of the hidden interior frames, and the associated gap in the middle of the center frame line successfully indicates where the frame has become detached. We have produced virtually identical results for thin, frame-stiffened composite panels of the type used in air-frame structures, examples being the wing skins, control surfaces, and stabilizers of fighter aircraft.

Microstructure Monitoring

Even though our discussion has centered on fault morphologies whose sizes fall in the centimeter to millimeter range, the structural acoustic method does not appear to be limited to any particular length scale. Indeed, the inversion algorithms themselves are independent of scale. What is required is that the structure be mechanically excited at frequencies whose structural wavelengths are short enough, no more than an order of magnitude larger than the fault dimension, and that the dynamic surface displacements be mapped with a spatial resolution an order of magnitude smaller than the fault size. Thus, for example, 10-μm flaws could be detected and localized near the surface of a typical solid using an excitation of several megahertz and a surface vibration measurement capable of a several micron resolution. That the structural acoustics methodology can be focused, as it were, down to relatively small dimensions has important implications for the detection and characterization of microflaws in many solid materials, including metals, composites, ceramics, and semiconductors.

By way of example, we have in fact successfully employed microscope SLDVs developed at NRL with super resolution to map the vibration over the surface of micron-thick silicon crystal micro-oscillators in the form of rectangular paddles about 100 μm on a side. In so doing, we have been able to detect and locate various faults in our fabricated structures. For example, consider the measured displacement map shown in Fig. 4 for a 373 kHz paddle vibration mode

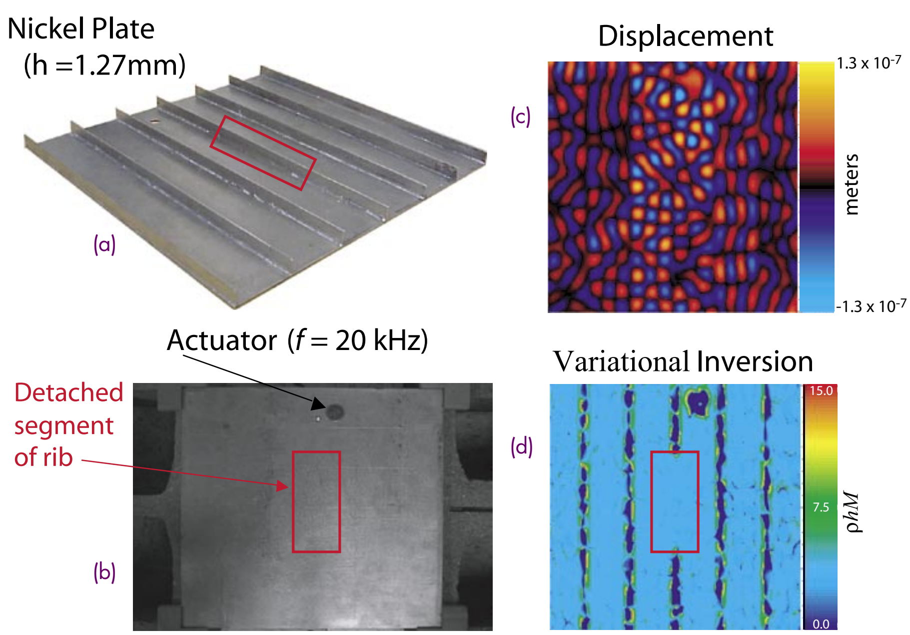

FIGURE 3
Experimental demonstration to detect and locate frame detachment in a rib-strengthened thin nickel plate. (a) Shows the ribbed side of the plate, and (b) shows the external measurement side with the red rectangle marking the hidden location of frame detachment. (c) Shows the SLDV-measured surface displacements caused by a point actuator in contact with the plate excited at 20 kHz, and (d) shows the result of applying the variational flexural inversion algorithm, where the obscured frames manifest themselves by the deep blue lines and the detached region by the absence of such.

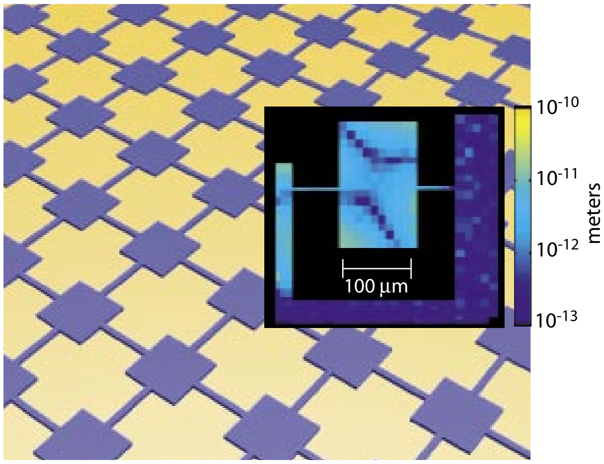

FIGURE 4
The insert displays microscope SLDV measurements of the dynamic displacements of a 100 μm silicon paddle oscillator and that of its supporting structure excited at 373.3 kHz. The color scale goes from 10^{-13} m (deep purple) to 10^{-10} m (yellow). Note the comparably large motions of the left-hand support structure, an unintended consequence of undercutting in the chemical etching fabrication process. The background illustrates a multielement array of paddle micro-oscillators with the inter-oscillator coupling produced by the narrow silicon beams.

where one can readily see comparable motions of the left support, a structure intended to be rigidly attached to the substrate but which had become released by unintentional undercutting in the chemical etching fabrication process. Further, NRL has extended the spatial resolution of its laser vibrometers down to tens of nanometers using the very near field of a tapered optical fiber tip.[3] The ability to generate such high resolution dynamic displacement maps together with the associated inversion algorithms will become an important tool in our work to understand the vibrational behavior of large arrays of interconnected micro-oscillators (background structure in Fig. 4). In these so-called "phononic crystals," our structural acoustic techniques will be able to reveal the *mechanical* condition and behavior of these structures, particularly that of the critically important interoscillator coupling members.

Assessing Wall Paintings and Underlying Structure at the U.S. Capitol Building

The structural acoustic fault detection methodologies developed here have applications beyond military structures. For example, the authors were invited to demonstrate and evaluate their new fault detection and localization techniques for assessing the integrity of art-bearing walls and ceilings in various rooms in the U.S. Capitol. The United States Capitol building (both House and Senate) has large expanses of important fine art and decorative paintings[4] executed directly on the original lime plaster. In support of a comprehensive infrastructure modernization program in the building, the integrity of the supporting structures is being evaluated so that degradations underlying the artwork can first be located and repaired.

The frescoes were painted in the nineteenth century by the Italian artist Constantino Brumidi[4] on a roughly 2-cm-thick structure consisting of three layers of plaster of varying composition supported by a thick masonry foundation. A successful nondestructive evaluation technique must be able to detect defects throughout the structure, including loss of cohesion within a plaster layer and delaminations between the layers or at the attachment of the mortar to the supporting wall structure.

Figure 5(a) shows the typical setup we used to carry out preliminary diagnostic studies, in this particular case for the Brumidi Corridor of the Senate Wing. Panels on the wall or ceiling were excited over a band of frequencies by the use of either a broadband shaker applied directly at a point on the structure or an acoustic speaker that exposed the walls and ceiling to acoustic energy. A scanning laser Doppler vibrometer was used to map the small-scale vibratory motion of the wall or ceiling over the area of interest using a serpentine grid pattern with a spacing of several centimeters. In addition to the Brumidi Corridor, measurements were also carried out in the Senate Reception Room, The President's Room (Fig. 5(b)), The House Appropriations Committee Room, The Parliamentarian's Office, and the Office of The Speaker of The House.

In general, our techniques were very successful at detecting and locating faults when they existed in the structure underlying the art. We were able to identify a variety of problems including areas of unconsolidated plaster, various size regions having delaminations between plaster layers, and places where there is complete detachment of the plaster from its typically brick foundation. Overall, our SLDV-based structural acoustic approach compared favorably to other techniques used at the Capitol including those employing radar and thermal imaging.

Figure 6 shows a result we obtained on a panel in the Brumidi Corridor. Figure 6(a) shows a *quantitative* color map representing our measured displacement data after processing with the |VV*| algorithm, which sums the absolute magnitude of the measured normal velocity at each spatial point and over each frequency bin. This clearly indicates six or so localized faults. They are attributed to simple, small areas of

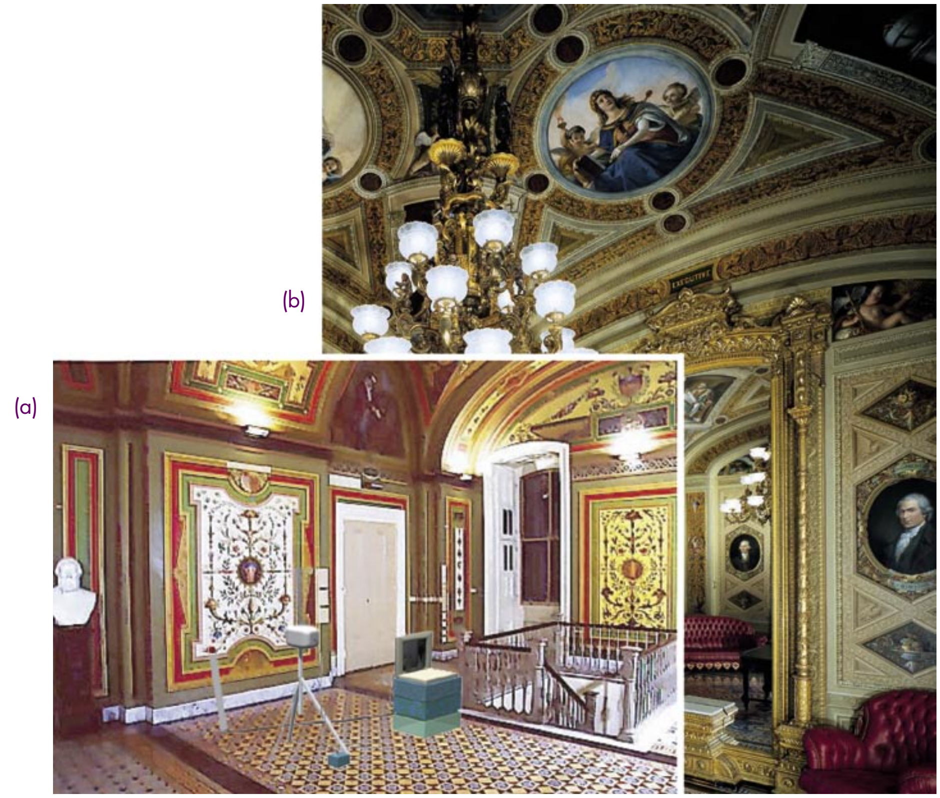

FIGURE 5
(a) Experimental arrangement for plaster wall assessments at the U.S. Capitol building showing the SLDV monitoring system, a shaker used to excite the art-laden walls, and a laptop computer data acquisition system in the Brumidi Corridor. (b) The President's Room where extensive measurements were made on the walls and ceiling.

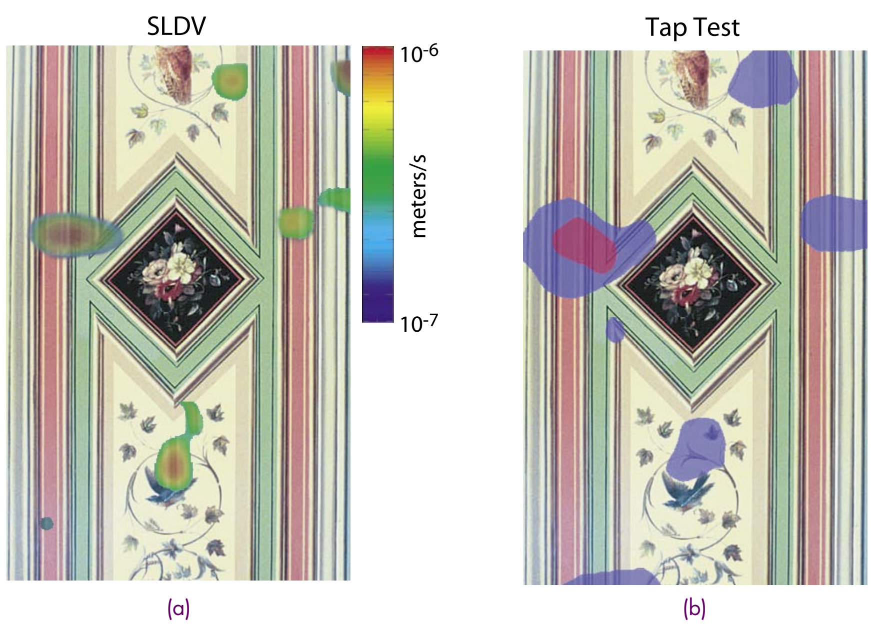

FIGURE 6
A comparison of the faults found by (a) our structural acoustic technique and by (b) a tap test in a fresco panel in the Brumidi Corridor of The U.S. Senate. Our technique is the result of the VV* algorithm, with the color scale showing velocity in m/s for a one newton force applied to the wall. The tap test is a labor-intensive, time-consuming process wherein a skilled practitioner taps sequentially with a small hammerlike tool on a large number of points on the surface while listening with his unaided ear to the audible response of the wall, from which he locates underlying faults.

delamination between the innermost plaster layer and its attachment to the brick supporting structure. In this particular case, the results can be compared to the available findings from what is called a "tap" test. In this age-old technique, a skilled conservator literally taps sequentially with a small hammerlike tool on a large number of points on the surface while carefully listening with his unaided ear to the audible response of the wall from which a *qualitative* fault map is generated. Although an experienced, skilled practitioner can often identify the existence (and sometimes type) of inhomogeneity, this is an impractical method for gathering—much less recording—such information, especially over large expanses. Nonetheless, Fig. 6 shows satisfying agreement between our laser-automated, quantitative, rapid method and the time-consuming, human-discerned result.

ON-PLATFORM SENSOR TECHNOLOGIES

Our discussion so far has focused on displacement monitoring techniques (laser Doppler vibrometry and NAH-processed microphone scans) in which the sensing is remote from the structure. Both these techniques can provide ultrahigh spatial sampling rates, an ideal feature for implementing our high spatial resolution inversion algorithms. There are cases, however, for which these remote sensing techniques are either geometrically impractical or undesirable from a data collection viewpoint. For such cases, we have been considering on-platform sensor technologies, which have potential for our fault monitoring methodology. Three attractive examples include multiplexed arrays of fiber Bragg grating (FBG) sensors, arrays of fiber-optic intensity (FOI) accelerometers, and wireless arrays (WA)[5] of electrical accelerometers.

The first two optically based techniques—FBG and FOI—have the advantage of immunity to electromagnetic interference, an important attribute in high-field environments. It is reasonable to speculate today that both techniques could be pushed to sensor counts in the hundreds, numbers that would be required for covering areas 10 to 30 times the fault size. Based on today's costs, large arrays of either type would not be inexpensive, with the less-costly being the FOI array. Wireless sensor arrays inspired by modern cell-phone systems are beginning to appear in a number of engineering applications, and the absence of signal wires or fibers would offer a great practical advantage in implementing our fault monitoring concepts. In such an array, wireless sensor/radio nodes would be distributed over the structure's surface. We estimate that as many as one thousand sensor/radio pairs could be deployed over a specific cell with many such cell sites communicating their multisensor information to a common base station. Such a sensor array with 10,000 nodes perhaps covering an area a thousand times the fault size would require less than a watt of power!

CONCLUDING REMARKS

The structural acoustic methodology discussed here offers a reliable, practical approach to mechanical health monitoring in a variety of structures important to the Navy, the DoD, and the Nation in general. It combines the suffusive nature of broadband structural vibration with the power of carefully designed inversion algorithms in order to detect and *locate* various faults within platelike structures. The methodology has general application, from large-scale structures, such as ships and aircraft, down to micro- and nanostructures. This approach is relatively new, and as the sophistication of the inversion algorithms grows, the fault detection performance and its identification ability will continue to advance. So far, we have addressed a number of applications and for the most part have implemented the techniques using a manually placed SLDV. As the future unfolds, we expect to also integrate structure-mounted sensors using emerging high-count sensor array technologies.

ACKNOWLEDGMENTS

The authors acknowledge the many technical contributions to these efforts of a number of colleagues, especially Drs. Brian Houston, Phil Abraham, Jim Tressler, Saikat Dey, Barbara Marchetti, Enrico Esposito, Andrew Kurdila, and Mr. George Adams. We also thank Leslie Chaplin for her efforts in preparing the artwork.

[Sponsored by ONR and The Architect of The Capitol]

References

[1] J.A. Bucaro, A.J. Romano, P. Abraham, and S. Dey, "Detection and Localization of Inclusions in Plates Using Inversion of Point Actuated Surface Displacements," *J. Acoust. Soc. Am.* **115**, 201-206 (2004).

[2] E.G. Williams, *Fourier Acoustics: Sound Radiation and Nearfield Acoustical Holography* (Academic Press, San Diego, CA, 1999).

[3] B.H. Houston, D.M. Photiadis, and J.F. Vignola, "Nanoscale Vibrometer Measurement Apparatus and Method," U.S. Patent #6,650,420, October 2003.

[4] B.A. Wolanin, "*Constantino Brumidi: Artist of the Capitol*," U.S. Government Printing Office, Washington, D.C. (1998).

[5] B.H. Houston and G.L. Main, "Wireless System for Hull-Based Sensing," U.S. Patent Application, Navy case # 80,207, October 7, 2002.

★

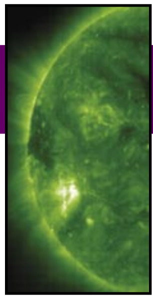

The Extreme Solar Storms of October to November 2003

S.P. Plunkett
Space Science Division

AN OVERVIEW OF SOLAR ACTIVITY AND SPACE WEATHER

In recent decades, humans have come to rely on space technology for an ever-increasing variety of purposes, including human exploration of the solar system, scientific research, national defense, and commercial activities. The field of space weather seeks to understand and predict variability in the space environment.[1] The Sun is the source of all space weather, and the origins of major space weather storms can be traced to explosive releases of magnetic energy from the solar atmosphere in the form of solar flares and coronal mass ejections (CMEs). A solar flare occurs when a sudden release of energy in an active region of the solar atmosphere leads to rapid heating of a localized region of the atmosphere, and rapid acceleration of charged particles to relativistic energies. A CME involves the expulsion of large amounts of ionized plasma and magnetic field from the Sun into interplanetary space (Fig. 1). A typical CME involves the ejection of about 10^{13} kg of plasma, at speeds from a few hundred km/s up to a few thousand km/s, into interplanetary space. A major scientific objective of contemporary research in solar-terrestrial physics is to understand how and why these events occur on the Sun, and how to predict their occurrence and their effects on humans in space and on technological systems both in space and on the ground.

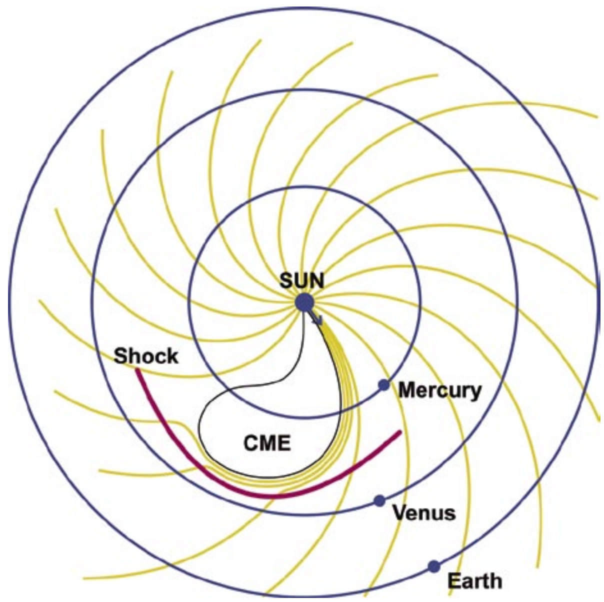

FIGURE 1
Sketch of the inner heliosphere, showing the spiral shape of the interplanetary magnetic field caused by solar rotation, and a CME driving a shock as it propagates outward from the Sun.

Impact of Space Weather

The potential impacts of space weather are numerous. Spacecraft and the instruments they carry can suffer adverse effects from direct particle bombardment or electrostatic discharge, ranging from temporary anomalies to complete failure of critical systems. Humans living and working in space can receive radiation doses well in excess of recommended limits. Star trackers that are frequently used to orient spacecraft can lose their ability to lock on to patterns in the background stars when high energy particles strike their detectors, thus causing spacecraft to lose attitude control. The impact of a CME on the Earth's environment can lead, under the right circumstances, to severe worldwide disturbances of the terrestrial magnetic field known as geomagnetic storms. The resulting particle acceleration and heating of the upper atmosphere can lead to increased drag on satellites in low Earth orbit, causing their orbits to change unpredictably. The ionosphere is usually disturbed during a geomagnetic storm, leading to difficulties with both terrestrial and satellite-borne communications systems that either transmit radio signals through the ionosphere or use it to "bounce" signals over large distances. For example, Global Positioning System (GPS) operations are affected by fluctuations in the total electron content (TEC) of the ionosphere along the path to the satellite. Spacecraft that use the Earth's magnetic field for guidance can lose orientation during a geomagnetic storm. At ground level, fluctuations in the magnetic field can induce significant currents (sometimes over 100 amps) to flow in long-distance pipelines and transmission lines for electrical power, leading to brownouts and blackouts and damage to expensive transformer equipment. The most famous example of this occurred in 1989, when a geomagnetic storm led to a failure of the electrical grid across the northeastern United States and Canada. The intense particle acceleration can also lead to beautiful auroral displays at much lower latitudes than the polar regions of the Earth where this phenomenon is usually visible.

The National Oceanic and Atmospheric Administration (NOAA) monitors and forecasts space weather for civilian purposes in the United States. NOAA has developed a set of space weather scales as a way to describe the environmental disturbances and potential impacts of geomagnetic storms, solar particle storms, and radio blackouts. The scales have numbered levels, ranging from 1 for the least severe events to 5 for the most severe events, and are analogous to the well-known scales used in terrestrial meteorology to classify hurricanes, tornadoes, and earthquakes.

OBSERVING THE SUN FROM SPACE: THE SOHO MISSION

The Solar and Heliospheric Observatory (SOHO)[2] observes the Sun continuously from an orbit around the L1 Lagrange point, located approximately 1% of the distance along an imaginary line from the Earth to the Sun (Fig. 2). SOHO is a joint mission of the European Space Agency (ESA) and the National Aeronautics and Space Administration (NASA) and has been operating almost continuously since launch in December 1995. SOHO carries 12 scientific instruments, including two in which NRL plays key roles. The first of these is the Large Angle Spectrometric Coronagraph (LASCO), a suite of telescopes that observes the outer atmosphere of the Sun (the solar corona) in visible light over a range of altitudes from 2 $R_\odot$ to 30 $R_\odot$ from the center of the solar disk (1 $R_\odot = 6.96 \times 10^5$ km, the radius of the Sun). This is accomplished by using an opaque occulting mask assembly in front of the telescope objective to block direct solar light, thus allowing the faint corona to be observed. White-light coronagraphs, such as LASCO, detect light that is Thomson-scattered off free electrons in the highly ionized corona. The principal investigator for LASCO is Dr. Russell Howard of the NRL Solar Physics branch. The second NRL instrument on SOHO is the Extreme Ultraviolet Imaging Telescope (EIT). EIT images the corona directly above the solar disk in four wavelengths in the extreme ultraviolet (EUV) region of the spectrum, corresponding to emission lines from coronal ions with peak emissivity at temperatures ranging from 5×10^4 K to 2×10^6 K.

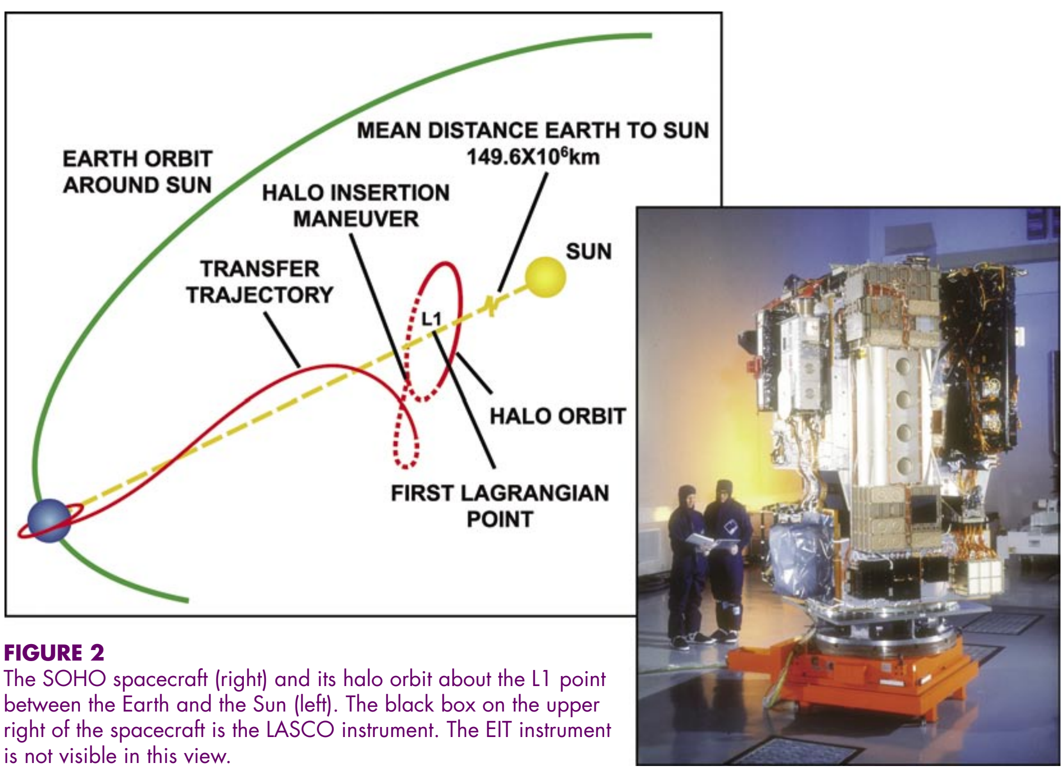

FIGURE 2
The SOHO spacecraft (right) and its halo orbit about the L1 point between the Earth and the Sun (left). The black box on the upper right of the spacecraft is the LASCO instrument. The EIT instrument is not visible in this view.

LASCO and EIT share common resources on the SOHO spacecraft, and together they provide a comprehensive view of activity in the corona.

HALLOWEEN FIREWORKS: THE EVENTS OF OCTOBER TO NOVEMBER 2003

Solar activity waxes and wanes with a periodicity of approximately eleven years (Fig. 3). At the peak of solar activity, known as solar maximum, about 5 CMEs/day occur from all regions of the solar disk. At solar minimum, the rate is only about 0.6 CMEs/day, mostly near the solar equator. The current solar cycle peaked in late 2000, and solar activity has generally been decreasing since about that time. In early October 2003, however, solar observers working with data from the SOHO mission were surprised to see evidence of unusually high levels of activity on the far side of the Sun. The Sun rotates on its axis with a period of 27 days at the equator, and on October 18, a large active region rotated into view just north of the equator, designated as NOAA active region (AR) 484. On October 22, AR 486 appeared on the east limb, about 15° south of the equator, and on October 27, AR 488 emerged close to disk center and about 10° north of the equator. From October 19 through November 4, these regions produced a combined total of 12 X-class flares, including two of the largest flares ever observed, along with numerous smaller M-class and C-class flares (Fig. 4). Solar flares are classified according to their peak X-ray flux. The brightest (and least common) flares are X-class flares, with peak X-ray flux above 10^{-4} W/m^2. M-class flares have one-tenth of the flux in X-class flares, and C-class flares have one-tenth of the flux in M-class flares. The X-flares in this period were all accompanied by large, energetic CMEs. The masses and kinetic energies of the CMEs were measured from LASCO images. The masses are in the top 5% and the kinetic energies are in the top 1% of all CMEs observed by LASCO over almost 9 years of operation.

OCTOBER 28 AND 29, 2003 SOLAR ERUPTIONS

On October 28, AR 486 was located close to the sub-Earth point on the solar disk, at 8° east of central meridian longitude, and 16° south in latitude (Fig. 5). It had developed into the largest active region of the current solar cycle, and had a highly complex appearance indicating a substantial amount of free energy in the magnetic field. At 11:10 UTC on that day, AR 486 produced one of the largest flares of this solar cycle, and the fourth largest flare ever recorded. This flare was classified as X17 (peak X-ray flux of 1.7 $\times 10^{-3}$ W/m^2). The event also produced a category R4 (severe) radio blackout on Earth. An extremely fast CME moving at an apparent speed of almost 2,500 km/s was observed in LASCO imagery. Since a coronagraph shows features projected onto a plane extending above the limb of the Sun at a right angle to the line of sight (the "plane of the sky"), this measured speed is a lower limit to the true speed of the CME. The mass of the CME was estimated to be in the range 1.4 to 2.1 $\times 10^{13}$ kg, yielding a kinetic energy in the range 4.2 to 6.4 $\times 10^{25}$ J. This is one of the most energetic CMEs observed by LASCO. The CME appeared as a bright ring surrounding the occulting disk that is used to block out the Sun's disk in the LASCO coronagraphs. Events like this are called "halo" CMEs, and they are indicative of material ejected along the line between the Sun and the Earth. A thin, sharp ring of emission was observed ahead of the CME, extending all the way around the occulting disk. This is identi-

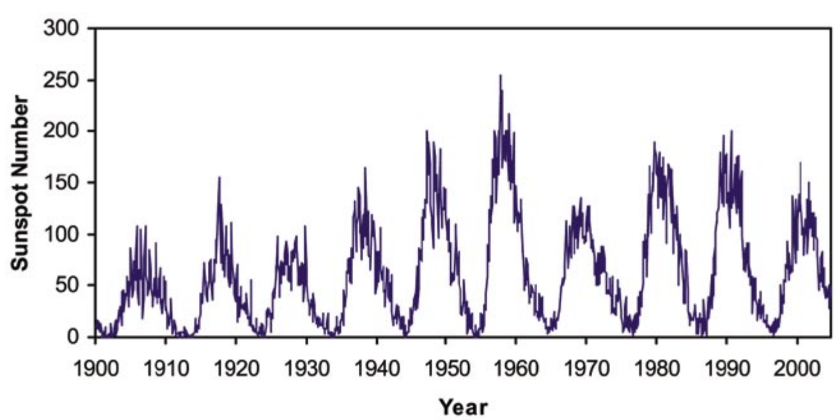

FIGURE 3
The monthly-averaged number of sunspots visible on the surface of the Sun since 1900. The number of spots and the associated level of solar activity vary with a period of about 11 years.

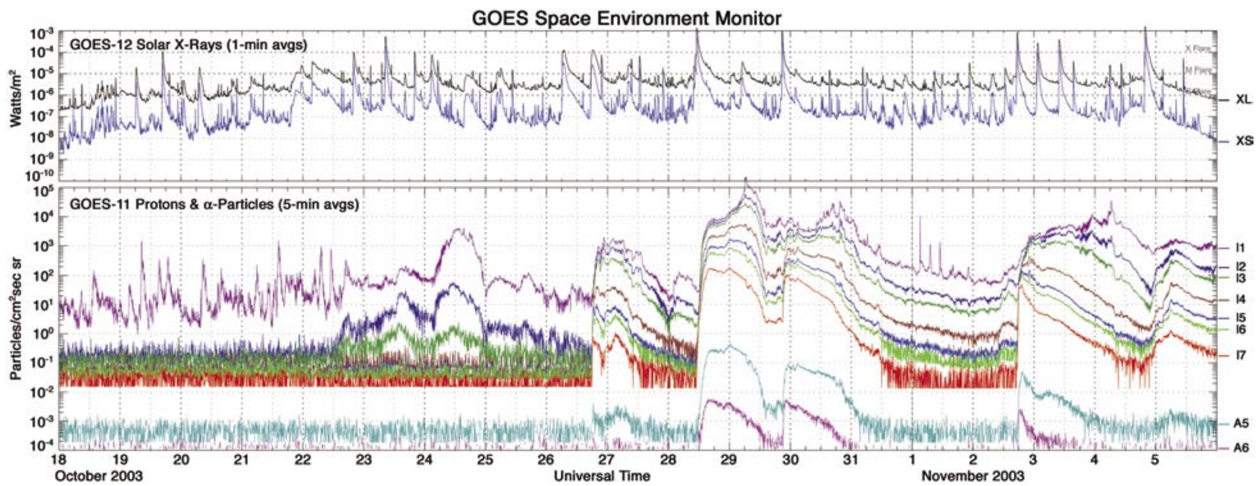

FIGURE 4
Solar X-ray and energetic particle fluxes measured by instruments on the NOAA GOES spacecraft from October 18 to November 5, 2003. The top panel shows the X-ray flux in two wavelength bands (1 to 8 Å in black, 0.5 to 3 Å in blue). Flares are identified as large, transient increases in the X-ray flux, with flare classes indicated on the right. The bottom panel shows protons in seven energy bands from >1 MeV to >100 MeV (traces labeled I1 to I7), and α-particles from 150-250 MeV (labeled A5) and 300-500 MeV (labeled A6).

(a) (b)

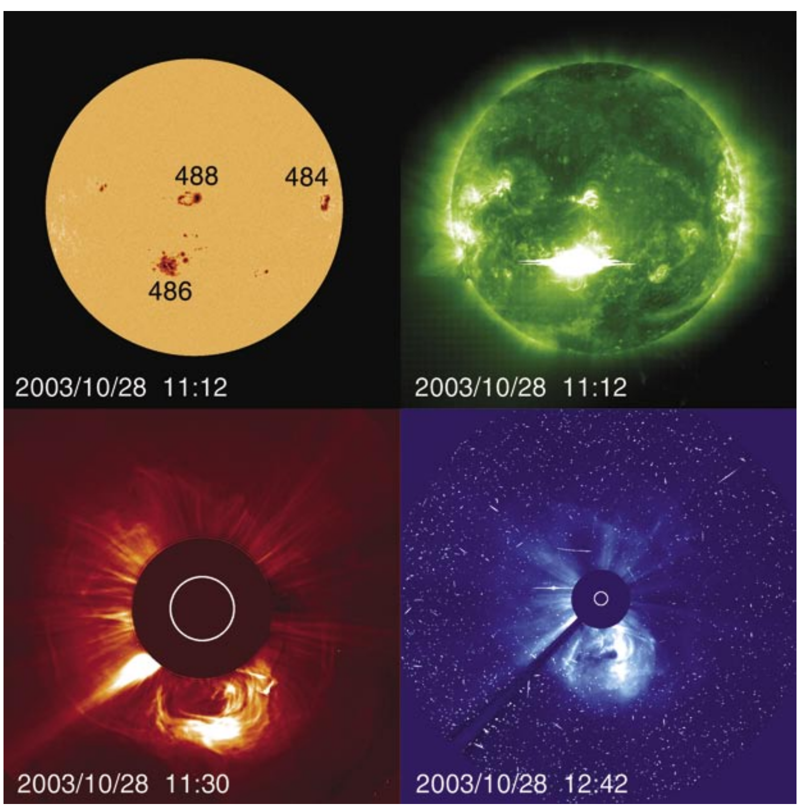

(c) (d)

FIGURE 5
X17 flare and CME on October 28, 2003. (a) Shows active regions that are visible as dark spots on the image of the Sun from the SOHO Michelson Doppler Imager (MDI). (b) The EIT image of the corona shows a bright flare in AR 486. (c) LASCO C2 and (d) C3 images show a fast halo CME. The bright specks in the C3 image are caused by energetic particles striking the camera during the exposure. The location and size of the Sun are indicated by the white circle, and the filled circle surrounding the Sun is the portion of the image that is blocked by the coronagraph occulting mask. The lower left portion of the C3 image is blocked by the mechanical structure that supports the occulter.

fied as a shock front created as the fast-moving CME plows into the ambient corona and solar wind ahead of it. When LASCO observers noted this event in the images arriving at the SOHO operations center, they immediately alerted the NOAA Space Environment Center that an event with potentially significant space weather consequences was headed towards Earth.

On the following day, October 29, AR 486 produced another major eruption. An X10 flare (peak X-ray flux 10^{-3} W/m^2) occurred at 20:49 UTC, resulting in a class R4 (severe) radio blackout at Earth. Associated with this flare was another extremely fast Earth-directed halo CME, with a measured speed just over 2,000 km/s, and a kinetic energy of 5.7×10^{25} J.

Particle Storm Reaches Earth Orbit

Following the CME and flare eruptions on October 28, an intense energetic particle event was observed in Earth orbit beginning around 11:50 UTC. Strong enhancements of the flux of both >10 MeV and >100 MeV protons were observed by the GOES spacecraft (1 eV = 1.6×10^{-19} J). The particle storm quickly reached a level of S3 (strong) on the NOAA space weather scales, and at its peak reached a level of S4 (severe), making it one of the largest of the current solar cycle, and the fourth largest particle storm since records began in 1976. An event of this magnitude is sufficient to cause passengers and crew on high-flying aircraft to receive a radiation dose approximately equivalent to one chest X-ray. As can be seen in Fig. 4, the particle event began with a very rapid increase in the flux of both protons and α-particles within a short period of time across a wide range of energies. The particle flux reached a maximum early on October 29, with the peak flux at lower energies occurring several hours later than at the highest energies. The flux then decayed slowly over the next several days, with a secondary enhancement late on October 29 following the X10 flare and CME from the same active region. The particle storm from the October 29 event reached a level of S3 (strong). The time profile of this combined particle event is typical of that expected if the particles are accelerated by a shock wave driven by a CME originating near central meridian longitude on the solar disk. The shock from the event on October 28 was detected at the L1 point by the Advanced Composition Explorer (ACE) spacecraft at 05:59 UTC on October 29, and it reached Earth at 06:13 UTC. The transit time for this CME from Sun to Earth was about 19 hours, making it one of the fastest on record. The CME on October 29 also traveled to Earth in about 19 hours, with the shock impacting the Earth's magnetosphere around 16:00 UTC on October 30. A typical CME takes about three days to travel this distance, and the fastest on record took about 15 hours in August 1972.

Solar Eruption Impact

Geomagnetic activity associated with the impact of these shocks and CMEs on the Earth's magnetosphere reached extreme levels. The arrival of the shock on October 29 triggered an abrupt perturbation of the Earth's magnetic field known as a "sudden commencement." This was followed by a category G5 (extreme) geomagnetic storm that lasted for 27 hours and was the sixth most intense storm on record (since 1932). Another G5 (extreme) geomagnetic storm resulted from the impact of the second shock and CME on October 30. Figure 6 shows the estimated planetary K index (Kp) for the three-day interval from October 29 to October 31. This index is a quasi-logarithmic measure of geomagnetic activity on a global scale, based on local measurements from a number of stations around the world, and updated every three hours. Values above Kp = 5, shown in red on the plot, indicate geomagnetic storm conditions. Values of Kp = 9 correspond to extreme storm conditions. Bright, colorful displays of the aurora, normally only visible from near-polar latitudes, were observed and photographed as far south as Florida on the nights of October 29 and 30.

NOVEMBER 4, 2003 SOLAR ERUPTION

By early November, AR 486 had rotated close to the west limb as viewed from Earth and was about to disappear from view onto the far side of the Sun. On November 4, AR 486 was located right on the limb, at 89° west of central meridian longitude, and the visible disk was devoid of any significant active regions (Fig. 7). Just as solar observers were about to breathe a sigh of relief, and activity appeared ready to return to normal levels, AR 486 produced the largest X-ray flare ever recorded, at 19:31 UTC on November 4. The flare saturated the GOES X-ray detector, and later analysis yielded a peak X-ray flux at the X28 level (peak flux of 2.8×10^{-3} W/m^2). Intense radio bursts across a broad range of frequencies were associated with the X28 flare. A category R5 (extreme) radio blackout resulted at Earth shortly after the flare. LASCO recorded an extremely fast CME, moving outward at a speed of 2,657 km/s. The mass of this CME was about 1.5×10^{13} kg, yielding a kinetic energy of 5.3×10^{25} J. Unlike the events of October

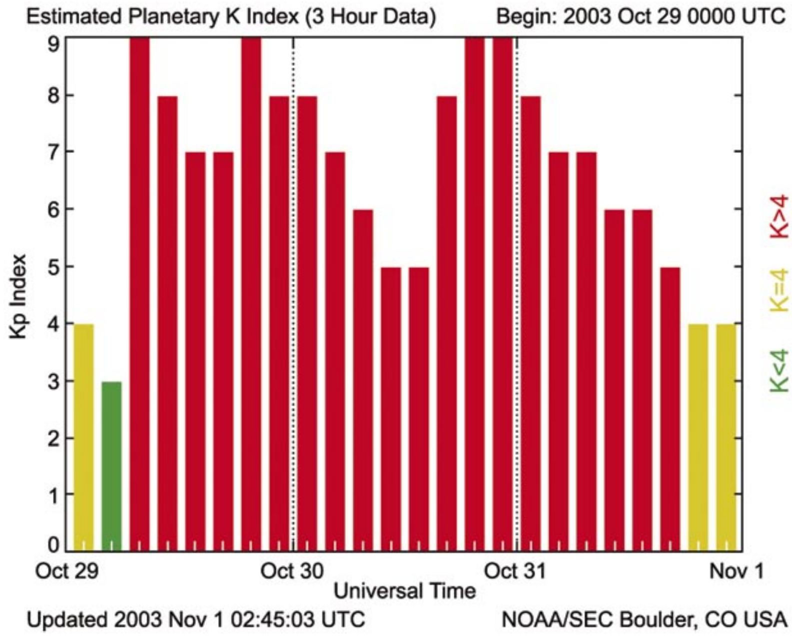

FIGURE 6
Geomagnetic Kp index from October 29 to October 31, 2003, showing severe storming in red.

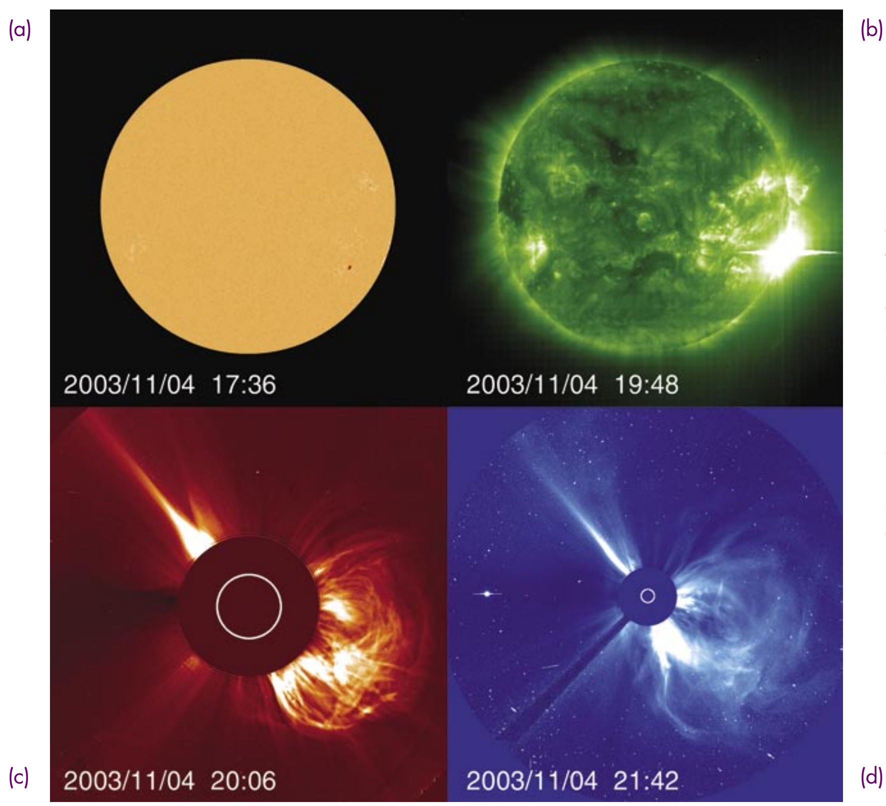

FIGURE 7
X28 flare and CME on November 4, 2003. (a) Shows that no large active regions are visible on the MDI image of the Sun. (b) Shows a flare visible on the limb in EIT. (c) LASCO C2 and (d) C3 show a large, fast CME with complex internal structure. The location and size of the Sun are indicated by the white circle, and the filled circle surrounding the Sun is the portion of the image that is blocked by the coronagraph occulting mask. The lower left portion of the C3 image (d) is blocked by the mechanical structure that supports the occulter.

28 and 29, in which the CMEs were observed almost head-on, this CME was observed edge-on, at almost 90° to the direction of propagation.

The particle flux in Earth orbit was already enhanced on November 4 due to an X8 flare and associated CME on November 2 (Fig. 4). As the particle flux was decaying, an enhancement in >10 MeV protons due to the X28 flare and associated CME was observed by GOES beginning at 22:25 UTC on November 4 (a much smaller enhancement was observed in >100 MeV protons). Although the flare occurred on the west limb, and the CME was not directed towards Earth, the particles were able to propagate to Earth because of the wide extent of the CME-driven shock and because the magnetic field lines along which the particles are constrained to travel form a spiral pattern connecting Earth to a solar longitude approximately 60° west of central meridian (Fig. 1). The particle flux rose gradually, with the >10 MeV proton flux peaking at 06:00 UTC on November 5, and then decayed slowly throughout the rest of that day. This time profile is typical of a particle event due to a CME-driven shock where the nose of the shock propagates well to the west of the observer, as was the case here. Because only the flank of the CME-driven shock propagated towards Earth, the shock was detected at L1 by the ACE spacecraft much later, around 19:00 UTC on November 6. For the same reason, despite the record size of the flare, and the large, fast CME, the particle storm at Earth only reached S2 (moderate) levels, and geomagnetic activity reached only a G1 (minor) storm level.

IMPACTS ON TECHNOLOGICAL SYSTEMS

Near-Earth and deep space satellites and space operations, communications and navigation systems, the airline industry, and electric utilities were adversely impacted by the high levels of solar and geomagnetic activity during this period. Other systems were able to modify their operations to mitigate potential effects, and still others were able to continue normal operations based on real-time data and space weather forecasts. The detailed solar imagery available from the LASCO and EIT instruments was invaluable to NOAA space weather forecasters in making the predictions that enabled operators to take appropriate measures to protect their systems.

Numerous NASA missions were impacted by the October-November activity. The crew on the International Space Station (ISS) was directed to relocate to a shielded location on the station on at least five separate occasions to avoid radiation hazards. The robotic arm on the ISS was powered down to protect it from possible radiation damage. The Martian Radiation Environment Experiment (MARIE) on the Mars Odyssey mission had a high temperature alarm on October 28 and was powered off. This instrument was not recovered. Contact with the Japanese Advanced Earth Observing Satellite II (ADEOS-2) was lost during a severe geomagnetic storm on October 24, caused by a CME associated with an X5 flare early on October 23. The ADEOS-2 payload included the $150 million NASA SeaWinds instrument, a microwave radar experiment designed to map ocean wind speeds and directions. Several other NASA spacecraft had to use backup systems for attitude control during the particle storms, when star trackers were temporarily rendered unusable by the large number of particle hits. Other spacecraft switched into safe modes and turned off instruments during the periods of increased activity.

Airlines and ground controllers experienced communications difficulties almost daily in late October and early November, with the most severe problems occurring on polar routes between North America and Asia. At least one major airline rerouted polar flights to a route with better satellite communications links. Another major concern for airlines during this period was the potential impact of increased radiation levels on passengers and crew. On October 28, the Federal Aviation Administration (FAA) issued their first ever advisory warning that flights traveling at latitudes greater than 35° were subject to excessive radiation doses. Both major U.S. airlines that operate over the pole rerouted flights to nonpolar routes in response to this advisory notice, thus significantly increasing operating costs and time for these flights. Flights between the United States and Europe flew at lower than normal altitudes during this period. The FAA's Wide Area Augmentation System (WAAS), which uses GPS for aircraft navigation, was seriously impacted during the severe storms on October 29 and 30, and resulted in commercial aircraft being unable to use the WAAS for precision approaches.

Electric utilities in North America experienced minimal disruption, partly because of preventive measures taken to counter the effects of induced currents on the power grid based on space weather forecasts. More significant impacts occurred in Europe, and a power system failure occurred in Malmo, Sweden, on October 30, resulting in a city-wide blackout.

LESSONS LEARNED

The observations presented here would not have been possible in any previous solar cycle. We now have available a fleet of spacecraft with advanced instrumentation that allows us to observe an eruption on the surface of the Sun, and track that eruption all the way from the Sun to the Earth. We also have the tools to forecast with reasonable accuracy the potential space weather impacts of an eruptive event. We can identify solar active regions that are likely to produce large flares and CMEs, and we know that these events are powered by the conversion of free energy stored in magnetic fields on the Sun. However, we still do not know the details of the underlying mechanism that triggers these eruptive events, and we lack the ability to reliably predict when they will occur, so that accurately forecasting space weather more than a few days in advance is not possible. Future progress on this issue will require close synergy between observations and theoretical modeling using advanced computing techniques.

The NASA Solar-Terrestrial Relations Observatory (STEREO) mission will be launched in 2006. This mission will consist of two nearly identical spacecraft along the Earth's orbit. One spacecraft will lead, the other will lag behind the Earth, and both will drift apart at a rate of about 22° per year. NRL is leading a consortium that will provide identical suites of imaging instruments for both STEREO spacecraft, as well as theoretical modeling and data analysis efforts. The Sun-Earth Connections Coronal and Heliospheric Investigation (SECCHI) will obtain unprecedented stereoscopic views of the Sun and the heliosphere to a distance beyond the Earth's orbit. This will allow three-dimensional imaging of CMEs from their origin at the Sun to their impact on Earth, and will substantially increase our understanding of the structure and dynamics of CMEs and our ability to predict space weather. STEREO will also allow us to view Earth-directed CMEs edge-on for the first time, thus revealing the detailed internal structure that is hidden in a head-on view. Some of the keys to understanding the potential space weather impacts of a CME, such as the topology of the magnetic field, lie in knowing these details about the internal structure. The edge-on view will also allow us to more accurately measure key parameters, such as the speed and mass of CMEs, that are difficult to determine from an end-on view.

In summary, the dramatic events of October and November 2003 demonstrate that our ability to observe and predict solar activity and its impact on technological systems in space and on the ground has improved dramatically in recent years. We expect significantly improved capabilities to be in place for the next solar cycle, when our society will be even more susceptible to the negative impacts of space weather. NRL is leading the way in research efforts in this field.

ACKNOWLEDGMENTS

The author acknowledges assistance from staff in the NRL Solar Physics branch in preparing this article, particularly Angelos Vourlidas, Dennis Socker, and Russell Howard. Assistance and advice from Daniel Wilkinson and Bill Murtagh at the NOAA SEC are also appreciated. The graphics were prepared by Mary Helen Gregory at Praxis, Inc. in Alexandria, VA. This work was carried out under NASA DPR S-13813-G.

References

[1] P. Song, H.J. Singer, and G.L. Siscoe, eds., "Space Weather," *Geophysical Monograph* **125**, American Geophysical Union, Washington, DC, 2001.

[2] B. Fleck, V. Domingo, and A.I. Poland, ed., "The SOHO Mission," *Solar Physics* **162** (1-2), (1995).

Acoustics

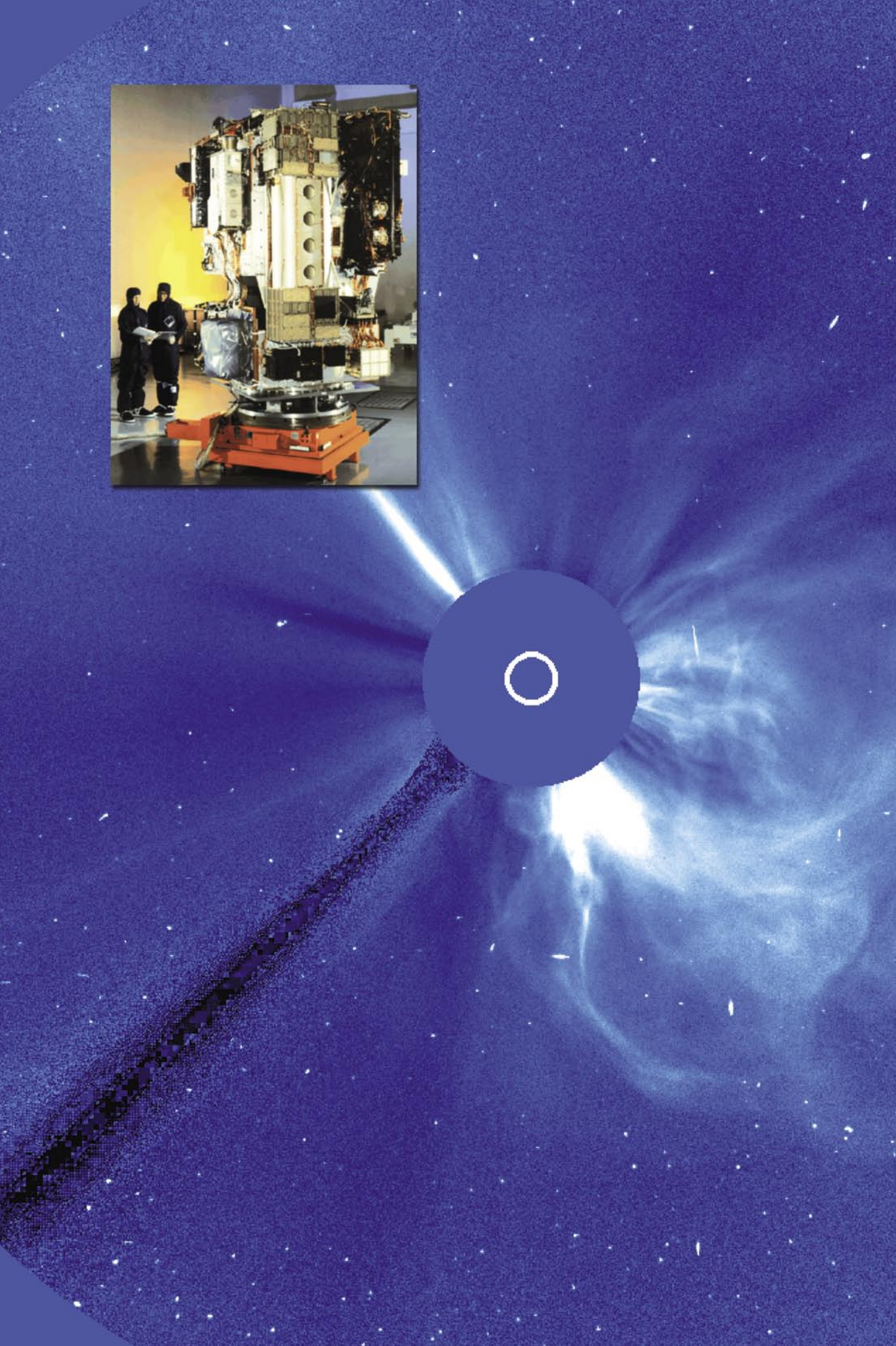

Photo caption: Image of the solar corona obtained with NRL's LASCO instrument. The feature emerging from the Sun at the right is a coronal mass ejection. These ejections can cause geomagnetic storms at the Earth. The SOHO is shown in the inset during testing.

Ambient Noise and Marine Mammal Acoustics

J. Newcomb,[1] G. Ioup,[2] G. Rayborn,[3] S. Kuczaj,[3] and N. Sidorovskaia[4]
[1]*Acoustics Division*
[2]*University of New Orleans*
[3]*University of Southern Mississippi*
[4]*University of Louisiana at Lafayette*

Introduction: The Littoral Acoustic Demonstration Center (LADC) is an Office of Naval Research funded consortium of scientists from the University of Southern Mississippi (USM), the University of New Orleans (UNO), the Naval Research Laboratory at Stennis Space Center (NRL-SSC), and the University of Louisiana at Lafayette (ULL). LADC was formed to conduct ambient noise and marine mammal acoustic measurements and analyses. Some of the marine mammal goals are to 1) investigate detection, identification, and tracking using bottom-moored hydrophones; 2) coordinate with scientists making visual observations and other acoustic measurements; and 3) evaluate, and modify if necessary, automatic detection and characterization computer algorithms when applied to marine mammal signals received on bottom-mounted hydrophones. The underlying desire is to provide products that will help to assess the effects of anthropogenic noise on marine mammal behavior and the development of mitigation procedures. Due to recent court rulings, the Navy has become concerned with the possible negative effects of sonar on marine mammals and the development of mitigation procedures. Not only do mitigation procedures have Navy applications, but they also apply to some aspects of commercial or scientific exploration of the oceans.

LADC has conducted experiments in the northern Gulf of Mexico and in the Ligurian Sea in cooperation with other organizations. Environmental Acoustic Recording System (EARS) buoys were deployed at sites with historically abundant sightings of marine mammals. EARS buoys are autonomous self-recording, single-channel, bottom-moored acoustic buoys developed by the Naval Oceanographic Office. Analysis approaches have included click production analysis, propagation modeling of sperm whale clicks, and spectral and wavelet transforms of sperm whale clicks.

Spectral Analysis Results: Often, data filtering and spectral analysis are the first steps toward the more complex analyses mentioned above. These two processes can allow the researcher to ascertain details of the data not readily apparent. Transient signals, such as marine mammal phonations, are often buried in the background ambient noise. The following illustrations are examples of some of the results of the spectral analysis from one of the Gulf of Mexico experiments conducted by LADC.

Figure 1 illustrates data from a time period that had a considerable diversity of noise. The upper plot illustrates 120 s of acoustic data from the EARS buoy. The lower left plot is a calibrated spectrogram of these data. Intensity in the spectrogram is represented by color, blue being the lowest and red being the highest intensities. It is well known that most distant shipping noise is below 300 Hz.[1] Thus, the higher intensity red in the lower frequencies of this spectrogram is considered to be due to distant shipping. There are some high-level peaks at the very lowest frequencies of this plot. The lower right plot is a spectrogram of the same data zoomed onto the lower frequencies. The red peaks at the lower frequencies can now be seen to occur every 10 s and are caused by a seismic survey airgun approximately 107 km distant. The lower right plot illustrates that the majority of the noise from the airgun at this distance is below 300 Hz.

Figure 2 illustrates a 15-s segment of data from the same exercise taken approximately 3 h later, after the seismic survey vessel has left the area. The upper left plot represents the acoustic time series data from the hydrophone. The lower left plot is the corresponding spectrogram. There are spikes in the upper plot that are not clearly distinguishable in the spectrogram. Again, note the higher intensities at the lower frequencies in the spectrogram. The upper right plot represents the same 15-s segment of data after the data were filtered to eliminate most of the distant shipping noise (i.e., frequencies below 300 Hz). The lower right plot is the corresponding spectrogram. The spikes, noted earlier in the unfiltered data, can easily be seen to be an entire series of spikes in the filtered acoustic data (upper right plot). These spikes are the clicks produced by a sperm whale and are referred to as a "click train." Again, the spikes are not easily distinguishable in the spectrogram (lower right plot).

Figure 3 illustrates a 5-s segment of data near the middle of the previous segment. This data segment has been filtered to eliminate the frequencies below 300 Hz. At this time scale, the click train is easily distinguishable from the filtered acoustic data (upper plot). In addition, the click train is readily apparent in the spectrogram (lower plot). As can be seen from the spectrogram, the clicks are very broadband and contain data from near 300 Hz up to above the upper frequency limit of the plot (about 5.8 kHz).

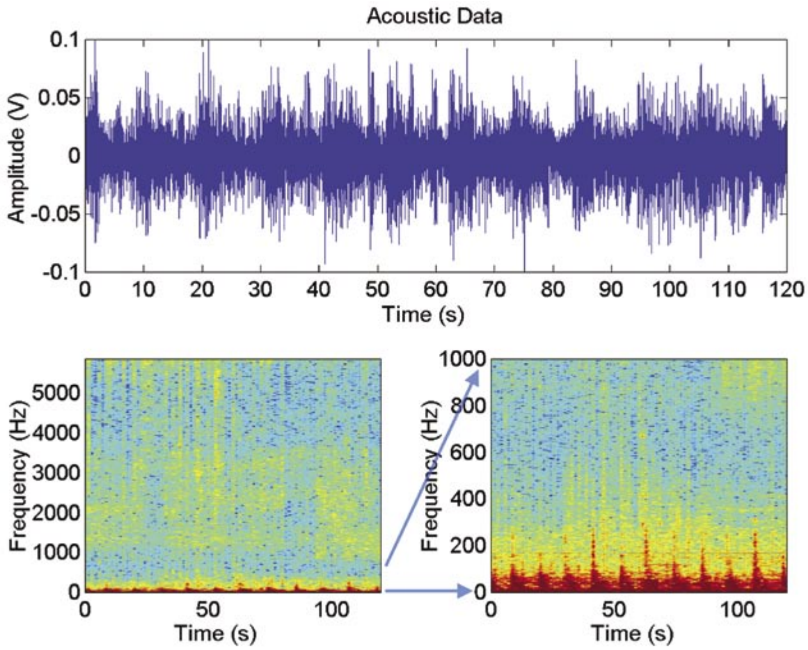

FIGURE 1
Example of 120 s of ambient noise (top plot) and corresponding spectrograms (lower plots). In the spectrograms, red indicates higher intensities and blue indicates lower intensities. The lower left plot displays the full bandwidth of the data and implies many different noise sources. The lower right plot displays only the lower 1000 Hz of the data, clearly showing shipping noise and seismic prospecting at the lowest frequencies.

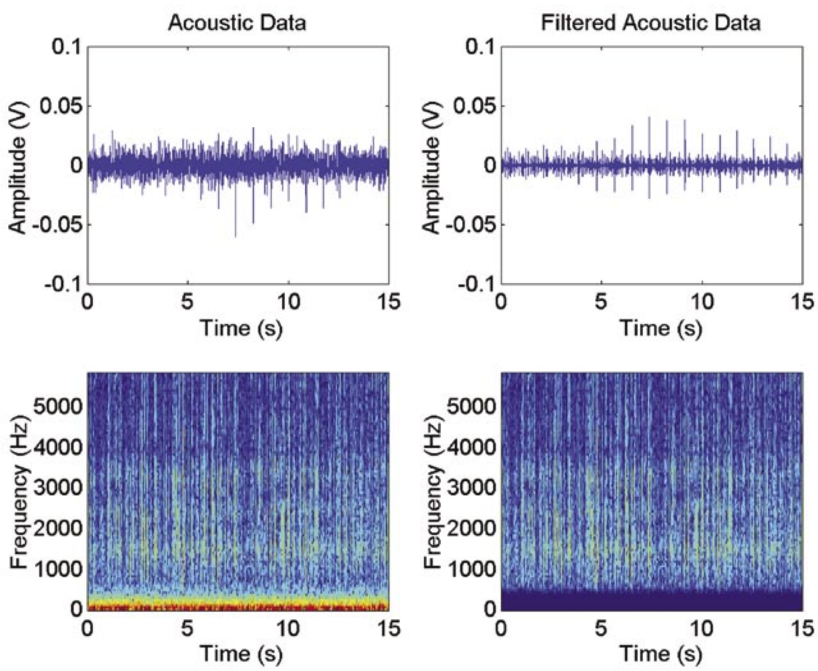

FIGURE 2
Examples of 15 s of ambient noise including a sperm whale click train (upper plots) with the corresponding spectrograms (lower plots). In the spectrograms, red indicates higher intensities and blue indicates lower intensities. The left plots are unfiltered data, and the right plots have been high pass filtered to eliminate contributions below 300 Hz. The click train is very evident in the filtered data.

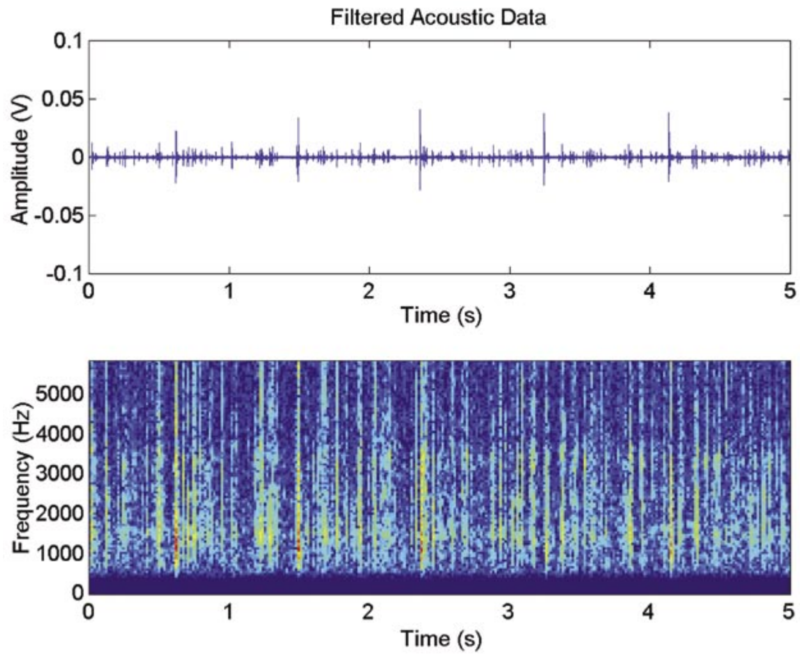

FIGURE 3
Exploded view of the middle 5 s of ambient noise shown in Fig. 2 (upper plot) with the corresponding spectrogram (lower plot). In the spectrogram, red indicates higher intensities and blue indicates lower intensities. The click train can now be seen clearly as broadband high intensity vertical lines in the spectrogram.

Summary: LADC has participated in four major marine mammal field experiments in cooperation with several other government and research scientists. LADC scientist and students are analyzing the data. To date, one Ph.D. and four M.S. degrees have been awarded to students working with these data. There are at least seven more students working toward their degrees. Preliminary results have shown the possibility of identifying individual sperm whale groupings from the spectral content of the click trains. This leads to the intriguing concept of eventually identifying individual mammals from their acoustic signature.

[Sponsored by ONR]

Reference

[1] G.M. Wenz, "Acoustic Ambient Noise in the Ocean: Spectra and Sources," *J. Acoust. Soc. Amer.* 34, 1936-1956 (1962). ★

Toward the Creation of the World's Smallest Radio

B.H. Houston
Acoustics Division
M. Zalalutdinov
Cornell University

Introduction: Micro- and nanoelectromechanical systems (MEMS and NEMS) promise revolutionary scientific and technological solutions to long-standing Navy problems that include a range of distributed sensor and signal processor applications. Breakthroughs in microminiaturization of remote sensors and radio transceivers as well as dramatic reductions in their power consumption are enabled by the development of a new class of high frequency micron- and nanometer-size components where signals are no longer associated with electric current or voltage but by time-varying mechanical parameters, such as displacement, curvature, and stress. High speed performance of such devices is governed by scaling laws that shorten the time of the mechanical response and bring resonance frequencies for micron-size mechanical structures into the MHz and GHz range.[1] By converting a radio-frequency (RF) electrical signal into the physical motion of micromechanical structures and exploiting their mechanical resonant properties, one can replace traditional RF components (e.g., quartz crystal, surface acoustic wave (SAW) filters, inductors) with their MEMS/NEMS counterparts. One of the goals of our research is to demonstrate a "radio-on-chip," an RF transceiver with dimensions less than 100 micrometers, where novel RF signal processing is implemented in these small mechanical structures and fully integrated with transistor circuitry.

Thermoelastic Activation: A critical element of this technology is thermoelastic activation of microresonators where we take advantage of ultrashort thermal response times at these small scales.[2] Figure 4(a) shows an optical image of a "dome resonator" fabricated in polysilicon with a resistive microheater. When an AC electric current is applied to the microheater, the resulting modulated local thermal expansion produces

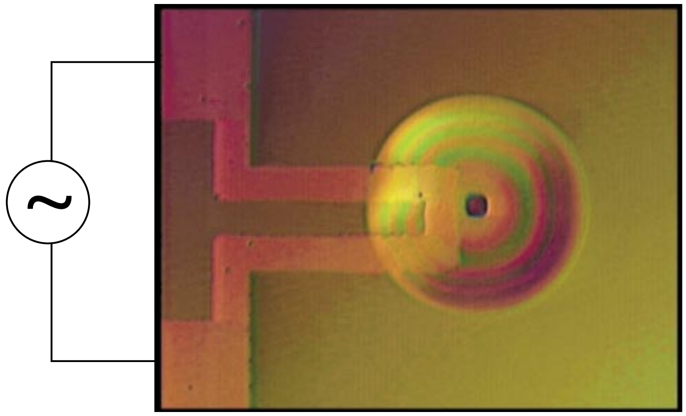

(a)

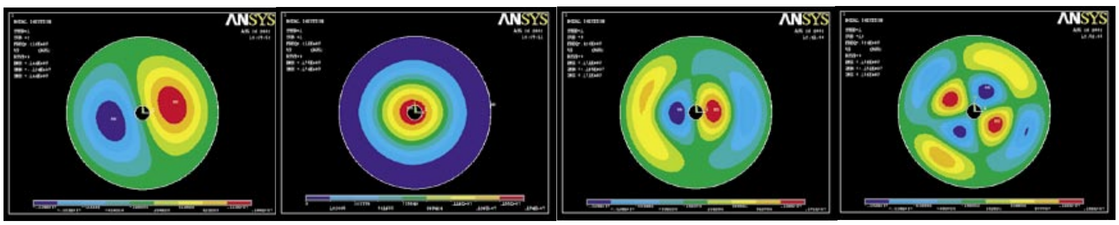

(b)

FIGURE 4
Dome-type micromechanical resonator (film thickness 200 nm, radius 15 μm, apex elevation 0.9 μm) with (a) resistive thermal actuator and (b) normal modes corresponding to different resonance frequencies.

large amplitude mechanical standing waves (Fig. 4(b)), when the frequency of the input current coincides with a mechanical resonance of the dome. A variety of methods—optical, capacitive, piezoresistive—can be used to detect this motion, converting it back to an electric signal for further processing.

MEMS-based Transmitter and Receiver: By amplifying the output signal of the mechanical resonator and applying it again to the thermal drive, we close a positive feedback loop and set conditions for limit cycle oscillations. The high spectral purity of these vibrations allows us to use the device as a local oscillator (LO) for an RF transmitter and thus substitute an off-chip quartz resonator. In our prototype of a MEMS-based FM transmitter, the self-sustained oscillations of the dome resonator provide the carrier frequency (up to 400 MHz), while the FM modulation is implemented by a fine tuning of the dome's resonant frequency in response to a base-band signal applied to an additional microheater (Fig. 5(a)). Recently, by utilizing an additional oscillator and phase-locking phenomena, we have demonstrated phase modulation as well.

For an RF receiver, the thermal incarnation of the signal enables a broadband mixer implementation. When a linear superposition of several signals at different frequencies is applied to the microheater, the resulting temperature oscillations can occur at sum and difference frequencies because the heating is proportional to V^2/R. These temperature oscillations can drive the mechanical resonator when a beat frequency coincides with the mechanical resonance of the dome. In that way, the microheater acts as a frequency converter, while the dome resonator acts as a narrow pass-band filter for the down converted signal. In the widely used superheterodyne RF receiver architecture, our thermomechanical mixer-filter replaces both the intermediate filter (IF, most commonly implemented as off-chip SAW) and a mixer (usually a Gilbert cell with significant power consumption). This combination of mixer and filter—a cornerstone of a superheterodyne receiver—largely determines the performance of the device. A simple two-tone intermodulation test of our MEMS mixer-filter produces a 3rd order input intercept point of +30 dBm for interferers spaced at a 50 kHz offset from the carrier frequency. This performance far exceeds 3G W-CDMA specifications (+10 dBm at 10 MHz offset).

Figure 5(b) shows a schematic diagram of a MEMS-based radio receiver. Here, a 30-μm-diameter dome-type resonator is shown with a 50-Ohm resistive actuator that provides mixing and filtering at f_{IF} = 14 MHz. We also utilize a side of the resonant peak of

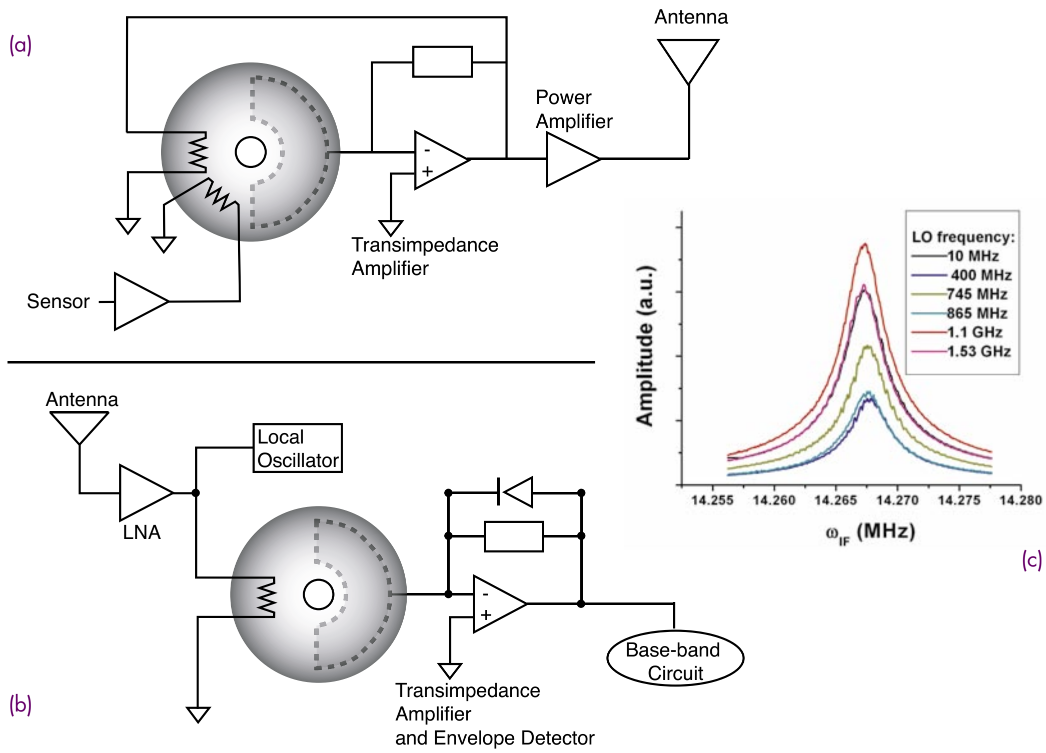

FIGURE 5
Schematic diagrams for (a) RF transmitter and (b) superheterodyne receiver; (c) shows resonant response of the dome to a downconverted RF signal.

the MEMS filter to demodulate FM signal (slope-type FM-AM conversion) in order to produce an audible signal from local FM radio stations. Since the thermal actuator is essentially an ohmic resistor, it can be designed to match exactly the output impedance of the front-end RF amplifier over a very wide frequency range. In our demonstration, we are able to select sources of RF signals in a frequency range from 10 MHz to 1.5 GHz by tuning the LO (Fig. 5(c)).

Conclusions: The significance of this demonstration derives from the fact that no other frequency-selecting RF component (i.e. neither coils nor quartz nor SAW devices) is required for our radio. Currently, we are working on a design of RF MEMS resonators that can be fabricated in a standard CMOS fabrication process. Further, our research efforts are also devoted to the expansion of the idea of MEMS-based signal processing to include coupled arrays of resonators (Fig. 6). A variety of complex RF components, from variable-width, high-order filters to broadband RF spectrum analyzers, can be built based on such arrays. It is our belief that such signal processors, when integrated with MEMS/NEMS-based sensors, will result in a powerful technology for distributed systems.

[Sponsored by ONR and DARPA]

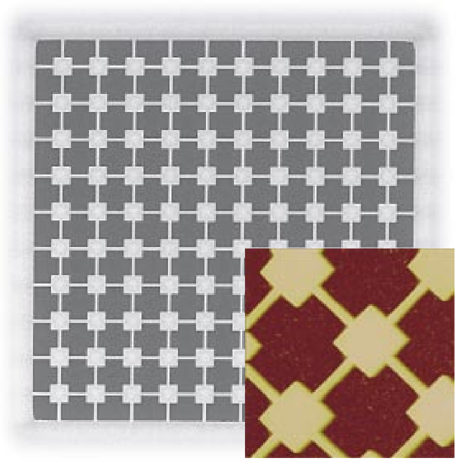

FIGURE 6
An array of coupled nanomechanical diamond resonators for RF signal processing.

References

[1] Y. Xie, S.-S. Li, Y.-W. Lin, Z. Ren, and C.T.-C. Nguyen, "UHF Micromechanical Extensional Wine-Glass Mode Ring Resonators," *Techical Digest*, 2003 IEEE International Electron Devices Meeting, Washington, DC, Dec. 8-10, 2003, pp. 953-965.

[2] M. Zalalutdinov, K. Aubin, R. Reichenbach, A. Zehnder, B. Houston, J. Parpia, and H.G. Craighead, "Shell-type Micromechanical Actuator and Resonator," *Appl. Phys. Lett.* **83**, 3815-3817 (2003).

Atmospheric Science and Technology

Photo caption: The VIKING rocket was designed by NRL to replace the V-2 rocket. Its first flight occurred in 1949.

NOGAPS-ALPHA Simulations of the 2002 Antarctic Stratospheric Major Warming

D.R. Allen,[1] S.D. Eckermann,[2] J.P. McCormack,[2] L. Coy,[2] G.L. Manney,[3] T.F. Hogan,[4] and Y.-J. Kim[4]
[1]*Remote Sensing Division*
[2]*Space Science Division*
[3]*New Mexico Highlands University/ Jet Propulsion Laboratory*
[4]*Marine Meteorology Division*

Introduction: A new high-altitude (~0-85 km) version of the Navy Operational Global Atmospheric Prediction System (NOGAPS) global spectral forecast model has been developed as a joint effort of NRL's Space Science, Remote Sensing, and Marine Meteorology Divisions. This NOGAPS-Advanced Level Physics and High Altitude (NOGAPS-ALPHA) model is formulated with a higher top level than the operational NOGAPS model and with a new hybrid vertical coordinate that transitions from terrain-following in the lower atmosphere to constant pressure levels in the stratosphere (Fig. 1). New physics packages were added to adequately simulate the higher altitudes. These include a new radiation scheme, new gravity wave drag parameterizations, and new prognostic ozone capability. In addition, a new initialization procedure was developed for the upper atmosphere, and capability for transporting multiple trace species was added. To assess the impact of these changes on model forecast skill, we examine NOGAPS-ALPHA hindcasts of the Southern Hemisphere (SH) during September to October 2002; this was an unusual period when the first ever Antarctic *major stratospheric sudden warming* (defined below) was observed.

NOGAPS Analyses and Forecast: A conspicuous feature of the 2002 SH meteorology was the splitting of the so-called polar vortex circulation in the middle stratosphere.[1] The top row of Fig. 2 shows SH polar orthographic maps of the 10 hPa (~30 km) NOGAPS operational geopotential height analyses for September 20-25, 2002 (at 12 coordinated universal time (UTC)). These analyses were made using the then-operational MultiVariate Optimum Interpolation (MVOI) system and represent our best synthesis of available observations of the atmospheric state at these times. The nearly pole-centered vortex on September 20 rapidly elongates and then splits into two pieces by September 25. This splitting, due to strong planetary-scale wave forcing emanating from the upper troposphere/lower stratosphere region, produces a major stratospheric sudden warming (hereinafter "major warming") defined by rapid warming of the polar region and reversal (from westerly to easterly) of the 10 hPa zonal mean zonal wind poleward of 60° latitude. Although major warmings are known to occur in the Northern Hemisphere, this was the first observed major warming in the SH. Five-day forecasts of this event, issued at the time by the operational NOGAPS running at Fleet Numerical (designated NOGAPS-ops; Fig. 2), show elongation of the vortex and development of two distinct lobes. Yet the vortex does not completely split by September 25.

NOGAPS-ALPHA Hindcast: We recently performed hindcasts of the major warming with NOGAPS-ALPHA. The NOGAPS-ALPHA hindcast initialized with MVOI analyses (designated ALPHA-ops) shows some improvement, with the two vortex cells slightly nearer separation after 5 days. NOGAPS-ALPHA hindcasts were also made by initializing with meteorological fields produced from a reanalysis of this period using the currently operational NRL Atmospheric Variational Data Assimilation System (NAVDAS). This hindcast (designated ALPHA-rean) shows the vortex on September 25 just separating into two parts, in better agreement with the analysis.

To quantify the differences, we compare 5-day forecast planetary wave activity on September 25, 2002 with a range of estimates compiled from seven different global analyses issued by various meteorological centers (Fig. 3, top row). The zonal wavenumber 1, 2, and 3 (indicating 1, 2, and 3 sinusoids around a latitude circle) geopotential height amplitudes at 10 hPa reveal that NOGAPS-ops forecasts overestimated wave 1 and underestimated wave 2. The ALPHA-ops hindcast shows reduced wave 1 and increased wave 2 that are both in better agreement with the analyses, while the ALPHA-rean hindcast shows much improved wave 1 and wave 2 amplitudes compared to the NOGAPS-ops and ALPHA-ops runs.

Forecast Skill Assessments: To assess more objectively the overall impact on forecasting skill, the lower row of plots in Fig. 3 shows geopotential height anomaly correlation (AC), a standard "skill score" metric, as a function of forecast day at 100, 500, and 700 hPa for a three-week series of forecasts during September to October 2002. Higher AC means better skill: a perfect forecast yields AC=1. At all levels, ALPHA-ops forecasts show improved skill over NOGAPS-ops, particularly for longer forecast times, highlighting the positive impact at all levels of the new NOGAPS-ALPHA model. ALPHA-rean shows

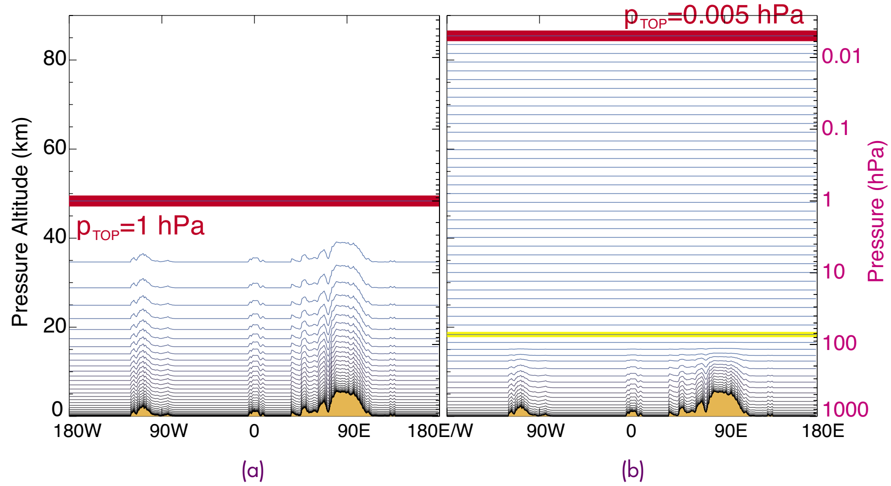

FIGURE 1
NOGAPS vertical model levels around 34.5°N latitude for (a) operational 30-level (L30) model with top at 1 hPa and (b) new NOGAPS-ALPHA 54-level (L54) model with top at 0.005 hPa. Yellow curve shows the first purely isobaric stratospheric level at ~72.6 hPa.

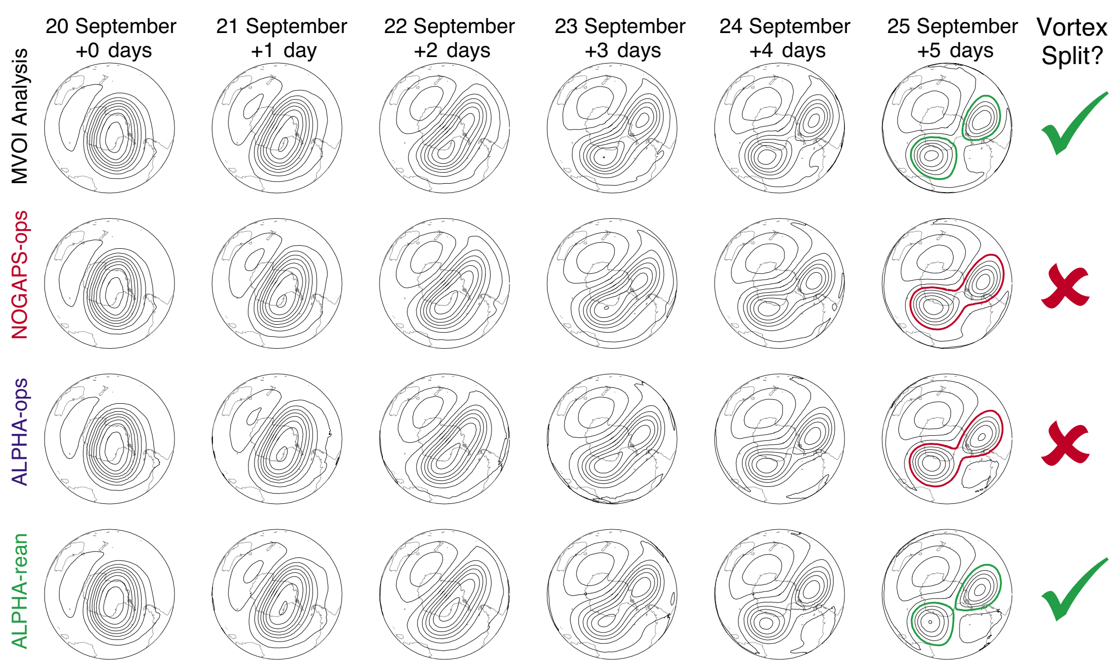

FIGURE 2
Geopotential height at 10 hPa (~32 km) over the SH for September 20-25, 2002. The top row is the NOGAPS MVOI operational analyses, while the next three rows include NOGAPS operational forecast (NOGAPS-ops), NOGAPS-ALPHA hindcast initialized with MVOI analyses (ALPHA-ops), and NOGAPS-ALPHA forecast initialized with the NAVDAS reanalyses (ALPHA-rean). All forecasts were initialized at 12 UTC on September 20, 2002. Contour interval is 400 m, starting from 28,000 m.

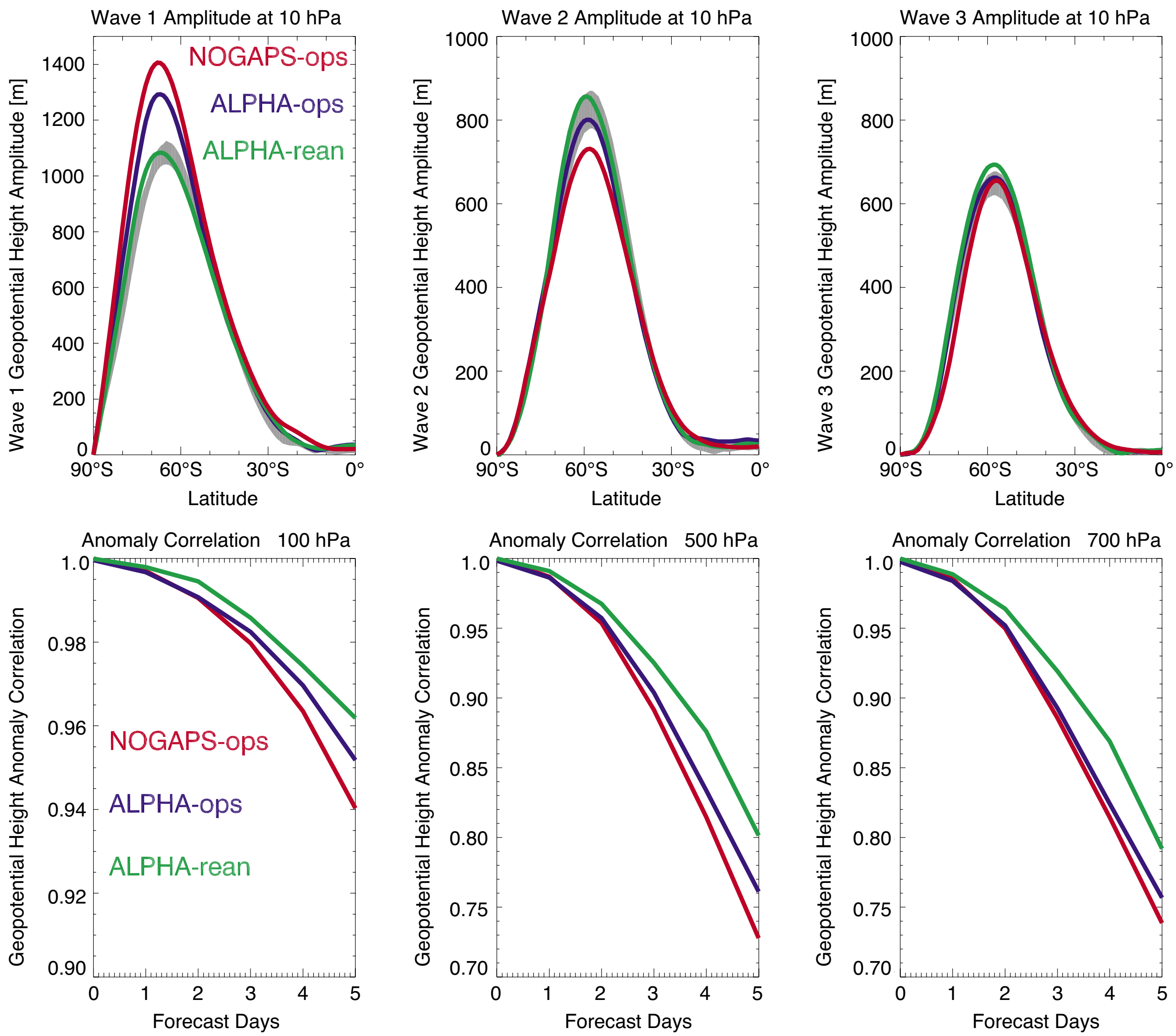

FIGURE 3
(Top row) geopotential height zonal wavenumber 1, 2, and 3 amplitude at 10 hPa on September 25, 2002 (12 UTC) over the SH for thre -
al
initialized on even-numbered days from September 18 to October 10, 2002 (12 UTC). The anomaly correlation for each forecast is calculated with the analyses used for initialization.

an additional, more substantial improvement, highlighting the impact of better global initial conditions from NAVDAS. At 500 hPa, Fig. 3 reveals a 1-day improvement in ALPHA-rean forecast skill compared with NOGAPS-ops. It is clear that the changes in both the forecast model (i.e., between NOGAPS and NOGAPS-ALPHA) and analysis system (between MVOI and NAVDAS) will positively impact forecast skill at high southern latitudes in both the troposphere and stratosphere.

[Sponsored by ONR]

Reference

[1] D.R. Allen, R.M. Bevilacqua, G.E. Nedoluha, C.E. Randall, and G. Manney, "Unusual Stratospheric Transport and Mixing During the 2002 Antarctic Winter," *Geophys. Res. Lett.* **30**(12), 1599, doi:10.1029/2003GL017117, 2003.

★

Coastal Atmospheric Effects on Microwave Refractivity

S.D. Burk,[1] T. Haack,[1] R.E. Marshall,[2] E.H. Burgess,[2] J.R. Rottier,[3] K.L. Davidson,[4] and P.A. Frederickson[4]
[1]*Marine Meteorology Division*
[2]*Naval Surface Weapons Center, Dahlgren Division*
[3]*Johns Hopkins Applied Physics Laboratory*
[4]*Naval Postgraduate School (NPS)*

Introduction: Sharp vertical gradients within thermodynamic profiles in the atmospheric boundary layer (BL) create abrupt changes in refractivity, thereby impacting electromagnetic (EM) wave propagation. This study uses NRL's Coupled Ocean/Atmosphere Mesoscale Prediction System (COAMPS™) to investigate refractive structure during a field experiment[1] conducted at Wallops Island, VA. Measurements include low-elevation radar frequency pathloss, meteorological conditions (e.g., from buoys, rocketsondes, helicopter profiles), and radar clutter returns.

EM propagation codes are useful for naval operations and decision-making; when supplied with accurate refractivity fields, they produce radar coverage diagrams. The fidelity of COAMPS™ refractivity analyses/forecasts, and their usefulness as input to microwave propagation codes, is evaluated here in a complex littoral setting.

Internal BLs and Refractive Effects: The Delmarva Peninsula along which Wallops Island lies is relatively flat but contains an intricate coastline, and the surrounding waters have pronounced spatial sea surface temperature (SST) variability. These factors contribute to complex BL structures (e.g., internal BLs, sea/land breezes).

Advection of warm, dry afternoon air from land across the cool Atlantic shelf water near Wallops produces a stable internal BL (SIBL) wherein surface sensible heat flux is downward, while latent heat flux remains upward. This SIBL tends to cool and moisten with fetch, thereby increasing the modified refractivity. The refractivity is represented by $M = A/T(P + Be/T) + Cz/R$, where T, e, z, and P are temperature, vapor pressure, height, and pressure, respectively, while A, B, and C are constant coefficients. Layers where the vertical refractivity gradient dM/dz is negative tend to trap, or duct, microwave energy launched at a low elevation angle. Conversely, layers in which dM/dz is strongly positive are subrefractive, and initially horizontal rays bend away from the Earth, yielding shortened radar detection ranges. If shown to be sufficiently accurate and reliable, analyses/forecasts of these effects on propagation can have clear value to many aspects of naval operations (e.g., ship self defense and Special Operations).

Case Study Results: Figure 4(a) depicts near-surface streamlines, surface temperature, and white, cloud-like isosurfaces of trapping ($dM/dz < 0$) at 3 a.m. local time (LT) on April 29, 2000. The land (blue) is significantly colder than the SST at this hour. The wind is northerly over most of the region, although a low-pressure center lies near the grid's eastern boundary. On the backside of the low-pressure center, dry subsiding air creates patchy, elevated trapping regions throughout the night.

With daytime heating, the situation changes dramatically. Figure 4(b) shows that by 3 p.m. LT, the land is substantially warmer than the coastal waters and the flow has shifted to the NW. Shallow, near-surface trapping layers develop in the SIBLs formed over coastal waters where the afternoon flow is offshore. No trapping is present in the onshore flow along the New Jersey coast. A 24-h-long trajectory descends from 1.3 km at point 1 to a height of 5 m near Wallops, being drawn onshore by the sea breeze. Dry air is advected along such parcel trajectories, altering the near-surface refractivity profile and making simple 2-D sea/land breeze concepts of limited value in this region.

Figures 5(a,b) and 6(a,b) illustrate the diurnal changes in coastal BL vertical structure that alter refractivity and EM propagation conditions. The vertical cross section angles across the model grid from the NW to SE (intersecting Wallops) and extends from

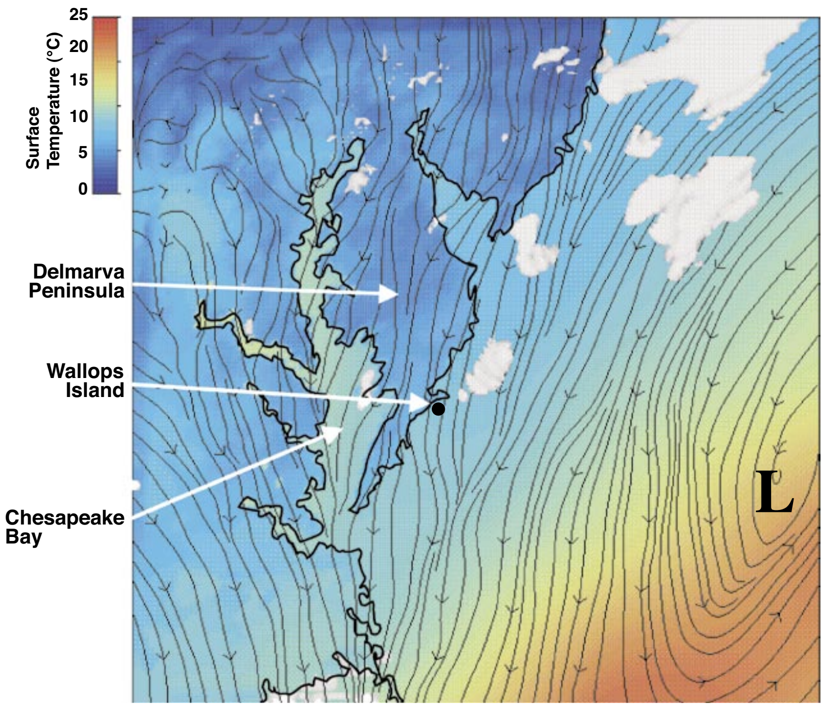

FIGURE 4(a)
COAMPS™ forecast valid 3 a.m. LT April 29, 2000 of color shaded surface temperture (°C), near surface streamlines, and white isosurface where *dM/dz* < 0 (e.g., microwave trapping regions).

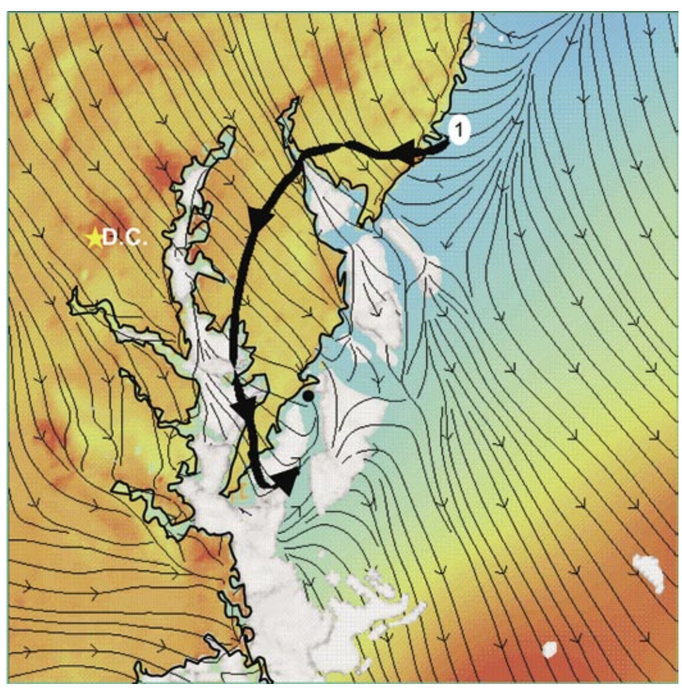

FIGURE 4(b)
As in (a), except at 3 p.m. LT. Also shown is a 24-h-long parcel trajectory beginning at point 1 (at 1.3 km) and ending at Wallops Island at 7 p.m. LT (at 5 m).

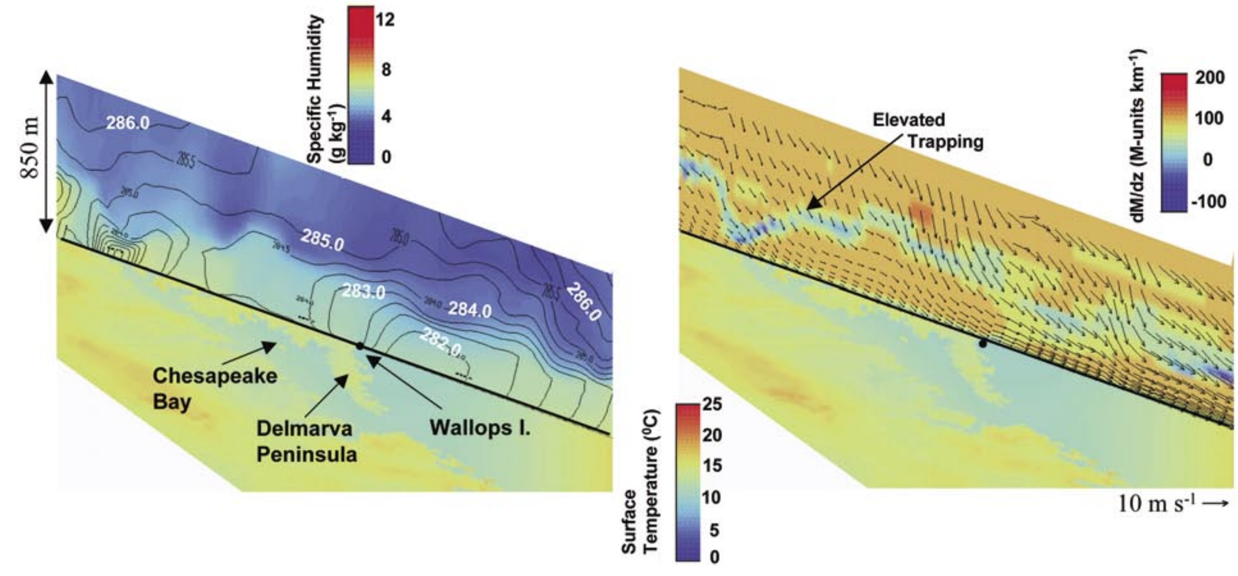

(a) (b)

FIGURE 5
COAMPS™ forecast valid 10 a.m. LT April 29, 2000 of surface temperature (°C) in the foreground. Cross sections of (a) color shaded specific humidity and potential temperature contours (K), and (b) wind vectors in the plane of the cross section and color shaded *dM/dz*. Blue regions indicate EM trapping, while dark red is subrefractive.

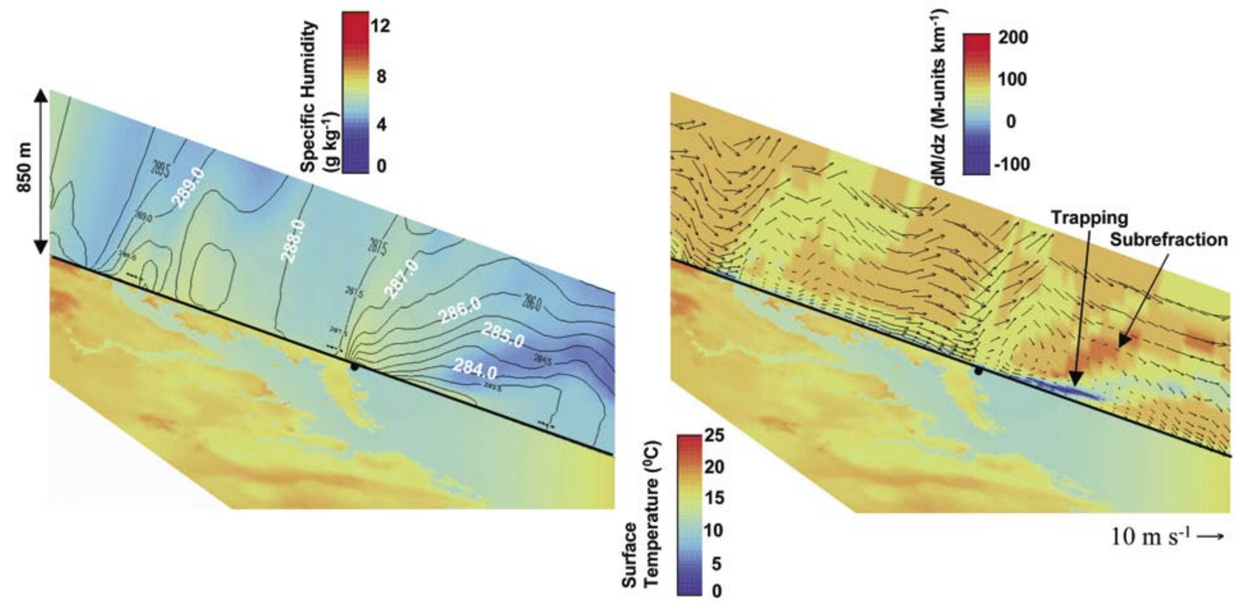

(a) (b)

FIGURE 6
As in Fig. 5 except 3 p.m. LT.

the surface to 850 m. Surface temperature is displayed in the foreground, while the vertical section shows contours of potential temperature along with shaded specific humidity (Figs. 5(a), 6(a)) or wind vectors and *dM/dz* (Figs. 5(b), 6(b)).

At 10 a.m. LT, Fig. 5(a) shows a fairly homogenous BL capped by a strong inversion and dry air aloft. Elevated trapping is present in Fig. 5(b) associated with the gradients at the top of the nocturnal BL. By 3 p.m. LT, a deep, warm, well-mixed BL has formed over land with a very shallow, stable BL over water (Fig. 6(a)). Dry air intrusion just offshore of Wallops results from advection of the type indicated by the trajectory in Fig. 4(b). The resultant strong vertical moisture gradients contribute to the shallow, surface-based duct that is seen in Fig. 6(b). A region of subrefraction, where moist BL air over land is advected aloft into dryer layers over the Atlantic, tops this trapping layer. Flow reversal associated with the sea breeze is evident in a thin layer over water.

Summary: High-resolution analyses/ forecasts of refractivity and EM propagation conditions for use in Naval operations are rigorously evaluated using extensive data sets that include both meteorological conditions and EM propagation measurements.[2] COAMPS™ hourly forecast fields have been archived for the 1.5-month period of the Wallops experiment and have been saved on the Master Environmental Library (MEL) database. RMS errors for this period formed between Naval Postgraduate School buoy measurements and COAMPS™ forecast values of wind speed, temperature, and relative humidity are 2.2 ms^{-1}, 1.3 °C, and 7.7%, respectively. This unique model and observational database are now available for wide usage in the EM propagation and atmospheric modeling research communities.

[Sponsored by ONR and SPAWAR]

References

[1] J. Stapleton, D. Shanklin, V. Wiss, T. Nguyen, and E. Burgess, "Radar Propagation Modeling Assessment Using Measured Refractivity and Directly Sensed Propagation Ground Truth," NSWCDD/TR-01/132, 49 pp., 2001.

[2] S.D.Burk, T. Haack, L.T. Rogers, and L.J. Wagner, "Island Wake Dynamics and Wake Influence on the Evaporation Duct and Radar Propagation," *J. Appl. Meteor.* **42**, 349-367 (2003).

Improving the Characterization of the Battlespace Environment with Satellite Brightness Temperature Assimilation

N.L. Baker, C.B. Blankenship, W.F. Campbell, and T.F. Hogan
Marine Meteorology Division
R.L. Pauley
Fleet Numerical Meteorology and Oceanography Center

Introduction: Satellite observations, particularly in data-sparse regions, are critically important for initializing the Navy's global and mesoscale numerical weather prediction (NWP) models used to provide tactical weather support. Advanced Microwave Sounding Unit A (AMSU-A) and AMSU-B are multichannel passive microwave radiometers that provide global observations of atmospheric temperature and moisture, respectively. Recently, the NRL Atmospheric Variational Data Assimilation System (NAVDAS) began operational assimilation of AMSU-A brightness temperatures T_b's for the Navy Operational Global Atmospheric Prediction System (NOGAPS), replacing the assimilation of temperature retrievals. AMSU-A assimilation significantly improves the Northern and Southern Hemisphere forecast skill and tropical cyclone track predictions. Assimilation of AMSU-B humidity profiles improves the representation of NOGAPS upper-tropospheric water vapor, and further reduces tropical cyclone track forecast error.

Motivation for Radiance Assimilation: NAVDAS was developed to assimilate satellite observations effectively. For satellite observations such as AMSU-A/B, radiative transfer theory relates the outgoing radiation to the vertical profiles of atmospheric temperature and moisture, and surface emissivity and skin temperature. Traditionally, satellite T_b's were used to retrieve temperature and humidity profiles. Because T_b's are integrated measurements with contributions from deep layers in the atmosphere, and are also imperfect, the retrieval problem is mathematically ill-posed; many possible vertical profiles of temperature and moisture may yield the same T_b. Consequently, retrieval errors are complex and difficult to specify correctly; T_b errors are simpler to characterize. Accurate error specification is required for proper observation weighting in the assimilation system as well as quality control and bias correction.

Because the relationship between the observed AMSU-B T_b's and atmospheric water vapor is strongly nonlinear, direct assimilation of AMSU-B T_b's will require modifications to NAVDAS. As a first step, the water vapor profiles retrieved from AMSU-B are assimilated.

Implementation of AMSU-A/B Assimilation: Successful assimilation of satellite T_b's requires careful channel selection and quality control, primarily to screen out observations with a strong signal from variables that are not well represented in the NWP model (e.g., cloud liquid water) or the radiative transfer model (e.g., scattering by precipitation). Recent NOGAPS changes implemented to make AMSU-A/B assimilation more effective include raising the model top and improving the model moisture fields and skin temperatures over land.

Bias correction is an essential component of radiance assimilation, as the innovations (differences between the observed and forecast T_b's) are often larger than the signal. The biases are satellite-specific—the same sensor flown on two different satellites will have different bias characteristics. Because these biases also vary with time, an automated bias coefficient updating system was developed for operational use at Fleet Numerical Meteorology and Oceanography Center (FNMOC). After each analysis cycle, new bias correction coefficients are calculated, tested, and updated without user intervention. If the new coefficients fail any test, the previous coefficients are retained and a brief problem summary is automatically emailed to the user, affording quick evaluation of potential problems both operationally and for research experiments.

NOGAPS Forecast Improvements with AMSU-A/B Assimilation: On June 9, 2004, NAVDAS began operational assimilation of AMSU-A T_b's for NOGAPS, replacing the assimilation of temperature retrievals. AMSU-A assimilation substantially improves the height, wind, and temperature forecasts for both hemispheres at all forecast lengths. For example, the two- to five-day NOGAPS forecast, as measured by the 500 hPa anomaly correlation, is increased by 5 to 7 h in the Northern Hemisphere (Fig. 7(a)), and by 14 to 16 h in the Southern Hemisphere (Fig. 7(b)). Similar improvements are observed at other levels, along with significantly fewer forecast "busts." Both the NAVDAS analyses and NOGAPS forecasts exhibit better fit with radiosondes. The predicted tropical cyclone tracks, which are critically important to the Navy, show error reductions (Fig. 8) up to 25 nautical miles (verified against Joint Typhoon Warning Center and National Hurricane Center postseason best tracks). The operational implementation of AMSU-A assimilation at FNMOC is one of the most important advances to NOGAPS in the past decade and is equivalent to 9 to 12 years of general system improvements.

Extensive testing indicates that AMSU-B water vapor retrieval assimilation corrects for known model biases by drying out the middle and upper troposphere. Moisture features are better represented, as

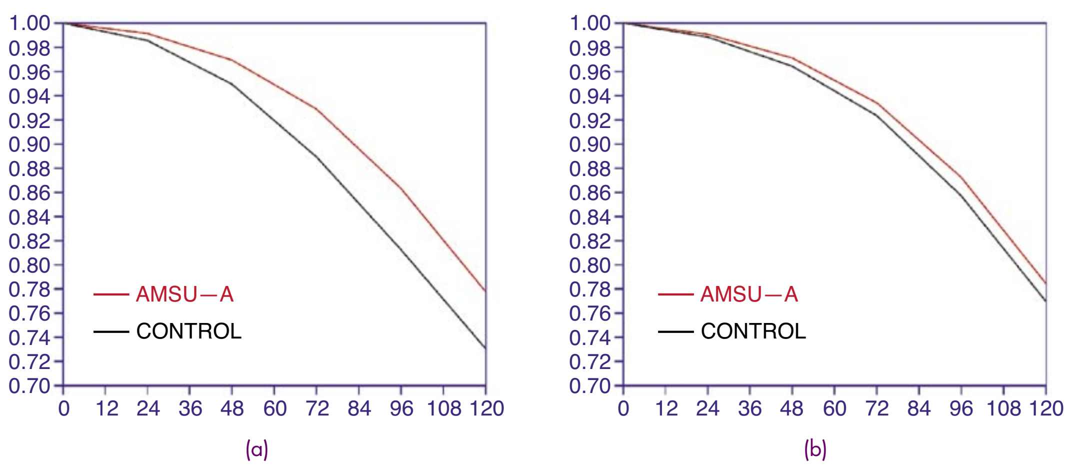

FIGURE 7
(a) Southern Hemisphere and (b) Northern Hemisphere 500 hPa height anomaly correlation vs forecast hour for July 16 to September 30, 2003. The test run (AMSU-A) included NAVDAS assimilation of AMSU-A T_b's, while the control run assimilated NESDIS ATOVS retrievals with NAVDAS.

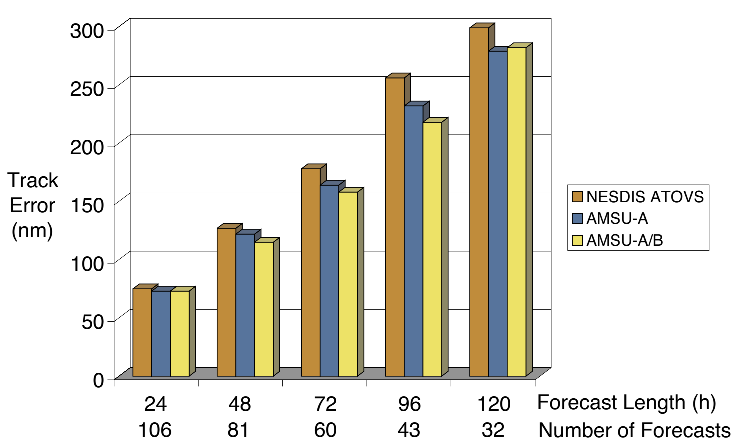

FIGURE 8
Comparison of the mean tropical cyclone track error vs forecast hour for the month of September 2003. Verification is against the postseason "best track." The numbers below the forecast length are the total number of forecast tracks for the month used in the comparison.

validated by geostationary infrared observations (Fig. 9) and stronger gradients. Overall, tropical cyclone forecasts are better with AMSU-B, with smaller errors in the forecast track and central pressure (Fig. 8). Transition of AMSU-B retrieval assimilation to FNMOC operations is targeted for 2005.

Looking to the Future: In the near term, NAVDAS will soon become operational for the Navy's mesoscale NWP model (COAMPS™—a trademark of the Naval Research Laboratory) at FNMOC, paving the way for improved analyses, forecasts, and tactical decision aids due to AMSU-A/B assimilation.

Over the next decade, the ability of polar-orbiting and geostationary satellites to observe the Earth environment will improve dramatically, largely due to the combined DoD and civilian National Polar Orbiting Environmental Satellite System (NPOESS). NRL scientists, along with their partners in the Joint Center for Satellite Data Assimilation, are actively developing assimilation techniques to be able to effectively utilize these new observations. While the costs of developing specialized satellite assimilation techniques are significant, the recent successes at NRL and other NWP centers have clearly demonstrated that substantial gains in analysis and forecast skill can be made through assimilation of these observations.

References

[1] N.L. Baker and W.F. Campbell, "The Impact of AMSU-A Radiance Assimilation in the U.S. Navy's Operational Global Atmospheric Prediction System (NOGAPS)," preprints, 13th Conference on Satellite Meteorology and Oceanography, Norfolk, VA, 2004.

[2] C.B. Blankenship, E.H. Barker, and N.L. Baker, "Assimilation of AMSU-B Humidity Profile Retrievals Using the NRL Atmospheric Variational Data Assimilation System (NAVDAS)," preprints, 13th Conference on Satellite Meteorology and Oceanography, Norfolk, VA, 2004. ★

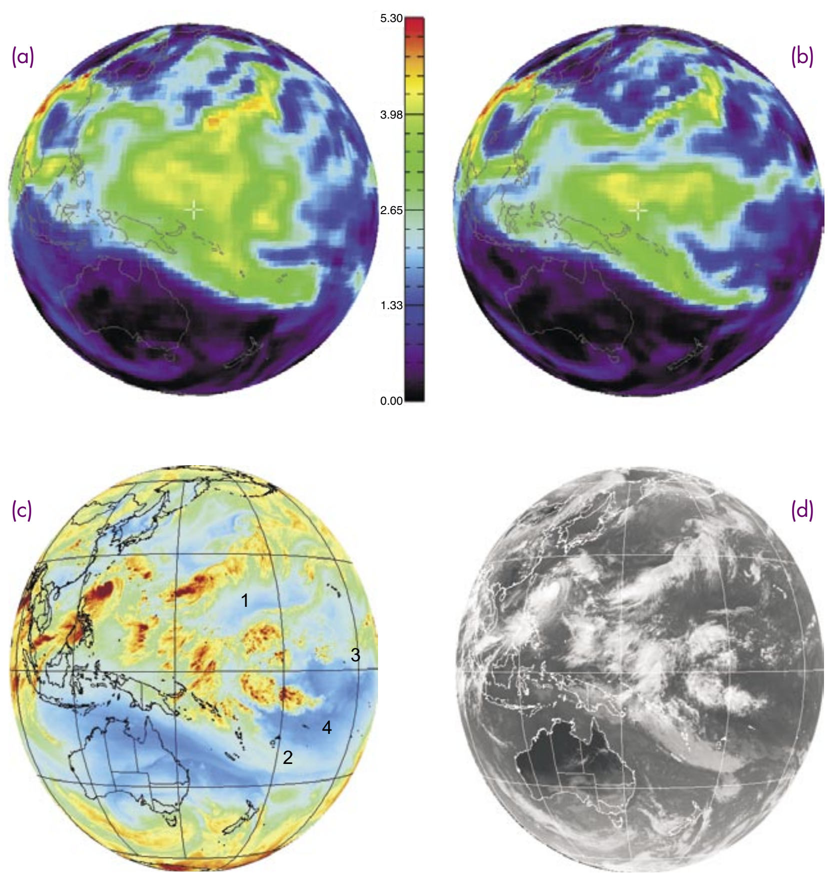

FIGURE 3
(a) Analyzed 500 hPa specific humidity (g kg^{-1}) at 06Z on August 10, 2004, control run; (b) AMSU-B run; (c) GOES-9 6.7 μm water vapor channel image at 0525Z; (d) GOES-9 infrared image at 0525Z. Features improved in the AMSU-B run include (1) dry channel north of the Intertropical Convergence Zone (ITCZ), (2) sharp feature at tail of South Pacific Convergence Zone, (3) sharp gradient in ITCZ, and (4) shape of dry region in Central Pacific.

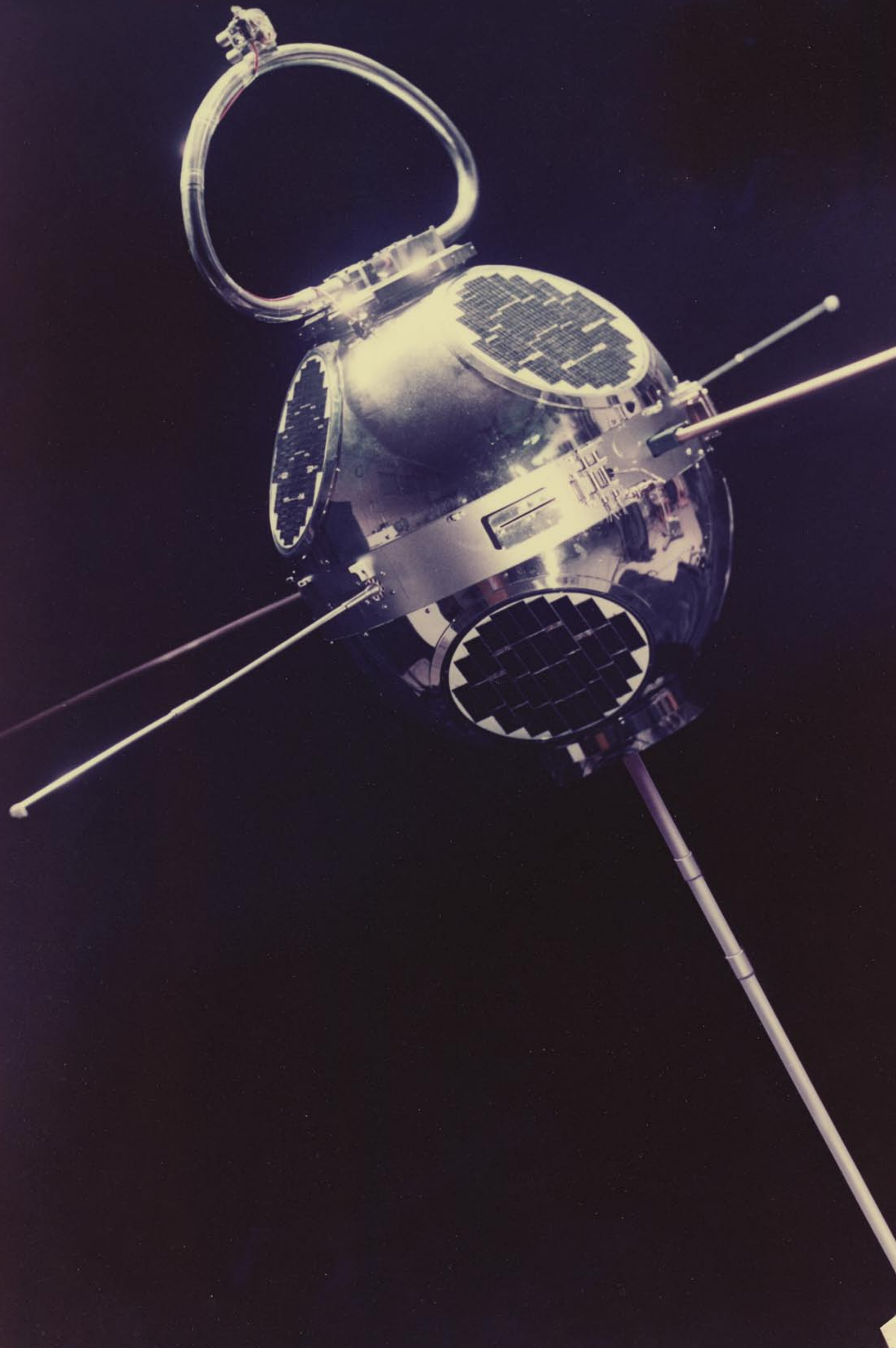

Chemical/Biochemical Research

Photo caption: The LOFTI IIB (LOw Frequency Trans Ionospheric) satellite was launched in 1963 to learn about VLF (approx. 10 kHz) radio waves ability to communicate with submerged submarines and to also penetrate the ionosphere.

Lab-on-a-Chip Analysis of Explosives

G.E. Collins,[1] J.D. Ramsey,[2] B.C. Giordano,[3] and M.P. Chatrathi[4]
[1] *Chemistry Division*
[2] *GeoCenters, Inc.*
[3] *ASEE Postdoc*
[4] *Arizona State University (Postdoc)*

Introduction: Laboratory analysis of complex "real-world" samples typically requires a series of time-consuming and labor-intensive steps that include sample preparation, separation, and detection. The emerging technology of microfluidic analytical devices, or "Lab-on-a-Chip" (LOC), allows these functions to be integrated onto a single compact platform. Such devices, due to the design simplicity available through advanced microfabrication technologies, permit the integration of various functional elements such as sample preparation and handling, sample loading, separation, and detection, onto a single microchip platform. Typical analytical microsystems rely on electrokinetic fluid "pumping" of the sample through a network of channels patterned in a planar (glass or plastic) substrate, eliminating the need for external pumps or valves. Microchip capillary electrophoresis (CE) has been shown to provide high-speed analysis with improved separation efficiencies, therefore, are very attractive for addressing some of the security needs currently facing our troops. These needs include the sensitive and selective detection of explosives, whether in oceanic environments (e.g., mines), or as improvised explosive devices (IED). Despite the advantages afforded by these devices, the reduced microfluidic channel dimensions directly affect the sensitivity of most traditional detection technologies and require integrating additional sample preconcentration techniques onto the microchip platform. We discuss the successful application of LOC to the analysis of explosive mixtures. We examine the integration of on-chip solid phase extraction (SPE) techniques for dramatic enhancements in sensitivity.

Microchip Design: Figure 1(a) shows the microchip design for integrating solid phase extraction on a packed bed of beads, the subsequent elution of analytes using an organic eluent, injection, separation, and detection. The channels (20-µm deep by 60-µm wide) are etched in a glass substrate and bonded with a cover glass plate to close the microfluidic network. All fluid flow is controlled electro-osmotically by the application of desired voltages to the individual reservoirs. A typical SPE injection sequence consists of first directing the sample across the micro-SPE column to the sample waste reservoir. This is followed by elution

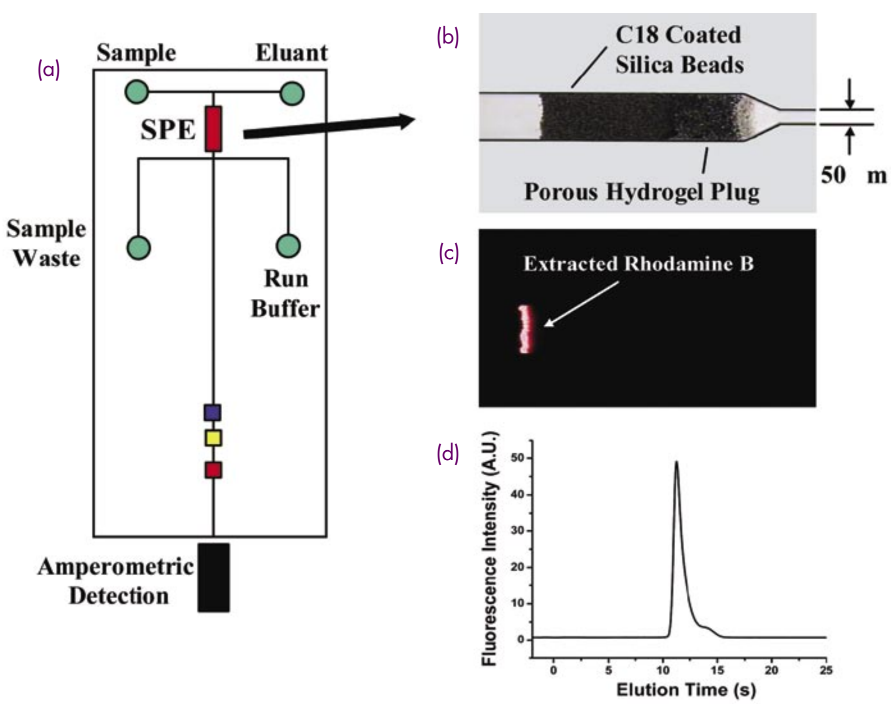

FIGURE 1
(a) SPE microchip design; (b) close-up of packed bed; (c) fluorescence microscope image of Rhodamine B loading onto packed bed; and (d) electropherogram for micro-SPE of 100 pM Rhodamine B.

of a concentrated band of analytes via subsequent application of voltage to the eluent reservoir. The eluted sample plug is introduced into the separation channel by application of another voltage sequence, leading to its separation into individual analyte bands using the appropriate run buffer.

Explosives Analysis on a Microchip: Because of their electrical neutrality, the electrophoretic separation of nitroaromatic explosives requires the introduction of a pseudo-stationary phase in the form of a surfactant added to the run buffer. Figure 2 shows a CE microchip separation of five different nitroaromatic explosives in the absence of any SPE. The electrochemical activity of nitro-functional groups permits amperometric detection of the separated bands as they elute from the end of the microchip. Despite the similarity in structure between these different aromatic explosives, the high resolving power of the LOC permits near-baseline resolution in just 100 s.

Solid Phase Extraction (SPE) on a Microchip: Although TNT (2,4,6-trinitrotoluene) and DNB (1,3-dinitrobenzene) detection limits have been achieved down to 60 ppb,[1] the demanding sensitivity requirements of explosive sensors in oceanic environments prompted us to investigate the incorporation of SPE techniques[2] directly on the microchip platform. Figure 1(b) is a close-up image of the micro-SPE bed. To contain the packing material, 5-μm C_{18} coated silica beads, within a microfluidic platform, a porous poly(methacrylate) polymer was synthetically crosslinked inside the channel by ultraviolet (UV) photoinitiation. Although the fluorescence image shown in Fig. 1(c) visually demonstrates the successful extraction of Rhodamine B (a model dye compound with similar hydrophobicity to aromatic explosives) onto a micro-SPE bed, the electropherogram shown in Fig. 1(d) for the on-chip SPE extraction and elution of a 100-pM sample dye indicates that the detection limits can be lowered into the femtomolar range. The quantitative nature of the extraction process is illustrated in Fig. 3(a). As expected, a linear increase in the fluorescence intensity of the eluted Rhodamine B was observed with increasing extraction time. The preconcentration factors range from 20 to 300 times, but it can be much larger, depending on the total extraction time. When coupled to the separation step, it is possible to concentrate and separate a series of neutral fluorescent dyes (Fig. 3(b)) in an experiment analogous to that needed for the detection of nitroaromatic explosives.

Summary: We have demonstrated successful direct coupling of micro-SPE enrichment with advanced separation techniques for model dye compounds. Efforts are underway to couple enrichment technologies with microseparation devices for the separation of nitroaromatic explosive mixtures, investigations which should ultimately lead to powerful detection schemes for explosives and other toxic analytes of concern to the DoD and analytical community alike.

[Sponsored by ONR and MIPT]

References

[1] J. Wang, M. Pumera, M.P. Chatrathi, A. Escarpa, M. Musameh, G. Collins, A. Mulchandani, Y. Lin, and K. Olsen, "Single-Channel Microchip for Fast Screening and Detailed Identification of Nitroaromatic Explosives or Organophosphate Nerve Agents," *Anal. Chem.* **74**, 1187-1191 (2002).

[2] Q. Lu, G.E. Collins, M. Smith, and J. Wang, "Sensitive Capillary Electrophoretic Microchip Determination of Trinitroaromatic Explosives in Nonaqueous Electrolyte Following Solid Phase Extraction," *Anal. Chim. Acta* **469**, 253-260 (2002). ★

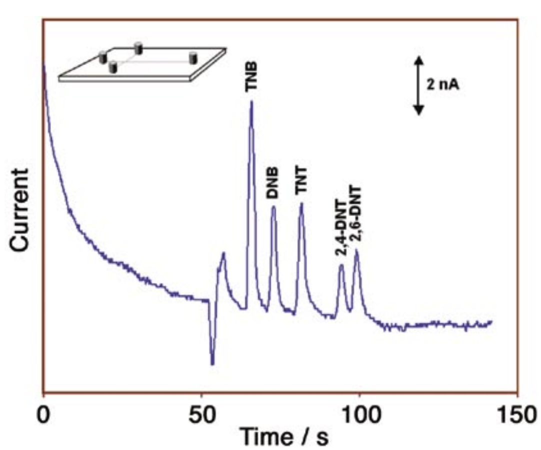

FIGURE 2
Microchip capillary electrophoretic separation and amperometric detection of five nitroaromatic explosives (2 ppm each). DNB = 1,3-dinitrobenzene; TNT = 2,4,6-trinitrotoluene; 2,4-DNT = 2,4-dinitrotoluene; 2,6-DNT = 2,6-dinitrotoluene.

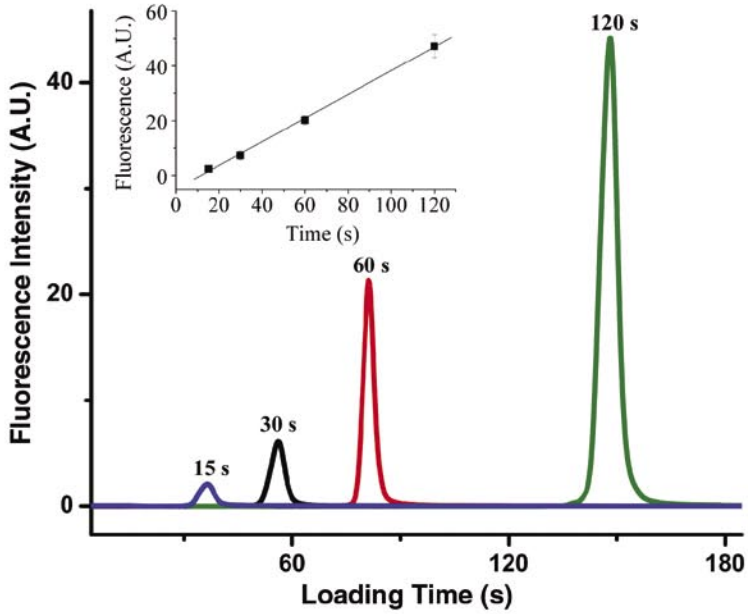

(a)

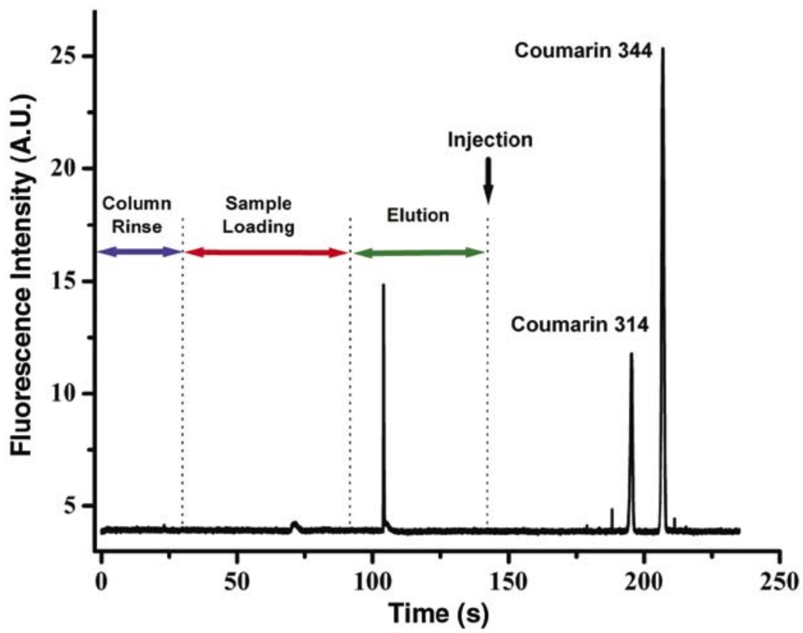

(b)

FIGURE 3
(a) Microchip SPE of 250-nm Rhodamine B for sequentially increasing load times;
(b) microchip separation of two neutral dyes following on-chip SPE.

Fire Suppression Properties of Very Fine Water Mist

J.W. Fleming, A. Awtry, and R.S. Sheinson
Chemistry Division
S. Ayers
Geocenters, Inc.

Introduction: Water mist is one of the best non-gaseous fire suppression replacement agents for Halon 1301 on a mass basis. In general, small drops are more effective than larger drops, but the highly complex nature of fires defies a simple generalization. Drop size is important but so are drop transport and evaporation behavior. Understanding each of these is critical to the design of water mist fire suppression systems.

Water spray systems like sprinklers in many buildings produce very large drops, generally above a millimeter in diameter. These systems ineffectively deliver much more water than is usually needed. Water mist systems that use low-pressure nozzles typically produce drops between ~200 μm and 1 mm. The production of fine water mist (drops below 200 μm) requires high-pressure nozzles. NRL studies in laboratory flames show that drops smaller than 40 μm are more effective than Halon 1301 on a mass basis at extinguishing methane/air and propane/air non-premixed flames.[1] Experimental and computer fire modeling studies indicate that effectiveness continues to increase with decreasing drop size. The case looks especially attractive for very fine water mist with drop diameters less than 10 μm.

Mist-generation and Detection: High-pressure mist systems do not typically generate sufficient quantities of very fine water mist. Small drops in high numbers can be produced by piezoelectric nebulization as recently demonstrated.[2] The misters incorporate an array of individual piezoelectric transducers. NRL, in coordination with Nanomist LLC, is exploring the characteristics of these small water drops in laboratory and real-scale fire suppression applications.

In these studies, mist drop size, number density, and velocities are measured using Phase Doppler Particle Anemometry. The amount of liquid water dispersed as drops is determined from optical density (OD) measurements using a diode laser. Oxygen measurements are obtained using three different instruments. The paramagnetic oxygen analyzer connected to an extractive sampling line typically reads high in the presence of water (both liquid and vapor) since water must be removed from the sampled volume before analysis. The zirconia oxygen analyzer, heated to approximately 600 °C for proper operation, reads low in the presence of water drops. These two instruments, although impacted adversely by the presence of water drops, provide important upper and lower bounds for the amount of oxygen present. NRL, in collaboration with the University of Heidelberg, developed an in situ oxygen sensor based on tunable diode laser absorption spectroscopy (TDLAS) to provide absolute oxygen number densities in the presence of mist.[3] The TDLAS oxygen sensor provides real-time, calibration-free, quantitative oxygen concentrations that are particularly important at times of high mist density.

Fire Suppression Performance and Mist Behavior: The very fine water mist was evaluated in a small corral (130 × 85 × 80 cm^3). Mist was brought in at one end of the corral and propelled with a small fan through a dryer vent hose. Mist samples withdrawn at the other end of the corral were sent to the drop size analyzer. A small 10-cm propane test flame was located near the middle of the corral (Fig. 4).

Parameters investigated in the small-scale laboratory tests included mist drop size and concentration as a function of time. Drop lifetime studies evaluated fire protection times possible with very fine water mist. Flame extinction studies show that very fine water mist achieves the theoretical quantitative flame-extinguishing potential for water in this environment (Fig. 5). A key finding in these studies was the time required for flame extinction. Unlike a gas, which quickly disperses and fills the space, very fine water mist requires time to disperse and build to a sufficient concentration to effect flame extinction (Fig. 6).

Mist build-up time is even more important in real scale. The large-scale compartment used for these studies is a 3 × 3 × 3 m^3 steel-walled compartment with standard Navy hardware designed to simulate a small Navy shipboard flammable liquid storeroom. The compartment contained typical shelving frames, ventilation, and storage accommodations consistent with Navy compartments. A 120-kW heptane pan fire was located in the center of the compartment, 1 ft above the floor.

Information collected as a function of time using an automated data acquisition system included temperature at various locations, concentration of gases including oxygen, and video (visual and IR) to determine fire-out status. The very fine water mist was able to successfully extinguish all pan fires tested. Average extinguishment times were around 5 min, with six mister units each delivering 0.1 liter of water per minute as a very fine mist. Extinguishment times decreased with increasing mist injection rate. The

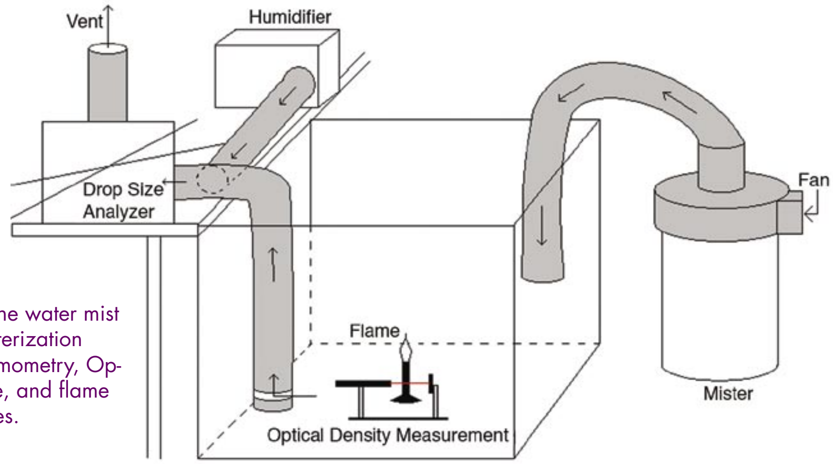

FIGURE 4
Laboratory scale corral for very fine water mist studies showing drop size characterization using Phase Doppler Particle Anemometry, Optical Density Measurement module, and flame for fire extinction evaluation studies.

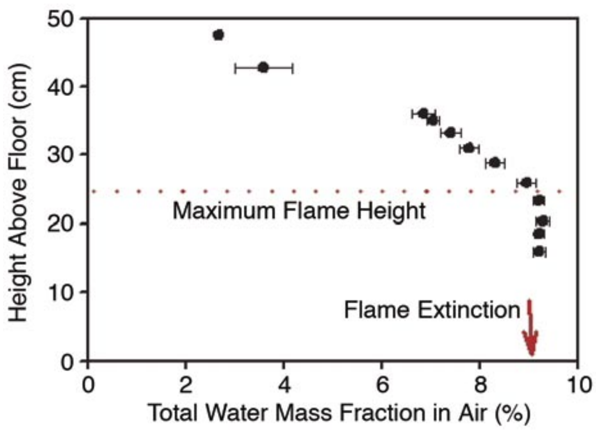

FIGURE 5
Height in corral vs water mass fraction (very fine water mist and vapor). Flame extinction studies show that very fine water mist achieves the theoretical quantitative flame extinguishing potential for water in this environment based on a thermal fire suppression mechanism.

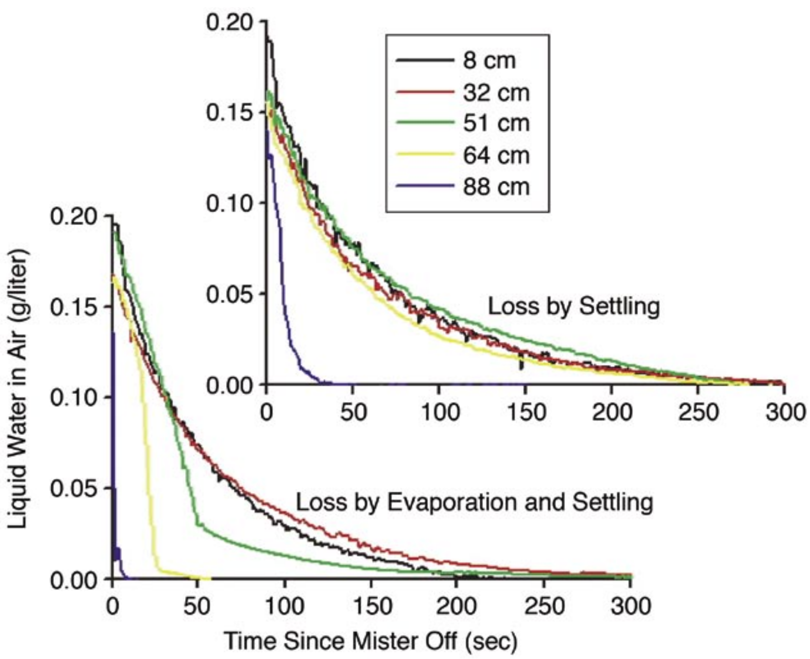

FIGURE 6
Fine water mist drop density decay time as a function of height. At least two competing loss mechanisms occur for the mist: settling and evaporation. The evaporation loss is rapid, until the surrounding environment becomes saturated with water vapor, then the slower settling mechanism dominates.

placement of a simple wall obstruction between mister and fire required more mist output to extinguish the fire in the same suppression time. Visual evidence showed that the mist did not reach all areas of the compartment. These observations highlight the importance of drop transport and fire threat location in the compartment to overall mist effectiveness.

Designing Water Mist Systems: Favorable environmental properties and high potential fire suppression effectiveness keep water mist in strong contention for protecting many Navy spaces formerly protected by Halon 1301. Laboratory and real scale evaluations indicate that very fine water mist has key advantages over mist with larger drop sizes. Very fine water mist drops behave more gas-like than larger drops, but still very differently than gaseous agents. Further understanding of drop size, lifetime, and transport behavior is necessary to provide practical guidance on very fine water mist fire suppression systems. The results presented here contribute to that understanding and provide data necessary for the further development of models to predict water mist suppression in real fire scenarios.

[Sponsored by ONR]

References

[1] E.J.P Zegers, B.A. Williams, R.S. Sheinson, and J.W. Fleming, "Dynamics and Suppression Effectiveness of Monodisperse Water Droplets in Non-Premixed Counterflow Flames," *Proc. Combust. Inst.* **28**, 2931-2938 (2000).

[2] NanoMist, LLC, Warner Robbins, GA.

[3] H.E. Schlosser, J. Wolfrum, V. Ebert, B.A. Williams, R.S. Sheinson, and J.W. Fleming, "In-Situ Determination of Molecular Oxygen Concentrations in Full-Scale Fire Suppression Tests Using TDLAS," *Proc. Combust. Inst.* **29**, 353-360 (2002). ★

HELGA II: Autonomous Passive Detection of Nuclear Weapons Materials

R. August and R. Whitlock
Chemistry Division

Introduction: During the televised debates of the recent presidential election, both candidates listed nuclear nonproliferation as their number one priority. Attempts by rogue nations and terrorist organizations to obtain weapons-grade nuclear materials make the headline news with alarming frequency. Unfortunately, nuclear materials emit little detectable radiation, making it very hard to prevent their being smuggled into this country or to find them once they are here. Most currently available radiation detection systems cannot sort out a nuclear weapon signature from naturally occurring radiation backgrounds with enough certainty and rapidity to interdict it in a realistic smuggling scenario. Consequently, the specter of a nuclear detonation in an American city looms large. Also, the possibility of a nuclear "USNS *Cole* incident" perpetrated on an American fleet far from home should not be ignored. In fact, Albert Einstein spoke of just such an incident in his first letter to President Franklin Roosevelt: "…a single bomb of this type, carried by a boat and exploded in a port, might very well destroy the whole port together with some of the surrounding territory."[1]

The Office of Naval Research and the Coast Guard has tasked the Naval Research Laboratory to produce the HELGA II prototype as a step toward addressing this problem. HELGA II is the modernization of HELGA (High Efficiency Large Germanium Array[2]), a national asset developed by NRL in the 1980s to detect faint gamma-ray sources in a natural environment, the same problem faced today when looking for smuggled nuclear materials. NRL, where the detection of nuclear weapons signatures in a natural environment has been studied for more than half a century, is uniquely qualified to produce such a device and to guide its effective use. For example, the U.S. Navy History web site[3] documents NRL's use of nuclear detectors during fly-overs of the Soviet fleet during the Cuban Missile Crisis in 1962.

Detector Requirements: The crux of the problem is that while nuclear weapons materials have unique spectral signatures in the gamma-ray region, a detector with high-energy resolution (selectivity), and high collection efficiency (sensitivity) is required to distinguish these signatures from the spectral signatures of a vast number of items found in the everyday, real-world background. The only detector material currently capable of this is germanium, but this material is expensive to produce and must be cooled to liquid nitrogen temperatures for effective operation. Consequently, nuclear detection systems have typically relied on lesser materials, the best of this class being NaI (sodium iodide). Although NaI has good gamma-ray collection efficiency, it has poor energy resolution, as shown in the Fig. 7. When considering realistic nuclear weapons signatures, NaI can do no better than state a probability that an inspected item might be nuclear weapons material. Germanium can make a positive identification. Real-world interdiction requires positive identification, and therefore requires germanium. In fact, because germanium allows positive

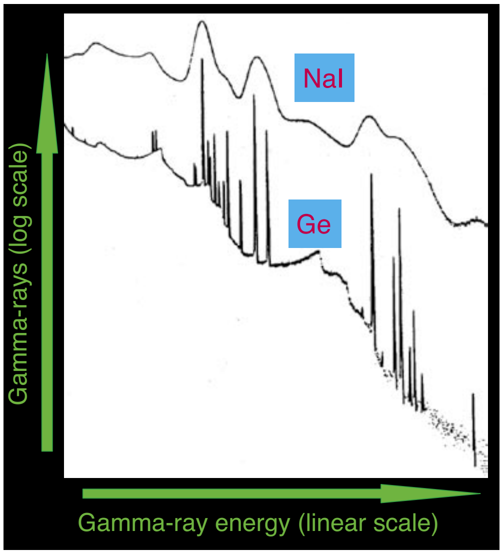

FIGURE 7
NaI and Ge comparative measurement of same multisource target.

identification, it provides a system where the identification can be made instantly by an onboard computer, rather than by waiting for nuclear experts to mull over a spectrum, as required by NaI. The HELGA II prototype was developed to prove that an autonomous identification system based on germanium can be developed and deployed in an affordable fashion.

When the original HELGA system was developed in the 1980s, germanium detectors were delicate laboratory devices that required liquid nitrogen for cooling. The HELGA project ruggedized germanium detectors for field use, but it could do nothing to alleviate the requirement for liquid nitrogen cooling. Nevertheless, HELGA collected interesting real-world data that characterized the capabilities of germanium detectors. Such data go far toward determining how effective germanium can be today at identifying nuclear materials signatures hidden in the real-world background.

Since the 1980s, mechanical coolers have been used with germanium detectors to supplant liquid nitrogen cooling. The HELGA II prototype uses a mechanically cooled germanium crystal for gamma-ray detection. The cooling is accomplished by a Sterling engine that is available commercially. The prototype was built by Canberra Industries. The HELGA II prototype is housed in a footlocker-sized enclosure that isolates it from water and mechanical shock. The prototype is designed to be as close to a commercial product as possible, therefore its peak analysis and identification software is the standard Canberra Industries product. However, like all commercial software, this software produces complex data suitable for analysis by scientists. What is needed is software that produces only the essential information required for Naval operations and implementation by Coast Guard personnel.

NRL Implementation: NRL added custom software that works in concert with the Canberra software to take the scientist out of the decision-making loop in the field. This algorithm takes into account the complexities of past data collected at sea by NRL, as well as the spectral characteristics of nuclear weapons materials and the implications of emerging threats such as clandestine radiation dispersal devices (RDD). Technical issues addressed include the nature of the target to be located and identified, the treatment of natural and anthropogenic backgrounds, shielding considerations, measurement ranges, and dwell times. The final output of the software is a simplified report of what threats, if any, were found. In its final form, HELGA II will be completely autonomous in performing the functions necessary to identify nuclear weapons materials and alert the appropriate personnel.

Possibilities: The HELGA II prototype will demonstrate deployment on a small boat, while paving the way for a large range of alternate deployment options: small and large boats, remotely controlled jet ski platforms, helicopters, and man-portable systems. Such flexible deployment scenarios allow a large range of surveillance options: small HELGA II craft such as boats and jet skis allow a wide zone of control around fleet assets; HELGA II craft of any size allow for covert surveillance of boats and ships; HELGA II buoys at choke points allow continuous surveillance of passing watercraft; man-portable systems allow detailed search and identification in ship boarding scenarios.

[Sponsored by ONR]

References
[1] http://www.anl.gov/Science_and_Technology/History/Anniversary_Frontiers/aetofdr.html, accessed 18 November 2004.
[2] L.A. Beach and G.W. Phillips, "Development of a Rugged HPGe Detector," *Nuc. Instr. Meth. Phys. Res.* **A242** 520-524 (1986).
[3] http://www.history.navy.mil/faqs/faq90-5c.htm, accessed 18 November 2004.

★

Microstructural Development in Friction Stir Welding

R.W. Fonda,[1] J.F. Bingert,[2] and K.J. Colligan[3]
[1]*Materials Science and Technology Division*
[2]*Los Alamos National Laboratory*
[3]*Concurrent Technologies Corporation*

Introduction: Friction stir welding (FSW) is a relatively new technique for joining metals. It uses a rotating tool to deform ("stir") the surrounding material together without any melting (Fig. 8). Although FSW was only developed in 1991,[1] it is already experiencing a rapid growth in applications because of its ability to consistently produce high quality welds with low distortion, even in materials considered "unweldable" by conventional techniques. In addition, the accompanying reductions in weld inspection and re-weld procedures can also provide significant cost benefits. However, despite this considerable interest in FSW, the microstructural evolutions occurring during FSW are still not well understood. Conventional studies typically examine only sections of the deposited weld, then use those observations to infer the processes that gave rise to those microstructural features. We have instead examined the microstructural evolution at its source—around the FSW tool. We have prepared a stop-action weld in Al-Li 2195 by interrupting the welding process and quenching the weld with cold water to "freeze in" the dynamic processes surrounding the tool and permit an analysis of the actual grain evolution and texture development occurring around of the FSW tool.

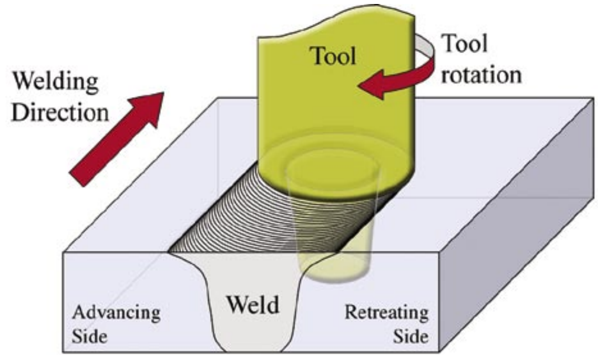

FIGURE 8
Schematic of the friction stir welding process.

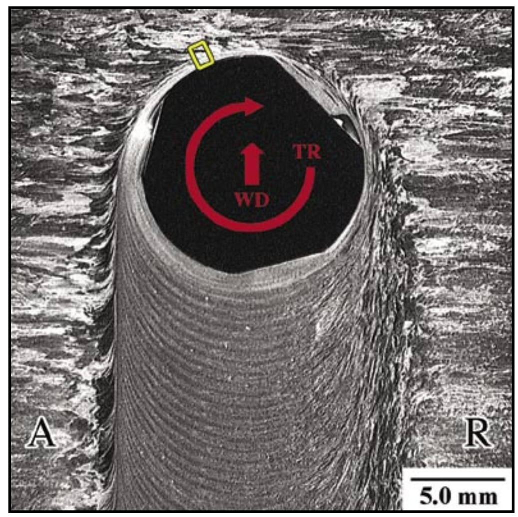

FIGURE 9
Optical micrograph of the friction stir weld with the embedded tool.

Deformation Structure: A cross section of the weld through the embedded tool (Fig. 9) reveals the severe deformation induced by the welding process. Because the tool is rotating while it moves through the material, the two sides of the weld exhibit different behaviors. On the advancing (left) side, there is a sharp boundary between the deformed grains and the deposited weld; on the retreating side, this boundary is obscured by the grains being sheared around into the wake of the tool. The material transport around the front of the tool also deforms the surrounding grains in the direction of the tool rotation. The grains on either side of the deposited weld exhibit a similar shear deformation.

The deposited weld is banded with a spacing equal to the tool advance per revolution. These bands are therefore likely due to an eccentricity in the welding process. On the other hand, the three flats on the threaded tool, which are used to enhance the material flow, do not produce any additional features in the deposited weld.

Grain and Texture Evolution: Ahead of the tool, the grains are preferentially oriented, with a distribution (crystallographic texture) typical of simple shear deformation. This texture becomes further refined as the material progresses around to the retreating side, where only a subset (the B components) of the initial shear texture is observed. In aluminum, these B texture components are produced by strong shear deformations at high temperatures, indicating that the material increases in temperature as it is swept around the tool. Behind the tool, the crystallographic texture parallels the banding observed in Fig. 9, alternating between only one and both of the B component variants.

A map of the crystal grain orientations ahead of the tool (Fig. 10(a)) reveals how the grain structure and texture develop within the deformation field surrounding the tool. The intense deformation and high temperatures adjacent to the tool produce the refined grains at the right of this figure. This grain-refined region becomes thicker toward the retreating side as more material accrues around the tool. Additional bands of refined grains appear farther from the tool, separated by regions (colored blue and pink), with a crystal orientation that is more resistant to the shear deformation. Analysis of the grain boundary misorientations across this figure demonstrate a continuous evolution of the lower angle boundaries to higher misorientations. Furthermore, higher resolution scans (Figure 10(b)) reveal a nearly constant "grain" size from the earliest stages of subgrain development (at left) to the fully refined grains. These observations indicate that the grain refinement process occurring during FSW is a continuous process. This process combines shear deformation with recovery of that deformation at the high temperatures achieved during welding, to produce subgrains with ever increasing misorientations as the strain and temperature are increased. The susceptibility of different initial grain orientations to the shear deformation produces the observed heterogeneity in this continuous grain refinement process. Thus, while dynamic recrystallization processes may contribute to the observed grain evolution, the primary mechanisms of grain refinement in this weld appear to be the concurrent processes of deformation and dynamic recovery.

Summary: This study has revealed, for the first time, the grain and texture development occurring around the tool in friction stir welding. We have shown how the shear deformation field and the thermal environment surrounding the tool contribute to the grain refinement process and texture development occurring ahead of the tool, and how those characteristics evolve as the material is swept around the tool.[2] Understanding the fundamental mechanisms of microstructural evolution involved in FSW will provide a foundation for further advances in weld property predictions and process development, expanding the use of this important technique into a growing number of potential Naval and commercial applications.

[Sponsored by ONR]

References

[1] W.M. Thomas, E.D. Nicholas, J.C. Needham, M.G. Murch, P. Templesmith, and C.J. Dawes, "Friction Stir Butt Welding," *Int. Patent App. PCT/GB92/02203* and *GB Patent App. 9125978.8*, Dec. 1991. U.S. Patent No. 5,460,317, Oct. 1995.

[2] R.W. Fonda, J.F. Bingert, and K.J. Colligan, "Development of Grain Structure During Friction Stir Welding," *Scripta Materialia* **51**, 243-248 (2004).

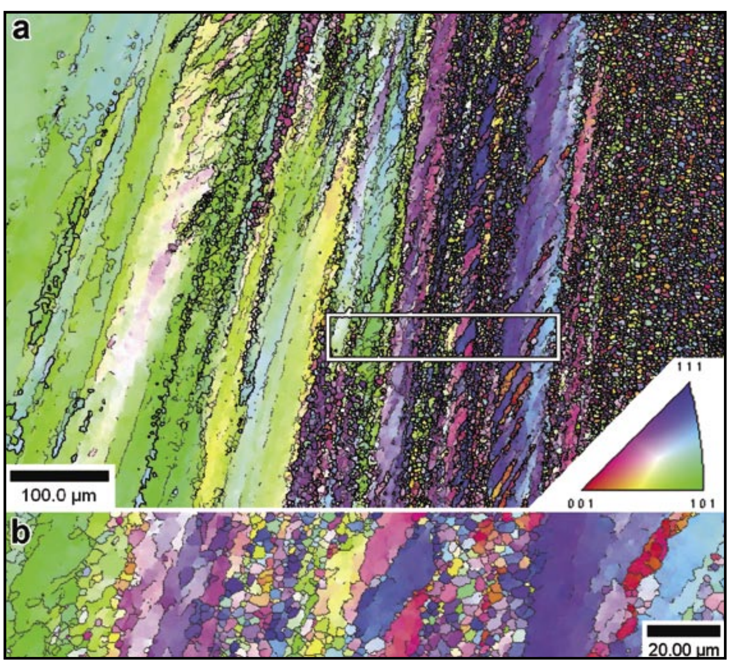

FIGURE 10
(a) Electron backscattered diffraction scan ahead of the tool (see Fig. 9) showing the grain and texture evolution. Colors indicate the crystallographic direction along the viewing direction (see inset). (b) High-resolution scan of the indicated region.

Electronics and Electromagnetics

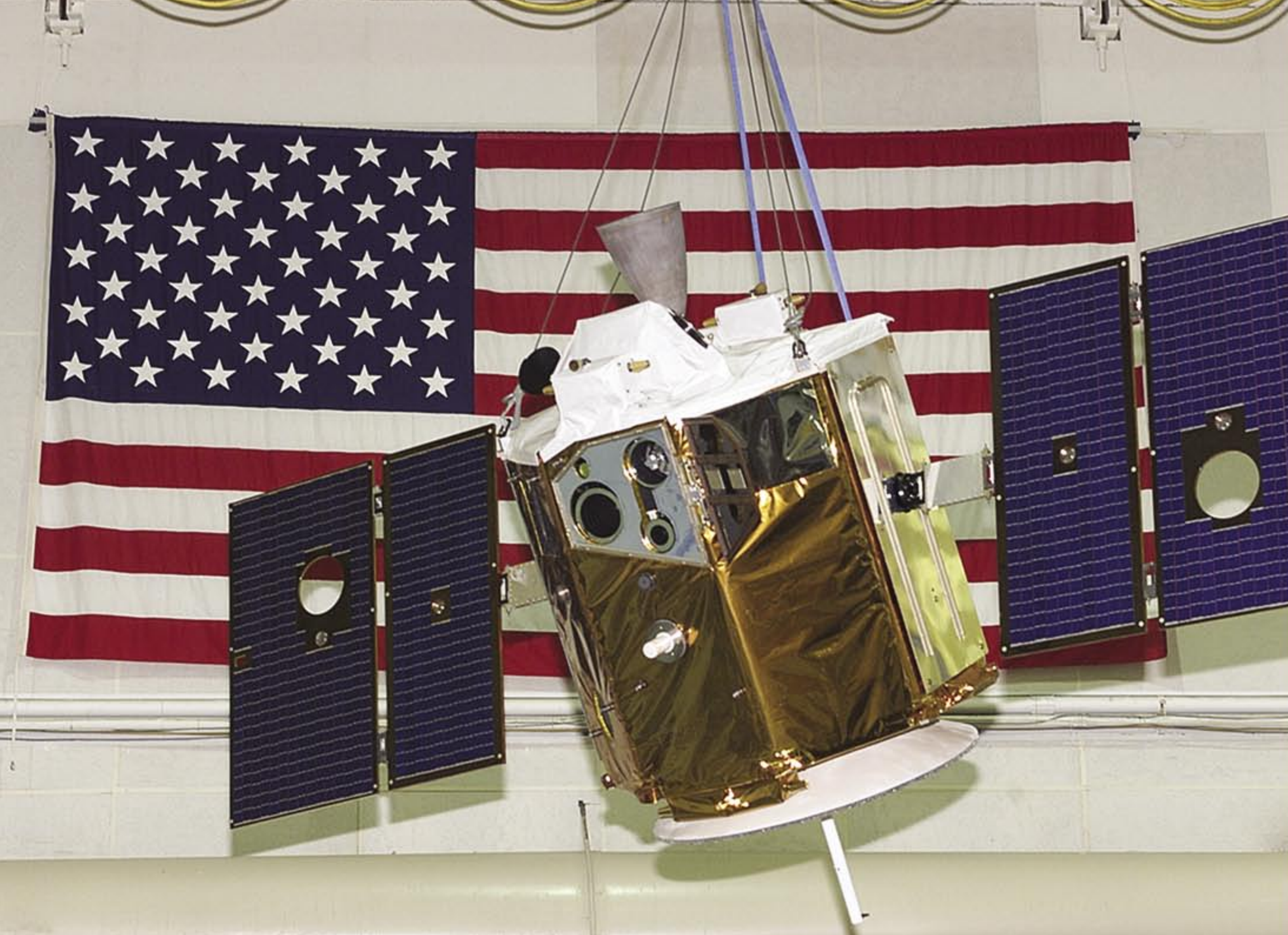

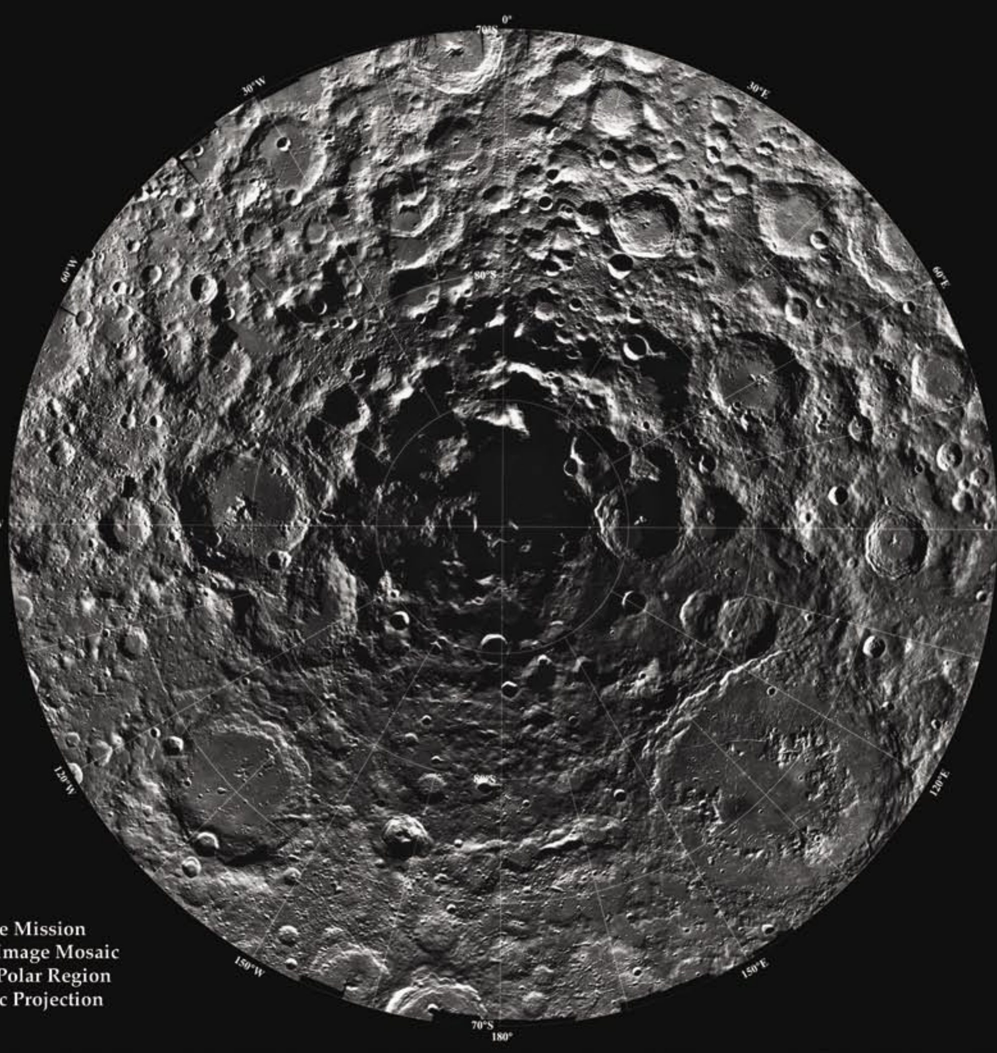

Clementine Mission
Uncontrolled Image Mosaic
Lunar South Polar Region
Orthographic Projection

Photo caption: Clementine was one of our most successful satellites. It tested a lot of technologies developed for the BMDO such as multispectral miniature cameras. It used the Moon as a target and in the process developed a multispectral map of the entire Moon. Shown is the lunar south pole where Clementine bistatic radar indicates water ice in the very cold valleys at the pole. The photo of the qualification model was taken during the ceremony at which NRL donated it to the National Air and Space Museum (NASM).

The Advanced Multifunction RF Concept (AMRFC) Test Bed

G.C. Tavik
Radar Division
I.D. Olin
SFA Inc.

Introduction: A glance at any Navy fighting ship underscores the goal of the technology being developed and demonstrated in this multidivision, multilaboratory program, sponsored and inspired by the Office of Naval Research. Today, single system antennas increasingly clutter our ships. Over just the ten-year 1980-1990 period, many ship classes that initially had fewer than 100 antennas needed nearly 150. Mutual signal interference, ship's signature, manning, spares, and life cycle costs all point to the need for a multifunctional concept in which systems are defined by their functions and by software that drives the electronics of a single antenna suite. In this program, hardware and software that emulate Emission Control, Normal, and Combat scenarios have been successfully combined in an active Proof of Principle demonstration at NRL's Chesapeake Bay Detachment (CBD).

System Flexibility Enables a Broad Spectrum of Functionality: The test bed operates over 6-18 GHz with functions broadly grouped: Communications, Electronic Warfare, Radar, and Calibration. Many functions within these groups have been selected for demonstration. Others that can be defined in terms of the apertures, hardware, and test bed software can be added later. Currently, Communications include line-of-sight using the Ku-band Tactical Common Data Link (TCDL) as well as satellite communications, both commercial Ku-band and a military link at X-band. Within Electronic Warfare, Electronic Attack (EA) provides noise and deceptive jamming. Electronic Surveillance (ES) fulfills High Probability of Intercept (HPOI) and Precision Direction Finding (PDF). A surface navigation function is demonstrated within the Radar function. Array and subsystem calibration, functional characterization, and diagnostics—all critical to dynamic maintenance of test bed operation—are part of the Calibration group. Other shipboard functions can now be added by using the hardware and software developed in this program.

The cornerstone for this work is the flexibility engendered by broadband dual-polarized phased array antennas that operate under the control of common system resource allocation manager (RAM) software. Together with a real-time control network, all the functions are defined. Figure 1 illustrates the receiver array partitioned (independently controlled parallel receive array channels, or ports, are shown separately

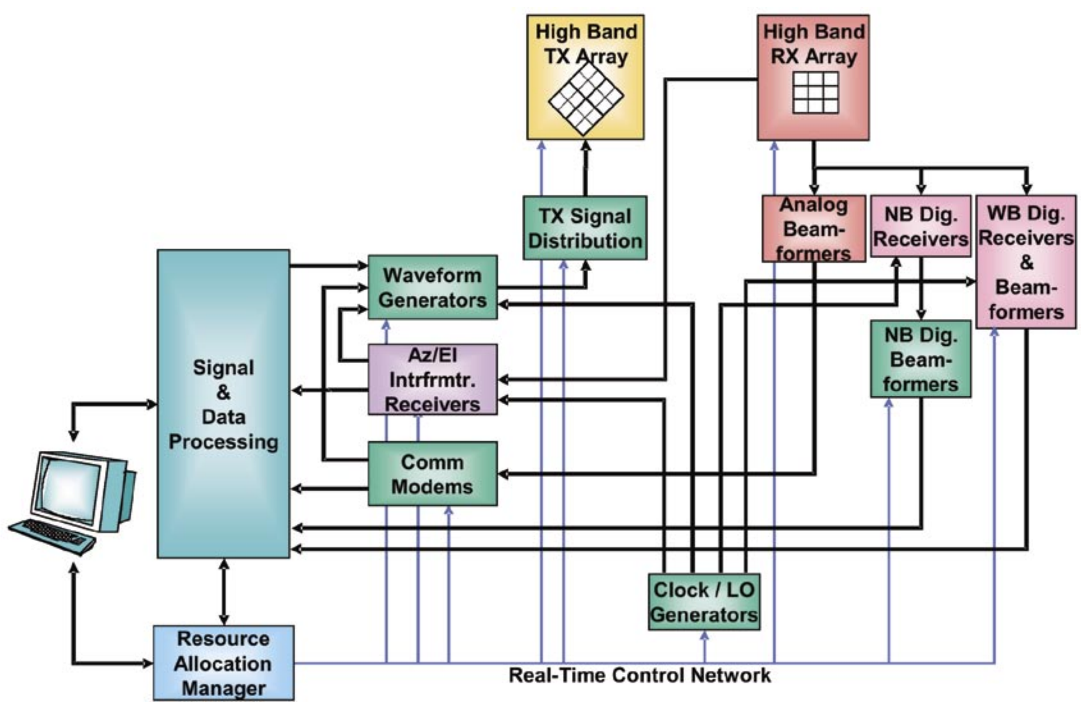

FIGURE 1
AMRFC receive array and transmit array, illustrating selectable partitioning to support RF functions. Difference in angle orientation reflect individual contractor's approach.

in the diagram) and grouped in several different ways; partitioning of the transmitter array into four quadrants is also shown. The receive array also includes a set of nine elements for an interferometer that supports the HPOI and PDF functions and two auxiliary elements for use in the EA function. Although the arrays operate in close proximity, the design of the installation provides greater than 100 dB isolation. This arrangement allows simultaneous use of both arrays, an important requirement for multifunction operation. It also suggests that offboard cooperative transmitters could be used to enhance ship stealth. Figure 2 is a high-level block diagram of the test bed. Receive array, receivers, and digital beamformers have been developed by Lockheed Martin, transmit array by Northrop Grumman, and analog beamformers by Raytheon. Other hardware and software (shown in green) were developed by employees of the Radar Division, Tactical Electronic Warfare Division, and Space Systems Department at NRL; Dahlgren Naval Surface Warfare Center; Patuxent River Naval Air Warfare Center; and Digital System Resources. All work leading to the design of these equipments was the result of an extensive review and critique process by an all-Navy team. Component specifications, such as transmitter modules and receiver components, were guided by the functional requirements selected for testing and others that may be needed in the future. A modular open-system software architecture was designed to accommodate new RF functionality, new hardware resources, and upgrading. This includes RF functional software, core operational software, and the test bed operating system.

AMRF Concept Successfully Demonstrated at CBD: Figure 3 is a view of the test site at CBD. The radomes and integrated antenna arrays are mounted on a 15-deg slope, emulating a shipboard deckhouse installation. Equipment packaging uses seven converted 20-ft shipping containers to protect equipment and to enable relocation to other sites or aboard ship. The CBD test site also provides an overwater test range with some receiver and transmit instrumentation located about 17 km across the bay at Tilghman Island.

Initial testing began in the summer of 2004. Functions in the Communication group demonstrated data links via two satellites, Telstar-11 and DSCS WLANT. Significantly, measured signals differed from predicted values by only 0.5 dB. It also included demonstration of Ku TCDL, including two simultaneous high-quality video feeds and full duplex voice communications, and tracking of air platforms to over 37 km and sea platforms to over 18 km. Detection ranges of the Radar function, operating over a 7-16 GHz band with a low-power single-pulse waveform, exceeded predictions. The Electronic Attack function, generated range gate pull off and multiple false targets countermeasures. It also successfully responded to four missile seekers and three targeting radars. Exercise of

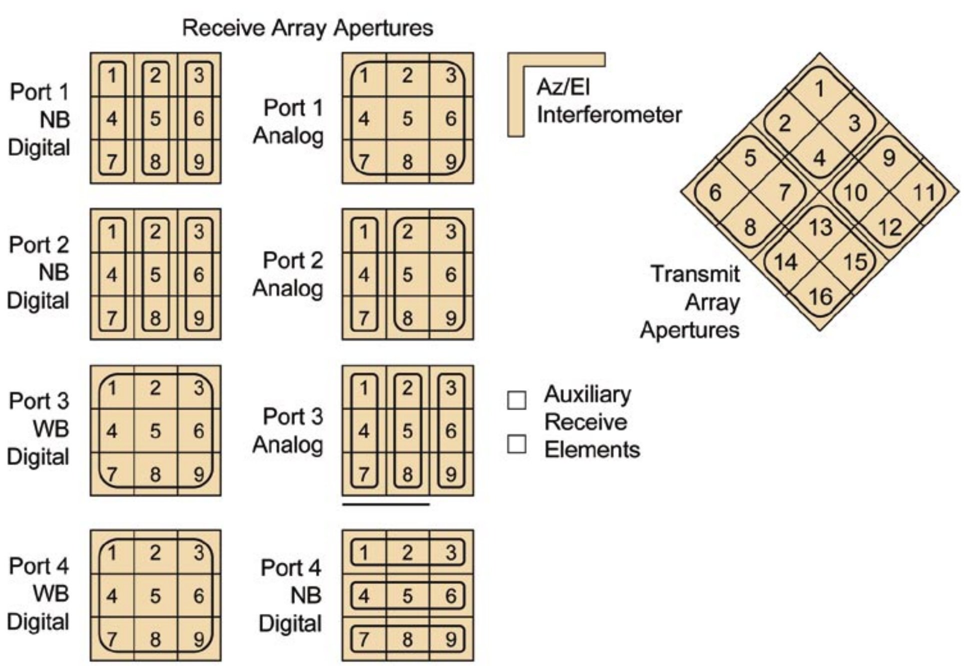

FIGURE 2
Test-bed functional block diagram of the major subsystems.

FIGURE 3
AMRFC test-bed at NRL's Chesapeake Bay Detachment Test facility.

the antenna polarization diversity, a part of this function, was also successful. The Electronic Surveillance function successfully demonstrated digital channelized receivers for each of the array embedded elements. Emitters of opportunity, including those aboard a P-3 aircraft, an NRL boat, and Tilghmann Island navigation radars, were successfully detected. The Calibration function is critical to the dynamic maintenance of the test bed operation. To date, it has provided initial function calibrations and implemented a transmit calibration mode.

The success of our contractor and Government team in fulfilling the goals of this program and in the various aspects of the design, hardware, software, and testing emphasize the recurring theme that the AMRFC test bed is dealing with various *functions*, rather than *systems*. The former implies flexibility; the latter reflects increasing proliferation of special above and below decks equipments.

[Sponsored by ONR] ★

Electronic Structure and Superconductivity in $Na_xCoO_2 \bullet yH_2O$

M.D. Johannes, I.I. Mazin, D.J. Singh, and D.A. Papaconstantopoulos
Materials Science and Technology Division

Introduction: The Navy has long had an interest in developing a superconducting homopolar motor for ship propulsion. A giant step toward practical implementation came with the discovery of high critical temperature, or high T_c, superconductors. These are compounds capable of carrying a resistanceless current at temperatures above that of liquid nitrogen. The performance of these motors depends sensitively on the ability to create and stabilize a large current density. Therefore, detailed understanding of the microstructure and underlying physics of superconducting materials is crucial to further technological development.

The experimental breakthrough of synthesizing high T_c compounds was accompanied by the realization that well-established theories explaining the microscopic origins of superconductivity could not adequately explain these new materials. The search for a coherent and complete description of unconventional superconductivity as a step toward development of even better devices and applications is therefore a primary concern of materials science theory.

Superconductivity is an intrinsically quantum mechanical phenomenon arising from pairing between electrons. Since each electron individually has its own quantum properties, the paired-state characteristics depend on the detailed properties of unpaired electrons in the normal (metallic) state. An instability of the Fermi surface(s) of this normal state causes condensation into a superconducting fluid of electron pairs. From an understanding of Fermi surface geometry, many properties of the superconducting state can be deduced.

$Na_xCoO_2 \bullet yH_2O$: The newly discovered[1] superconductor, $Na_xCoO_2 \bullet yH_2O$ (NCO) has a relatively low critical temperature (T_c = 4K), but it shares several important commonalities with traditional high T_c materials: it is a layered, transition metal compound (Fig. 4), its superconducting phase depends on electron doping, and a growing body of evidence indicates an unconventional pairing state. On the other hand, NCO is a Co-, rather than Cu-based compound, and the triangular arrangement of ions is different from the square plaquettes common to most high T_c structures.

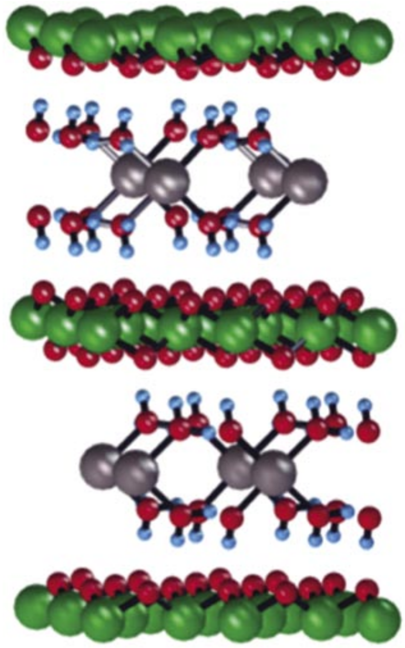

FIGURE 4
Crystal structure of Na_xCoO_2•yH_2O: green spheres denote Co, gray Na, red O, and blue H.

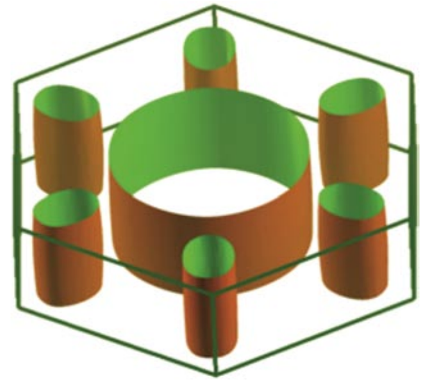

FIGURE 5
Calculated Fermi surface of Na_xCoO_2•yH_2O.

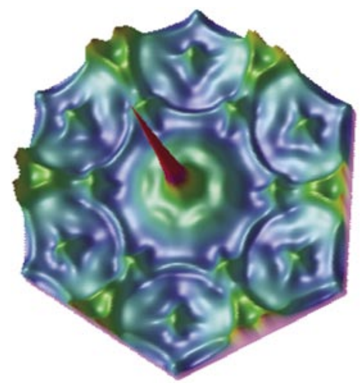

FIGURE 6
Calculated imaginary part of the magnetic susceptibility at low frequency as a function of the two-dimensional wave vector (in arbitrary units).

NCO therefore provides a unique opportunity to investigate how superconducting properties depend on the particularities of structure and chemistry.

Computational Approach: Density functional theory (DFT) methods, developed by W. Kohn (for which he later won a Nobel prize) with ONR support, provides a state-of-the-art description of the quantum ground state of condensed matter systems. For the research reported here, we used several computational implementations of DFT, developed both inside our group (the NRL tight-binding method) and outside. This allowed high-precision computation of the electronic structure, Fermi surface geometry, and magnetic properties, all fundamental to understanding superconductivity.

Symmetry and Superconductivity: Our calculations show that the hexagonal, quasi-two-dimensional structure of NCO is reflected in the symmetry of its Fermi surfaces (Fig. 5). The six smaller cylindrical surfaces, when translated by a particular vector, can be made to lie directly atop one another, or "nest." This nesting gives rise to spin fluctuations with the wavelength of the nesting vector. We calculated the real and imaginary parts of the low-frequency susceptibility (Fig. 6) and found strong peaks, indicating the positions of nesting-driven spin fluctuations in reciprocal space. Depending on the symmetry properties of the superconducting state, these spin fluctuations can either be constructive or destructive to the formation of electron pairs. Our analysis shows[2] that spin fluctuations in NCO are destructive to all previously considered superconducting states. A superconducting state is generally characterized by a wave vector-dependent order parameter and a particular spin pairing. To be compatible with the calculated nesting properties, the superconducting state of NCO would need to be both triplet, meaning that both electron spins are aligned, and have spatial s-wave symmetry, implying a uniform order parameter. Such a superconducting state has been discussed before in connection with liquid helium but it has never been observed experimentally. Most interestingly, this state violates the Pauli exclusion principle for the electron pairs since the multiplication of the even (triplet) spin part with the even (s-wave) spatial part produces an overall wavefunction that does not satisfy the necessary condition of having odd parity. The Pauli principle is, however, restored by introducing an odd parity in the frequency part of the order parameter. The proposed state, although extremely unusual, not only follows from our calculations but is also compatible with all currently reported experimental evidence.

Summary: Computational investigation of superconducting compounds provides insight into how experimentally tunable parameters, such as doping or pressure, affect the underlying mechanisms that give rise to superconductivity. Careful study of the electronic structure properties of NCO reveals the possibility of a truly unusual type of superconductivity, more unconventional yet than even the enigmatic high-temperature superconductors. A final understanding of unconventional superconductors could provide the basis for development of new, high critical temperature materials for which potential applications in both Naval and civilian technologies are nearly unlimited.

[Sponsored by ONR]

References

[1] K. Takada, H. Sakurai, E. Takayama-Muromachi, F. Izumi, R.A. Dilanian, and R. Sasaki, "Superconductivity in Two-dimensional CoO_2 Layers," *Nature* **422**, 53-55 (2003).

[2] M.D. Johannes, I.I. Mazin, D.J. Singh, and D.A. Papaconstantopoulos, "Nesting, Spin-fluctuations, and Odd-gap Superconductivity in $Na_xCoO_2 \cdot yH_2O$," *Phys. Rev. Lett.* **93**, 433-439 (2004).

★

6.2 Å InAsSb High Electron Mobility Transistors for High-Speed and Low Power Consumption

N.A. Papanicolaou, B.P. Tinkham, J.B. Boos, B.R. Bennett, R. Magno, D. Park, and R. Bass
Electronics Science and Technology Division

Introduction: An extensive effort has been made within both the military and commercial sectors to reduce the power consumed by millimeter- and microwave solid-state amplifiers. Low power consumption is essential in applications that require lightweight power supplies and long battery lifetimes. With the increased reliance on small platforms such as autonomous sensors, unmanned-air-vehicles, satellites and man-portable systems, the need for reduced operating power is becoming especially important to the DoD. NRL has long been recognized as a world leader in the material growth and fabrication of high electron mobility transistors (HEMTs) in the AlSb/InAs material system.[1] The HEMT, which is an advanced version of the common field-effect transistor, uses band-gap engineered layer designs with feature sizes on the atomic scale to precisely control the material properties within the structure. When compared to InP or GaAs-based HEMTs (Fig. 7), the high performance of the AlSb/InAs HEMTs arises from the superior electronic properties of this material structure grown by molecular beam epitaxy (MBE) with a lattice constant of 6.1 Å. When combined with nanoscale patterning using electron-beam lithography, these HEMTs constitute the state of the art in high-frequency performance at low operating voltage. Recently, the NRL AlSb/InAs HEMT material growth and fabrication technology was transitioned to Northrop-Grumman Space Technology through a Cooperative Research and Development Agreement (CRADA). This resulted in the demonstration of the first X-band and W-band monolithic microwave integrated circuits in this material system.[2,3]

In pursuit of electronic devices that can operate at even higher speed and lower bias voltage, the Electronics Science and Technology Division is developing HEMT technology using MBE-grown InAlSb/InAsSb layers with a lattice constant of 6.2 Å. In addition to a higher electron velocity in the channel, the incorporation of Sb in the channel layer also results in a more desirable band alignment, which acts to confine the holes to the channel. This reduces the gate leakage current, which is a problem with present AlSb/InAs HEMTs. Another positive feature is that InAlSb is stable in air, unlike pure AlSb, which is prone to oxidation. This stability simplifies the fabrication process and makes the devices more amenable to commercial manufacturing. InAsSb-channel HEMTs using novel, high-quality 6.2 Å MBE-grown material have been successfully fabricated for the first time and have exhibited state-of-the-art low voltage performance.

HEMT Design: The HEMTs use a uniform alloy of $InAs_{0.7}Sb_{0.3}$ as the channel layer and adjacent $In_{0.2}Al_{0.8}Sb$ barrier layers, all with a lattice constant of 6.2 Å. This heterostructure results in the formation of a high-mobility two-dimensional electron gas (2DEG) in the undoped InAsSb channel. Figure 8 shows a cross section of the layer design. This device structure is grown on semi-insulating GaAs substrates with an intermediate 1.5-μm thick AlSb buffer layer, which is necessary to relax the strain due to lattice mismatch. The center 50 Å of the top InAlSb barrier was doped n-type with Te to a level of approximately 10^{19} cm^{-3}

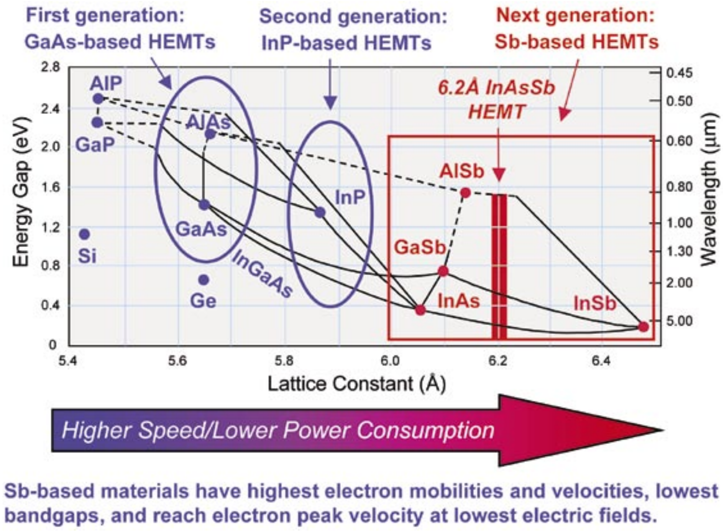

FIGURE 7
Energy gap vs lattice constant chart showing high-speed, low-power semiconductor trend in HEMT technologies.

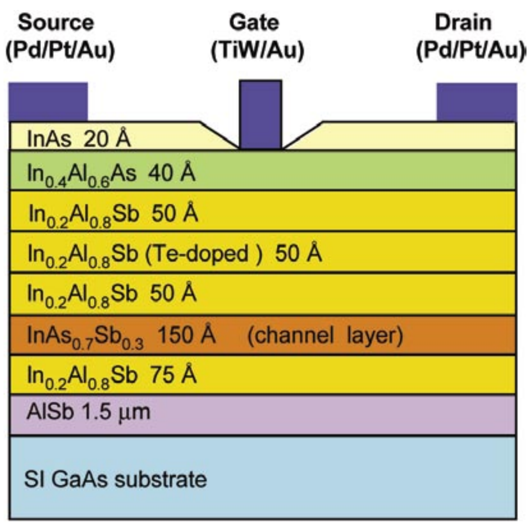

FIGURE 8
Cross section of the 6.2 Å InAlSb/InAsSb HEMT layer design.

to provide the donor carriers (electrons) for the 2DEG in the channel. This allows the electrons in the channel to travel faster in the 2DEG since they are not impeded by the ionized impurity scattering that would otherwise occur if the InAsSb channel were doped. The final layers consist of 40 Å $In_{0.4}Al_{0.6}As$ and a 20 Å InAs cap layer to facilitate low ohmic contact resistance. The $In_{0.4}Al_{0.6}As/In_{0.2}Al_{0.8}Sb$ composite design enhances the insulating property of the barrier and enables the use of a gate recess etch into the upper barrier material prior to gate metal definition. The sheet carrier density and mobility of the starting material were 1.8×10^{12} cm^{-2} and 18,000 cm^2/V-s, respectively. For mixed-anion MBE growth, the anion incorporation into the channel layer is not a linear function of group V flux and relies on several different growth variables such as temperature and growth rate. We arrived at 420 °C for the growth temperature of our channel layer by growing a series of samples and comparing mobility as a function of growth temperature.

DC and Microwave Characterization: The HEMTs were fabricated using alloyed Pd/Pt/Au source-drain ohmic contacts and a TiW/Au gate metalization that was defined using advanced electron-beam lithography. Figure 9 shows a typical set of drain characteristics for HEMTs with a 0.2 μm gate length and a 1 μm source-drain spacing. The drain current I_{DS} is plotted vs the drain voltage V_{DS} with the gate voltage V_{GS} as an additional parameter that controls

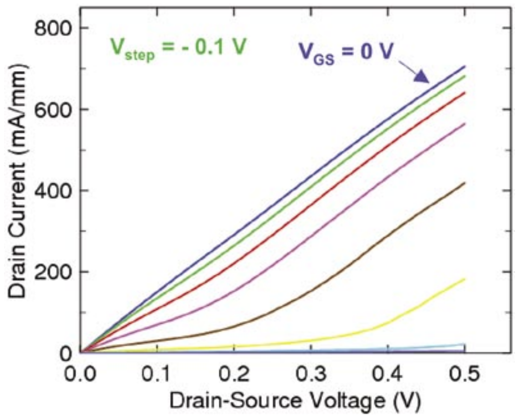

FIGURE 9
Drain characteristics for a HEMT device with L_G = 0.2 µm, L_{DS} = 1.0 µm, W_G = 27 µm, V_{GS} = 0.1 V/step.

the drain current. The gate pinchoff voltage is –0.5 V. At a drain voltage of only 300 mV, a transconductance ($g_m = \Delta I_{DS}/\Delta V_{GS}$) above 800 mS/mm is observed from V_{GS} = –0.25 to –0.5 V, with a maximum value of 1.3 S/mm occurring at V_{GS} = –0.35 V. The transconductance at this drain voltage is the highest observed for any HEMT reported in the literature. The microwave S-parameters of the HEMTs were measured on-wafer from 1 to 40 GHz and yielded a unity power gain cutoff frequency of 80 GHz at a drain voltage of 0.6 V. The extremely high frequency capability and low consumed power of these devices makes them a leading candidate technology for the next generation of high-speed, low-power electronics.

[Sponsored by ONR and DARPA]

References

[1] J.B. Boos, W. Kruppa, B.R. Bennett, D. Park, S.W. Kirchoefer, R. Bass, and H.B. Dietrich, "AlSb/InAs HEMT's for Low-Voltage, High-Speed Applications," *IEEE Trans. Electron Dev.* **45**, 1869 (1998).

[2] B.R. Bennett, B.P. Tinkham, J.B. Boos, M.D Lange, and R. Tsai, "Materials Growth for a Manufacturable InAs High Electron Mobility Transistor Technology," *J. Vac. Sci. Technol. B* **22**(2), 688-694 (2004).

[3] W.R. Deal, R. Tsai, M. Lange, J.B. Boos, B. Bennett, and A. Gutierrez, "A W-Band InAs/AlSb Low Noise/Low Power Amplifier," *IEEE Micro. Wireless Comp. Lett.* (2005).

★

New Dimensions in Radiation Effects

B.D. Weaver
Electronics Science and Technology Division

Introduction: For satellites to be useful in space applications, they must survive the harsh radiation environment of Earth's van Allen belts. Onboard components are continuously bombarded by high-energy protons, electrons, ions, and cosmic rays, which degrade device performance and ultimately cause system failures. Thus in maximizing a satellite's operating lifetime, it is important to know how various devices will respond to radiation damage, and to incorporate radiation-tolerant components into the design.

Radiation Effects: When high-energy particles strike a device, they create structural defects that can alter device performance. The effect of defects on performance depends largely on the physics of device operation. Consider, for example, the case of conventional electronic devices—devices for which the physical dimensions are sufficiently larger than the carrier mean free path that carrier transport occurs by diffusion. Enough is known about how conventional electronic devices respond to induced disorder that their radiation tolerance can often be predicted by referring to existing data. Minority carrier devices, for instance, are generally quite sensitive to radiation damage because induced defects can trap charge carriers, serve as centers for recombination, and thereby affect the carrier concentration. In contrast, radiation-induced defects in majority carrier devices act mainly to scatter carriers in three dimensions (3D), and so have little effect on performance because transport is already diffusive and 3D. As a result, majority carrier devices are generally much less sensitive to radiation damage than minority carrier devices. If carrier transport is not conventional—for example, if electrons move ballistically or if transport occurs in fewer dimensions than three—then existing databases of radiation effects are not likely to exist. In this case, radiation tolerance must be determined directly by experimentation.

Reduced dimension has a particularly striking effect on radiation tolerance. Perhaps the best example is that of low- and high-temperature superconductors (LTSs and HTSs). In an isotropic LTS, paired carriers scatter elastically from radiation-induced defects but do not depair because all directions are effectively the same. In HTSs, paired carriers exist only in two-dimensional (2D) Cu-O planes. When they scatter from radiation-induced defects, the probability is high that they will be ejected from their planes and thus cease to contribute to the superconducting state. As a result, HTSs are about three orders of magnitude more sensitive to radiation damage than isotropic LTSs. In high electron mobility transistors (HEMTs), in which carriers move from source to drain via a 2D electron gas (2DEG), the dominant radiation effect arises from high-efficiency scattering of carriers out of the 2DEG. Similarly, in resonant tunneling diodes, the main radiation effect arises from high-efficiency scattering out of 2D quantum wells. As evidenced by the fact that a single defect in a carbon nanotube can mean the difference between a metallic and a semiconducting state, quasi-1D devices show evidence of being even more sensitive to disorder than 2D devices. Given the current emphasis on miniaturization and the trend of increasing disorder-sensitivity with decreasing dimensionality, the suitability of future devices for space application has been doubtful.

Until now.

Cellular Devices: Recent radiation damage experiments on conventional (3D) photodiodes, 2D multiquantum well (QW) photodiodes, and quasi-0D quantum dot (QD) photodiodes have shown, surprisingly, that QW devices can be 10-30 times more radiation-tolerant than bulk devices, and QD devices, can be 300-1000 times more tolerant. In these devices radiation tolerance actually increases as dimensionality is reduced. The reason, NRL researchers believe, is that QD (and to a lesser extent, QW) devices are composed of a large number of individual subdevices that act in concert to produce the overall response, much in the same way that cells in the as human pancreas collectively produce insulin. In this sense, each quantum dot can be likened to a *cell* and the congregation of cells can be called a *cellular device*.

Because charge carriers in QD cellular devices are confined to nearly 0D they cannot migrate to and interact with remote defects. As a result, the radiation-sensitivity of QD devices does not depend on the minority/majority carrier status or on the presence or absence of diffusive transport. Instead, it depends on whether a given cell has been hit by an incident particle, and if so, how much damage the particle has done. That is, in conventional and most nonconventional devices, performance is affected when mobile carriers encounter and interact with defects, but in cellular devices *the defects must come to the carriers*. This change in paradigm is thought to be the cause of the high radiation tolerance of QD devices.

To further understand this phenomenon, NRL scientists have altered a formalism from the 1940s for describing the survivability of irradiated living tissue into a theory of radiation effects for cellular devices in general. The new "cell theory" combines methods from probability and statistics to determine the fraction of damaged cells as a function of particle fluence, and uses displacement damage theory to describe the function of an impaired cell. The overall device response turns out to be a function of the particle fluence, the cross-sectional area presented by an average cell to an incident particle, and the effectiveness with which an average impact destroys a single cell's function. Remarkably, cell theory predicts that if all other parameters remain the same, decreasing the cell size always leads to an improvement in radiation tolerance.

This discovery could feasibly revolutionize the way radiation-resistent components are designed.

[Sponsored by ONR] ★

Near-Imaging Field Tower Implementation (NIFTI)

D.L. King
Space Systems Development Department

Introduction: The Naval Research Laboratory's Midway Research Center (MRC) located in Stafford, Virginia, has a mission to provide highly precise and repeatable signals for tailored, precision calibration and testing of national and tactical systems. Their numerous assets include three 60-ft diameter antennas, which are required to provide highly accurate RF signals. Because of their size and location, they are difficult to characterize through farfield measurements, which is as much as 25 miles away, nor is it possible through close-in nearfield measurements. A midrange calibration system has been designed and is being implemented that transforms these nearfield measurements into a farfield pattern. This provides corrected effective isotropic radiated power (EIRP), tilt angle, axial ratio, boresight, and gain, which can then be applied to the command and control system for the antennas. The Near Imaging Field Tower Implementation (NIFTI) system has proven itself during prototype tests to accurately derive farfield parameters from nearfield measurements.

Overview: The system was developed and tested using the Antenna Tracking Subsystem (ATS)-3 antenna. This antenna scans across a reflector that is mounted to an azimuth-over-elevation positioner at the Calibration Tower (Cal Tower), which is 884.5684 ft. away (Fig. 10). Nearfield amplitude and phase data are collected as the ATS-3 antenna generates a continuous wave (CW) tone and scans across the Cal Tower antenna in a series of eight cuts, each cut is 22.5 deg apart. Before this occurs though, the Bullseye (the point the NIFTI scan is centered on) is determined, which allows for amplitude and phase correction

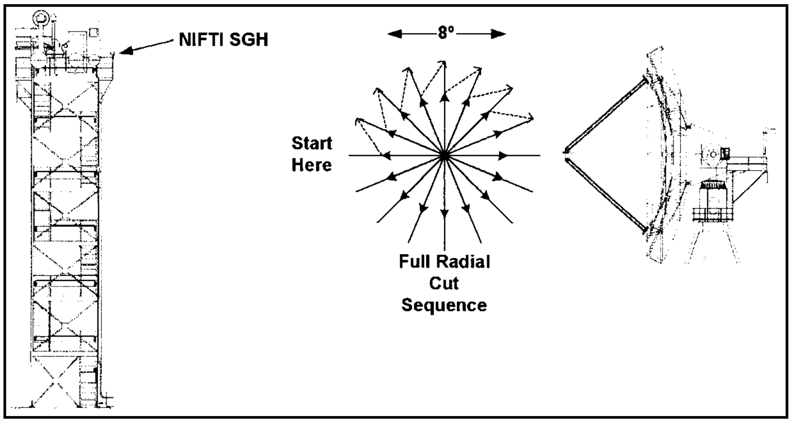

FIGURE 10
System diagram.

between each of the cuts. These data are then transformed to a farfield pattern using a Fourier transform (FT) technique (Fig. 11).

After postprocessing the nearfield data, the following information is stored and available for the user:

- Frequency—frequency that was entered by the operator
- Bias—site gain minus the calculated gain
- Feed input power—input power at the feed in dBm
- Axial ratio—calculated axial ratio in dB
- Polarization tilt—tilt in degrees from the horizontal
- Azimuth at peak gain—azimuth at peak gain
- Elevation at peak gain—elevation at peak gain
- Peak gain—peak gain in dB
- Peak EIRP—EIRP in dBm
- Average beam width—average beamwidth in deg
- Azimuth Nearfield Bullseye—azimuth in nearfield data
- Elevation Nearfield Bullseye—elevation in nearfield data
- Azimuth mispointing error—antenna azimuth pointing error
- Elevation mispointing error—antenna elevation pointing error
- Specified polarization—polarization entered by the operator
- Sensed polarization—polarization predicted by the antenna farfield calculator (afc)

This information is then used by the site to update the information contained in the Command and Control system to more accurately report the EIRP being transmitted out of the ATS. This information is then passed on to the client for use in their analysis.

Antenna Locations: By using the FT method, up to 0.5 deg of mis-centering can be tolerated with less than 0.1 dB of error.[2] To determine the locations of the antennas, NRL's Astrodynamics and Space Applications Office (Code 8103) surveyed control points and MRC assets by geodetic differential GPS survey methods.[3]

Capabilities: Through testing,[2] we have shown that we can detect boresight position to an accuracy of better than one-tenth of the 3 dB beamwidth at 18 GHz, or close to 0.005 deg. The overall RMS error for the system was calculated to range from 0.5 to 0.7 dB from 2.7 to 18 GHz, respectively. The power sensor calibration, phase errors, and sampling/truncation errors are the major contributors to this error. The RMS errors for all frequencies in feed power, gain, and EIRP are 0.76, 0.23, and 0.80 dB, respectively.

A separate calibration process occurs to calibrate the relative phase and amplitude to the network analyzer. This is needed to accurately determine the polarization axial ratio, tilt, and circular polarization of the 60-ft antennas. The calibration is done by mounting standard gain horns at 45-deg angles approximately 60 ft from the base of the Cal Tower to provide equal power to both horn ports.

System: The antenna used to collect the signals radiated from the ATS is a General Instruments (GI) A6100 2-18 GHz dual-polarized, calibrated, gravity-referenced, circularly symmetric quad-ridged horn that is mounted on the northwest corner railing of the Cal Tower platform (Fig. 12). The horn gain and losses through the coupler were determined in the anechoic chamber and referenced to a standard gain horn (SGH). The antenna is mounted on top of an EDCS

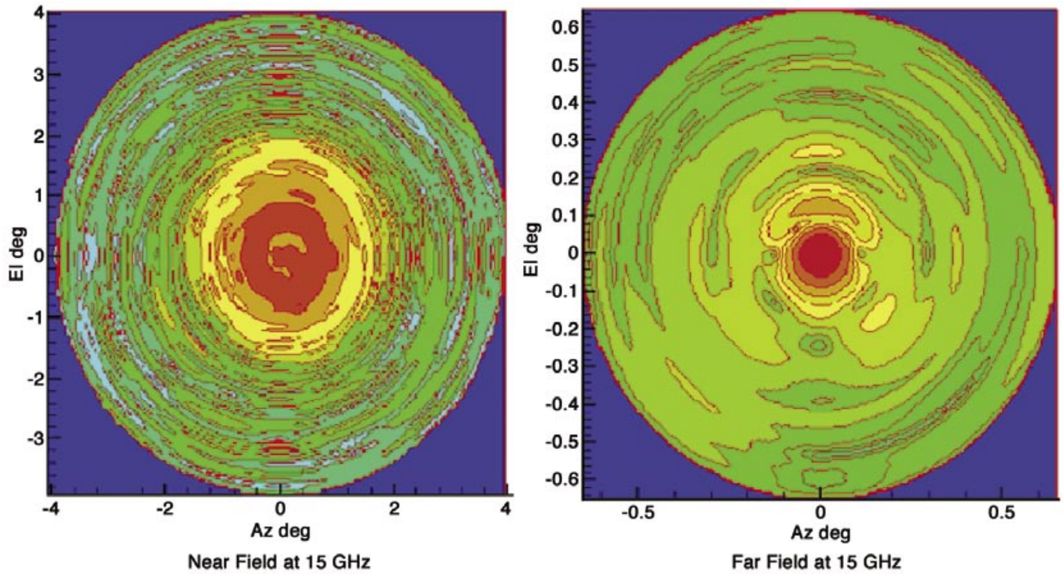

FIGURE 11
Nearfield and farfield contour plots.

FIGURE 12
NIFTI horn assembly.

3404a antenna control unit. Numerous pieces of test and measurement equipment were also installed in the Cal Tower as part of the NIFTI system. These include: National Instruments PXI-1045 chassis, National Instruments GPIB-ENET/100, Agilent E4419B power meter, Agilent 8341B sweep synthesizer, Agilent 8511A frequency converter, Agilent 8530A IF/detector (microwave receiver), Agilent 85395C display/processor, Datum fiber optic receiver, and Digital pulse generator.

Conclusion: NIFTI is an effective technique to calibrate EIRP, farfield directivity and beamwidth, polarization, and pointing information; it is also effective in determining azimuth/elevation encoder timing accuracies (necessary for accurate tracking), uncovering amplifier instabilities, and determining feed misalignments. Amplifier instabilities are also easily "seen" as spikes in the amplitude and phase of the nearfield data; the data collection system is also setup to do stability checks at the center of the nearfield pattern. Finally, beam mispointings in the farfield for focused feeds are indicative of feed misalignments, which can be accurately characterized with the use of either the farfield data or the nearfield phase asymmetry characteristics.

[Sponsored by SPAWAR]

References

[1] W. Lippincott, T. Gutwein, M. Smythers, and P. Souza, "Near-Field Calibration for Large Reflectors," *Proceedings 2002 Antenna Measurement Techniques Association Symposium*, Cleveland, Ohio, November 2002, pp. 401-406.

[2] W. Lippincott, T. Gutwein, M. Lundmark, and R. Eisenger, "Near-Field Remote Calibration Systems for MRC 60-ft Reflectors," internal NRL Code 8103 report, October 2004.

[3] J. Middour and A. Hope, "Report of the 2003/2004 Survey of Control Points and Assets at the Midway Research Center," internal NRL Code 8103 report, August 2004.

★

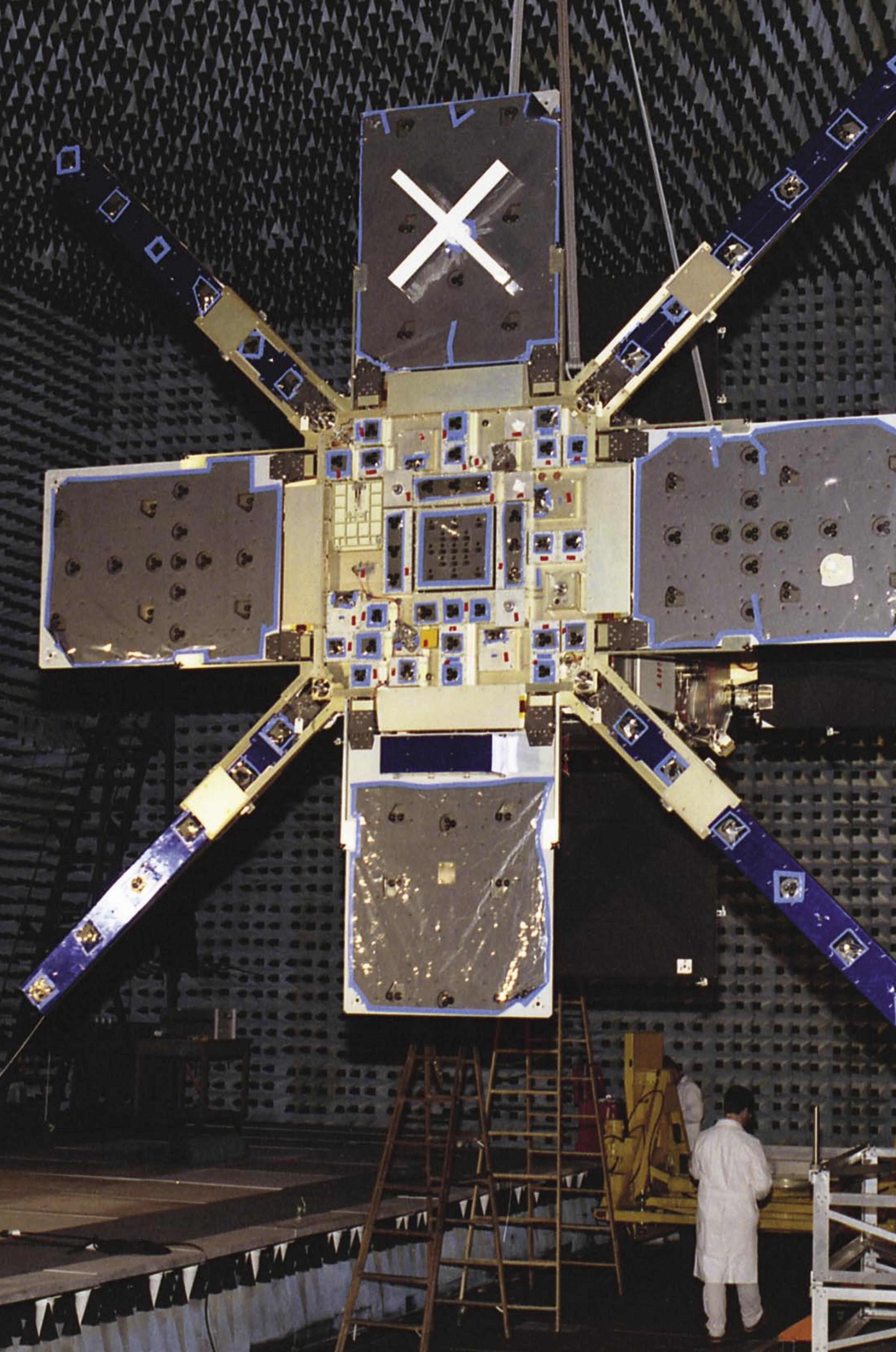

Energetic Particles, Plasmas, and Beams

Photo caption: Low power Atmospheric Compensation Experiment (LACE) is shown in an anechoic chamber with a good view of the laser detector "scoreboard." During a successful test from Hawaii, almost all of the laser energy was focused on the small 1 square foot area at the center.

Big Light: Optical Coherence over Very Large Areas in Photonic-Crystal Distributed-Feedback Lasers

W.W. Bewley, I. Vurgaftman, C.S. Kim, J.R. Lindle, M. Kim, C.L. Canedy, and J.R. Meyer
Optical Sciences Division

Introduction: High-power midwave-infrared (mid-IR) semiconductor lasers, emitting in the λ = 3 – 5 μm wavelength range, are needed to jam heat-seeking-missile threats to U.S. planes and ships. Because of their potential for compactness and low-cost, they are viewed as ideal long-term sources for infrared countermeasure (IRCM) systems. The most straightforward way to scale up the output power is to widen the stripe of gain material that is lasing. However, this strategy is usually ineffective because optical coherence is generally lost once the stripewidth exceeds a few wavelengths. The beam then tends to break into multiple modes, or filaments, that lase independently of one another, rather than maintaining optical coherence over the entire gain region. The result is a rapidly diverging output beam that becomes much too diffuse to be useful when it reaches a missile nosecone several kilometers away.

Device Concept: NRL has recently developed a new class of semiconductor lasers that maintain an exceptional degree of optical coherence over very large device areas. This is the photonic-crystal distributed-feedback (PCDFB) laser, shown schematically in Fig. 1 with an overlayed scanning electron micrograph (SEM) of one of the patterned devices. A two-dimensional (2D) rectangular grating is etched into the tilted gain stripe to diffract the lasing mode propagating along the directions $\boldsymbol{P}_1$, $-\boldsymbol{P}_1$, $\boldsymbol{P}_2$, and $-\boldsymbol{P}_2$. For example, the grating reflects light that was originally propagating along $\boldsymbol{P}_1$ into the opposite direction $-\boldsymbol{P}_1$, and also simultaneously diffracts it by angles of $\pi - 2\theta$ and 2θ into the directions $\boldsymbol{P}_2$ and $-\boldsymbol{P}_2$. The first process is analogous to the distributed feedback mechanism (DFB) that induces strong spectral selectivity in conventional 1D DFB lasers. The other two processes diffractively couple regions of the gain medium that are widely separated spatially. The net result is that optical coherence is imposed over the entire gain stripe, which can now be very wide, whereas the diffractive propagation strongly suppresses the usual tendency of the mode to collapse into narrow filaments. This is accomplished with a modest penalty in the device's quantum efficiency (roughly a factor of two). Our numerical simulations project that for any given semiconductor material system, the PCDFB configuration should produce more power in a spectrally pure single mode than any other configuration.[1] The PCDFB geometry is applicable to semiconductor lasers emitting at wavelengths extending from the ultraviolet to the Terahertz regime.

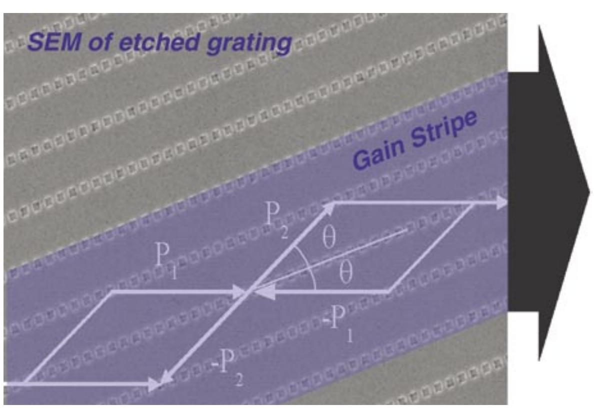

FIGURE 1
Schematic of the major propagation directions and the alignment with the facets for a rectangular-lattice PCDFB laser, overlaid with a scanning electron micrograph of the etched 2D grating.

Practical Realization of the Edge-Emitting PCDFB Laser: Our first experimental demonstrations of the PCDFB laser concept have used optically pumped antimonide type-II "W" quantum well active regions that emit in the mid-IR.[2] For the device shown in Fig. 1, a second-order grating with θ = 16° was defined in a top GaSb layer by electron-beam lithography and reactive ion etching. By tuning the operating temperature of the laser, the peak of its gain spectrum was brought into resonance with the grating wavelength of $\lambda \approx$ 3.7 μm. The solid blue curve of Fig. 2 illustrates the far-field profile measured for this PCDFB laser when a 350-μm-wide stripe was pumped in pulsed mode at 10 times the lasing threshold.[3] Note that even though the stripewidth exceeds the wavelength by two orders of magnitude, the profile has a single lobe with an extremely narrow angular divergence of 0.8° full-width at half-maximum (FWHM). Since this corresponds to just over 3 times the theoretical minimum, the diffraction limit, it demonstrates that a high degree of optical coherence is maintained across the wide stripe. At a stripewidth of 150 μm, the output was basically diffraction-limited, and even for a 600-μm stripe the profile retained a single lobe with only slightly greater divergence (1.2° FWHM). By contrast, the dashed red curve shows the analogous result for a typical unpatterned Fabry-Perot laser fab-

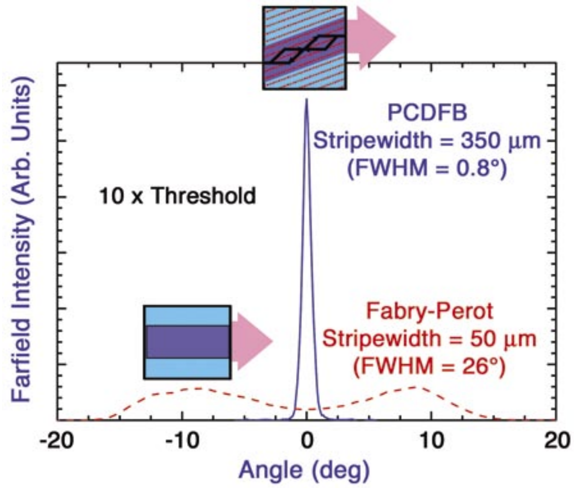

FIGURE 2
Far-field profiles for a mid-IR PCDFB laser with stripewidth 350 μm (solid blue) and a typical Fabry-Perot laser with stripewidth 50 μm (dashed red). Both were optically pumped at 10 times the lasing threshold.

ricated from similar material with a pump stripewidth of only 50 μm. In that case, the total divergence angle of the double-lobed far-field profile is 26°. Without the PCDFB grating, the beam quality is quite poor because optical coherence is lost when no mechanism exists for coupling the widely separated lateral regions of the stripe. These PCDFB results are far superior to any reported previously for such wide stripes in the mid-IR, making this approach quite promising for IRCM applications.

Surface-Emitting PCDFB Lasers: In the "edge-emitting" geometry discussed above, the output is extracted from a cleaved facet whose reflectance also helps to define the cavity. Since the output aperture is much wider laterally than along the growth direction (into the page of Fig. 1), most edge-emitting semiconductor lasers produce a highly elliptical beam that requires further shaping before it is useful. However, we have designed and fabricated a surface-emitting (SE) version[4] of the PCDFB laser, whose fundamental mode yields a circularly symmetric output. Figure 3 illustrates schematically that a hexagonal 2D grating again imposes optical coherence over a broad lateral area via diffraction of the in-plane lasing mode. In this case, there are no facets and the output is emitted normal to the wafer surface by an additional diffraction process, indicated by the red arrow. Mid-IR SE PCDFB lasers with optically pumped type-II "W" active regions were recently fabricated and tested in the laboratory. The near-field IR camera picture shown as the inset in Fig. 3 indicates a beam profile with nearly circular symmetry. Beam divergences as small as ≈ 6 times the diffraction limit have been observed for a pump-spot diameter of 800 μm. This provides further evidence for strong optical coherence over extremely large areas.

[Sponsored by ONR]

References

[1] I. Vurgaftman and J.R. Meyer, "Photonic-Crystal Distributed-Feedback Quantum Cascade Lasers," *IEEE J. Quantum Electron.* **38**, 592-602 (2002).

[2] J.R. Meyer, C.A. Hoffman, F.J. Bartoli, and L.R. Ram-Mohan, "Type-II Quantum-Well Lasers for the Mid-Wavelength Infrared," *Appl. Phys. Lett.* **67**, 757-759 (1995).

[3] C.S. Kim, W.W. Bewley, C.L. Canedy, I. Vurgaftman, M. Kim, and J.R. Meyer, *IEEE Phot. Tech. Lett.* **16**, 1250-1252 (2004).

[4] I. Vurgaftman and J.R. Meyer, "Design Optimization for High-Brightness Surface-Emitting Photonic-Crystal Distributed-Feedback Lasers," *IEEE J. Quantum Electron.* **39**, 689-700 (2002).

★

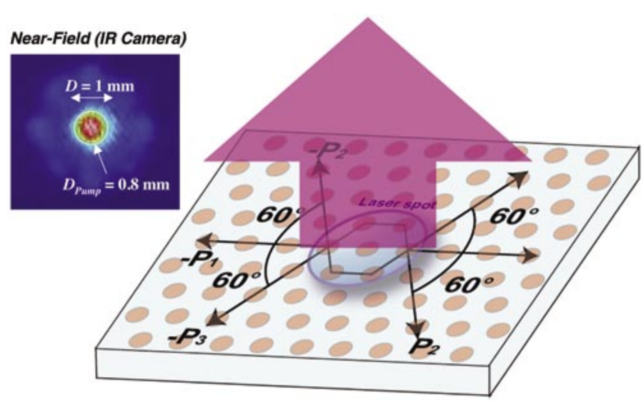

FIGURE 3
Hexagonal-lattice surface-emitting PCDFB laser, showing major propagation directions. The experimental near-field profile (taken with an IR camera) shown as the inset indicates the near-circular symmetry of the output beam.

Recent Breakthroughs in VHF Interferometry

A.S. Cohen,[1] W.M. Lane,[1] N.E. Kassim,[1] T.J.W. Lazio,[1] R.A. Perley,[2] W.D. Cotton,[2] J.J. Condon,[2] and W.C. Erickson[3]
[1]*Remote Sensing Division*
[2]*National Radio Astronomy Observatory*
[3]*University of Tasmania*

Introduction: The NRL-National Radio Astronomy Observatory 74 MHz (4-m wavelength) receiver system on the Very Large Array (VLA) telescope (an array of 27 25-m radio antennas located in Socorro, New Mexico) has, for the first time, demonstrated the capacity for both high sensitivity and high angular resolution observations in the VHF band. A number of instrumental, algorithmic, and computational advances have allowed us to compensate for the ionospheric phase corruptions that have made high-resolution imaging a challenge at such a long wavelength until now. This project has turned the VLA, previously a centimeter-wavelength instrument, into the world's most capable meter-wavelength instrument, in which we regularly achieve resolutions as small as 150 microradians. This capability has enabled us to embark on many scientific projects. It has also spawned plans for building even more capable long-wavelength instruments such as the Long Wavelength Array (LWA), which an NRL-led collaboration is now developing. In this article, we describe two of the many projects now ongoing: the VLA Low Frequency Sky Survey, and probing even higher resolutions by extending the 74 MHz receivers to the nearby Pie Town (New Mexico) station.

The VLA Low Frequency Sky Survey (VLSS): The VLSS is a 74 MHz survey of the entire sky visible from the VLA (3/4 of the total sky). It will reach an average sensitivity level of 0.1 Jy/beam (1 Jy = 10^{-26} W Hz^{-1} m^{-2}), and a resolution of 400 microradians. Ionospheric phase distortions are corrected using a grid of celestial sources to provide multiple simultaneous pierce points through the ionosphere and determine ΔTEC corrections at the level of 10 milliTEC units. Once a region is imaged, we use an automated source-finding algorithm to catalog all sources detected with at least 5-sigma certainty. We are releasing all data to the public as soon as it has been reduced and verified. These data are available on our project website (http://lwa.nrl.navy.mil/VLSS) in the form of a searchable source catalog and a postage stamp image server. Our first major data release occurred on June 15, 2004; it consisted of approximately half of the visible sky. We plan to observe most of the remaining area in early 2005 and release the data online later that year. This resource, available to the entire scientific community, expands the growing virtual online observatory to this previously unavailable wavelength.

Figure 4 shows the current survey area and plots all 32,000 detected sources. Figure 5 shows images of a representative sample of sources that are large enough to be resolved at this resolution.

Several scientific goals can be addressed with these data. A primary goal is the detection of high redshift (very distant) radio galaxies, which this survey is ideally suited for. These radio galaxies are relatively more luminous at long wavelengths than nearby galaxies. We will also use these data to search for diffuse emission in clusters of galaxies (cluster halos and relics) that results from cluster collisions and mergers, and can help our understanding of structure formation in the early universe. It may also be possible to find unusual classes of pulsars, such as those with submillisecond periods or those that reside in binary star systems. We will likely be able to map supernovae remnants and regions of neutral hydrogen gas throughout the galactic plane. Many known objects will be better understood with the knowledge of how their overall spectral index evolves at this long wavelength. Finally, this comprehensive data set will allow us to construct a long-wavelength sky model that is vital to the design of the next generation of long-wavelength telescopes such as the LWA.

Probing Higher Resolutions with the Pie Town Link: For long-wavelength astronomy to reach its full potential, it must reach similar resolution to that achieved with centimeter-wavelength observations, or about an order of magnitude more than that which the 74 MHz VLA is now capable. For this reason, the next generation of long-wavelength radio telescopes, such as the LWA, will require interferometric baselines lengths up to 500 km. The main difficulty with this is that no one has ever been able to remove the ionospheric phase corruptions on such long baselines with the precision necessary to achieve the desired resolution across the full field of view.

The NRL team has recently taken a first step toward this goal by expanding the 74 MHz system on the VLA to include an antenna from the Very Long Baseline Array (VLBA) located at Pie Town, New Mexico. Using the Pie Town Link, a fiber-optic connection that allows this antenna to function as if it

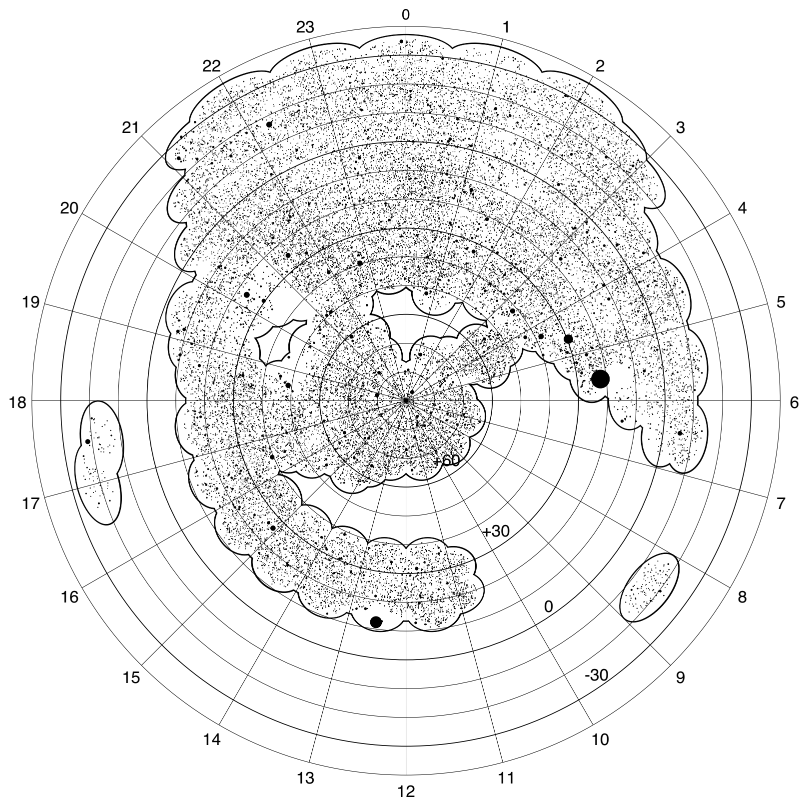

FIGURE 4
Current status of the VLSS. Over 32,000 sources have been detected and about half the visible sky imaged. Close-up maps and source catalogs are available in our first data release (http://lwa.nrl.navy.mil/VLSS). Sources are plotted with dots, with diameters proportional to the square roots of their measured flux densities.

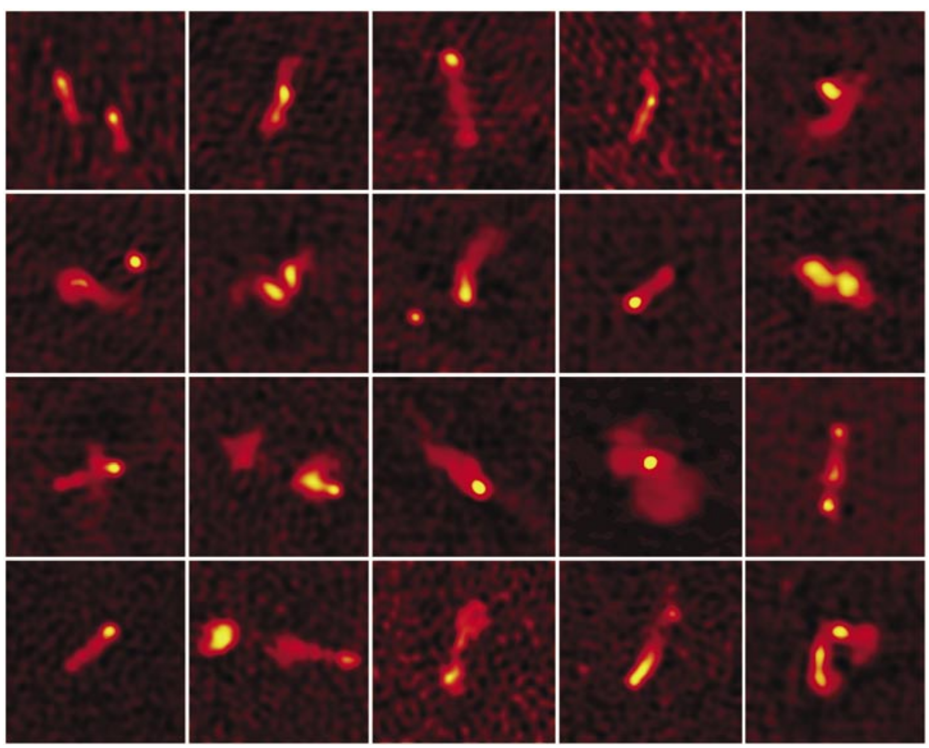

FIGURE 5
Close-up maps of a sample of VLSS sources that are large enough to be resolved at this frequency. Each map is 6 milliradians across.

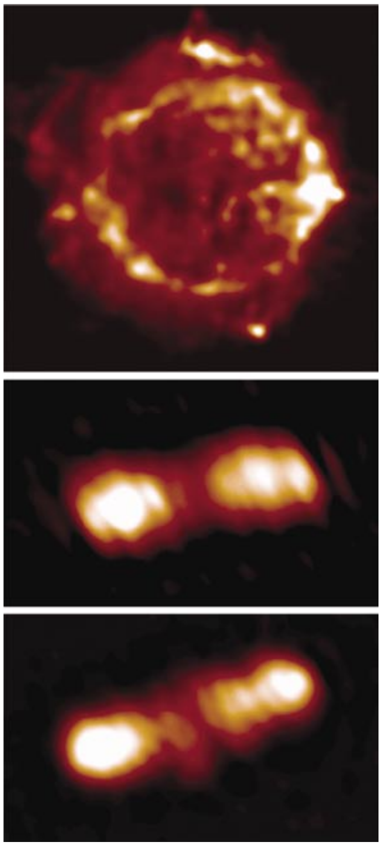

FIGURE 6
Recent 74 MHz Pie Town Link images of Cassiopeia A (top, Ref. 1), Hercules A (middle, Ref. 2), and Cygnus A (bottom).

were part of the VLA, the maximum baseline length is expanded from 35 km to 73 km. Completed just last year, we have successfully used this system to observe several bright astronomical objects at a full theoretical angular resolution of ~60 microradians. Figure 6 shows some of the recent images produced with this system. Scientifically, this has allowed us to probe the fine-scale spectral properties of a variety of sources. Technically, we have doubled the longest baseline over which ionospheric phase distortions have been properly calibrated at this frequency, bringing us closer to the baseline scales of future meter-wavelength instruments.

[Sponsored by ONR]

References
[1] N. Gizani, A.S. Cohen, and N.E. Kassim, "First Results of the 74 MHz VLA-Pie Town Link. Hercules A at Low Frequencies," *MNRAS* submitted, 2004.
[2] T. Delaney, L. Rudnick, T. Jones, R. Fesen, U. Hwang, R. Petre, and J. Morse, "X-Ray and Radio (and Optical) Observations of Cassiopeia A," in *X-Ray and Radio Connections*, L.O. Sjouwerman and K.K. Dyer, eds., (Blackwell Publishing, Oxford, U.K., 2004).

★

Cosmic Rays from Gamma Ray Bursts in the Galaxy

C.D. Dermer[1] and J.M. Holmes[1,2]
[1] *Space Science Division*
[2] *Thomas Jefferson High School for Science and Technology*

Introduction: Gamma-ray bursts (GRBs) are brief flashes of γ-ray light emitted by sources at cosmological distances. Recent observations link GRBs with star-forming galaxies and a rare type of evolved high-mass star that explodes as a supernova when its core collapses to a black hole. Most core-collapse supernovae, by contrast, form neutron stars. In either case, the supernova explosion ejects a remnant that expands into and shocks the interstellar medium. These shock waves accelerate high-energy cosmic-ray protons and ions. The supernovae that form neutron stars are thought to accelerate cosmic rays to energies reaching 10^{14} eV. The much more energetic GRB shock waves, with speeds very close to the speed of light, are thought to accelerate the highest energy cosmic rays, with energies reaching and exceeding 10^{20} eV.

Because the Milky Way is actively making young high-mass stars, GRBs will also occur in our Galaxy. The rate of GRBs in the Milky Way is very uncertain because of the lack of precise knowledge about the opening angle of GRB jets, but it could be as frequent as once every 10,000 years. Acceleration of cosmic rays by GRB jets, and propagation of cosmic rays through the magnetic field of our Galaxy and across the universe, can explain the spectrum of cosmic rays at the highest energies (Fig. 7).[1]

Over the age of the Galaxy, there is a good chance that a nearby powerful GRB, with a jet oriented toward Earth, could have lethal consequences for life. It has recently been argued[2] that such an event contributed to the Ordovician extinction event 440 Myrs ago. Understanding cosmic-ray propagation and effects on materials is important to estimate radiation damage on spacecraft, cosmic-ray effects on humans in space, and the origin of cosmic rays.

Methodology: To assess cosmic ray transport from a GRB, a 3D propagation model was developed to simulate the sequence of irradiation events that occurs when a GRB jet is pointed toward Earth. The cosmic rays move in response to a large-scale magnetic field that traces the spiral arm structure of the Galaxy, and they diffuse through pitch-angle scattering off magnetic turbulence waves. The magnetic field of

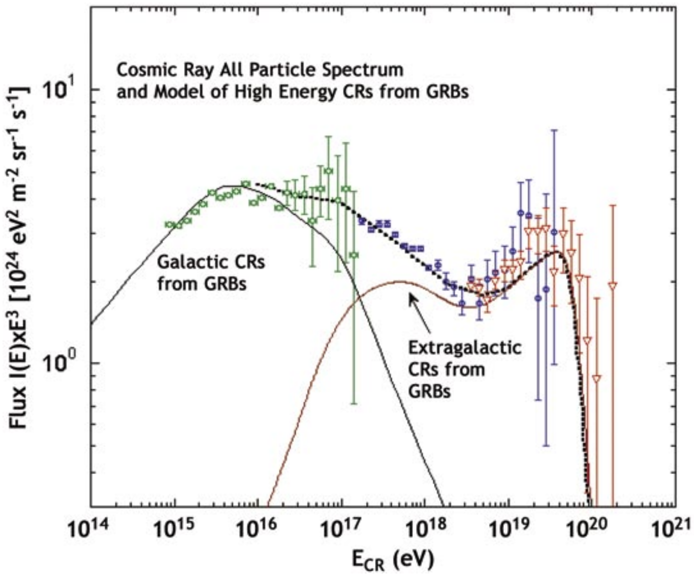

FIGURE 7
Fit of a model[1] to cosmic-ray data from the KASCADE, Hi Res-I and Hi-Res II cosmic ray experiments (see Ref. 1 for sources of data). High-energy cosmic rays are accelerated by GRBs in the Galaxy and throughout the universe in this model.

the Galaxy is modeled as a bisymmetric spiral for the Galaxy's disk and a dipole magnetic field for the Galaxy's halo. The evolution of the particle momentum is found by solving the Lorentz force equation. A Monte Carlo simulation of pitch-angle scattering and diffusion was developed that takes into account the energy dependence of the cosmic-ray mean free path.

Figure 8 displays the cosmic-ray halo that surrounds a GRB source 14,000 years after the GRB event. The geometry of the radiations is modeled by twin radial jets of cosmic rays with a jet-opening half-angle of 0.1 radian. A conical shell forms as a result of protons and neutron-decay protons with energies above 10^{18} eV. Beamed cosmic-ray protons and neutrons that decay near the GRB form "wall" features, as seen in the view from overhead for a transverse jet. This is a consequence of the rapid diffusion along the field vs the slower cross-field diffusion, and by magnetic mirroring effects of the jetted cosmic rays in the spiral arm structure of the Galaxy.

Discussion: About once every several hundred million years, the Earth is blasted by GRB photon and neutral radiations of sufficient intensity to have significant effects on the biota. Such an event might have been responsible for trilobite extinction in the Ordovician epoch through destruction of plankton.[2] The prompt high-energy X rays, γ rays, and cosmic rays produce cascade UV flux and odd nitrogen compounds that destroy the ozone layer, possibly accounting for the pattern of extinction events. Cosmic rays from GRBs would also have affected biological evolution from DNA radiation damage by the elevated ground-level muon fluxes induced by prompt and delayed cosmic rays. These radiations could have initiated the ice age that followed the onset of the Ordovician extinction event.

Figure 9 shows the time-dependence of the flux of neutrons and protons from a GRB source located 3,260 light years from the Earth. The prompt flux has greater lethality and effect compared to the delayed cosmic rays. The combined radiations could make a two-phase event that produced the Ordovician extinction event. Our simulations also show unusual effects that arise from a propagation model that combines both ray tracing and diffusive pitch-angle scattering. Astronomy missions with significant NRL involvement, such as NASA's Gamma ray Large Area Space Telescope (GLAST), will be able to test this GRB model for cosmic-ray origin.

[Sponsored by ONR and NASA]

References

[1] S.D. Wick, C.D. Dermer, and A. Atoyan, "High Energy Cosmic Rays from Gamma-Ray Bursts," *Astroparticle Phys.* **21**, 125-148 (2004).

[2] A.L. Melott, B.S. Lieberman, C.M. Laird, M.V. Medvedev, B.C. Thomas, J.K. Cannizzo, N. Gehrels, and C.H. Jackman, "Did a Gamma-Ray Burst Initiate the Late Ordovician Mass Extinction?" *Internat. J. Astrobiology* **3**, 55-61 (2004). ★

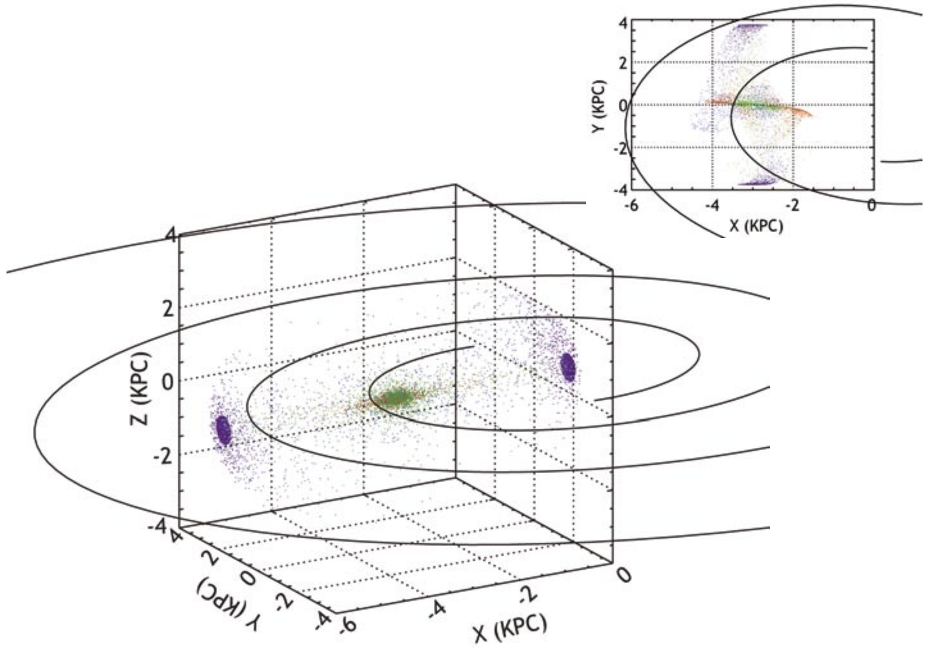

FIGURE 8
Cosmic-ray halo formed 14,000 years after a GRB, with radial jets oriented along the Galactic plane, that took place at 3 kpc from the center of the Galaxy. For clarity, equal numbers of cosmic rays are injected per decade, with cosmic rays color-coded by energy. Cosmic rays with energies in the ranges 10^{16} to 10^{17}, 10^{17} to 10^{18}, 10^{18} to 10^{19}, and 10^{19} to 10^{20}, are indicated by red, yellow, green, light blue, and dark blue symbols, respectively. Inset shows view from overhead for a GRB with jets oriented in the transverse direction.

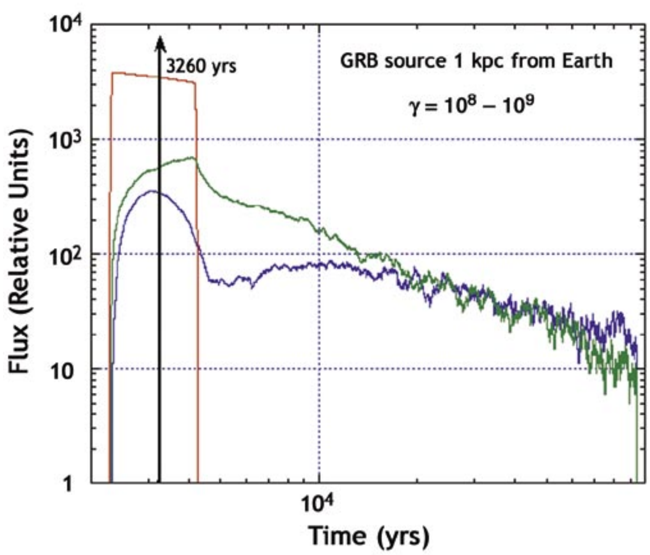

FIGURE 9
Fluxes of 10^{17} to 10^{18} eV cosmic rays received at Earth from an on-axis GRB that occurred 3,260 light years away. The red, green, and blue curves represent cosmic-ray neutrons, neutron-decay protons, and protons, respectively. The prompt flux actually lasts for minutes to hours, rather than the 2,000 yrs indicated by the figure, which reflects the approximations of the numerical method.

Information Technology and Communications

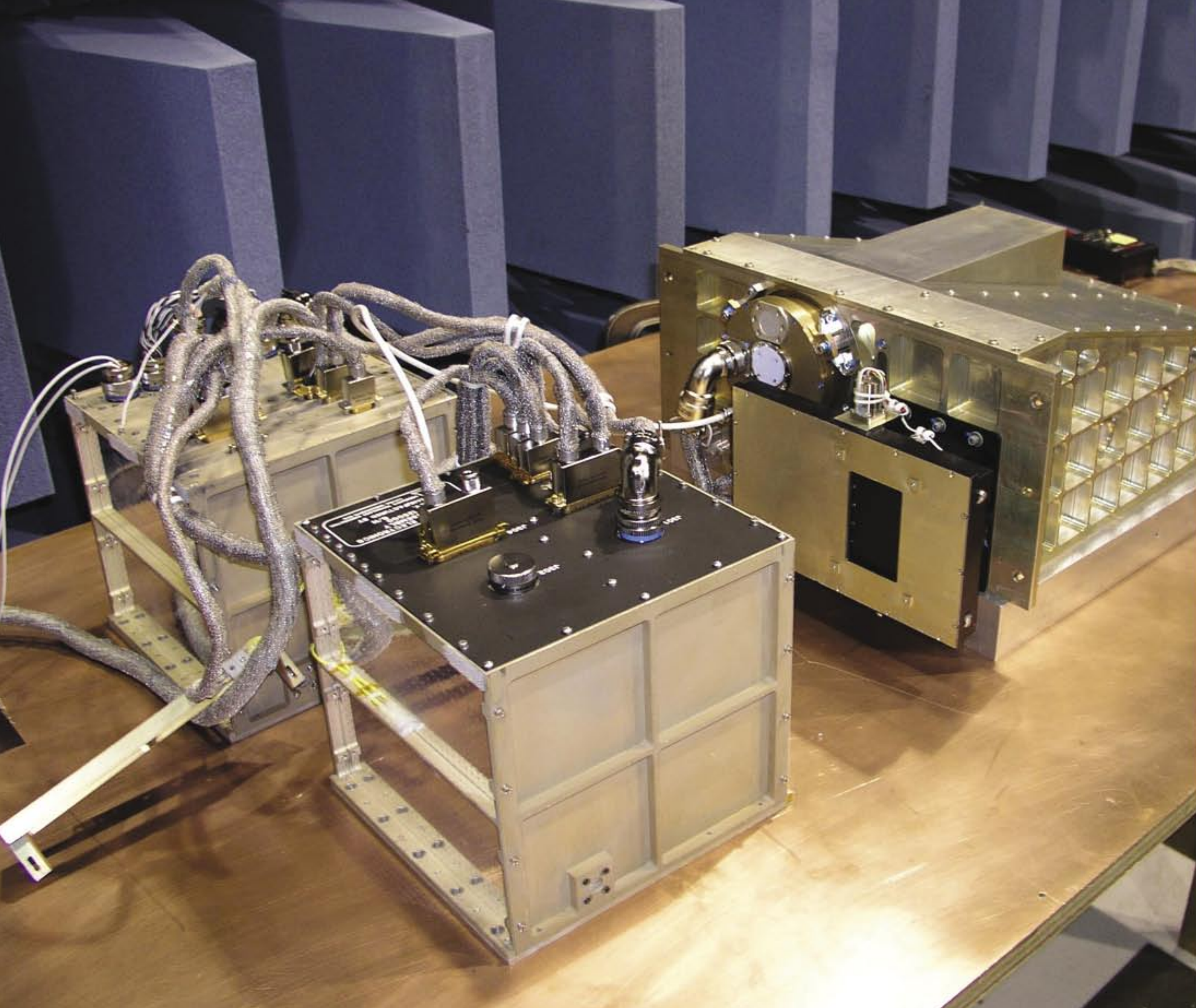

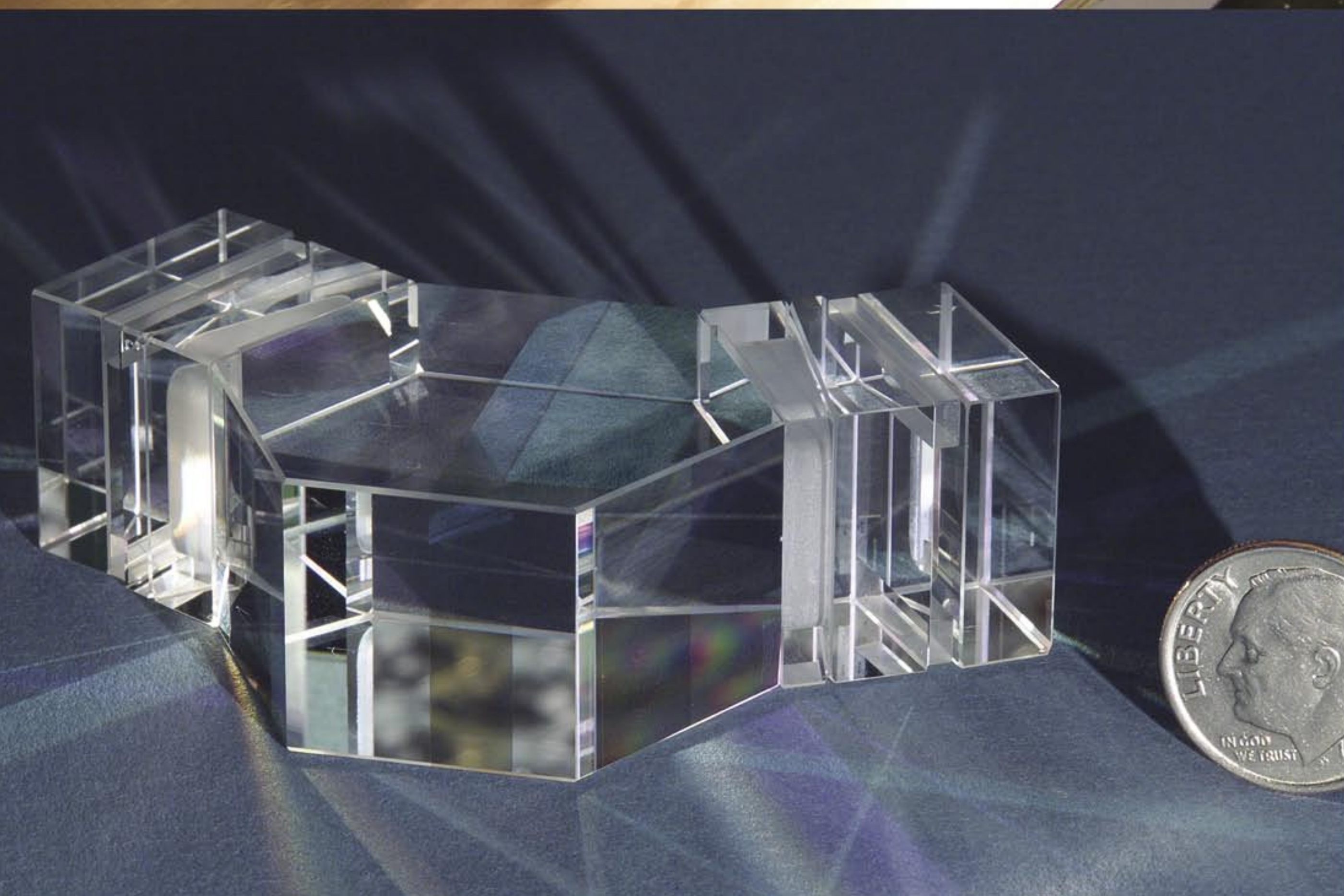

Photo caption: The core optical component of SHIMMER is an interferometer that replaces a traditional 2-m spectrometer. It has been used to determine trace constituents in the upper atmosphere.

Scalable High-Assurance Technology for Detecting Compromised Host Computers

J. McDermott, W. Snook, and J. Luo
Information Technology Division

Introduction: Explosive improvements in commercial computer technology and tight budget constraints have driven the military to use commodity operating systems as the foundation for its latest information technology. Unfortunately, the ability of commodity operating systems to protect themselves has not greatly improved. (Commodity systems are defined as those that are both widely available and widely used.) As a result, it is difficult to build an information system that can protect military data according to its criticality and value. Additional technology is needed to strengthen the security infrastructure of military information systems. The problem we are addressing here is not one of nuisance attacks such as the viruses reported by the news media.

Deceptive Interpreters: For military and other national security systems, the problem we are concerned with is deceptive interpretation. The problem of deceptive interpretation occurs when some portion of a computer system is modified to present a false picture of reality.[1] A deceptive interpreter is a malicious agent that is capable of observing and changing the results of computations on its host system, according to a predefined strategy. Deceptive interpreters are able to change inputs for commands, the sequence of commands executed, or the information returned by computation in a way such that their policies are enforced.

Deceptive interpreters are analogous to the reference monitor concept for access control. The difference is that reference monitors are beneficial security mechanisms that enforce legitimate policies on the system. Deceptive interpreters, on the other hand, enforce malicious policies (which we call strategies) to the detriment of the host system. Another difference is that a deceptive interpreter must not be detected. A necessary strategy for any deceptive interpreter is that the deceptive interpreter itself must be hidden. Reference monitors can simply adopt fail-stop policies to exert control over systems; any request that violates the policy can be rejected and reported. Deceptive interpreters, on the other hand, cannot reveal their presence and must provide responses that appear legitimate. The originator of the legitimate commands must be misled without realizing it.

Rootkits: The most common use of deceptive interpreters is in association with a rootkit. After attackers gain root or administrative access to the system, they can install malicious tools including backdoors, sniffers, and tools to cover their tracks. These tools will run with root privilege and have the ability to fully control the system. However, backdoors and sniffers by themselves tend to have large signatures that could be easily detected. What makes rootkits exceptionally dangerous is the incorporation of deceptive interpreters that hide their presence. Deceptive interpretation can fool both automated tools and human system administrators into thinking their systems are safe. They enable a rootkit and its malicious payload to operate for an extended period of time, thus drastically prolonging the system compromise and escalating the damage.

The constant stream of new security vulnerabilities demonstrates that much of our technology is exploitable and at risk from deceptive interpretation. To inject deceptive interpretation into a military information system, it is only necessary to tamper with one link in the entire chain of computation (Fig. 1); preventing deceptive interpretation requires every link to be made tamper-proof. On the other hand, the effort for detecting deceptive interpretation is somewhere in the middle of those two extremes. Successful detection depends on monitoring the link that gets tampered with and recognizing that the tampering has occurred. The fundamental consequence of deceptive interpretation is that the host can no longer be trusted to inspect itself. A new technology is needed.

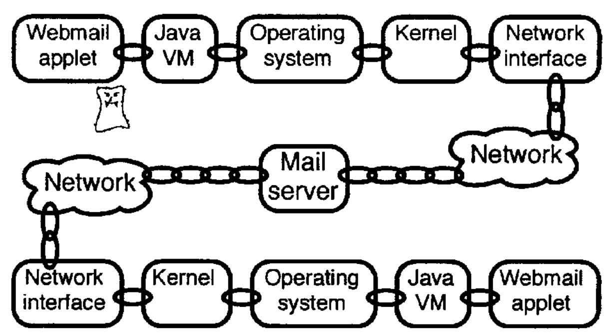

FIGURE 1
Tampering with the chain of computation.

Secure Attention Instruction: NRL researchers have focused on tamper-resistant hardware, software, and cryptographically protected means of detecting unauthorized modifications to commodity operating systems. The secure attention instruction concept provides a scalable infrastructure for detecting and reporting compromised network hosts. This will provide a high-assurance security foundation for information-grid-based military systems.

A secure attention instruction can be a machine language operation code, an interpreted byte code, or a system call. In any of these forms, the effect is to cause the secure attention instruction (SAI) processor to perform a safety check of the host computer's software. The results of this check are signed by the SAI processor, using a cryptographic key that is protected inside the SAI processor. The results returned by the instruction cannot be used on the host computer that is protected by the secure attention instruction; a deceptive interpreter could tamper with that use. However, the results of a secure attention instruction can be checked on another host that is known to be secure. If this trusted host (called a mint) has the proper keys, it can confirm and report the authenticity of the results. If the safety check fails, security measures can be invoked to isolate, remove, or otherwise deal with the deceptive interpreter. If the mint sets a timer for each secure attention instruction that it creates, it can use the corresponding time-out event as a notification that the instruction may have been discarded by a deceptive interpreter. Security measures may be invoked on this time-out. Finally, since the secure attention instruction processor protects the keys it uses to authenticate the results, the deceptive interpreter cannot forge a result.

Figure 2 illustrates most of the key concepts needed to effectively construct a scalable secure attention instruction infrastructure. Part (a) shows all the components needed to use secure attention instructions in a simple network having a hierarchy of security domains. Part (b) is loosely structured as a unified modeling language (UML) collaboration diagram; it lists all the interactions involved in executing one secure attention instruction.

We begin by describing the objects shown in Fig. 2(a) moving clockwise from Mint P at the top. Mint P is a mint because it can create secure attention instructions that are a bit like currency in the sense that they are hard to forge. Because the figure includes three mints, we give each mint a name corresponding to its security domain; "P" is the label for the root domain of the entire network. The key in each mint represents the cryptographic material that allows the mint to create authenticatable and secret secure attention instructions. In the context of this section, we define a secure attention instruction as the string of bits that results when a mint applies a cryptographic function to a command such as x, y, or z. In the future, we plan to publish a description of the cryptographic exchange between a mint and an SAI device, but for now we assume that the protocol has already been established. Each mint also implements a policy of some sort to regulate the creation of secure attention instructions.

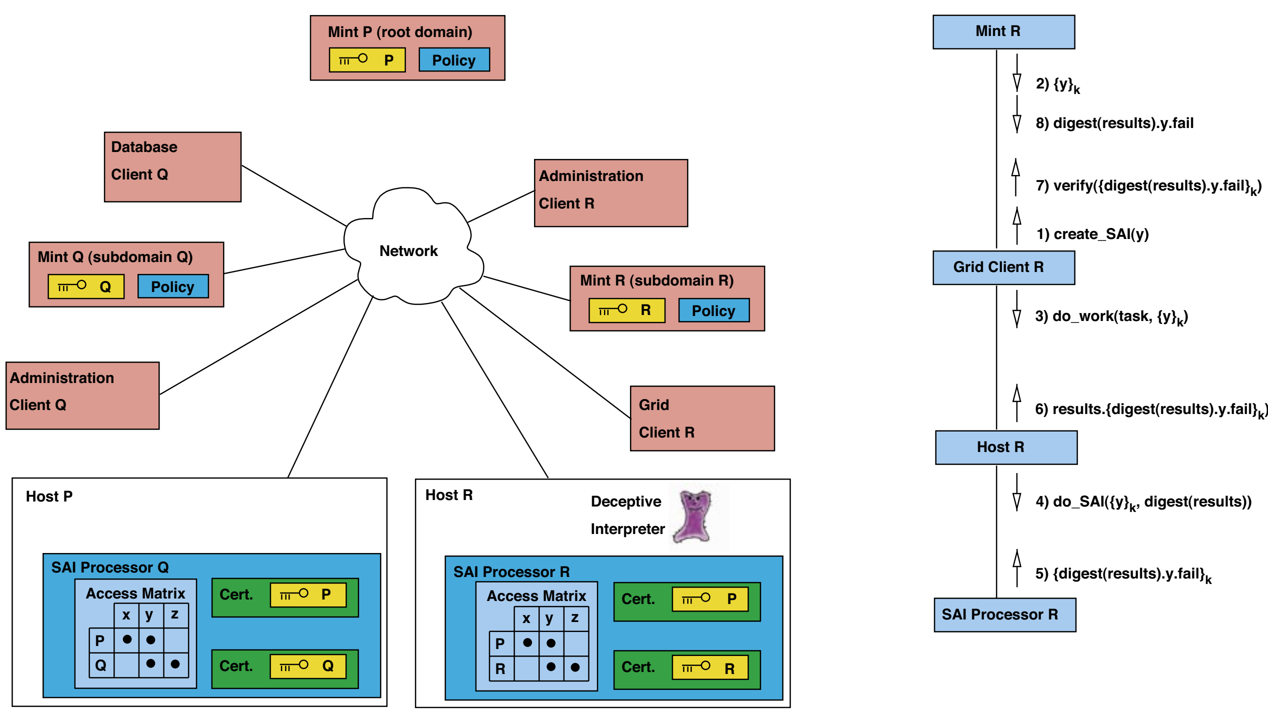

FIGURE 2
Key concepts for secure attention instructions.

Because Mint P is the root mint, it is not connected to the network, and its policy is to only create secure attention instructions for a small number of root domain administrators. The root mint does not create secure attention instructions often. When it does, the instructions contain commands for key management and other sensitive operations. We are making the assumption that the mint is trusted, and that it uses one of the many existing mechanisms to authenticate the administrators.

Next, Administration Client R represents the process (or computer) that the administrator for subdomain R uses to monitor and configure SAI processors within subdomain R.

Mint R has a different domain and policy than Mint P, but it is otherwise very similar. The policy of Mint R allows it to create two types of secure attention instructions, distinguished according to their commands. The first type, created only for subdomain administrators, is used to configure SAI processors. The second type, created for clients in the subdomain, implements the true purpose of the secure attention instruction. It allows clients to bind the results of some task performed on a remote computer to the results of a deceptive interpretation scan performed on the remote computer's SAI processor. The other important thing about the subdomain mint policy is that can include a timer for each secure attention instruction.

Grid Client R represents a process that a normal member of subdomain R uses to access grid computing services. Host R is a computer containing an SAI processor and running some sort of network daemon (such as Globus Toolkit). The computer is configured with a device driver and other appropriate software so that the daemon can interpret secure attention instructions by passing them on to the the SAI processor. Also, the icon with "fangs" represents a deceptive interpreter that has taken over a portion of the operating system on Host R in order to alter the results produced by the daemon. The SAI processor within Host R contains three interesting items. First, it has a "Cert," or certificate, for domain P and another for subdomain R. The certificates contain cryptographic material and other information allowing the SAI processor to authenticate and decrypt secure attention instructions minted by Mint P or Mint R. The third item is an access matrix that the SAI processor consults before carrying out commands. According to the matrix, SAI Processor R will honor commands x and y from Mint P, honor commands y and z from Mint R, and refuse all other commands. After the the SAI processor executes a command, it will typically return a result that can be authenticated and encrypted by the mint that issued the command.

Host Q, Administration Client Q, and Mint Q are configured for subdomain Q; otherwise, they are the same as their counterparts in subdomain R. Database Client Q is used for accessing a database service; otherwise, it is the counterpart of Grid Client R.

Figure 2(b) shows the basic exchange involved in executing a secure attention instruction. As mentioned earlier, the figure is loosely based on a UML collaboration diagram. The labeled boxes correspond to items in part (a) of the figure, and the lines between the boxes indicate collaboration. The numbered lines of text represent messages with semantics similar to a function call. The messages with parameters enclosed in "( )" are like function calls, and the other messages are like return values. Each message starts with an arrow that points to its destination, and the messages are placed near their origin.

The secure attention instruction exchange proceeds in the following way. Grid Client R begins by asking Mint R to create an SAI containing the command y. (In an actual protocol implementation, the intended SAI processor should be specified here. Many other precautions would also need to be taken, so we use this simplification here for the sake of clear notation.) Mint R then responds with the SAI as requested. Next, in message 3, the client instructs Host R to perform a task and execute the SAI for y when it is finished. Host Device R performs the task and produces a result. Because the task specification included a description of the semantics for y, the host device took a digest of its results and passed them with the SAI to the SAI processor (message 4). The SAI processor performed command y which detected the presence of a deceptive interpreter in Host R. The processor then cryptographically bound its results to the host's digest and dispatched message 5. Next, the host appended the SAI result to its full task result and sent message 6 back to the client. The client extracted the SAI result and asked the mint to verify it in message 7. Upon receiving the message, the mint stopped the corresponding timer, noted the deceptive interpreter, and returned the digest and the result of y to the client. Finally, the client recalculated the digest and considered the result of the SAI. By using the SAI infrastructure, the client determined that the results were generated on the computer containing SAI Processor R and that they were not trustworthy because a deceptive interpreter was present.

NRL's proof-of-concept prototype will demonstrate the feasibility of integrating secure attention instructions with host safety checks or scans. It will also prototype the scalable infrastructure needed to mint, confirm, and manage secure attention instructions.

Because we have limited resources, we chose to implement our prototype as a PCI-bus peripheral protecting the open-source Linux kernel. Intelligent peripherals have the necessary local processing power and interface restriction capabilities to be relatively omniscient (as bus masters) but tamper-resistant. An Intel IQ80310 prototyping board provides these features and saves hardware prototyping effort.

[Sponsored by ONR]

References

[1] G. Karjoth and J. Posegga, "Mobile Agents and Telcos Nightmares," *Annales Telecommun*, **55**(7/8), 29-41 (2000). ★

Virtual Targets for the Real World

D.G. Brown,[1] Y. Baillot,[2] K.C. Pfluger,[3] S. Julier,[2] and M.A. Livingston[1]
[1] *Information Technology Division*
[2] *ITT Advanced Engineering and Sciences*
[3] *Reallaer LLC*

Introduction: Live-fire training keeps warfighting capabilities at peak effectiveness. However, the cost of procuring real targets—only to be destroyed—is prohibitively expensive. The United States Marine Corps (USMC) uses a variety of target proxies, such as derelict vehicles, piles of waste, and even "pop-up targets," all of which are nonreactive, stay in fixed locations from year-to-year, and often do not resemble the real targets. Trainees simply do not get the opportunity to fire live rounds at realistic-looking and moving targets. However, Augmented Reality (AR) can help by merging virtual entities with the real world for training exercises. We describe an AR system that provides virtual targets for training of USMC Fire Support Teams.

Augmented Reality: In an AR system, the user wears a tracked see-through head-mounted display with stereo headphones that is connected to a computer containing a database of spatial information related to the venue of the training exercise. By measuring the user's position and view direction in the real world, three-dimensional (3D) computer graphics and spatially located sounds are displayed to appear to exist in the real world. A miniaturized and ruggedized computer, batteries, and wireless networking make the AR system man-portable. Figure 3 shows a mobile AR prototype system. In the case of AR for training, the virtual information overlay consists of realistic 3D renderings of entities: individual combatants, tanks, planes, ships, etc.

Entities in Training: Entities in training exercises fall into one of three categories: *live* entities are real people and vehicles participating in a training exercise; *virtual* entities are human-controlled players in virtual worlds; *constructive* entities are driven by algorithms in computer simulations. AR provides a natural way for all three types to mix together. Live entities observe virtual and constructive entities through the AR system. Interactions such as shooting are conveyed from the AR system back to the constructive and virtual simulation systems.

Application of AR for Fire Support Team Training: The USMC's Fire Support Team training begins with small-scale (1:40) pneumatic mortars on a field at the Marine Corps Base, Quantico, Virginia. The purpose of this training is to hone the communication skills between the forward observer and the Fire Direction Center (FDC). In the current training plan, a forward observer visually locates targets, identifies and determines grid coordinates using binoculars and a map, and recommends a call for fire to the FDC. Once the shots are fired, the training instructor (not a part of the operational fire support team) determines the accuracy of the shots and the effect on the target: catastrophic hit, mobility hit, or no effect. The calls for fire are adjusted until the team has the desired effect on the target. Before introducing the AR system, the team fired on static and unrealistic proxy targets.

The system, based on the Battlefield Augmented Reality System,[1] was demonstrated at Quantico in October 2004. It provides a head-mounted display for the forward observer and a touch screen for the instructor, each showing virtual targets on the real range. Figure 4 shows the observer's view of virtual targets and buildings on the range. The observer can have the computer simulate a magnified view (including a reticle), similar to the view binoculars provide, to determine target identity and grid coordinates. The targets move along preset routes and are started and stopped by the instructor through a simple interface. As before, the forward observer calls for fire on the targets and a real round is fired. The instructor sees where the round lands in the augmented touch screen view and designates the effect on the target. Through a dynamic shared database,[2] the forward observer sees that effect and revises the call for fire. Figure 5 illus-

FIGURE 3
Mobile Augmented Reality (AR) prototype system.

FIGURE 4
Observer's view of virtual targets and buildings on the range.

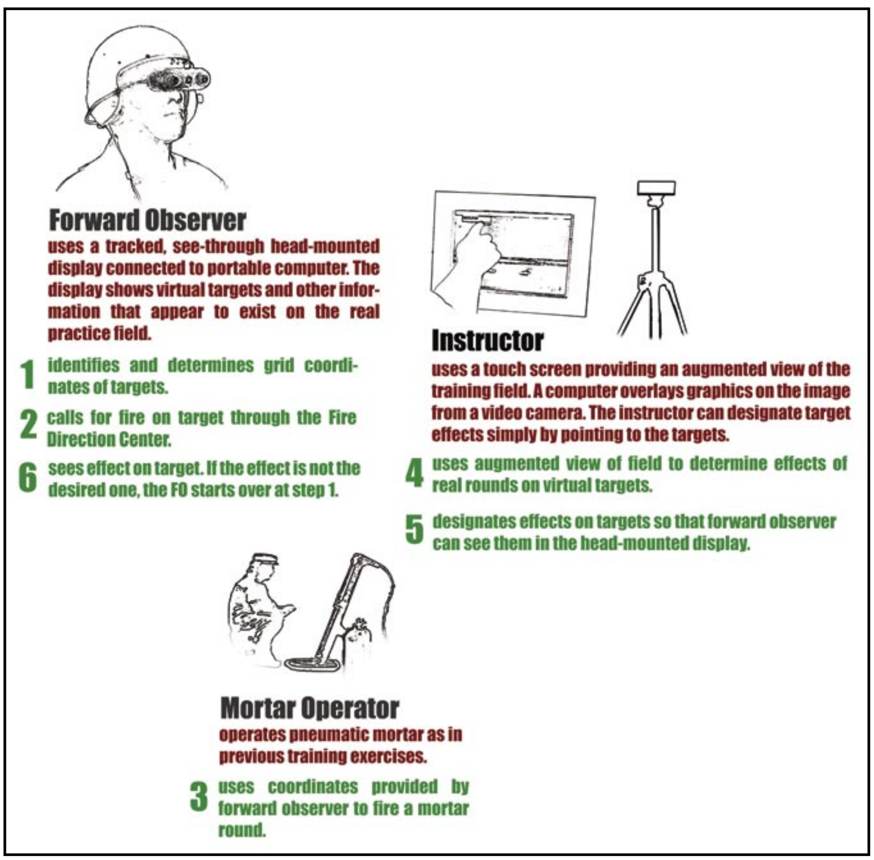

FIGURE 5
Augmented Reality (AR) system's major components and steps in the system's usage.

trates the major components of the system and steps in the system's usage. Augmented Reality was inserted into the training plan with no significant changes to the duties and actions of the participants, except that they can now fire on moving targets.

The virtual targets for training were well received by the mortar trainees and instructors at Quantico; however, rigorous studies and measurements of effectiveness are yet to be done. The system can also insert virtual terrain and control measures into the display, and both capabilities were preliminarily tested at Quantico. Future plans include refining the system, taking it to a full-scale live fire range such as the Marine Corps Air Ground Combat Center, Twentynine Palms, California, and completing a Semi-Automated Forces (SAF) interface for more intelligent targets.

[Sponsored by ONR]

References

[1] S.J. Julier, Y. Baillot, M. Lanzagorta, D. Brown, and L.J. Rosenblum, "BARS: Battlefield Augmented Reality System," in *Proceedings of the NATO Information Systems Technology Panel Symposium on New Information Processing Techniques for Military Systems*, Istanbul, Turkey, October 2000.

[2] D. Brown, S.J. Julier, Y. Baillot, M.A. Livingston, and L.J. Rosenblum, "Event-based Data Distribution for Mobile Augmented Reality and Virtual Environments," *Presence* **13**(2), 211-221 (2004).

★

Course of Action Analysis in the Global Information Grid

R. Mittu
Information Technology Division
J. Walters
ITT Advanced Engineering and Sciences

Introduction: The Department of Defense (DoD) is investing resources to support the development of the Global Information Grid (GIG)[1] a services-oriented architecture (SOA) based on web services technology (Fig. 6). The GIG will enable interoperability between all levels of military systems, sensors, simulations, operational users, autonomous software agents, etc., in tasks that range from purely administrative through complex Command and Control functions throughout the DoD. This article discusses the participation of NRL in a GIG proof-of-principle prototype that uses web services to provide the connectivity between the Global Command and Control System (GCCS),[2] Joint Warfare Simulation (JWARS),[3] as well as intelligent software agents to support Course of Action Analysis (CoAA). We also describe two of the many challenges that software agents must overcome to realize the full potential of the GIG.

Web Services and the GIG: The World Wide Web Consortium (W3C)[4] is leading the development of web technology, including web services technology such as the Universal Description Discovery Interface (UDDI), Web Service Description Language (WSDL), and Simple Object Access Protocol (SOAP). The UDDI defines web registries to which businesses can upload information about themselves and the services they offer. A WSDL document describes the locations of services and the operations supported by that service. The SOAP is a simple markup language for describing messages between applications. It is used to interact with UDDI registries to locate WSDL documents and to interact with the corresponding service described within the WSDL.

The GIG infrastructure will provide an open environment in which all military systems and users can seamlessly share information, without restrictions and limitations imposed by the current operational DoD architecture, which provides stovepiped interconnectivity between components (e.g., interface points between systems or components are inflexible and nonrobust to change or adaptation). The GIG represents a transformational shift, from stovepiped to a more flexible architecture, providing the opportunity for systems and users to dynamically discover and interact with other systems/users via web services. Figure 6 shows the GIG layers.

GIG Proof-of-Principle Prototype: Simulations are increasingly being used during operations to perform CoAA and develop real-time forecasts of future battlefield conditions. The Defense Modeling and Simulation Office (DMSO) is sponsoring a prototype to demonstrate (1) the utility of web services for providing interconnectivity between GCCS, JWARS, and intelligent agents; (2) the value added in using a standard data model to enable semantic interoperability between each component; and (3) the role of intelligent agents to support meaningful CoAA. NRL is responsible for developing the intelligent software agents; the Naval Warfare Development Command (NWDC) is responsible for web-service interfaces for GCCS and CACI Federal for the overall integration effort as well as the web service enhancements to JWARS.

GCCS is an automated information system designed to support situational awareness and deliber-

Domains	*Examples:* •Warfighting •Business •Intelligence
Applications	*Examples:* •Deployable Joint C2 Program •Business Management Modernization Program
GIG Enterprise Services	*Examples:* •Electronic Mail •Application Hosting •Weapon-Target Pairing
Transport	*Examples:* •Defense Information System Network •Joint Tactical Radio System •Transformational Communication System
Management	*Examples:* •Doctrine •Standards •Governance •Architecture •Policy •Engineering

FIGURE 6
Layers of the Global Information Grid (GIG).

ate and crisis planning through the use of an integrated set of analytic tools and flexible data transfer capabilities. The GCCS system correlates and fuses data from multiple sensors and intelligence sources to provide warfighters the situational awareness needed to be able to act and react decisively. JWARS is a campaign-level model of military operations that provides users with a representation of joint warfare to support operational planning and execution, force assessment studies, systems effectiveness, and trade-off analyses, as well as concept/doctrine development. The field of software agents is emerging as an important computing paradigm. Many definitions of software agents exist in the literature, but a general definition of a software agent according to Ref. 5 is "a computer system that is situated in some environment, capable of autonomous action in this environment in order to meet its design objective."

In the proof-of-principle evaluation (Fig. 7), GCCS is initialized with Unit Order of Battle (UOB) data that represent known locations of forces prior to plan execution. JWARS is also initialized with this UOB to ensure consistency with the force representation in GCCS. A tactical system will inject tracks into the GCCS track database as the execution of the plan unfolds, while JWARS will generate the corresponding expected track movements. Both sets of tracks will be made available to software agents that will compare deviations between the actual vs expected track positions, determine whether certain tracks enter regions of interest (or, alternatively, fail to do so) in a given time period or instant. They will also compare expected vs actual force blue/red ratios in regions of interest. The thresholds or failure conditions associated with these events, as specified by the user, will trigger the agents to send alerts to the JWARS Situation Monitor. The user may then spawn look-ahead excursions in JWARS to evaluate multiple options (i.e., CoAA), selecting the one that maximizes a set of objective functions.

The Command and Control Information Exchange Data Model (C2IEDM)[6] gateway will map the information exchanged between services onto the C2IEDM vocabulary. The C2IEDM is an extensible model representing Information Exchange Requirements for Command and Control that has been developed through the participation of experts from 27 nations.

The technology is currently undergoing experimentation in a laboratory environment and, through feedback from subject matter experts, the capability will be refined to provide these unique CoAA services to the broader GIG community through participation in integrated demonstrations.

Summary: This article has described a GIG proof-of-principle prototype that leverages web services to enable the connectivity between GCCS, JWARS, and intelligent agents to support CoAA. Many challenging issues remain regarding the roles intelligent software agents may play in the GIG, including their use for intelligently discovering services as well as potentially supporting the process of mapping information between the GIG Communities of Interest (COI). The C2IEDM vocabulary may not be persistent throughout the GIG. The proof of principle will enable us

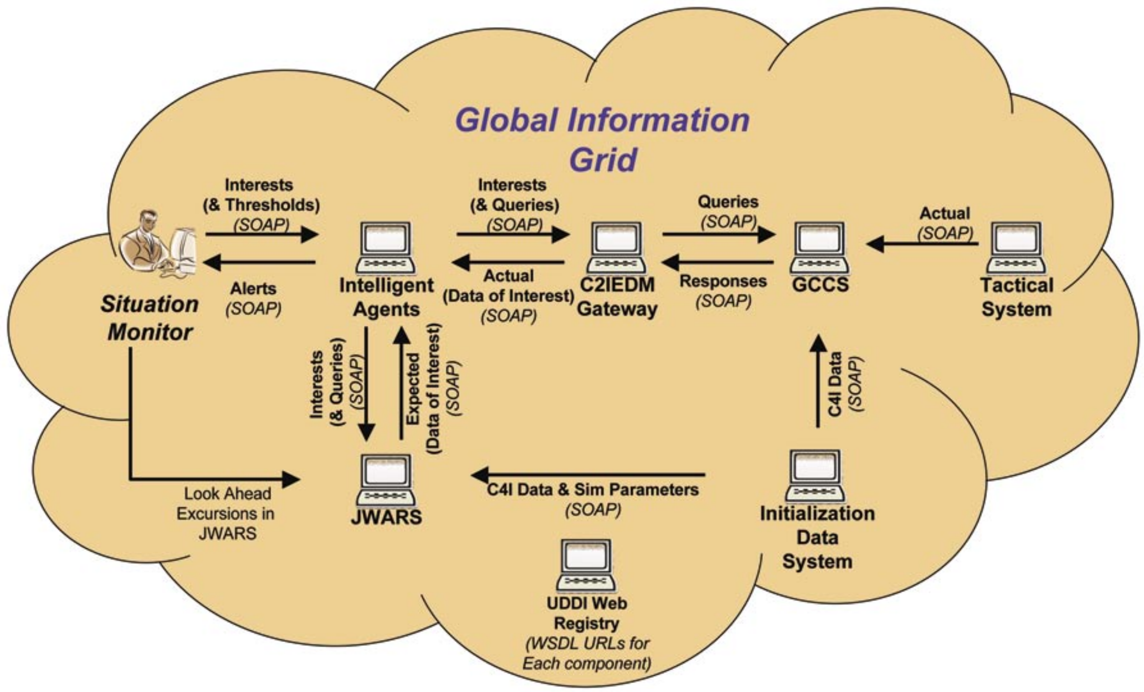

FIGURE 7
The JWA0RS, GCCS, and Intelligent Agent Web Service Federation.

to explore the use of semantic web technologies and human-agent cooperation and agent learning techniques to address these problems in the longer term.

[Sponsored by DMSO]

References

[1] Global Information Grid (GIG), Web Addresses: http://ges.DoD.mil, http://www.disa.mil/ns/gig.html.

[2] GCCS Common Operational Picture Reporting Requirements, CJCSI 3151-01A (19th January 2003).

[3] Joint Warfare Simulation (JWARS), Web Address: http://www.caci.com/business/systems/simulation/jwars.shtml.

[4] World Wide Web Consortium (W3C), Web Address: http://www.w3c.org.

[5] M. Wooldridge, *An Introduction to MultiAgent Systems* (John Wiley & Sons, U.K. 2002).

[6] Command and Control Information Exchange Data Model (C2IEDM), Web Address: http://www.mip-site.org. ★

Automic Change Detection and Classification (ACDC) System

M.C. Lohrenz, M.L. Gendron, and G.J. Layne
Marine Geosciences Division

Introduction: The authors are developing an Automated Change Detection and Classification (ACDC) system for the Mine Warfare (MIW) group at the Naval Oceanographic Office (NAVOCEANO). ACDC detects features in sidescan imagery, classifies the features (e.g., as minelike or not), and searches through historical databases of previously detected features to perform change detection (i.e., to determine whether the feature is new or pre-existing, relative to earlier surveys). The completed ACDC system will assist mine countermeasures (MCM) warfighters to more quickly and reliably identify minelike contacts in sidescan, thereby reducing warfighter fatigue, reducing risk to the warfighter, and shortening timelines for completion of MCM objectives.

ACDC consists of five major components: (1) clutter detection, (2) feature completion/classification, (3) geospatial searching, (4) clustering, and (5) scene matching. Depending on the quality of sidescan imagery to be analyzed, each of these steps can be performed autonomously (i.e., with no human intervention) or as a computer-assisted function (in which ACDC suggests statistically likely outcomes to the operator, who makes a final determination).

Clutter Detection: Minelike objects, also called minelike echoes or simply clutter, show up in sidescan imagery as bright spots, with adjacent shadows facing perpendicularly away from the center of the scan track, or nadir. ACDC includes a real-time algorithm that detects these bright spots and shadows by using a pair of geospatial bitmaps. Each pixel in the small "snippet" of imagery containing the object is assigned a corresponding bit in both bitmaps (Fig. 8). All bits in both bitmaps are initially cleared (value = 0). Each pixel in the image snippet that is brighter than some predetermined bright intensity threshold triggers a "set bit" (bit value = 1) in the bright spot bitmap, while each snippet pixel that is darker than a predetermined shadow intensity threshold sets a bit in the shadow bitmap. The clutter-detection algorithm compares the two bitmaps (using Boolean operations) to determine whether there is a bright spot and adjacent shadow in the appropriate configuration to be considered an object of interest. The algorithm outputs a confidence level to indicate whether the object should be analyzed further (i.e., how likely it is minelike). The operator can choose to manually review the objects and confidence levels, selecting those to be processed further, or the algorithm can run autonomously, such that objects with confidence levels greater than some predefined threshold will be automatically selected for the next phase of ACDC processing.

Feature Completion and Classification: Features of various shapes and sizes are traditionally discerned in sidescan by the shadow's dimensions, which vary as a function of both beam angle and feature size.[1] Shadows are detected more easily and reliably than bright spots in sidescan; bright spots often appear smaller or larger than the actual object. ACDC corrects this by using an adaptive filter to "complete" the feature's bright spot, reducing or enlarging it based on the shadow. The feature then can be classified more accurately by using dimensions of both the shadow and the completed bright spot. The filter outputs a snippet of imagery that contains only three gray-scale values: black for shadow bits, white for completed bright spot bits, and gray for all other bits (Fig. 9).

Geospatial Search: ACDC's geospatial search algorithm searches historical databases, such as the NAVOCEANO Master Contact Data Base (MCDB), to find previously detected features that are spatially close to each newly detected feature. The MCDB contains imagery from past sidescan surveys, along with snippets and descriptive attributes of classified features from those surveys. The search algorithm attempts to match each newly detected feature with spatially close historical features while correcting for estimated position errors (e.g., feature migration and Global Positioning System errors) in both the new and historical features. If no matches are successful, the newly detected feature is marked as a new object not seen before in the historical data. If a single match is made (i.e., one historical feature matches the new feature), they are assumed to be the same. If more than one historical feature matches a new feature, ACDC passes the new feature and all possible historical matching features to the next phase of processing.

Scene Matching: The final phase of ACDC—change detection—will be accomplished via two scene-matching algorithms being developed this year. A *feature-matching* algorithm will input wavelet coefficients to a neural network and match historical features (extracted during the geospatial search) with newly detected features. Wavelet networks have been proven to match complex features well, e.g., in face recognition.[2] To reduce the numerous false detections common during feature matching, an *area-matching* algorithm will match bounded regions of clustered features with corresponding regions of historical features, using another wavelet network and a single-pass clustering algorithm, described below.

Clustering: The authors developed the Geospatial Bitmap (GB) clustering algorithm as a fast, efficient, and repeatable method of clustering into bounded regions any set of unique elements, defined by any coordinate system, lying in *n*-dimensional space.[3] The clustering is accomplished by mapping each element into one or more predefined geometric "expansion shapes" using GBs. Any mapping resulting in a shape with dimension less than or equal to the dimension of the element space can define a cluster. Thus, two-dimensional (2D) clustering (e.g., clustering minelike elements in sidescan imagery) can be accomplished by expanding the elements into ellipses, rectangles or triangles, while 3D clustering can use spheroids, boxes, or cones. Elements that grow together will be contained within a common cluster (Fig. 10).

The GB clustering algorithm is a good choice for applications that require automated clustering in realtime: it is single-pass (i.e., noniterative), requires no seed points, and is order-independent (i.e., the ordering of elements has no effect on the resultant clusters). In addition to clustering the elements, the algorithm produces a bounded polygon to define each cluster boundary and calculates a measure of clutter density, which is the number of clustered elements divided by the area of the cluster polygon. ACDC uses this clustering algorithm to identify regions of high, medium, and low clutter density in sidescan. MCM warfighters use clutter density to determine whether an area of interest should be swept for mines prior to an operation.

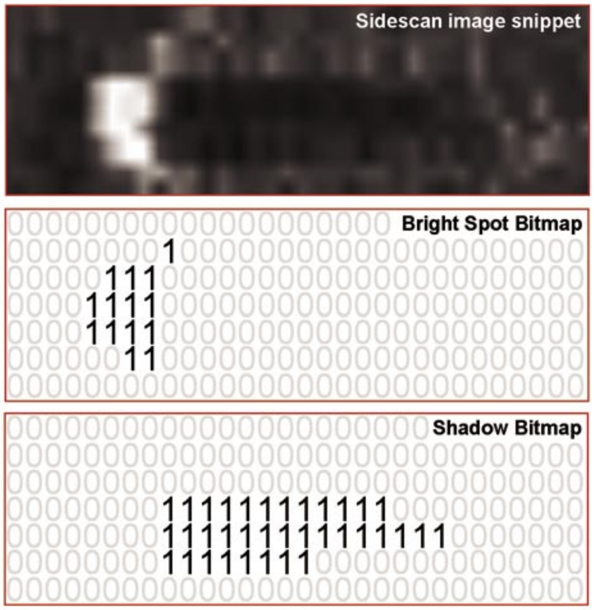

FIGURE 8
Geospatial bitmaps are used to detect bright spots and shadows in sidescan imagery.

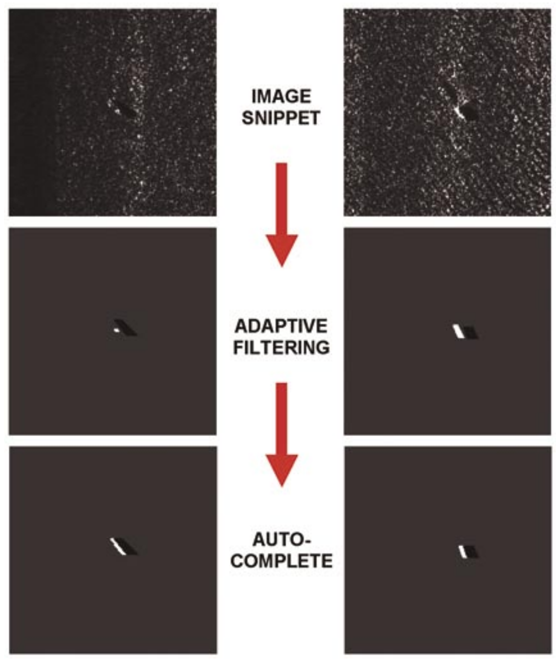

FIGURE 9
A feature's bright spot is "completed," based on its shadow. In the series on the left, the bright spot is enlarged to match the shadow. On the right, the bright spot is reduced.

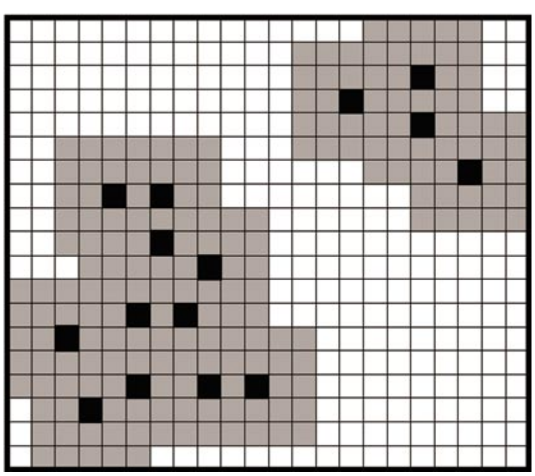

FIGURE 10
Geospatial bitmaps are used to cluster geographically close points.

Summary: The authors are developing ACDC to assist MCM warfighters in more quickly, reliably, and consistently identifying minelike contacts in sidescan imagery, thereby reducing warfighter fatigue, reducing risk to the warfighter, and significantly shortening timelines for completion of MCM objectives. Algorithms to perform clutter detection, feature completion and classification, geospatial searches of historical data, and clustering have been developed and demonstrated during recent naval exercises, including CCOA Delta Box/USS *Scout* (Ingleside Naval Base), BLUEGAME (Norway), and CJTFEX-04 (Camp Lejeune). Scene-matching algorithms are being developed this year to provide ACDC with a near-real-time change detection capability, in both computer-assisted and fully autonomous modes.

Acknowledgments: The authors thank Dr. D. Todoroff (ONR 32), Captain R. Clark and Dr. E. Mozley (SPAWAR PMW 150), Mr. J. Hammack (NAVOCEANO N5), Mr. R. Betsch (NAVOCEANO N82), and Mr. S. Martin (N752) for their support of this project.

[Sponsored by ONR, N752, and SPAWAR]

References

[1] J.P. Fish and H.A. Carr, *Sound Underwater Images: A Guide to the Generation and Interpretation of Sonar* (American Underwater Search and Survey, Ltd., 1990).

[2] V. Krueger and G. Sommer, "Affine Real-Time Face Tracking using Gabor Wavelet Networks," presented at ICPR, Barcelona, Spain, September 3-8, 2000.

[3] M.L. Gendron, G.J. Layne, and M.C. Lohrenz, "A Technique to Efficiently Cluster Points in *n*-dimensional Space Using Geographic Bitmaps," Naval Research Laboratory, provisional U.S. Patent application filed July 7, 2004 (Navy case number 84,921).

★

Integration of User-Developed Software with SIMDIS

W.A. Doughty, J. Binford, and D. Graves
Tactical Electronic Warfare Division
D. Emminizer
ITT Advanced Engineering and Sciences

Introduction: SIMDIS is a software toolkit that provides two- and three-dimensional interactive graphical and video display of live and postprocessed simulation, test, and operational data. SIMDIS has evolved from a display tool for the output of missile models to a premier government off-the-shelf (GOTS) product for advanced situational awareness and visual analysis. Figure 11 illustrates the various applications of SIMDIS to the Department of Defense (DoD) community. Since its inception as an Office of Naval Research-sponsored project, the toolkit has experienced significant userbase growth, with more than 1,000 current registrations within the DoD community. The toolkit has also undergone significant improvements in features and functionality. To better support the growth in capabilities, and to allow the community to customize the toolkit for their needs, a modularized plug-in applications programming interface (API) was designed and implemented. This plug-in API facilitates the integration of custom user-developed software with the SIMDIS toolkit. The plug-in approach improves the software development process by promoting modularization and reuse of software components. The approach also provides users with the ability to independently add new features to the SIMDIS toolkit based on the user's specific requirements. These new features can be added without the knowledge of, or access to, the SIMDIS source code.

Modularization of Software Components: Throughout the development cycle, enhancements and features specific to certain users have been continually integrated into the SIMDIS application's source code. While this approach has been very successful, the new product starts to overgrow its original design and, as such, becomes more complicated to use and maintain. This complexity problem is greatly improved through the use of modularization, and is one of the driving factors behind the development of the plus-in API.

User-Developed Software Modules: Specialized knowledge is necessary to develop and maintain many user-requested features, a problem that further complicates custom development. A good example relates to recent efforts in processing test and training range data from DoD ranges. Each range has a unique data format that requires development of interface software for display with SIMDIS. Typically, NRL developers work with range personnel to understand their specific data and implement the software required to integrate with the toolkit. The software is maintained by NRL and must be revised and upgraded with each change to the range data format. Providing users with the ability to develop and maintain their own software modules eliminates the need for SIMDIS developers to be directly involved with routine range software maintenance.

SIMDIS Plug-in API: Implementing a plug-in software architecture for SIMDIS solves the complex-

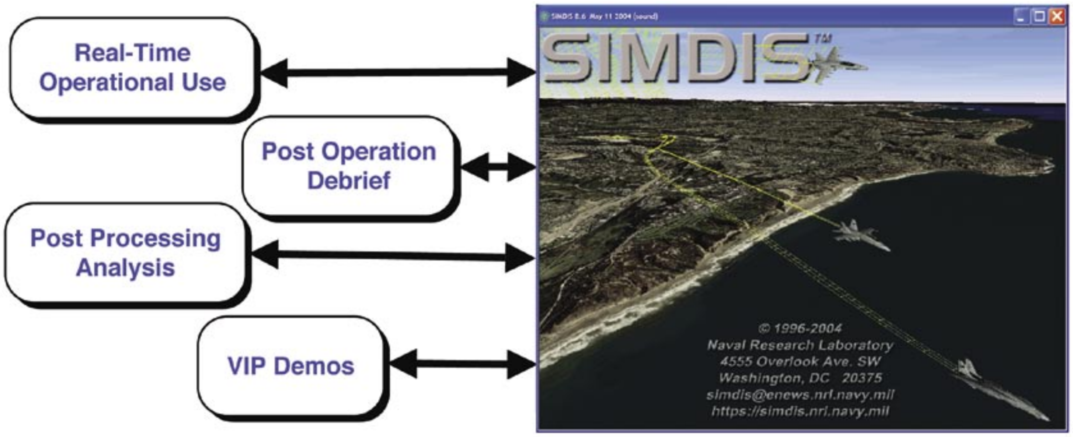

FIGURE 11
SIMDIS is a set of GOTS software tools used by DoD ranges and system centers to support 3D analysis and visualization of test and training missions for air, sea, and undersea warfare areas.

ity problem. A plug-in architecture allows third-party developers to read and write SIMDIS data, create custom pull-down menus, and generate specialized user defined graphics. Figure 12 illustrates the relationship between SIMDIS, the plug-in API, user applications, and external data sources.

A plug-in API provides modularity and structure to SIMDIS, while allowing users to create specialized components that can be shared with other users. SIMDIS provides the display engine and data maintenance functionality for all plug-ins. Plug-ins provide the unique or enhanced functionality to the base tool.

The plug-in API developed for SIMDIS is cross-platform capable. Just as SIMDIS supports Linux, SGI, Sun, and various Windows operating systems, the plug-in API is supported across all four architectures. Plug-in applications are dynamically loaded library (DLL) files for Windows platforms and shared object (SO) files for UNIX systems. Both formats allow users to add custom software modules to the SIMDIS runtime environment.

Several difficulties arise when developing a plug-in interface capability. An important issue is backward compatibility. Although new releases of SIMDIS support newer versions of the plug-in API, each release must utilize version management to allow plug-ins created with previous API versions to remain compatible. Another issue is that improperly developed plug-ins may not only fail to function properly, but may cause the entire SIMDIS application to fail. Special consideration and testing must be performed on all plug-ins prior to their inclusion in an operational fielded version of the software. Ultimately, the development of the plug-in API results in careful tradeoffs between power, flexibility, speed, fail-safe capabilities, and ease of use.

Applications: Over the past year, the Southern California Offshore Range (SCORE) has been a key sponsor of the plug-in API development for SIMDIS. As such, many of the initial plug-ins supported the SCORE users, providing realistic test cases to improve the overall plug-in API design.

One of the initial SCORE plug-ins was a special analysis tool that enabled real-time calculations and display of exercise platform data, such as relative slant and ground distances, true and relative bearing angles, and RF and optical horizon calculations. The plug-in adds a special GUI in the SIMDIS toolkit applications that provide the operator, during a Fleet exercise, the ability to select any number of object pairings for monitoring relative angle and range information.

Another plug-in developed for the SCORE range focuses on exercise events. This Event plug-in was developed to read XML-formatted events using the Simple Object Access Protocol (SOAP) on a standard TCP/IP network connection. The events are items such as marking buoy drops during an antisubmarine warfare exercise, and are entered into a separate non-NRL application by the exercise operators. This application acts as a server, providing the data over the network using the SOAP protocol. The Event plug-in then receives and displays the information on the SIMDIS 3D application for use by the local and remote exercise operators.

The SCORE Pan Tilt Zoom (PTZ) Control plug-in monitors and directs range surveillance cameras located on San Clemente Island. Using track data sources fused and visualized by the SIMDIS application, SCORE operators track platforms and view the digital video of remote cameras in real-time. Figure 13 shows the PTZ Control plug-in tracking a ship with SIMDIS. It pictures the method for directing a camera

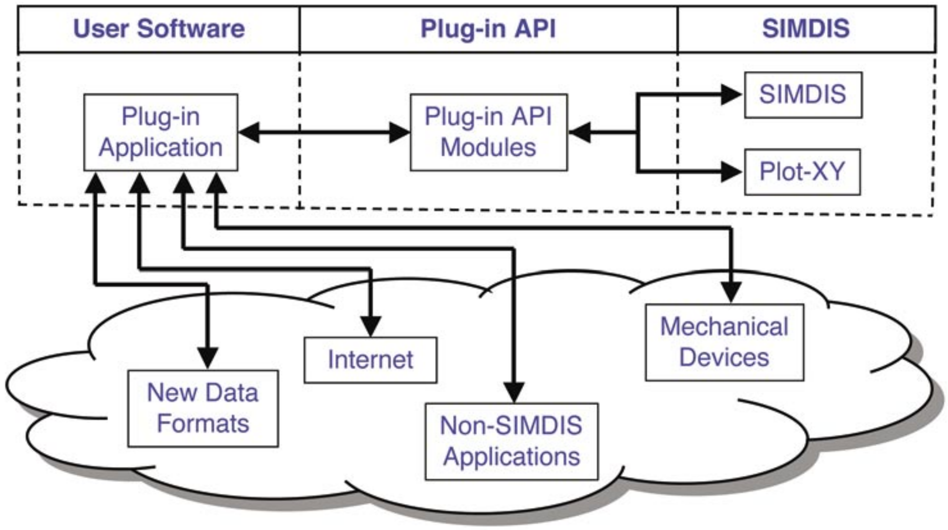

FIGURE 12
Integration of external data sources with SIMDIS through the plug-in API.

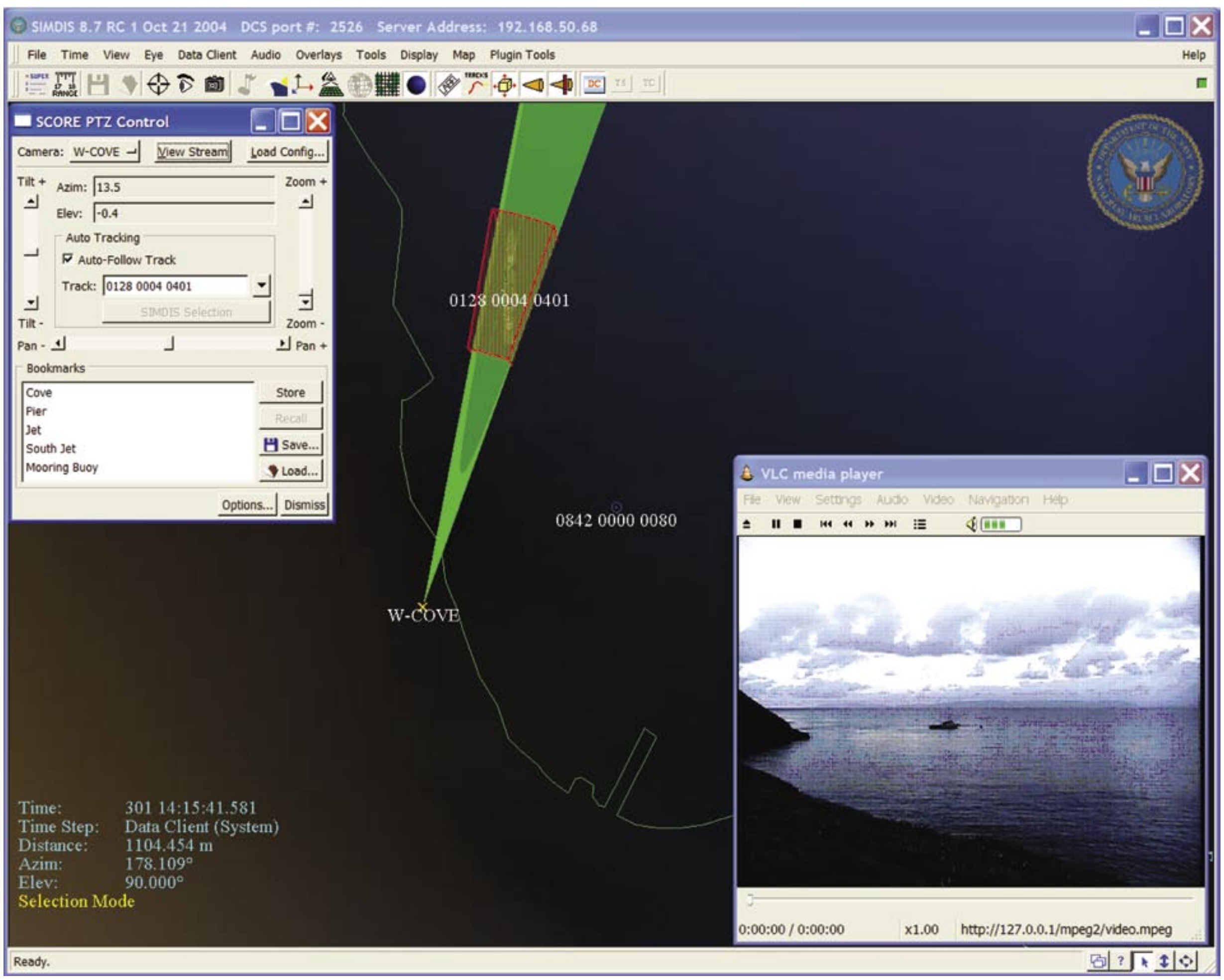

FIGURE 13
SCORE PTZ Control plug-in directs a camera to follow the radar track of a ship and simultaneously displays the live video.

to view the ship, as well as the real-time streamed video display.

The Pacific Missile Range Facility (PMRF) has sponsored the development of a new two-dimensional GOTS open-source plotting application, called Plot-XY. Plot-XY is designed to be compatible with the SIMDIS plug-in API, so that plug-ins written for one application can be loaded by the other. The plot application relies solely on plug-ins to supply data for graphing. Plug-ins are included in the Plot-XY distribution for reading native SIMDIS file formats, the SIMDIS Data Client Server (DCS) network format, and the PMRF iNet network and file formats. Plot-XY is easily configured to import other data formats through plug-ins.

Summary: The NRL SIMDIS toolkit continues to gain acceptance within the DoD community. The addition of the powerful plug-in API capability is a much-needed enhancement. It allows users to modify and add capabilities to satisfy their own requirements. Users can add these capabilities without the need to understand or even possess the SIMDIS source code. The plug-in API also allows greater modularity in adding new features, resulting in a more maintainable baseline of the SIMDIS toolkit. Overall, the plug-in API will be of great benefit as common modules are shared, providing an impetus and mechanism to encourage greater software reuse and interoperability within the DoD community. For more information on SIMDIS, visit the website at https://simdis.nrl.navy.mil.

[Sponsored by SCORE and PMRF] ★

Materials Science and Technology

Photo caption: A V-2 rocket at its launch pad at the White Sands Missile Range in New Mexico. These rockets first flew in 1946 and were used by NRL scientists, including Richard Tousey and Herbert Friedman, to establish a program of space science that still exists at NRL.

Transparent Ceramics: Magnesium Aluminate Spinel

G.R. Villalobos, J.S. Sanghera, and I.D. Aggarwal
Optical Sciences Division

Motivation: There is a need for high-strength, rugged materials that transmit in the visible and mid-infrared (0.4 to 5 μm) wavelength region. These materials are needed for applications requiring transparent armor, including next-generation high-speed missiles and pods, as well as protection against improvised explosive devices (IED).

Material Selection: Silicate glasses are suitable for most common window uses, but they are too weak to be used as a practical transparent armor and as windows and domes in high-speed missiles and pods. Additionally, missile domes and pod windows must transmit to 5 μm but silicate glasses do not transmit well beyond 2 μm. Zinc sulfide transmits to beyond 5 μm, but it is too weak to be used. However, magnesium aluminate spinel is a polycrystalline ceramic material that has excellent optical and mechanical properties. It transmits from 0.2 to 5.5 μm, and ballistic testing has shown that 1/4 in. of spinel has the same resistance as 2.5 in. of bulletproof glass. Spinel is, therefore, an excellent candidate for transparent armor in light vehicles and goggles or face shields on infantry helmets. Unfortunately, there is no transparent spinel product in the marketplace, despite the fact that it has been studied sporadically since the 1960s. A review of the literature clearly indicates that attempts to make high-quality spinel have failed to-date because the densification dynamics of spinel are poorly understood.

Dynamics of Densification: Spinel is generally densified with the use of LiF sintering aid. Without LiF sintering aid, the material tends to be translucent, gray, and highly scattering. It is widely known that the LiF vaporizes during densification and must be removed from the material before complete consolidation or it will manifest itself as white cloudy regions.

We conducted extensive research into the dynamics involved during the densification of spinel. This research has shown that LiF, although necessary, also has extremely adverse effects during densification. Additionally, its distribution in the precursor spinel powders is of critical importance. These discoveries have allowed NRL to fabricate spinel to high transparency with extremely high reproducibility that will enable military and commercial use of spinel.

Figure 1 is a high-resolution scanning electron microscope (SEM) micrograph of a cloudy area showing that it is composed of small (300-500 nm) crystals that have not densified. Energy dispersive spectroscopy (EDS) analysis suggests that the small grains are made up of an MgO-rich phase. MgO has a considerably higher melting temperature than spinel and will not densify as readily at the lower sintering temperatures used for spinel. The pores and small crystals lead to optical scattering, resulting in the cloudy regions. It became apparent that LiF preferentially reacts with the Al_2O_3 in spinel, thereby leaving MgO-rich areas behind.

Inhomogeneous distribution of the LiF in the precursor powders further degrades the ability to densify spinel. Areas with large amounts of LiF react to a greater extent than those having the correct amount, while the areas deficient in LiF do not densify completely and leave large amounts of porosity. Tradition-

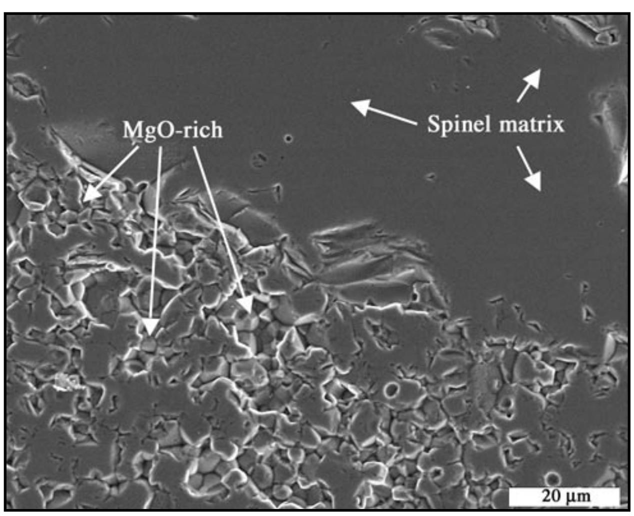

FIGURE 1
Small grained, partially sintered MgO-rich phase in $MgAl_2O_4$ spinel matrix.

ally, common wisdom has been used to increase the amount of LiF to increase the likelihood of having LiF throughout the spinel powder. Unfortunately, this just increased the extent of the LiF/Al_2O_3 reaction zones.

NRL Breakthrough: Traditional bulk mixing processes used to mix sintering aid into a powder leave a fairly inhomogeneous distribution of sintering aid that must be homogenized by extended heat treatment times at elevated temperatures. The homogenizing temperature for LiF/spinel occurs at the temperature of fast reaction between the LiF and the Al_2O_3. To avoid this, we developed a new process that uniformly coats the spinel particles with the LiF sintering aid. This allows us to reduce the amount of LiF necessary for densification (since we do not have to compensate for LiF-deficient regions) and to rapidly heat through the temperatures of maximum reactivity. Figure 2 compares spinel disks densified with and without using the NRL technique. The traditional sample appears opaque because of the high degree of optical scattering, while the NRL sample is transparent. The transmission of the NRL sample is within 1% of the maximum theoretical bulk transmission. Antireflection coatings will increase the total transmission to >99%. These results make spinel the de facto material of choice for transparent armor applications.

Conclusion: NRL has identified various reactions that had previously prevented the densification of magnesium aluminate spinel to high transparency and high yield. Based on these discoveries, we have developed particle-coating techniques that are used to routinely fabricate transparent spinel with extremely high reproducibility. Consequently, a company is pursuing a technology licensing agreement to manufacture spinel to enable its use as an armor material for personnel and light vehicle protection against small arms and improvised explosive devices as well as many other applications. The availability of spinel windows and domes will impact both military and commercial applications.

[Sponsored by ONR] ★

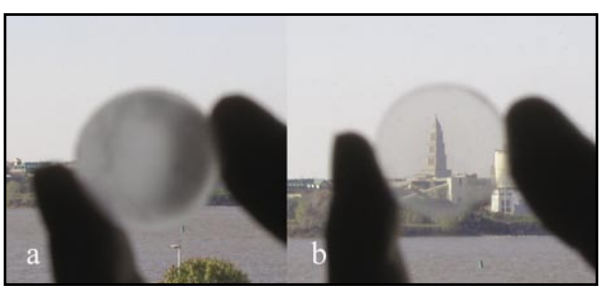

FIGURE 2
Looking across the Potomac River to the Masonic Temple, approximately two miles. (a) Traditional mixed spinel (b) NRL developed transparent spinel.

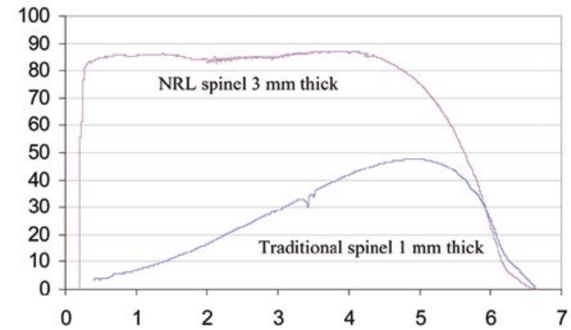

FIGURE 3
NRL spinel transmits within 1% of the theoretical bulk transmission throughout its range, while the traditional spinel has poor transmission resulting from scattering losses.

Surface Hardening with LAPPS

D. Leonhardt, S.G. Walton, and R.A. Meger
Plasma Physics Division
C. Muratore
Wright-Patterson Air Force Base

Introduction: LAPPS (Large Area Plasma Processing System) was invented[1] in NRL's Plasma Physics Division and Materials Science and Technology Directorate. It uses a 2-5 keV electron beam to ionize and dissociate gas molecules, species that are then used to modify the surface properties of various materials. This novel approach to plasma generation provides a direct scalability of the system and higher control over reactive chemical species compared to conventional plasma processing systems used in the semiconductor and coatings industries. The scalability is simply dictated by the dimensions of the electron beam, allowing unprecedented surface areas to be treated uniformly. The process/chemical control is provided by the electron beam/molecule interactions, which ensures that all chemical reaction pathways are accessible, as opposed to conventional plasma systems.

The ability to increase the hardness of a material while preserving its intrinsic properties provides tremendous advantages in choosing materials for demanding applications. Thin layers of well-known hard coatings are frequently used, but adhesion problems (lattice and temperature coefficient matching) limit their utility. For metals, incorporating nitrogen into the surface's lattice (surface nitriding) is highly desirable because the nitrided layer is physically part of, yet significantly harder than, the bulk material. Equally important in surface nitriding is maintaining sufficiently low temperatures to preserve the properties of the bulk material.

Technical Approach: The unique plasma chemistries provided by LAPPS are ideal for surface nitriding; large amounts of atomic nitrogen species (N^+ and N) are produced[2] in these plasmas, independent of workpiece or system configuration. Figure 4 (top) shows the generalized layout of LAPPS, including a voltage/temperature controlled substrate stage. The middle photo of Fig. 4 shows the working device with a 0.5^2-m active area, generated by a 2 keV e-beam that is 1-cm thick by 50 cm wide (into photo) and travels 1 m in the vacuum chamber. The bottom picture shows an end-on view of the device interior configured for wafer processing (wafers in photo are 150 mm in diameter).

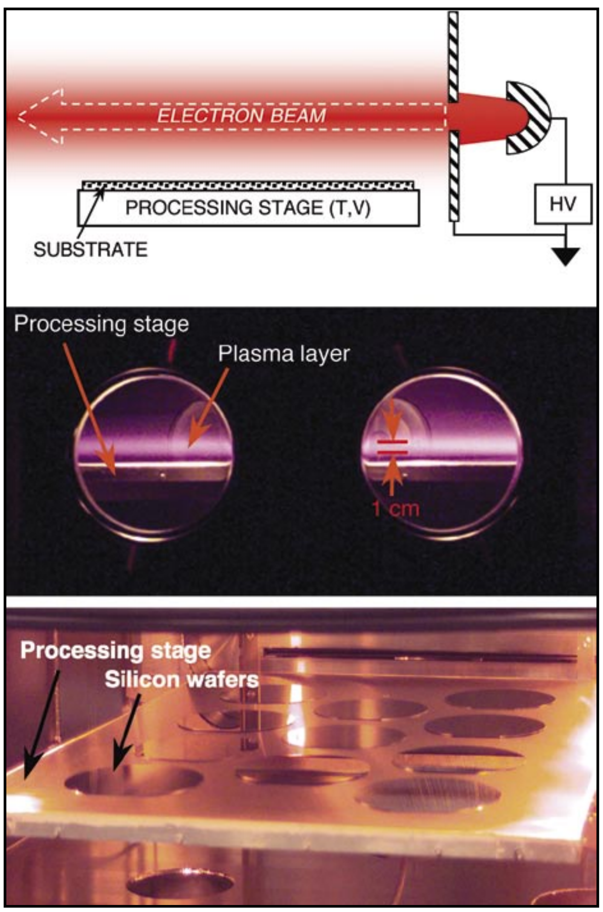

FIGURE 4
Large Area Plasma Processing System (LAPPS) layout(s). Top figure is schematic representation of electron beam, plasma source, and materials' processing stage. Middle photo is 0.5 × 1 m (×1 cm) LAPPS, with nitrogen working gas. Bottom photo is end-on-view of LAPPS (electron beam would emerge from slot at top of photo) showing multiwafer processing capability.

To produce nitrided surfaces in stainless steel, pieces of stock architectural material (3-mm thick) were exposed to nitrogen-based plasmas produced in a smaller (15 × 30 cm active area) system. To improve nitrogen diffusion into the surface, the substrate was heated to temperatures between 325 and 462 °C, and biased to –350 Vdc to reduce oxide formation via ion bombardment (sputtering). This nitriding rate increased with temperature, however, at 462 °C the corrosion resistance of the bulk material was compromised because of chromium nitride precipitation in the stainless steel.

Nitriding in LAPPS allows a chemical activation energy of 1.4 eV/atom, which is lower than any previously reported nitriding process and means that high nitriding rates occur at low temperatures. The hardness of the surface was also increased by a factor of six at all of the temperatures. Further scientific studies[2,3] showed that these dramatic improvements were correlated with the high flux of atomic nitrogen (N^+ and N) generated in LAPPS. These critical species, particularly the atomic ion, are more abundant in these plasmas because of the availability of the appropriate reaction pathways. By incorporating more atomic ion flux in this process, the reactive chemical (atomic nitrogen) component is used in conjunction with the additional localized energy (ion kinetic energy from the external bias), effectively delivering species to the surface that both sputter clean and promote surface diffusion.

Figure 5 shows the results of stainless steel nitriding at 462 °C in LAPPS. The top photograph is a cross sectional view of a sample that was chemically etched to clearly show the interface between the nitrided surface layer and bulk material. The bottom plot is the surface hardness measured along the workpiece cross section, showing the transition from the bulk material (2.6 GPa) to the nitrided surface (>15 GPa). The inset photo shows the impression left by the indenter (hardness measurement). The bulk stainless steel material shows significant deformation by the indenter while the nitrided surface was only slightly marred. From the thickness of the nitride layer and assuming a diffusion-controlled nitride layer growth mechanism, an average growth rate of 6.5 $\mu m/h^{1/2}$ is obtained for this LAPPS process, the highest value reported for a plasma-based stainless steel nitriding process.

Summary: The ability to improve the surface wear of critical components without changing a material's desirable characteristics is of paramount importance in many military and commercial applications. The

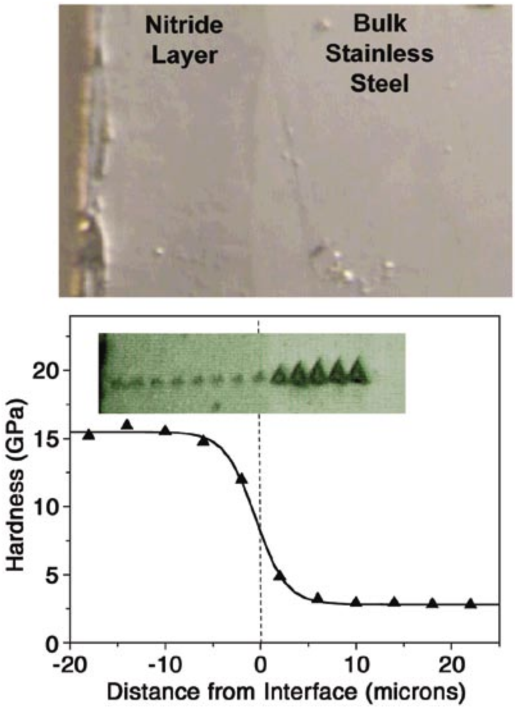

FIGURE 5
Cross sectional views of stainless steel surface nitrided in nitrogen-based LAPPS. Top photo shows chemically etched cross section where the interface between the nitrided surface and bulk material can be clearly seen. Bottom plot shows the variation in surface hardness across interface; inset photo shows indentations left behind from hardness measurements.

LAPPS tool has demonstrated tremendous capabilities in nitriding the surface of stainless steel, primarily due to the large flux of useful nitrogen species it can produce. The increased ion flux to the surface, along with a large nitrogen atom flux, allowed nitride layers to be produced at low processing temperatures (< 460 °C), preserving the intrinsic corrosion-resistant properties of the bulk stainless steel throughout the material. Applying this technique to other metals offers promising capabilities to the Navy's present and future forces.

[Sponsored by ONR]

References

[1] S.G. Walton, D. Leonhardt, C. Muratore, R.F. Fernsler, and R.A. Meger, "Electron Beam Enhanced Nitriding Systems (EBENS)," U.S. Patent 5,874,807, issued February 23, 1999; see also Navy Case Number 96,085, submitted June 22, 2004.
[2] C. Muratore, S.G. Walton, D. Leonhardt, R.F. Fernsler, D.D. Blackwell, and R.A. Meger, "The Effect of Plasma Flux Composition on the Nitriding Rate of Stainless Steel," *J. Vac. Sci. Technol. A* **22**, 1530-1535 (2004).
[3] C. Muratore, D. Leonhardt, S.G. Walton, D.D. Blackwell, R.F. Fernsler, and R.A. Meger, "Low Temperature Nitriding Rate of Stainless Steel in an Electron Beam Generated Plasma," *Surf. Coat. Technol.* **191**, 255-262 (2005).

★

Cavitands: Container Molecules for Surface Plasmon Resonance (SPR)-Based Chemical Vapor Detection

D.K. Shenoy
Center for Bio/Molecular Science and Engineering

Introduction: Hazardous chemical vapors pose a serious challenge to the security and well-being of our nation and to our forces abroad. These can be dangerous chemical warfare agents (CWAs) and explosives or health hazards such as toxic industrial chemicals and materials (TICs and TIMs). A long-standing problem with chemical vapor detectors is their susceptibility to false alarms, which results in disruption of normal activities. In detectors that use a chemically sensitive coating layer, such false alarms are caused by inadequate selectivity toward target molecules. Therefore, there is a critical need to develop novel chemical coatings that can enhance selectivity of detection for specific targets or analytes. Cavitands solve this problem by enhancing the selectivity of detection towards chemical vapors.

Cavitands: Inspired by the exquisite specificity of biomolecules such as antibodies for target antigens, supramolecular chemistry is attempting to do the same for small molecule targets through the use of synthetic receptors called cavitands.[1] These molecules have the potential to be selective, because of their unique biomimetic nanostructures. Cavitands derive their name from the shape of their cavities (Fig. 6). These molecules are designed to bind target molecules to form guest-host complexes. By tuning the cavity depth, shape, and chemical functionality that controls the synergistic interactions with analyte molecules, cavitands for a range of molecular targets may be designed and synthesized. This strategy for selectivity-enhancement is fundamentally different from that used in other chemically selective coatings (for example, polymers) that rely on the solubility of the targets with the coating layer.

Although target molecules may bind selectively to such tailored cavitand molecules, it is equally important to transduce the binding event by using an appropriate technique that has high sensitivity. We show that, by using a real-time, label-free, optical technique called surface plasmon resonance (SPR, see Fig. 7), refractive index changes induced by analyte-cavitand interactions provide selective signals for sensitive chemical vapor detection.

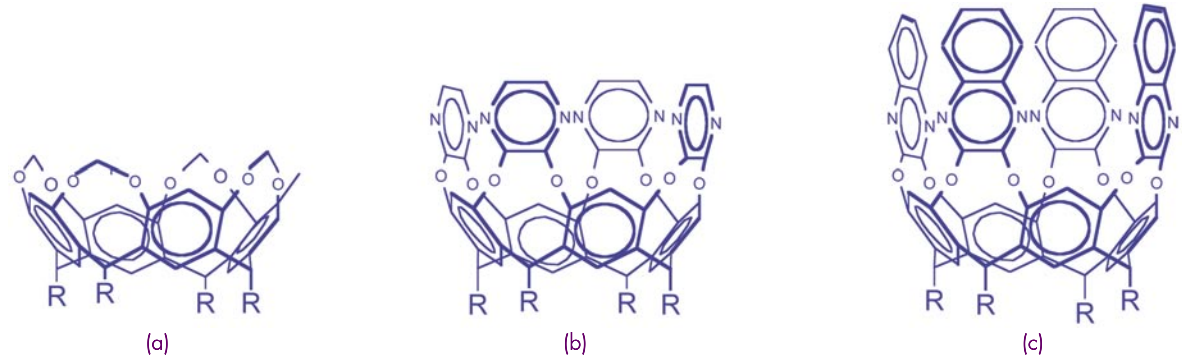

FIGURE 6
Three cavitands: (a) MeCav (methylene-bridged), (b) PzCav (pyrazine-bridged), and (c) QxCav (quinoxalines-bridged) with varying depths and therefore complexing ability with target molecule.

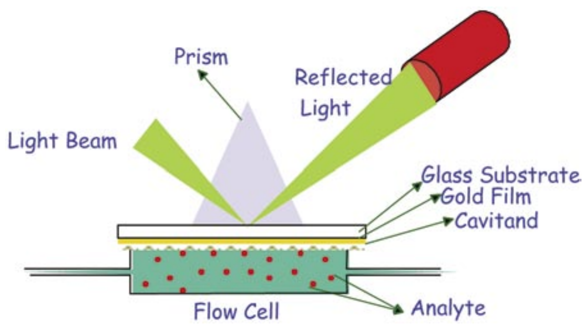

FIGURE 7
The surface plasmon resonance (SPR) experimental arrangement using angular interrogation.

Cavitands are evaluated at NRL through a collaboration with Professor Enrico Dalcanale at the University of Parma, Italy. Three cavitands named MeCav (for methylene-bridged), PzCav (pyrazine-bridged), and QxCav (quinoxalines-bridged) were chosen to demonstrate selectivity toward aromatic vapors. The presence of alkyl tails (R) at the bottom of the cavity is to make them soluble in common solvents such as chloroform. Cavitand solutions (0.38 mM) in chloroform were spin coated onto surface plasmon resonance substrates (50-nm thick gold-coated cover glass). Spin coating was performed at 4000 rpm for 60 s at room temperature. The spin coating parameters gave a film thickness (confirmed using spectroscopic ellipsometry) of nearly 4 nm. For targets, a variety of analyte vapors belonging to different chemical classes were studied. QxCav with the deepest cavity was designed to form guest-host complexes with aromatic vapors, whereas cavitands with shallower cavities (such as MeCav and PzCav) were not expected to be as selective toward such guest molecules.

Surface Plasmon Resonance (SPR): An SPR experimental set up based on the Kretschmann configuration (Fig. 7) was used for all the measurements. The glass prism, made of standard BK7 glass (refractive index n = 1.5, Howard Jonson Optical Laboratories), was index matched to the gold-coated cover glass that was used as the sample substrate (n = 1.51) using an index-matching liquid from Cargille Inc. The thickness of the gold film was nominally 50 nm, and it had an underlying chromium adhesion layer of about 2-nm thickness. A 635-nm diode laser (Lasermax, Inc.) was used as the light source. A Glan Thompson linear polarizer (Karl Lambrecht, Inc.) was placed in the path of the light beam to ensure that only p-polarized light (surface plasmons are excited by p-polarized light) was incident on the glass prism. The reflected light was monitored using a photodiode (818 Series, Newport Corporation) calibrated for the chosen wavelength. Variable angles were selected by means of a stepper-motor-controlled goniometer with an angular resolution of 0.01 deg. The experimental data acquisition system was computer-controlled, with a typical angular scan (from 40 to 80 deg) taking about 8 min.

SPR Shifts: Figure 8 shows surface plasmon angle shifts observed due to three different cavitands that were spin-coated onto three separate SPR substrates. The red curve with the smallest plasmon angle minimum (~ 46 deg) is that from a bare gold substrate with no cavitand coated; successively higher shifts were obtained due to MeCav, PzCav, and QxCav coated substrates, respectively. It is observed (see Fig. 6) that the presence of polarizable groups on the molecules causes a larger shift of the plasmon angle (plasmon angle increase follows the sequence QxCAv > PzCAv > MeCav). These baseline shifts were subtracted from the signal due to interaction of cavitands with analyte vapors.

Cavitand Selectivity toward Chemical Vapors: Figure 9 shows the plasmon angle shifts due to the

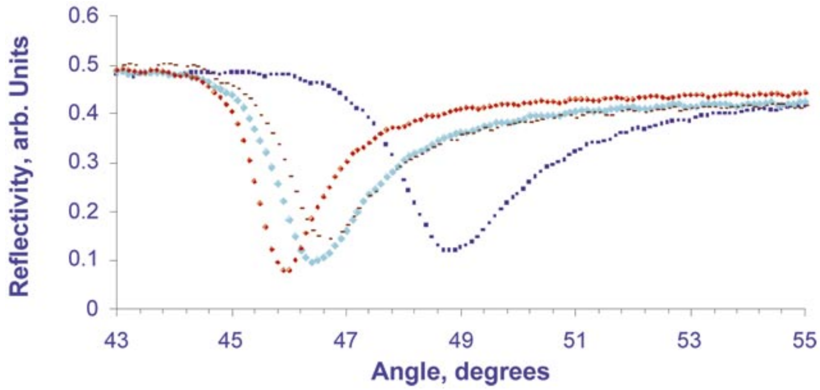

FIGURE 8
Minima in each of the raw data curves corresponds to the surface plasmon angle. The plasmon angle minima starting from left to right are for (a) bare gold, (b) MeCav-coated substrate, (c) PzCav-coated substrate, and (d) for QxCav-coated substrate.

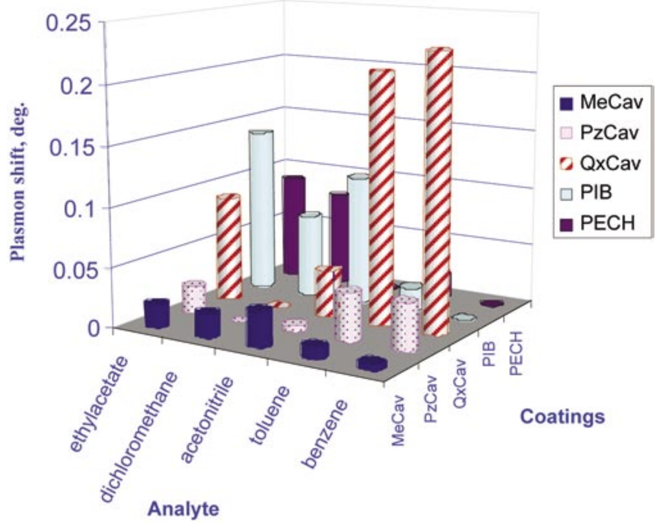

FIGURE 9
Selectivity patterns observed for different chemical vapors using the three cavitands, MeCav, PzCav, and QxCav. The comparison is for a fixed concentration of 100 ppm for all vapors. Also shown for comparison are the results for the polymer coatings, PECH and PIB. The quinoxalines-bridged cavitand molecules, QxCav, are highly selective toward aromatic vapors due to the complementary cavity size and interactions.

interaction of various target analytes belonging to vapors of different chemical classes (ethyl acetate, dichloromethane, acetonitrile, toluene, and benzene) with the three different cavitands. For comparison of the selectivity of the cavitands with other sensing layers, we carried out similar experiments with polymer-coated layers. Specifically, the signals obtained due to exposure of the same vapors with two polymer coatings, polyepicholorhydrin (PECH) and polyisobutylene (PIB), were compared. These specific polymer coatings have been demonstrated in the past to show selective response toward aromatic vapors. Figure 9 shows that, for a given concentration of the vapors (100 ppm), the polymer sensing layers do not generate an observable signal. This is despite the fact that the polymer films were about twice as thick as the cavitand films obtained under identical spin-coating conditions. This clearly demonstrates the higher selectivity of the cavitands.

As pointed out earlier, the depth of the cavitands plays a role in selectivity. MeCav, with a shallow cavity, shows hardly any response toward the aromatic vapors, while PzCav, with a slightly deeper cavity, shows a signal well above baseline. However, QxCav, with the deepest cavity, shows the largest SPR signal response toward the aromatic vapors, benzene and toluene.[2] Clearly therefore, the enhancement in selectivity due to the size and shape of the cavities plays an important role in enhancing the signal due to the cavitand-analyte interactions. Figure 9 shows a pattern of response to several analytes using the cavitand and polymer sensing films. Such patterns may be used with pattern recognition algorithms to identify known and possibly unknown analytes. This has the additional advantage of higher signal response due to the high selectivity of cavitands. We have also recently shown that the morphology of the cavitand-coated film does not influence the selectivity.[3] This will allow simple industrial processes to be used for coating cavitand films onto sensor surfaces.

The interaction forces that stabilize the guest-host complexes (between cavitand and target analyte) are noncovalent in nature. This allows us to recycle the cavitands in a sensor and can be accomplished either by raising the temperature of the coating layer or forcing a stream of nitrogen gas over it. An important feature of the cavitands is that they are highly robust, synthetic receptors. This allows them to be integrated into rugged detectors.

Conclusions: Cavitands have been shown to be highly promising as supramolecular nanostructures for the selective complexation of chemical vapors. This selectivity arises due to the size, shape, and interaction complementarity between the target analyte and cavitands. The methylene-bridged cavitands (MeCav) with shallow cavities do not complex aromatic vapors, the pyrazine-bridged cavitands (PzCav) show intermediate selectivity, whereas the quinoxalines-bridged cavitands (QxCav) with the deepest cavities show the best selectivity for aromatic vapors. A comparison with polymer coatings, PECH and PIB, shows that cavitands have higher selectivity despite the fact that the polymer coatings are more than twice the thickness of the spin-coated cavitand films. Combined with the fact that cavitands are robust synthetic receptors, they are promising materials for the selective detection of hazardous chemical vapors. We have recently shown that a new SPR system based on wavelength interrogation with real-time detection capabilities can be used to obtain sub-ppb sensitivity to DMMP (sarin simulant) vapors. The next challenge is to demonstrate the selectivity of cavitands in real-world environments where interferents are present. We expect the high selectivity of cavitands to significantly reduce the false alarm rate in future chemical detectors.

Acknowledgments: I wish to acknowledge Dr. E. Feresenbet, my former NRC Research Associate, Prof. E. Dalcanale at the University of Parma, Italy, and Dr. C. Dulcey at NRL for the SPR set up.

[Sponsored by ONR and the Joint Services NMCBD Program]

References

[1] D.J. Cram and J.M. Cram, "Container Molecules and Their Guests," *Monographs in Supramolecular Chemistry*, Royal Society of Chemistry, ed. J.F. Stoddart, U.K., 1994.

[2] E. Feresenbet, E. Dalcanale, C. Dulcey, and D.K. Shenoy, "Optical Sensing of the Selective Interaction of Aromatic Vapors with Cavitands," *Sensors Actuators B* **97**, 211-220 (2004).

[3] D.K. Shenoy, E. Feresenbet, and E. Dalcanale, "Effect of Thin Film Processing on Cavitand Selectivity," *Langmuir* **19**, 10454-10456 (2003).

★

Seawater Deoxygenation: Problem or Solution?

J.S. Lee, R.I. Ray, and B.J. Little
Oceanography Division
E.J. Lemieux
Chemistry Division

Background and Motivation: Laboratory experiments were designed to test the hypothesis that oxygen is required for aggressive corrosion of carbon steel exposed to natural seawater. Uncoated carbon steel was maintained for 1 year under the following stagnant conditions: (1) natural seawater open to air, and (2) anaerobic natural seawater stripped of oxygen. Hamilton[1] recently proposed a model for corrosion of carbon steel due to anaerobic sulfate-reducing bacteria (SRB) in which sulfate, an intermediate electron acceptor, is reduced to sulfide. In his model, sulfide reacts with iron to form a corrosion product that ultimately transfers electrons to oxygen. Consistent with that model, most reported cases of aggressive SRB-induced corrosion of carbon steel in marine waters are in environments with some dissolved oxygen in the bulk medium. However, Hamilton's theory does not address corrosion rates in anaerobic waters with multiple electron acceptors.

Experimental Chambers: Chambers were built to expose carbon steel to natural seawater with and without oxygen (Fig. 10). Epoxy-mounted carbon steel coupons were oriented in rows both vertically and horizontally to simulate tank sidewalls and bottoms, respectively. Chambers were filled with natural seawater from the Naval Research Laboratory's Corrosion Facility at Key West, Florida. Seawater was deoxygenated using a premixed inert gas containing CO_2. The chamber filled with natural, oxygenated seawater was open to air via a 1-in. tube. The chamber filled with anaerobic water was maintained in an anaerobic hood with an atmosphere of 5% CO_2, 10% H_2, and the balance N_2.

Electrochemical Methods and Results: Open-circuit potential (E_{corr}) was monitored continuously, and linear polarization resistance (LPR) measurements used to determine polarization resistance (R_p) were performed on each sample every 1-3 months. The inverse ($1/R_p$) is the proportional instantaneous corrosion rate, given in ohms^{-1}. Figure 11 shows the average E_{corr} values by row. E_{corr} values for all samples started at approximately –0.75 $V_{Ag/AgCl}$. No appreciable difference in E_{corr} was observed as a function of placement

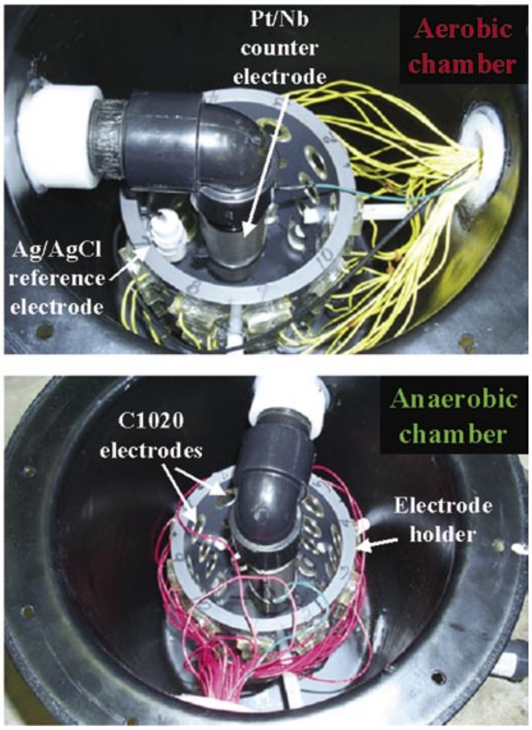

FIGURE 10
Heavy gauge plastic experimental chambers each containing Ag/AgCl reference electrode, Pt/Nb mesh counter electrode, cylindrical electrode holder, and 36 individually addressable C1020 electrodes (27 vertically orientated, 9 horizontally orientated).

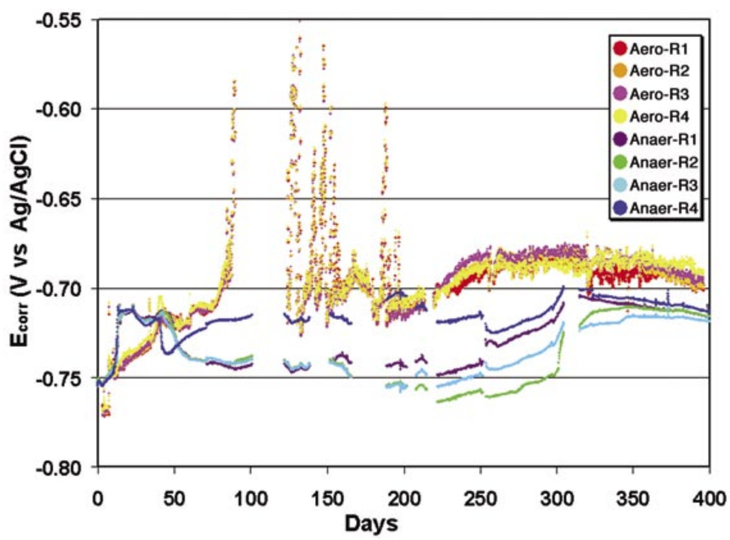

FIGURE 11
Average E_{corr} (vs Ag/AgCl) over time values for C1020 samples in stagnant aerobic (aero) and anaerobic (anaer) conditions displayed by row (R). R1, R2, R3 – vertically orientated samples, with R1 being at the top of the tank, R3 toward the bottom, and R2 between the two. R4 – horizontally orientated sample at the bottom of the tank.

in the aerobic chamber. In contrast, stratification of E_{corr} values was observed between rows in the anaerobic chamber. $1/R_p$ values, calculated for each electrode, were averaged by row and exposure type (Fig. 12(a), (b)). Between 23- and 35-days, corrosion rates for all samples were relatively low with the lowest in the anaerobic chamber (Fig. 12(c)). At the same time, $1/R_p$ values indicated stratification within the aerobic chamber. Row 1 electrodes, closest to the air/water interface, had the highest average corrosion rate, while row 4 electrodes had the lowest. After more than 100 days exposure, the $1/R_p$ measurements indicated that the highest instantaneous corrosion rate was measured in the horizontal (bottom, row 4) coupons exposed to anaerobic seawater. In general, instantaneous corrosion rates for the anaerobic condition were two orders of magnitude higher than the aerobic condition.

Corrosion Morphology: Corrosion products formed under aerobic and anaerobic seawater conditions were predictably different in appearance and composition. Under aerobic conditions, iron oxides

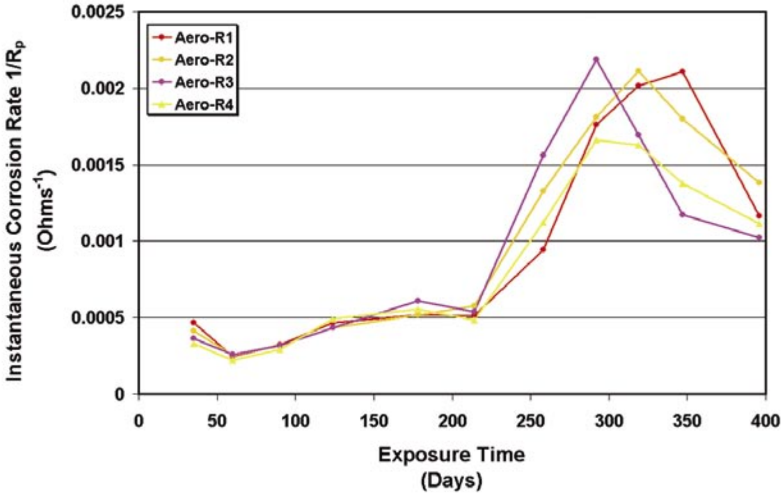

(a)

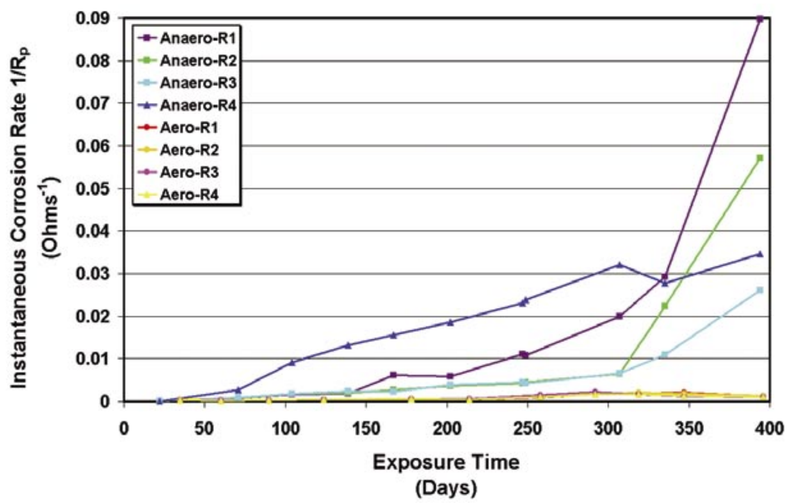

(b)

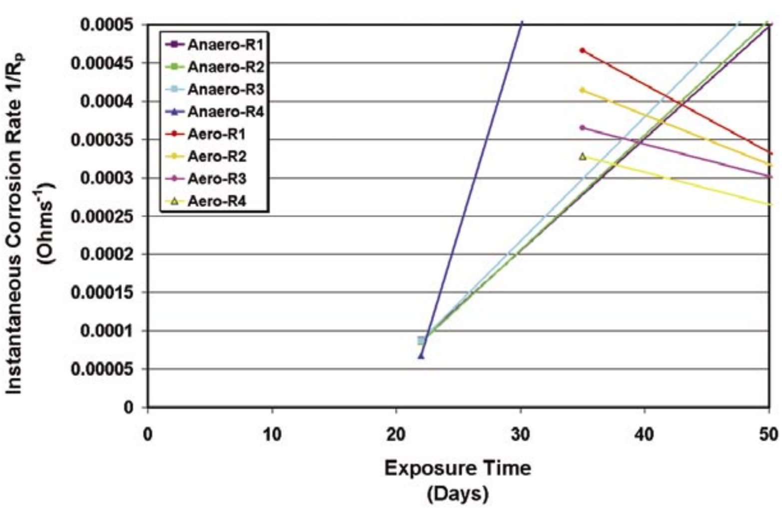

(c)

FIGURE 12

$1/R_p$ (instantaneous corrosion rate) over time (days) for C1020 samples in stagnant (a, b) aerobic and (b) anaerobic conditions. Aer

rates are shown in (c) for both aerobic and anaerobic conditions. R1, R2, R3 – vertically orientated samples, with R1 being at the top of the tank; R3, toward the bottom, and R2 between the two. R4 – horizontally orientated sample at the bottom of the tank. Average values displayed.

persisted on the surfaces of all coupons/orientations throughout the experiment and corrosion was uniform. Coupons exposed in anaerobic seawater were covered with black iron sulfide corrosion products and corrosion was localized (i.e., pitting). Iron sulfides are inherently unstable, and their disruption can give rise to corrosion cells between iron sulfide in direct electrical contact with the underlying steel (cathode) and the exposed-steel surface (anode).

Consequences of Deoxygenation: Experiments described here demonstrate that corrosion of carbon steel is more aggressive under totally anaerobic conditions compared to exposures in oxygenated seawater. Corrosion was more severe on the horizontally oriented samples than on the vertically oriented coupons in both exposure conditions. Corrosion of carbon steel exposed under totally anaerobic conditions was typical microbiologically influenced corrosion by sulfate-reducing bacteria (SRB). Microbial populations increased over 5 orders of magnitude in the anaerobic chamber. Hamilton[1] concluded that the activities of microorganisms produced kinetically favored pathways of electron flow from the metal anode to the universal electron acceptor, oxygen. He observed that microbial ecosystems are characterized by aerobic and anaerobic zones that operate as a continuum via redox couples. Interactions between oxygen and sulfate depend on redox cycling via intermediate electron carriers. Hamilton further stressed that biofilm growth is a dynamic process and microorganisms within the biofilm are in a constant state of flux. Individual bacterial species and bacterial consortia are characterized by their primary energy source and electron donor and terminal electron acceptor. Oxygen is the terminal electron acceptor for aerobic species, but for anaerobic species (e.g., SRB) there are alternate electron acceptors, including nitrate, sulfate, ferric iron, and CO_2. It is possible that in the complex chemistry of seawater and biofilms there are electron acceptors other than oxygen to drive electron transfer and corrosion reactions.

Summation: Corrosion of carbon steel was more aggressive in totally anaerobic conditions than in aerobic conditions. Anaerobic conditions did not inhibit corrosion, and oxygen was not required for aggressive localized corrosion. This work indicates the danger of predicting long-term corrosion involving deoxygenation in short time periods (less than 1 month) where results indicate deoxygenation is favorable, as opposed to extended periods where SRB can instigate localized corrosion.

[Sponsored by ONR and UMD]

References

[1] W.A. Hamilton, "Microbiologically Influenced Corrosion as a Model System for the Study of Metal Microbe Interactions: a Unifying Electron Transfer Hypothesis," *Biofouling* **19**, 65-76 (2003).

★

Ocean and Atmospheric Science and Technology

Photo caption: GRAB was the first reconnaissance satellite the U.S. put in orbit. GRAB has recently been donated to the National Air and Space Museum (NASM). It is located right next to the Corona Photo Satellite, which was launched about 2 weeks later. GRAB taught us a great deal about surveillance from space.

A Real-Time Coastal Ocean Prediction Experiment

D.-S. Ko, C. Rowley, P. Martin, R. Allard, J. Dykes,
and R. Preller
Oceanography Division

Introduction: A test of the rapid relocatability of NRL coastal ocean prediction systems was carried out during the Maritime Rapid Environmental Assessment 2004 (MREA04) Trial in the Portuguese coastal waters. The ocean circulation capability was first demonstrated in response to the oil spill from the tanker *Prestige* off the northwest coast of Spain and in support of Operation Iraqi Freedom. A nested Navy Coastal Ocean Model (NCOM) assimilated satellite altimeter sea surface height anomalies, sea surface temperatures, and in situ CTD temperature and salinity profiles collected onboard the NATO Undersea Research Center's (NURC) R/V *Alliance*. The Distributed Integrated Ocean Prediction System (DIOPS) provided real-time predictions of nearshore waves, tides, currents, and surf conditions.

Ocean Circulation Model: An experimental real-time ocean nowcast/forecast system[1] was rapidly developed for the Portuguese coastal waters for the MREA04 Trial. The area of coverage extended from 8°W to 11°W and from 36°N to 40°N. The NCOM ocean model consisted of a 4-km resolution host grid, with a 1-km nested grid covering the central coastal region of the host grid. A 40-layer hybrid vertical grid was used with sigma layers from the surface down to 140 m and fixed-depth layers from 140 m to the bottom. Bathymetry was obtained by combining data from several sources at spatial resolutions ranging from 2 min to 6 s. Figure 1 shows the NCOM grid and bathymetry used during MREA04.

Initial and open-boundary conditions of sea surface elevation, temperature, salinity, and currents were provided by the 1/8th-deg global NCOM that is being run in real time at NRL. Tidal forcing was provided by superimposing tidal elevation and transports on the (nontidal) boundary conditions from global NCOM, providing tidal potential forcing over the interior of the model domain. The tidal boundary data were obtained from the global tidal database developed at Oregon State University.[2] Freshwater discharge was provided for the Mondego, Tagus, Tamega, Sado, and Odelouca Rivers. Atmospheric forcing consisted of hourly fields of surface air pressure, wind stress, solar radiation, and surface heat flux from the 27-km resolution Coupled Ocean Atmosphere Mesoscale Prediction System (COAMPS™) Europe analysis/forecast model.

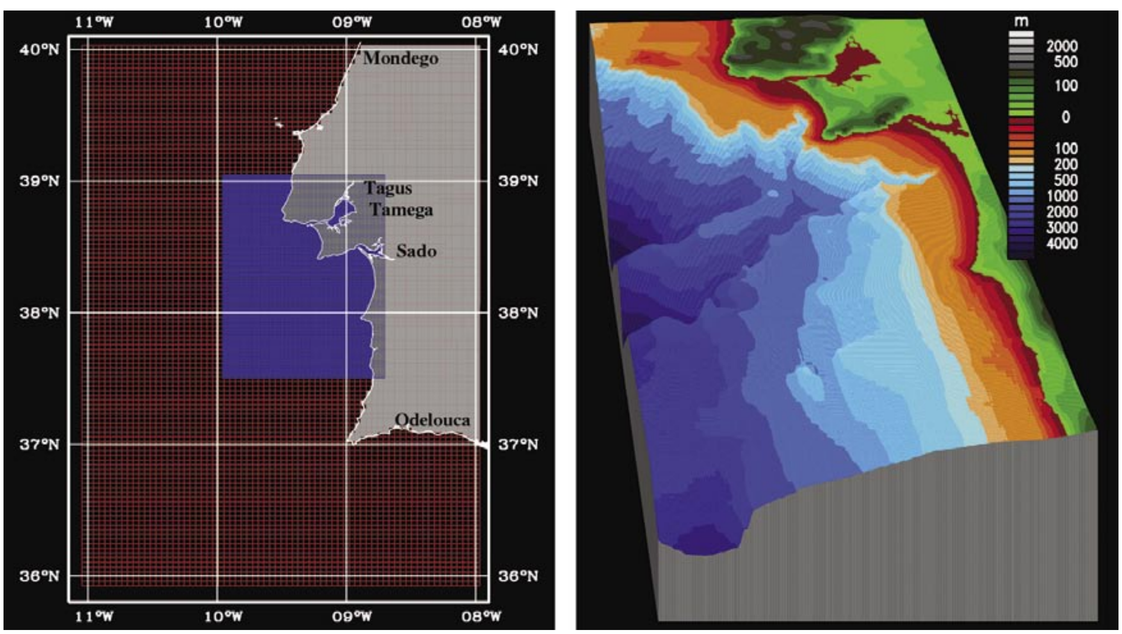

FIGURE 1
Left: Nested NCOM grid for MREA04 Trial. Outer grid (red) has horizontal 4-km resolution inner grid (blue) has 1-km resolution. River discharge locations are annotated. Right: 3D depiction of model topography (m) for 1-km NCOM nest. Note canyon feature that extends close to the coast.

The MREA04 NCOM system provided daily 72-h forecasts of sea level variation and 3D ocean currents, temperature, and salinity fields during the experiment period of 27 March to 18 April 2004. NCOM assimilated temperature/salinity analyses generated from satellite altimeter (GFO, JASON-1, ERS-2) sea surface height anomaly and satellite-derived sea surface temperature. In addition, the nested NCOM system assimilated CTD temperature/salinity profiles collected by the R/V *Alliance* during the MREA04 cruise. A 3D temperature salinity estimation was produced from satellite data using the Modular Ocean Data Assimilation System.[3] The CTD profiles were combined with satellite estimates using an optimum interpolation scheme to produce the analyses. Model sound speed compared well to observations. NCOM output was used by NURC in a prototype surface drift prediction using linear and nonlinear hyper-ensemble statistics on atmospheric and ocean models. Figure 2 (top) depicts a 72-h forecast of surface ocean currents overlaid on sea surface temperature for 10 April 2004. Figure 2 (bottom) shows the different salinity structure obtained when CTD data are assimilated into the NCOM model.

Nearshore Modeling System: DIOPS, a wave, tide, and surf prediction system[4] was run aboard the R/V *Alliance* during the MREA04 Trial during the period 28 March – 11 April 2004. A triple nested SWAN wave model forecast was initialized from wave spectra provided by the Fleet Numerical Meteorology and Oceanography Center. The PCTides tide

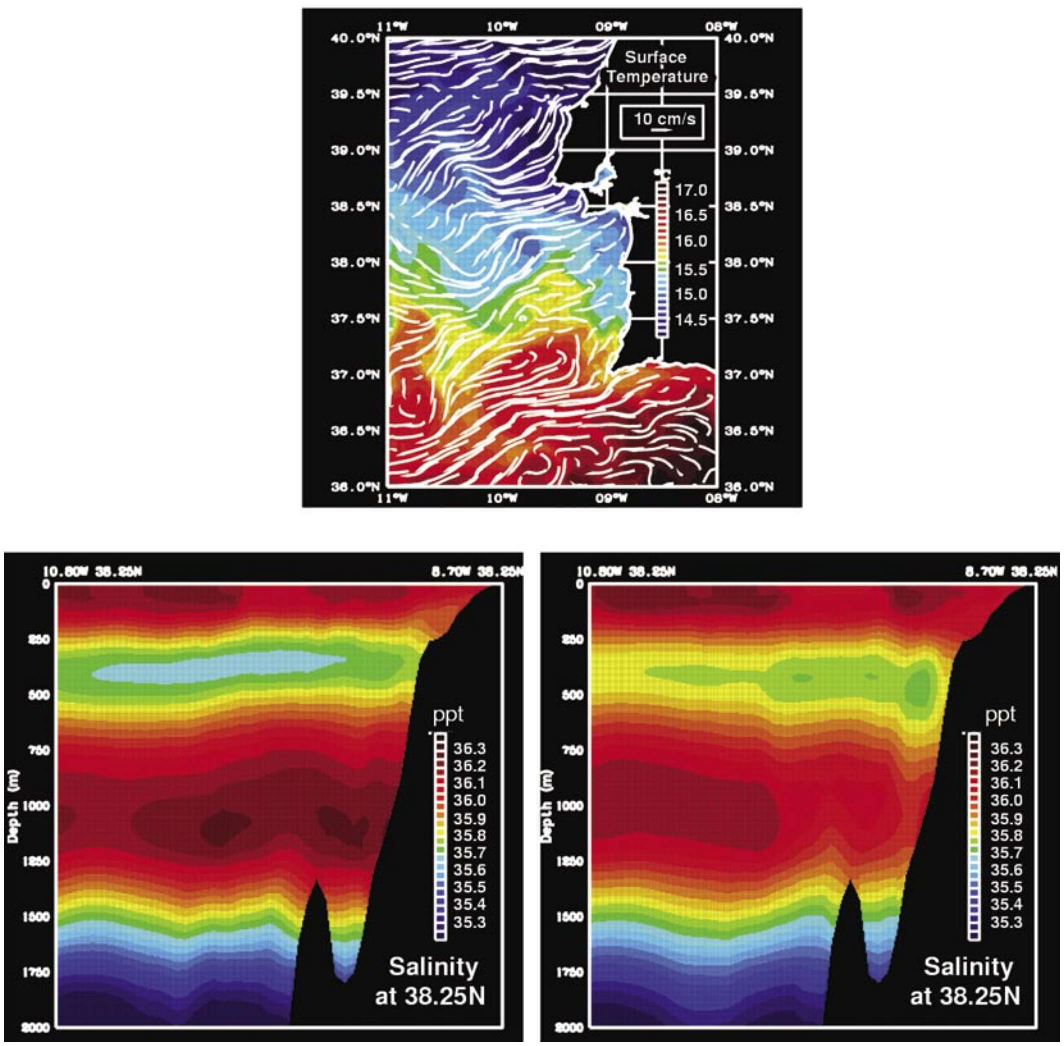

FIGURE 2
Top: NCOM surface analysis for 10 April 2004. White vectors illustrate surface ocean currents overlaid on sea surface temperatures (°C). Bottom: Vertical slice of salinity (ppt) distribution: (left) CTD profiles are assimilated into model; (right) CTD profiles are not assimilated into model.

model provided 48-h predictions of water levels near Pinheiro da Cruz, Portugal. Both wave and tide predictions were used in nearshore wave models and by international hydrographic survey teams. Figure 3 shows the SWAN nested model grid with resolutions ranging from 20 km (host grid) to 1 km near the coast (inner blue box). The Delft3D modeling system provided 10-m resolution nearshore wave and circulation predictions near Pinheiro da Cruz, Portugal. The nearshore modeling was complemented with a beach survey experiment in which video cameras and three NORTEK current meters were deployed. Modeled wave height and direction (Fig. 3) show very good agreement with a Portuguese WaveRider buoy near Sines (97-m water depth). PCTides water levels shown in Fig. 3 compare favorably with in situ data, with tidal amplitude RMS errors of 1 cm and phase errors less than 10 min.

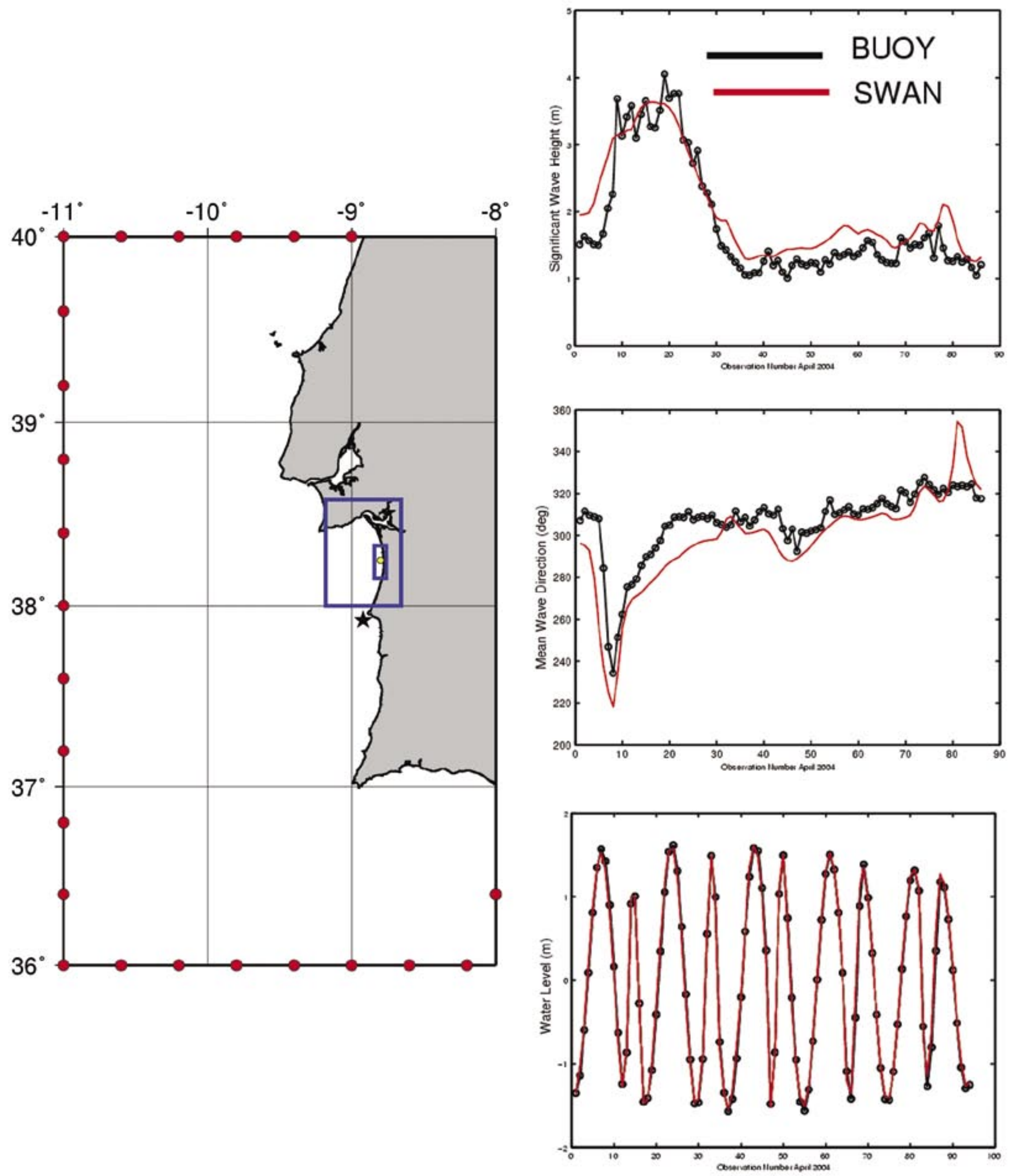

FIGURE 3
Left: Nearshore SWAN wave model domain. Red circles denote locations of directional wave spectra applied to host model grid boundary; blue boxes show inner nests. Black star denotes location of Portuguese wave buoy near Sines: yellow circle denotes location of water level measurements near Pinheiro da Cruz. Right top: Comparison of SWAN wave height at Sines buoy. Black line denotes buoy data, red line denotes SWAN. Middle: Buoy (black) vs SWAN (red) mean wave direction. Bottom: PCTIDES water level (red) vs observed (black) near Pinheiro da Cruz located in center of inner blue box.

Summary: The prototype systems demonstrated during MREA04 show that realistic depictions of ocean circulation, thermal structure, wave, and tidal features are generated with a rapidly relocatable ocean prediction system. Wave height and direction show very good agreement with observations. Water levels from PCTIDES showed excellent agreement with observation. These capabilities will allow the U.S. Navy warfighting community to better exploit the marine environment for tactical mission planning and execution.

Acknowledgments: We acknowledge Dr. E. Coelho and Dr. M. Rixen of the NATO Undersea Research Center for providing in situ CTD profiles collected during MREA04 aboard the R/V *Alliance*.

[Sponsored by NRL, ONR, and PMW 180]

References

[1] D.S. Ko, R. Preller, and P. Martin, "An Experimental Real-Time Intra-Americas Sea Ocean Nowcast/Forecast System for Coastal Ocean Prediction," *Proceedings of the 5th AMS Conference on Coastal Atmospheric and Oceanic Prediction and Processes*, 97-10 (2003).

[2] G.D Egbert, A F. Bennett, and M.G.G. Foreman, "TOPEX/Poseidon Tides Estimated Using a Global Inverse Model," *J. Geophys. Res.* **99**, 24821–24852 (1994).

[3] D.N. Fox, W.J. Teague, C.N. Barron, and M.R. Carnes, "The Modular Ocean Data Assimilation System (MODAS)," *J. Atmos. Ocean. Tech.* **19**, 240-252 (2002).

[4] R. Allard, J. Christiansen, T. Taxon, S. Williams, and D. Wakeham, "Real-time Wave, Tide, and Surf Prediction," *2004 NRL Review*, pp. 201-203.

★

Analysis of the Spectral Signature of Breaking Waves

P.A. Hwang and D.W. Wang
Oceanography Division

Introduction: Wave breaking plays an important role in air-sea interaction processes that affect the world's climate and the cycle of greenhouse gases in Earth's atmosphere. Over many decades, wave breaking is assumed to be spectrally broadbanded. Investigation of source function balance of short ocean waves, however, leads to the conclusion that dissipation function displays a quasi-singularity behavior. In other words, the spectral property of wave breaking is localized in wavenumber, with a strong signature at wave components near 1 m or shorter, depending on the degree of swell influence. The result is consistent with observed properties of radar sea spikes and frequency characteristics of sea surface sound generated by bubble clouds.

Analysis: For wind-generated waves, the dissipation source term remains the most difficult to formulate. Reference 1 describes an approach to establish the dissipation function in the equilibrium region of gravity waves where nonlinear wave-wave interaction is much weaker than wind input and breaking dissipation. Theoretical and experimental studies of the energy transfer from wind to waves have led to the wind input parameterization function,

$$S_w(k) = m\sigma\,(u_*/c)^2\,N(k), \tag{1}$$

where k is wavenumber, $m \approx 0.04$, σ is intrinsic frequency, u_* is wind friction velocity, c is wave phase speed, and N is wave action density. Expressed in terms of dimensionless spectral density, $B = k^4 = \sigma N/g$, where g is gravitational acceleration, the input and dissipation functions can be written as $S_w(k) = m(u_*/c)^2 gk^{-4}B(k)$ and $D = gk^{-4}f(B)$. Equating S_w and D leads to the implicit equation for the unknown dissipation relation $f(B)$,

$$\frac{\partial B}{\partial \xi} = m\left[\frac{\partial}{\partial B}\left(\frac{f(B)}{B}\right)\right]^{-1}, \tag{2}$$

where $\xi = (u_*/c)^2$. It is concluded that if the variation of B with u_*/c can be established reliably, $f(B)$ can be derived from Ref. 2.

Application to Field Data: By applying a free drifting operation to minimize Doppler frequency effect, spectra of short waves between 0.02 and 6 m (0.5 to 12 Hz) are collected from the open ocean.[2] The environmental conditions cover a wide range of wind speeds and sea states (Table 1). The data are further divided into wind seas (Subset 1) and mixed seas (Subset 2). Figure 4 shows scatter plots of $B(u_*/c)$; the data can be represented by a power law function, $B(u_*/c) = A_0(u_*/c)^{a_0} = A_0\xi^{a_0/2}$. The coefficient and exponent, A_0 and a_0, are given in Figs. 5(a) and 5(b). For a power law dissipation relation,[1] $f(B) = A_dB^{a_d}$, A_d and a_d can be calculated by

$$a_d = 1 + \frac{2}{a_0}, \tag{3a}$$

$$A_d = mA_0^{1-a_d}. \tag{3b}$$

The results are given in Figs. 5(c) and 5(d).

Discussions and Conclusions: The presence of a localized region in wavenumber where the spectral

Table 1 — Summary of Experimental Conditions

	No. of Spectra	U_{10} (m/s)	u_* (m/s)	H_s (m)	T_a (s)
Subset 1	291	3.6 - 14.2	0.11 - 0.55	0.21 - 2.84	1.93 - 6.33
Subset 2	106	2.6 - 10.2	0.063 - 0.40	0.21 - 0.75	2.07 - 4.68

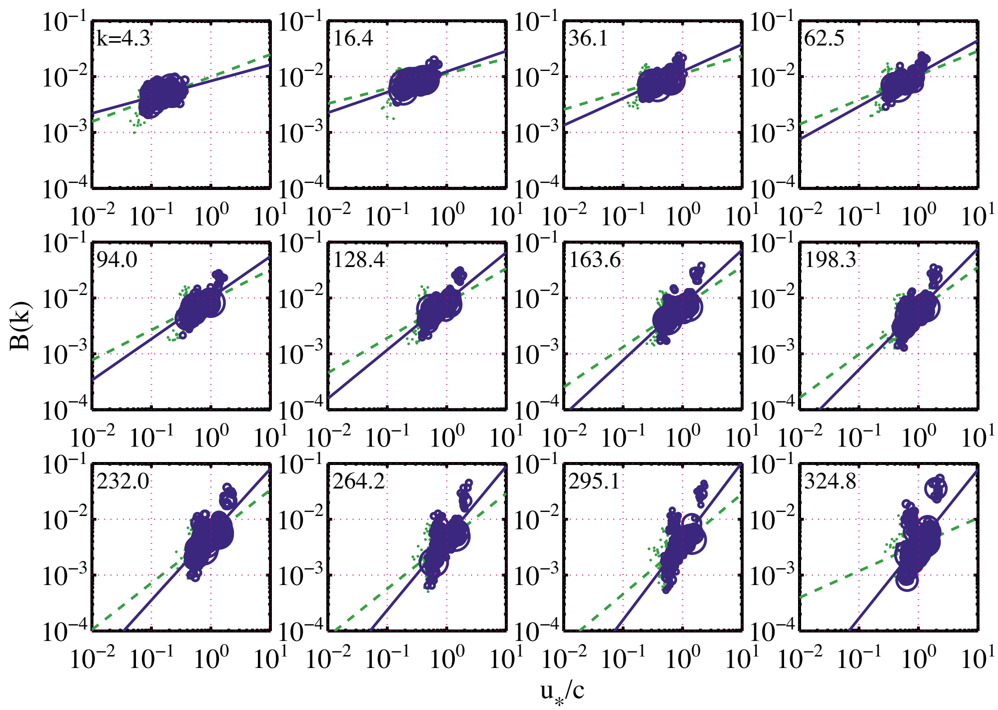

FIGURE 4
Scatter plots of $B(u_*/c)$ for different spectral wave components. The wavenumber is marked at the top left of each panel. Circles and solid curves are for Subset 1, dots and dashed curves are for Subset 2 (from Ref. 2).

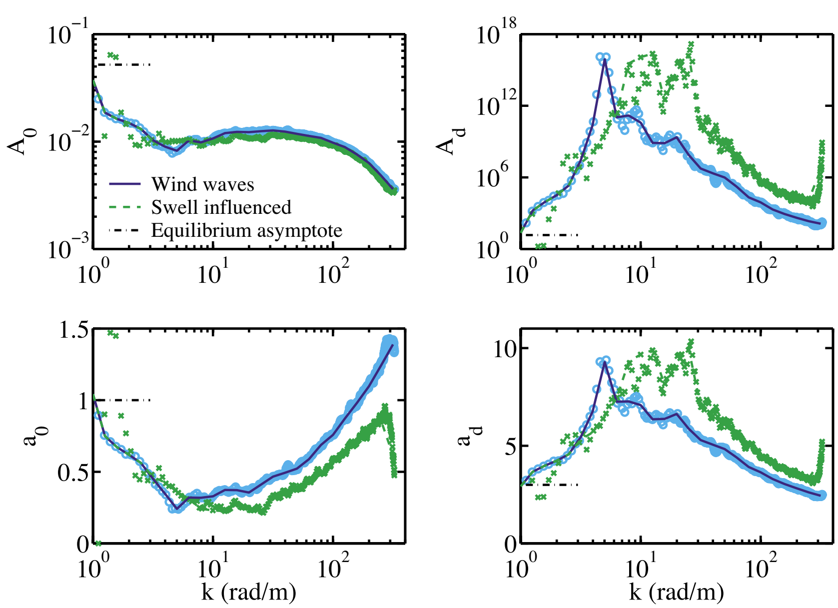

FIGURE 5
(a) A_0, and (b) a_0 of the empirical power law function $B(u_*/c)$, and (c) A_d, and (d) a_d of the dissipation power law function f(B). Note that the range of A_d covers 18 orders of magnitude. For wind seas, the coefficient increases about four orders of magnitude between $4 < k < 6$ (breaker size ranges between 1 and 1.5 m). In the presence of swell, the breaking scale moves to higher wavenumber, $7 < k < 30$ rad/m (breaker size ranges between 0.2 and 0.9 m). (From Ref. 2.)

density is only weakly dependent on the forcing wind condition (Fig. 5(b)) suggests that wave growth is quenched by strong dissipation in that region. For Subset 1 (wind waves), a_0 decreases to less than 0.5, with a minimum of 0.22, for λ between 0.16 and 2.1 m. Correspondingly, the dissipation function in this region shows a very nonlinear dependence on B, as strong as B^{10} and approaches a delta-function (Fig. 5(c)-(d)). These wavelengths are sufficiently long that viscous dissipation or parasitic capillary generation as an energy sink of gravity waves may be neglected. Wave breaking as the major dissipation mechanism can be reasonably assumed. These results indicate that the length scale of breaking wind waves is localized in the range of about 0.16 to 2.1 m. The presence of swell broadens the breaking scales toward shorter waves (breaker size ranges between 0.2 and 0.9 m), possibly through wave-current interaction.

[Sponsored by ONR]

References

[1] O.M. Phillips, "On the Response of Short Ocean Wave Components at a Fixed Wavenumber to Ocean Current Variations," *J. Phys. Oceanogr.* **14**, 1425-1433 (1984).

[2] P.A. Hwang and D.W. Wang, "An Empirical Investigation of Source Term Balance of Small Scale Surface Waves," *Geophys. Res. Lett.* **31**, L15301, doi:10.1029/2004GL20080.

★

Discrete Particle Model for Surf Zone Sediment Transport

J. Calantoni and K.T. Holland
Marine Geosciences Division
T.G. Drake
Office of Naval Research

Introduction: Sediment transport in nearshore wave bottom boundary layers drives coastal geomorphologic change and can result in bathymetric changes of more than a meter in as little as a few hours, particularly in the region where waves are breaking. Predicting the evolution of surf zone bathymetry is of significant importance, with economic, legal, engineering, scientific, and military implications. Most formulae for predicting sediment transport in surf zone subsume the smallest scale physics of the phenomena by parameterizing interactions between grains. In contrast, computer simulations can be performed to directly model the collective and individual motions of sediment grains immersed in fluid. This type of simulation, known as a Discrete Particle Model (DPM),[1] is a cutting-edge research tool that is being used and further developed at NRL for studying nearshore sediment transport. In addition to sediment transport, such models, based on molecular dynamics, have a broad range of applications. For example, the DPM described here has been used to study objects impacting sediments and the formation of geologic faults. As well, similar models have been applied to traffic flow, schooling fish, crowd control, and other problems in which the particulate nature of the phenomena is of critical importance.

Discrete Particle Model: The DPM simulates the two-phase flow of fluid and sediment by coupling a one-dimensional (1D) eddy-viscosity fluid to 3D particles (Fig. 6). The DPM considers three types of interactions: grain-grain, grain-fluid, and fluid-fluid.[1] Grain-grain interactions occur between discrete elements representing sand grains. Sand grains may be represented with spheres or nonspherical elements composed of two overlapping spheres called composite particles. The particle interaction model is known as a "soft sphere" model, such that two particles may be in contact for many simulation time steps where collisions between grains are modeled with springs and friction.[2] Grain-fluid interactions include forces of buoyancy, drag, and added-mass. The model is fully coupled at every simulation time step so that the fluid exerts force on the sediment particles and the sediment particles exert equal and opposite force back on the fluid (Newton's Third Law).[3] Fluid-fluid interactions are accomplished by solving a 1D eddy viscosity model in which fluid turbulence is implicitly included through a mixing length determined by the vertical distance of the fluid from the mobile sediment layer. The effects of fluid turbulence on sediment transport rates are not well understood. Work is currently underway on the next generation of the DPM to couple a fully turbulent, 3D, direct numerical simulation of the fluid to the particles.

Research Applications: As part of an advanced research initiative, the effects of heterogeneous sediment characteristics such as size, density, and shape on bulk sediment transport rates are being explored using the DPM. These characteristics can be uniquely specified for every grain represented in a simulation, up to the present limit of 10^5 particles. Recently, the DPM was used at NRL to study the effect of particle shape on sediment transport rates.[2] A bulk property of natural sand is the angle of repose, or the angle at which a pile of sand will avalanche. Beach sands typically have an angle of repose around 33°. Similarly, glass spheres have an angle of repose around 26°. Using spheres to represent sand grains in the

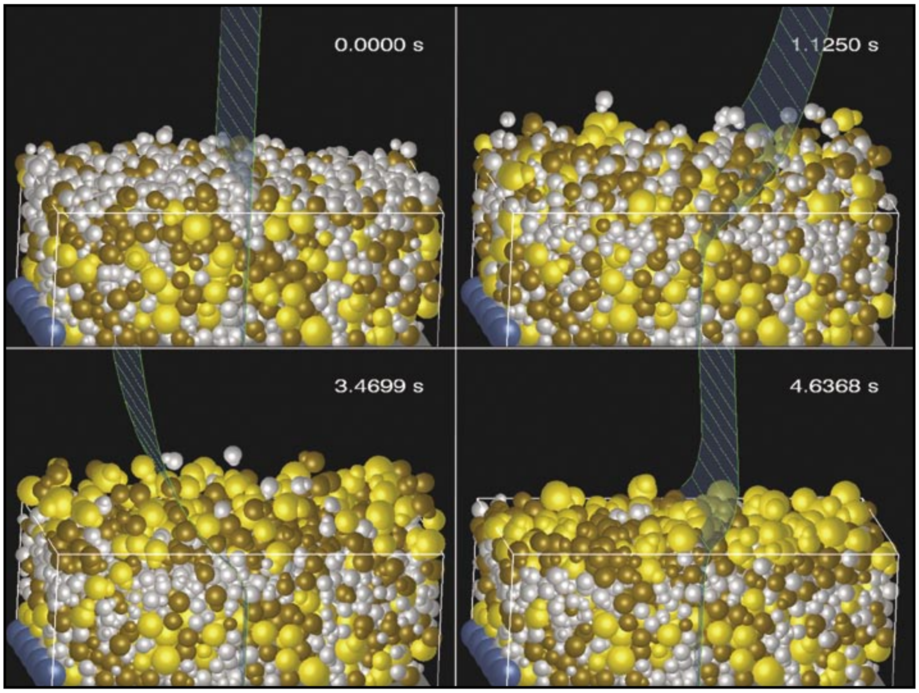

FIGURE 6
Four successive snapshots from a simulation with composite particles driven by a single oscillating wave. The fluid is represented with the green sheet. The grains are colored by size where the smallest particles are grey and the largest are yellow. The median particle diameter is 0.001 m. There is a hard bottom with a row of particles attached to the left of the plane to avoid wholesale sliding. The boundaries are periodic in the horizontal directions (0.02 m by 0.01 m), such that a particle exiting on one side is immediately inserted on the opposite side. The volume of particles is outlined with a white box. At time 0 s, the particles and fluid are at rest. At time 1.125 s, the fluid and particles have begun motion to the right. Notice that the bed has dilated in response to particle motion. At time 3.4699 s, the wave has reversed direction and motion is to the left. At time 4.6368 s, the particles have come back to rest and the fluid is beginning to accelerate back to the right again. Notice that many particles deep in the bed never experience any motion. As well, the particles that have moved near the top of the bed have sorted by size, with larger grains (yellow) above smaller grains (gray).

DPM will therefore result in behaviors inconsistent with natural grains. To alleviate this discrepancy, we constructed composite particles by overlapping two spheres (with different radii) to form a particle shape that possesses an angle of repose near that of typical beach sand. The simulations with composite particles do a much better job of reproducing sediment transport rates from laboratory experiments[3] (using beach sand) than do the simulations with spherical particles (Fig. 7).

A modified version of the DPM is being used to study large-scale morphodynamics in the swash zone. We are investigating the processes driving bed level changes at the shoreline of a beach. In this implementation, the fluid portion of the DPM has been replaced with a 2D Navier-Stokes solver. Here, the fluids exhibit vertical motions as the free surface moves up and down, while some portion of the beach face is repeatedly submerged and exposed. The first implementation of the model allows one-way coupling between fluid and particles, where particles feel the force from the fluid but do not exert any reaction force back onto the fluid. Figure 8 is an example from this version of the DPM. Here we model a thin strip of grains (~3 m long) running perpendicular to the shoreline. The grains are spherical and represent gravel with 0.01-m diameter. The bed was initially planar and has begun to form a step after a couple swash cycles. Similar morphology has been observed in the laboratory under similar conditions.

Summary: Despite the accessibility of the phenomena of interest, namely the motion of sand under waves on the beach, traditional approaches to modeling beach evolution are not robust, mainly because of our failure to understand the fundamental interaction forces driving sediment transport under waves. The DPM described here is a research tool that puts NRL at the forefront of small-scale sediment transport modeling. We are not trying to model every grain

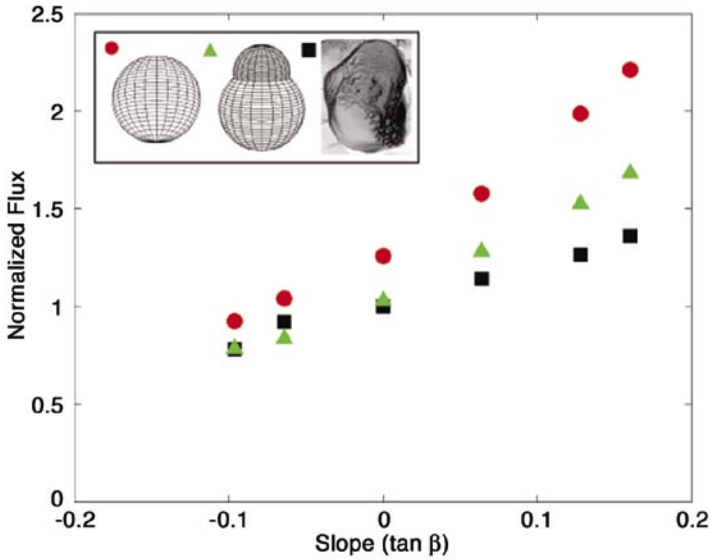

FIGURE 7
The influence of grain shape is tested. The normalized flux, representing the amount of sediment displaced, is plotted against the local bed slope for simulations with spheres (red circles), simulations with composite particles (green triangles), and laboratory experiments with beach sand (black squares). For all points, the wave simulated was constant while the bed slope is varied. The range of values for each point typically does not exceed the size of the symbol. The graphic inset shows the representative particle shape for each of the symbols used in the plot. The median particle is 0.001 m for all cases.

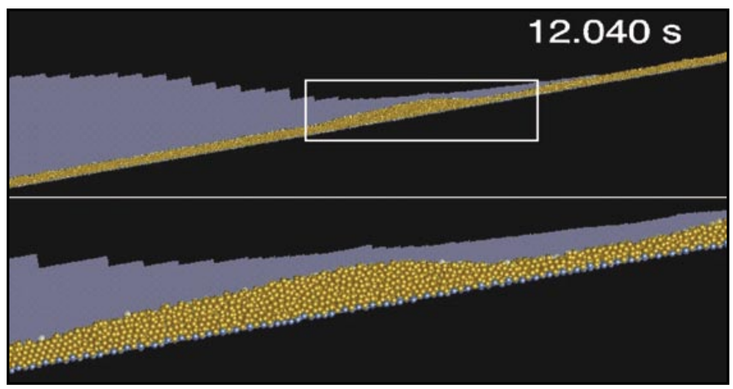

FIGURE 8
Snapshot from a DPM simulation of swash zone morphology. The domain in the upper panel is over 3 m in length and just 0.03 m into the page (boundary is periodic into the page). The median particle diameter is 0.01 m. The simulation uses more than 5,000 particles. The white box outlines the area shown in the bottom panel. The blue particles are fixed to the plane to prevent particles from simply rolling down the hill. The blue shading represents the position of the water.

of sand on the beach. Instead, we model small but relevant collections of grains where results obtained at fundamental length and time scales are parameterized into simple formulae for use at larger length and time scales. Our ability to model large-scale morphodynamics (meters to kilometers and hours to days) will directly benefit Naval operations such as mine warfare, amphibious landings, and special operations.

Acknowledgments: The image of the sand grain (inset, Fig. 7) provided by Dr. A. Reed, Code 7430. Swash zone modeling depicted in Fig. 8 results from collaboration with Dr. J.A. Puleo at the Center for Applied Coastal Research, University of Delaware.

[Sponsored by ONR]

References

[1] T.G. Drake and J. Calantoni, "Discrete Particle Model for Sheet Flow Sediment Transport in the Nearshore," *J. Geophys. Res. Oceans* **106**(C9), 19859-19868 (2001).

[2] J. Calantoni, K.T. Holland, and T.G. Drake, "Modelling Sheet-Flow Sediment Transport in Wave-Bottom Boundary Layers Using Discrete-Element Modelling," *Phil. Trans. Roy. Soc. London, Series A-Math. Phys. Eng. Sci.* **362**(1822), 1987-2001 (2004).

[3] D.B. King, "Studies in Oscillatory Flow Bedload Sediment Transport," Ph.D. dissertation, University of California, San Diego, 1991, 184 p.

★

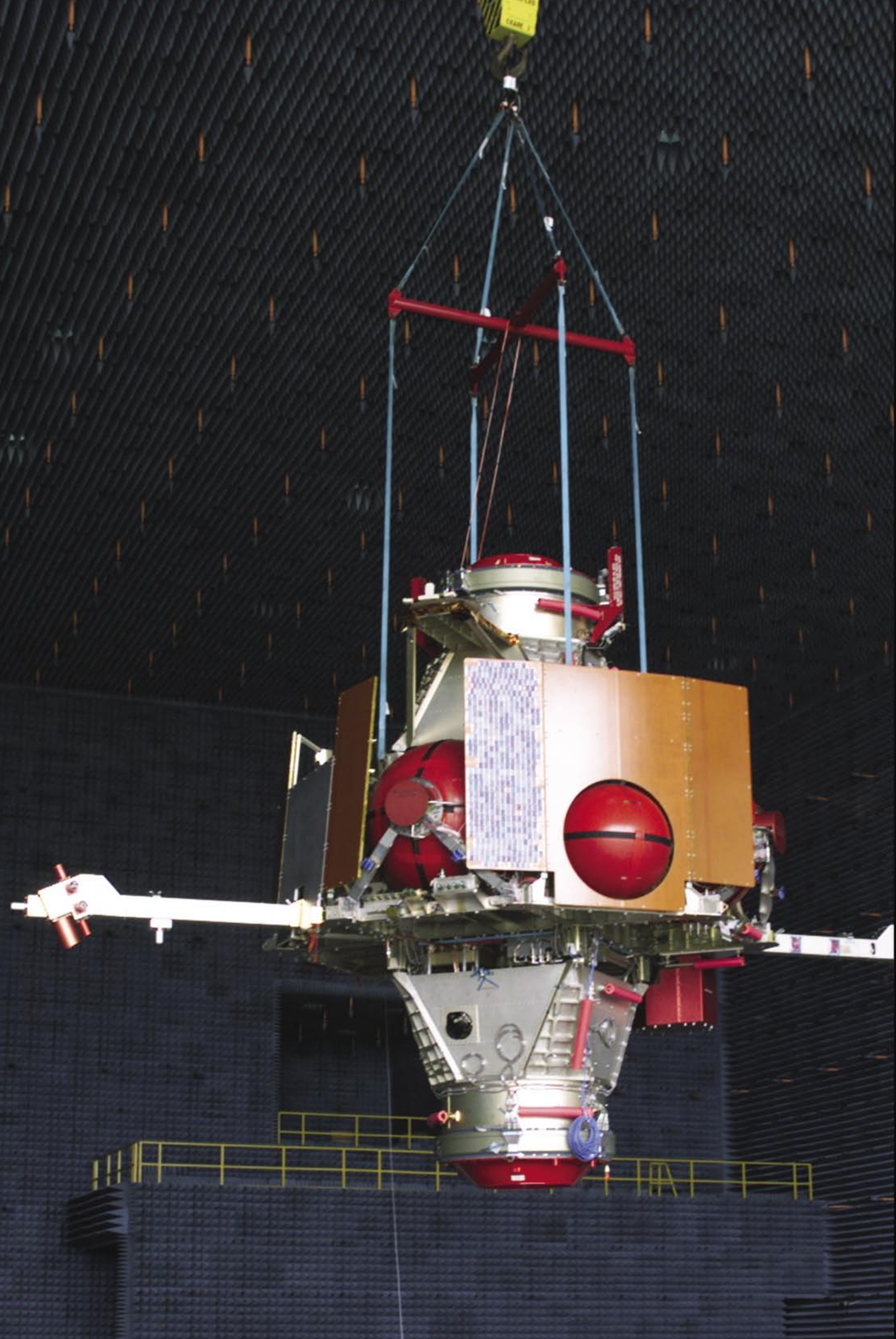

Photo caption: The Interim Control Module (ICM) is the third manifestation of this large transfer stage. First named the Shuttle Launch Dispenser (SLD), it was renamed the Titan Launch Dispenser (TLD) after the Challenger accident and is now a man rated, three-axis stable stage for operations in low-Earth orbit. It can be launched on either the Shuttle or the Atlas V or Delta IV evolved expandable launch vehicles (EELVs).

High Power RF Photodiodes

D.A. Tulchinsky and K.J. Williams
Optical Sciences Division

Introduction: For both analog and digital optical transmission systems, high-power photodetectors are becoming increasingly important. Analog communications systems for antenna remoting, phased array antennas, and photonic analog-to-digital converter systems require high fidelity with large dynamic range. To build optical links for these systems means that the optical to electrical converters (i.e., the photodetectors) must be able to operate at high photocurrent levels to minimize noise figure while providing the required dynamic range. In the digital domain, fiber optic systems are rapidly being developed for next-generation ethernet and secure communication systems. One approach to producing high-performance systems is to increase the optical power incident on the wide-bandwidth photodetectors so that the photogenerated RF output power (voltage swing) can directly drive the digital logic circuits. This approach eliminates the complications and expense of postdetection, wide-bandwidth, flat-phase RF amplifiers but requires higher performance photodiodes.

Two factors limit a photodiode's output power: space-charge screening of the intrinsic region electric field, and thermal considerations.[1] Space charge screening arises from the spatial distribution of photogenerated carriers as they transit the photodetectors depletion region. These charge carriers create an electric field that opposes the external-bias electric field. At sufficiently high optical power levels, the space-charge-induced electric field is strong enough to collapse the bias electric field, resulting in loss of the RF signal. Thermal limitations are the result of the geometry and thermal conductivity of the photodiode layers.

Traditional high-speed p-i-n photodiodes are made of an InGaAs optically absorbing layer grown on a lattice-matched InP substrate, with the composition and thickness of the various layers carefully chosen to balance the trade-offs between the power handling and frequency response for the photodiodes. We describe a new photodiode structure, jointly developed through a collaboration between the University of Texas–Austin and the Optical Sciences Division of NRL. These photodiodes use a partially depleted absorbing (PDA) layer to balance intrinsic-layer space charge effects and minimize thermal heat loading.[2] These devices have improved previous results by generating 10 times higher photocurrents than contemporary commercially available devices.

Partially Depleted Absorber (PDA) Photodiodes: Figure 1 shows the structure of the PDA photodiode. In a conventional semiconductor p-i-n photodiode, light generates electron and hole pairs in the optically absorbing intrinsic region (*i*-region) and they then travel in opposite directions to the contact layers. In both the InGaAs and InP semiconductor material systems, the velocity of electrons is higher than that of the holes, so the depletion region charge is dominated by slow moving holes. This velocity mismatch leads to a charge imbalance within the depletion region leading to space charge effects. In the PDA photodiode, charge

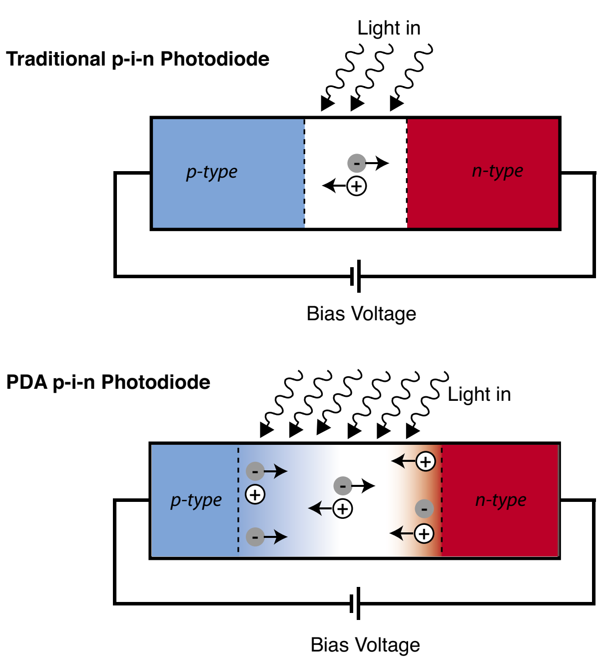

FIGURE 1
Schematic layer structure diagram comparing a traditional p-i-n photodiode to a partially depleted absorber (PDA) photodiode.

balance is accomplished by the *p*-doped and *n*-doped optical absorbers on each side of the *i*-region. The *p*-doped absorber injects electrons into the *i*-region while the *n*-doped absorber injects holes. In this implementation, electron injection is stronger than that of holes due to the different thicknesses of the absorbers on each side of the *i*-layer. Furthermore, the design of these diodes includes a thinned *i*-layer to further reduce space-charge effects and minimize thermal loading of the depletion layer. However, thinning the optically absorbing *i*-layer has the deleterious effect of lowering the optical responsivity. This limitation is mitigated in the PDA photodiode design by using a graded doping of the optically absorbing regions on either side of the *i*-layer to increase optical absorption.

Performance Results: Figure 2 shows a summary of the saturated photocurrent as a function of bias voltage at several different RF frequencies. The saturated photocurrent is detected by measuring a 1 dB (20%) drop in RF signal response at a specified frequency while a separate continuous wave (CW) unmodulated optical signal is applied to the photodiode. For a 100-µm diameter diode, measured at 300 MHz, the peak saturation photocurrent observed was 500 mA. For a 34-µm diameter diode, the peak saturation photocurrent observed was 153 mA at 5 GHz and 107 mA at 10 GHz. These photocurrents are five to ten times higher than commercially available detectors at these frequencies. For the case of the 100-µm diode, the initial slope of the saturation current with applied voltage fits a straight line with a slope of ~189 mA/V. This initial slope corresponds to a reversed bias series resistance of 5.3 Ω. We believe the extremely large photocurrents generated by these detectors are a direct result of the low series resistance of these photodiodes. Above a bias of 1-2 V, Joule heating (I^2R) limits the saturated photocurrent.

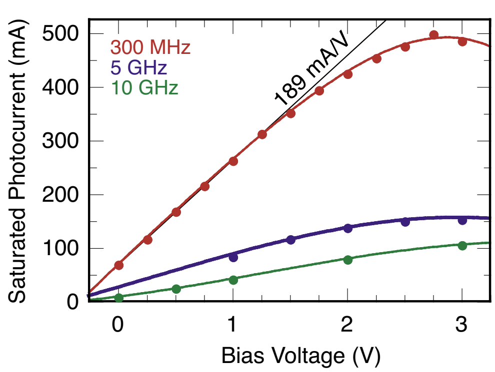

FIGURE 2
Saturated photocurrent as a function of bias voltage for a 100 µm diameter PDA photodiode measured at 300 MHz, and a 34-µm diameter PDA photodiode measured at 5 and 10 GHz. The straight line indicates an initial slope of 189 mA/V = 1/(5.3 Ω).

Figure 3 shows the RF power generated by a 100 MHz 100% amplitude modulation depth, 150 mW optical beam incident on a 100-µm diameter PDA photodiode with a fixed average photocurrent of 130 mA as a function of applied voltage. At low applied voltages, the external bias limits the possible output voltage swing (and maximum output RF power) due to the large signal I × V loading from the output impedance. This condition causes the photodiode terminal voltage to decrease to near zero (i.e., clipping behavior). At higher applied voltages, the output RF power exceeds 25 dBm until it begins to saturate above 6 V bias. When 2 GHz amplitude-modulated light is incident on a 34-µm diameter photodiode, 130 mA of photocurrent is able to generate upwards of 24.5 dBm of RF power to a 50 Ω load. With 6 GHz amplitude-modulated light incident upon a 34-µm PDA photodiode, the diode is slightly RF response limited due to its 3 dB bandwidth of 7 GHz. However, it is still able to generate upwards of 23.5 dBm at this frequency. These are the highest reported output RF powers directly generated from a photodetector.[2]

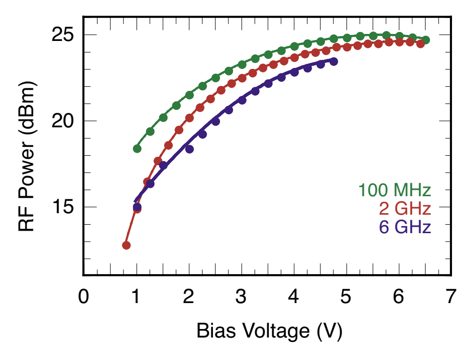

FIGURE 3
Peak RF power generated from a 100% amplitude modulation depth optical source as a function of bias voltage from a 100-µm diameter PDA photodiode at 100 MHz and from a 34-µm diameter PDA photodiode at 2 and 6 GHz.

Summary: We have described high-saturation-current, wide-bandwidth photodiodes. The partially depleted-absorber photodiode has achieved record high current (bandwidth) outputs of 500 mA (300 MHz), 153 mA (5 GHz), and 107 mA (10 GHz). The maximum RF output power generated from these partially depleted-absorber photodiodes exceeds +23.5 dBm from DC to 6 GHz.

Acknowledgments: We thank our collaborators X. Li, N. Li, S. Demiguel, and J.C. Campbell from the Microelectronics Research Center at the University of Texas Austin for support.

[Sponsored by DARPA]

References

[1] K.J. Williams and R.D. Esman, "Design Considerations for High Current Photodetectors," *J. Lightwave Tech.* **17**, 1443-1454 (1999).

[2] D.A. Tulchinsky, X. Li, N. Li, S. Demiguel, J.C. Campbell, and K.J. Williams, "High-Saturation Current Wide-Bandwidth Photodetectors," *IEEE J. Sel. Topics Quant. Electron.* **10**, 702-708 (2004).

★

NRL Portable Adaptive Optics for Optical Interferometry

S.R. Restaino, J.R. Andrews, C.C. Wilcox, and G.C. Gilbreath
Remote Sensing Division

Introduction: Our ability to collect reliable visual or infrared imagery of exo-atmospheric objects, both astronomical and man-made, is limited by two factors. The first is the turbulence of the Earth's atmosphere: for telescopes larger than 10 to 20 cm, turbulence introduces significant wavefront distortions. The second factor that limits our ability to image ever finer details is the maximum practical size of a single telescope. The largest telescopes are currently 10 m in diameter, corresponding to a resolution limit of ~ 0.2 arc sec at visual wavelengths. One approach to overcoming the size limitation is to build an array of several smaller telescopes to synthesize an equivalent telescope of a diameter equal to their largest separation. This technique is known as interferometry. However, if the individual telescopes are larger than 10 to 20 cm, atmospheric turbulence is still a problem to be reckoned with. One way to solve this problem is to develop a system that removes the wavefront distortions in real time. Such systems are known as adaptive optical systems, or adaptive optics (AO) for short. Combining AO with interferometry will increase our ability to image finer details on fainter objects.

The NRL System: AO systems have been developed and tested at various astronomical and DoD facilities.[1] However, current AO systems are extremely complex, expensive, and heavy, and do not lend themselves to easy duplication for multitelescope systems. Within this context, we have started a program to develop and demonstrate the feasibility of a small, portable, and affordable AO system that can be easily duplicated. We have based our system on the emerging technologies of micro-electro-machined (MEM) mirrors and liquid crystal devices (LCDs). Our system is an order of magnitude smaller, cheaper, and less complex than conventional AO systems.

Figure 4 is a schematic diagram of the layout of our AO system. The main components of this system are the wavefront sensor, the reconstructor/controller system, and the corrective element.

The wavefront sensor is the component that senses the effects of the turbulence on the incoming beam of light. There are many ways of performing this task;[1] in our case, we use a so-called "Shack-Hartmann" sensor. This sensor consists of an array of lenslets that breaks the incoming beam into several sub-beams and then focuses them onto a fast-readout camera. The differential motions of the images from the sub-beams indicate the variations in wavefront tilt in each sub-beam caused by atmospheric turbulence.

The camera output goes into the reconstructor/controller computer system. The task of this component is to reconstruct the effect of the atmosphere from the camera signals, and then to send a series of signals to the corrective element to remove these effects. Since corrections are normally required at the rate of several tens to hundreds of times per second,

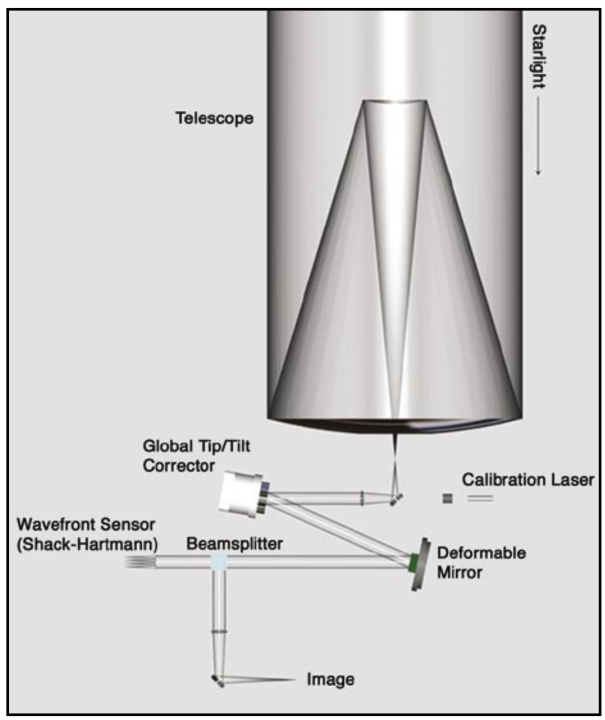

FIGURE 4
Schematic diagram of a generic adaptive optics system.

it is critical for the controller to monitor the status of the system and ensure that the signals to the corrective element are sent in a timely fashion.

Finally, the corrective element is the component that physically removes the effects of the turbulence. Several types of corrector with different physical characteristics and capabilities are available. The MEM mirror used in our current test system is composed of a very thin metallic membrane lying on a layer of electrodes. The reconstructor/controller calculates and applies a voltage to each electrode; the resulting electrostatic force pulls the membrane inward at that point. Since, in general, the voltage for each electrode is different, the shape of the mirror is changed.

Testing: The system was tested on a 1-m telescope at the Naval Observatory Flagstaff Station (NOFS). The results of this ground-breaking experiment are reported in Refs. 2 and 3. Figure 5 shows the image of the bright star α Lyrae (Vega). The left-hand side shows the image seen by the telescope without the help of the AO system; the right-hand side shows the same stellar image with the help of the AO system. Figure 6 is a cross cut of the images in Fig. 5. The dashed line is the cross cut of the open-loop image, i.e., no AO used, and the solid line is the closed loop, i.e., AO used, cross cut.

[Sponsored by ONR]

References

[1] F. Roddier (editor), *Adaptive Optics in Astronomy* (Cambridge University Press, Cambridge, UK, 1999).

[2] S.R. Restaino, J. Andrews, G.C. Gilbreath, D. Payne, and C. Wilcox, "Portable AO System," *J. Micromach. Microelectron. Microlitho.*, accepted for publication, 2005.

[3] S.R. Restaino, "Experimental Results from a MEM-based AO System," *S.P.I.E.* **5348**, 160-165 (2004).

★

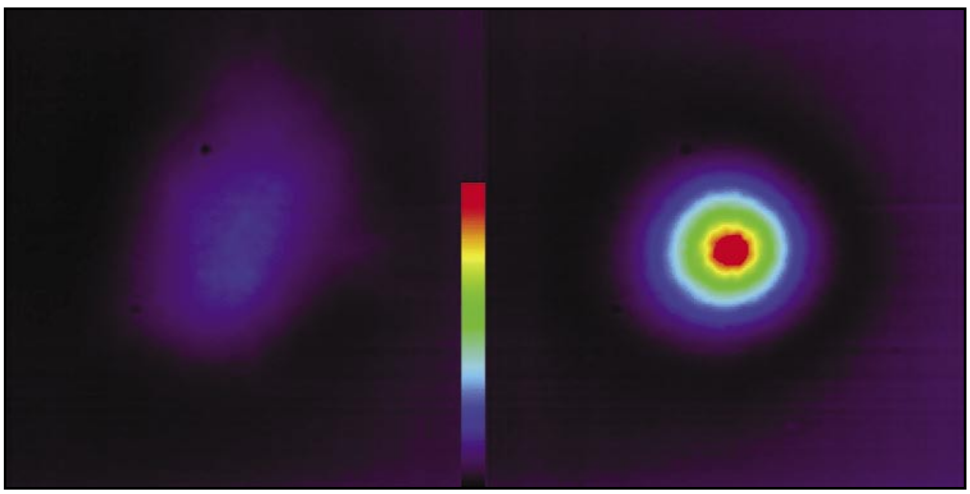

FIGURE 5
Image of the bright star alpha Lyrae (Vega). Each image is an average of 30 frames. The left side shows the open loop, i.e., no adaptive optics, and the right shows the same image with the adaptive optics system on, i.e., closed loop.

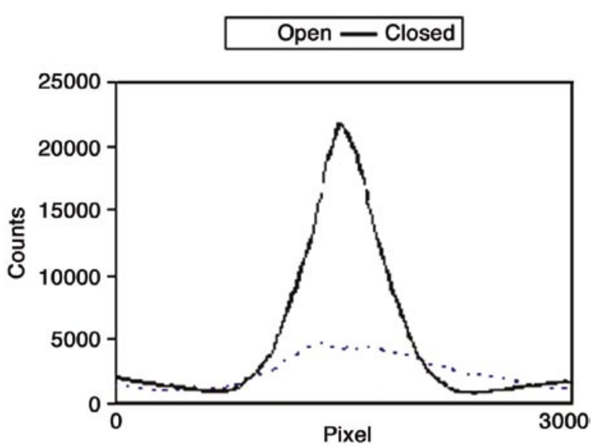

FIGURE 6
Cross cut of the two images in Fig. 5. The solid line is the cross cut of the closed loop image and the dashed line is the cross cut of the open loop image.

Deployable Unmanned Systems for Targeting, Exploitation, and Reconnaissance (DUSTER)

D.C. Linne von Berg, J.G. Howard, M.R. Kruer, and J.N. Lee
Optical Sciences Division

Introduction: The Deployable Unmanned Systems For Targeting, Exploitation, and Reconnaissance (DUSTER) program is developing and demonstrating networked ground and airborne command, control, exploitation, and dissemination systems for use with simultaneous, multiple, dissimilar, tactical unmanned aerial vehicles (UAVs). The initial four key goals of this program include (1) demonstration of simultaneous multiple dissimilar UAV screening and control from ground and airborne control and display stations (CADS); (2) development of modular reusable digital avionics and payloads for small tactical UAV systems; (3) demonstration of joint manned/unmanned control station operation; and (4) demonstration of real-time netcentric dissemination and relay of intelligence, surveillance, reconnaissance, and targeting (ISRT) information. The purpose of this effort is to develop and demonstrate technologies that will enhance the military's ability to deploy, control, exploit, fuse, and disseminate sensor data from various manned and unmanned systems directly to the forward-deployed forces that need the real-time ISRT information.

The "Mother-ship" Concept: The goal of the initial phase of the DUSTER program is to demonstrate the "mother-ship" concept of using a single CADS system for the control, exploitation, and dissemination of information from both onboard manned sensors and multiple remote UAVs simultaneously. The sensor systems incorporated into the control and display stations include visible and midwave infrared (EO/MWIR) panchromatic sensors and visible through short wave infrared (VNIR-SWIR) hyperspectral (HSI) sensors of various types (including step-stare, push-broom, whisk-broom, and video). The data received by CADS from the onboard or extended airborne UAVs can be relayed directly to the ground, disseminated to an airborne relay aircraft, or exploited onboard the mother-ship platform to provide real-time tracking and targeting of hard-to-find and mobile targets. Demonstrated exploitation capabilities include real-time screening, construction of a geo-referenced mosaic image, change detection, stereo imaging, moving target tracking, and networked dissemination to distributed exploitation nodes (man-pack, ground vehicle, and command centers). Use of the mother-ship control station concept allows for more rapid exploitation and greater dissemination range from individual UAVs to a given ground station or command center than was previously achievable. Additional relay capabilities, such as sending data via satellite communication are also included. As Fig. 7 shows the simultaneous control of multiple onboard and UAV-based sensor from the common control station allows controllers and imagery exploiters to retask, exploit, and disseminate data and intelligence information from each sensor in real time while remaining at a safe stand-off distance.

Initial System Implementation and Real-time Flight Demonstrations: The DUSTER program is leveraging and improving existing Navy UAVs, sensors, avionics, and data-link technologies and is developing a single CADS system that can be hosted on airborne, shipboard, and mobile ground platforms for use with both manned and unmanned sensor systems. Existing ground-launched tactical UAVs (e.g., Dragon Eye/ATR, Finder, TERN, etc.) are used and the UAV-provided intelligence, surveillance, reconnaissance, and targeting information is exploited and disseminated from the CADS systems over various integrated communication links. The initial configuration of the DUSTER system was demonstrated during simultaneous, multiple UAV flights at Aberdeen Proving Ground (Maryland) in June 2004 (using Finder and ATR UAVs) and August 2004 (using TERN and ATR UAVs). A final Phase I demonstration was performed in September 2004 in Montana. For this demonstration, the Montana National Guard deployed military targets and the ATR and TERN UAV systems transmitted persistent surveillance imagery in real time to the NRL-developed Chevrolet Suburban-based and man-pack CADS units (Fig. 8). The exploited data were subsequently transmitted over wireless networks and satellite communication channels to networked, distributed ground stations and command centers. Figure 9 shows the video imagery window, real-time video imagery mosaicing, and situational awareness screen provided by CADS. These screens indicate the instantaneous field of view of the sensors, the total imagery history of the flights, and the actual location of the UAVs in flight overlaid on DoD imagery and mapping databases.

Summary and Acknowledgments: The initial flight demonstrations of the DUSTER program have

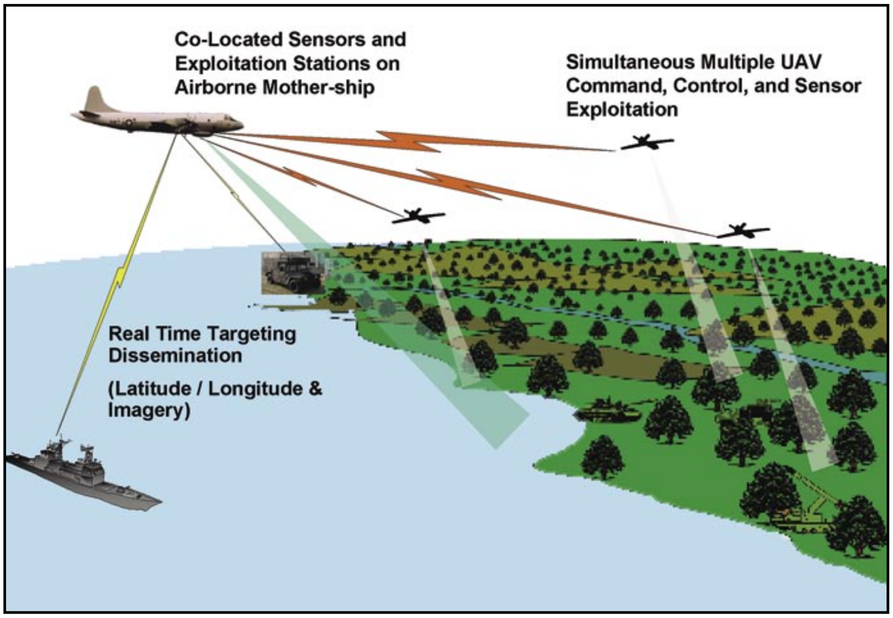

FIGURE 7
Mother-ship concept: simultaneous control of multiple onboard and UAV-based sensors from the common control station.

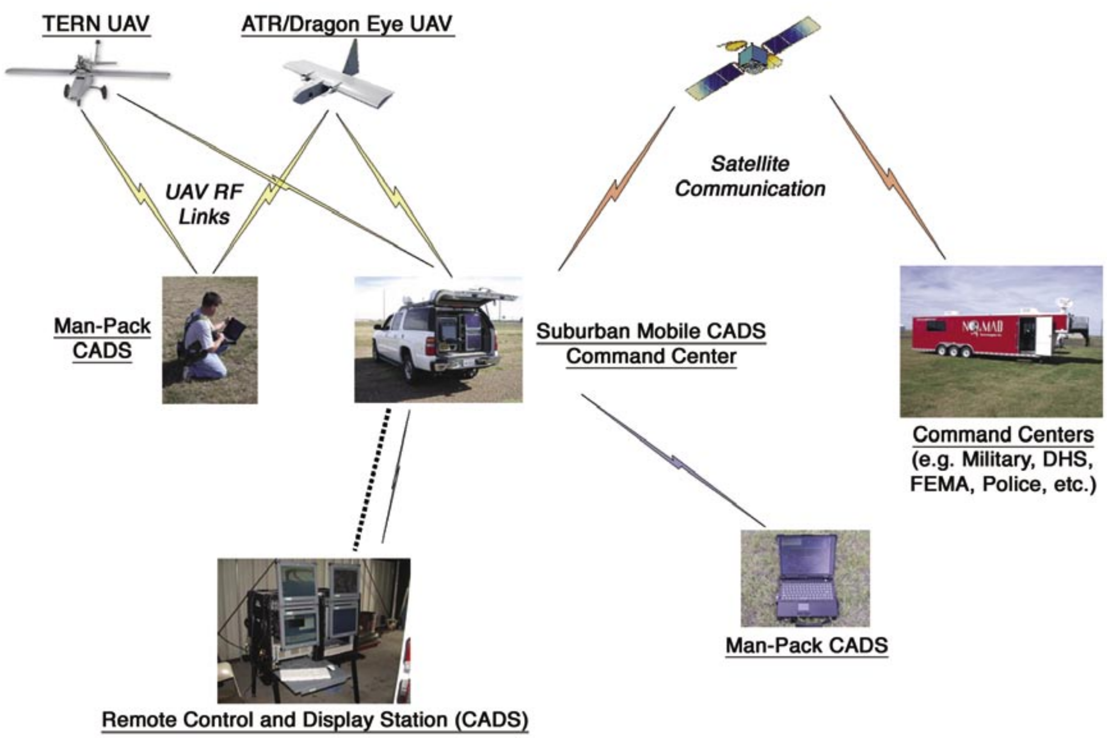

FIGURE 8
DUSTER September 2004 Montana flight demonstration.

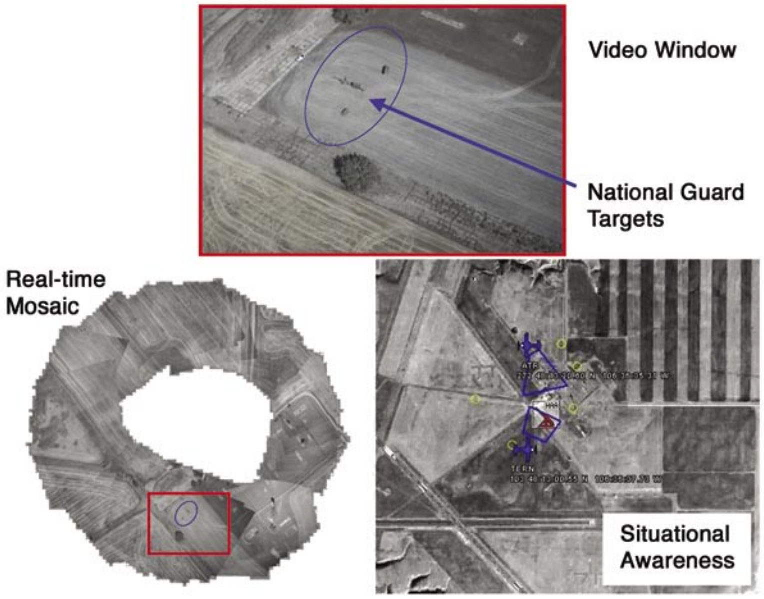

FIGURE 9
CADS video, mosaicing, and situational awareness screens.

shown great promise for the mother-ship concept of controlling, exploiting, and disseminating simultaneous, multiple, dissimilar UAVs and ISRT information from a common control and display station. Significant support for the DUSTER system development and demonstrations was provided by NRL Codes 5700 (Finder, TERN UAVs), 6100 (Dragon Eye/ATR UAV), 8100 (Suburban System Integration), and the Space Dynamics Laboratory (CADS upgrades). Future DUSTER program plans include development of airborne-launched UAVs coupled with an integrated CADS system on the NRL P-3 and potentially other aircraft.

[Sponsored by ONR] ★

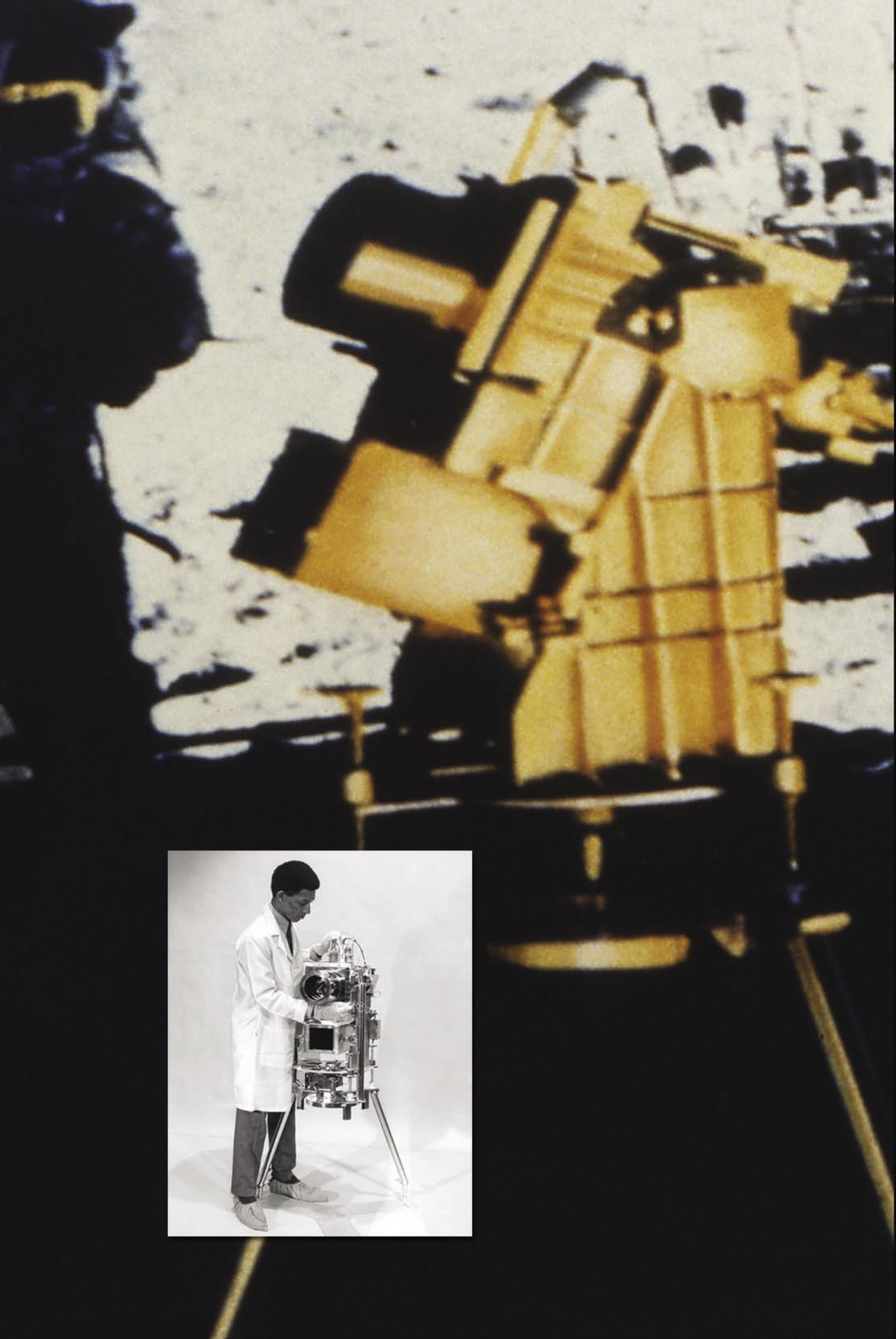

Photo caption: An ultraviolet camera developed by NRL was brought to the lunar surface and operated by the Apollo 16 astronauts. It was the first space astronomical observatory and provided images of the sky and Earth.

NRL's FINDER UAV: A Counterproliferation Asset

A. Cross
Tactical Electronic Warfare Division

Introduction: NRL's significant technological advances and breakthroughs made in the areas of low Reynolds number (LRN) aerodynamics, in-flight deployability, advanced composite structures, and microdigital electronics applied to unmanned air vehicles (UAVs) has enabled rapid prototyping and testing of unique autonomous vehicles. The Flight Inserted Detector Expendable for Reconnaissance (FINDER) UAV is an example of the integration of these capabilities in action. The vehicle potentially adds a highly capable, small, affordably expendable asset to the military or homeland defense inventory. This article highlights it's capabilities, development timeline, and overall significance.

During the FINDER effort, the goal was to produce a warfighting component within the Chemical Combat Assessment System (CCAS) segment of an Advanced Concept Technology Demonstration (ACTD). A number of field tests (most notably at: Edwards Air Force Base, Indian Springs Air Force Base, and the Nevada Test Site) were used to prove the system's potential value as a reconnaissance tool. FINDER was developed as a multi-use low-cost UAV. The vehicle can readily be modified to accept a number of different payloads. These can range from real-time Battle Damage Assessment (BDA) via optical imaging and acoustic sensing, to active determination of the presence of hazardous chemical/biological agents. In this case, FINDER was integrated with a U.S. Army-developed payload to determine the presence and concentrations of chemical agents within a Weapons of Mass Destruction (WMD) facility. Figure 1 illustrates the CCAS system architecture.

Program Overview: The FINDER mini-UAVs are carried into the target area attached to the wing hard points on a Predator UAV. Each FINDER contains point chemical sensors and an integrated sample collector. The mini-UAVs are dispensed from the Predator and descend to intercept and interrogate a suspect post-strike plume. This allows the Predator to stay at higher altitudes, enhancing its survivability and its ability to avoid contamination. NRL tailoring of a microprocessor-based autonomous navigation and flight control system, long-range communications, a propulsion system, and a unique deployment methodology were critical in allowing FINDER and its payload to achieve numerous successes within the CCAS development.

Figure 2 shows FINDER's integration on the Predator and a deployment. Key CCAS sensor information is collected onboard the Predator and distributed to the warfighter in near-real-time, using existing Predator and theater communications infrastructure.

The FINDER project was initiated in June 1999. Full development of the vehicle structure and fabrication of prototype units was completed at NRL. Advanced autopilot development, communications, and autonomous flight testing of the prototypes began in August 2000. The full CCAS system was targeted for a military utility demonstration as a participant in the Counterproliferation 2 ACTD in May 2003.

FINDER has participated in multiple field exercises over an 18-month period. The system was tested and evaluated in six highly visible field exercises during fiscal year 2003. These exercises were designed to prove the feasibility of the FINDER concept of operations. Reports by the Air Force's Technical Assessment Team (AFOTECH) have documented the successes of those exercises. AFOTECH has acknowledged the CCAS system and FINDER's potential operational capability. Its positive reports have provided the impetus for the Defense Threat Reduction Agency (DTRA) to purchase residual units in 2004 for warfighter use. DTRA and the Office of the Secretary of Defense (OSD) have hailed the development and testing of the Chemical Combat Assessment (CCAS) system and the FINDER component as a major accomplishment toward providing a capability to detect and track chemical agents in real time.

During the development period, more than 20 units were manufactured, integrated, and tested by NRL. Under Predator GCS control, the FINDER has completed 18 nominal deployments from the Predator pylon at altitudes up to 20,000 ft. Additionally, the FINDER's capability to be controlled by line-of-site (LOS) and via satellite communications (SATCOM) has been demonstrated in flight testing. FINDER has validated an endurance capability of 7 hours and has demonstrated the potential to fill an operational capability gap. Accordingly, NRL has been tasked to deliver and support a number of units to DTRA on behalf of the U.S. Air Force for the immediate future.

Significance: FINDER supports European Command requirements for a chemical BDA tool. The FINDER air vehicle and payload provides real-time local area meteorological data, Predator stand-off BDA capability, critical sample collection, return of sample to a safe area, and extended range operations.

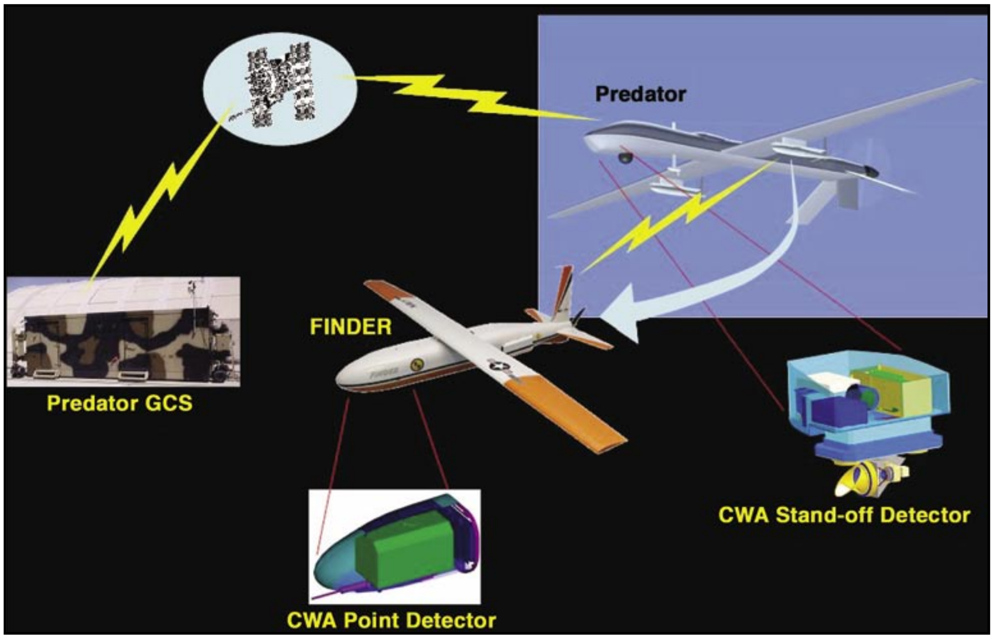

FIGURE 1
Chemical Combat Assessment Systems (CCAS) overview.

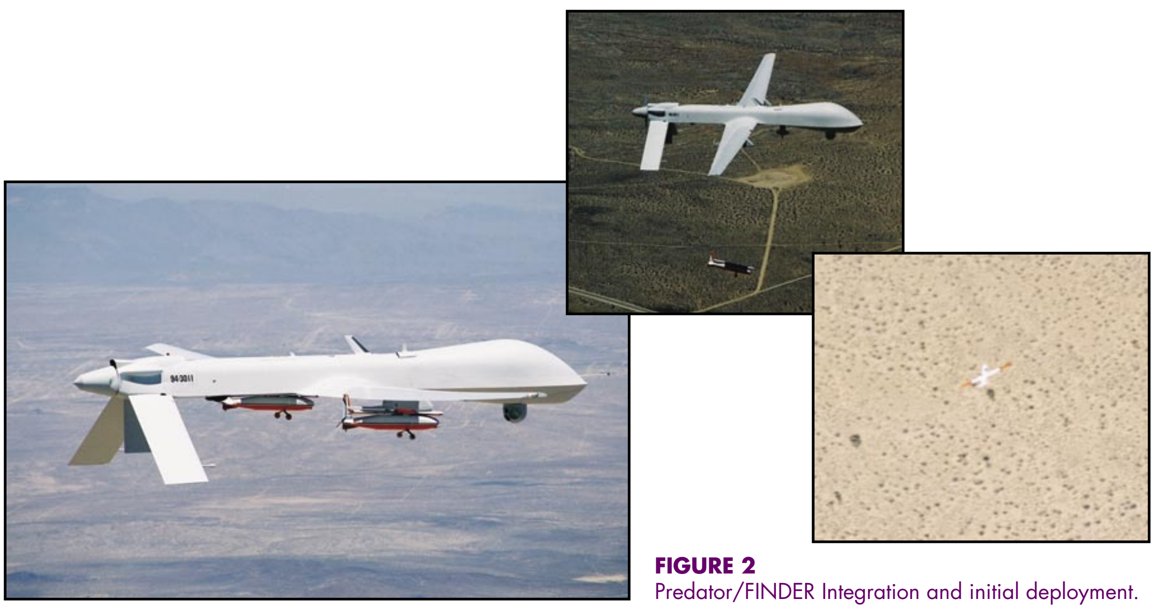

FIGURE 2
Predator/FINDER Integration and initial deployment.

FIGURE 3
FINDER growth options: alternative deployment methods and payload modularity.

As vehicle systems and payload technologies evolve, FINDER possesses the flexibility to accept a wide variety of modular payloads and deployment options. Figure 3 shows a demonstrated deployment alternative that was an outgrowth of the CCAS-specific vehicle development. Future growth capabilities are already being discussed for implementation as follow-on options. They include: close-in targeting support capability, toxic chemical/precursors sensing, biological detection capability, Navy sea-basing options, and radiological hazard sensing.

[Sponsored by OSD and DTRA] ★

Automated Terrain Classification Using Polarimetric Synthetic Aperture Radar

J.-S. Lee,[1] M.R. Grunes,[2] E. Pottier,[3] and L. Ferro-Famil[3]
[1]*Remote Sensing Division*
[2]*Praxis Inc.*
[3]*University of Rennes, France*

Polarimetric Synthetic Aperture Radar: In the last 30 years, synthetic aperture radar (SAR) has been established as a primary remote imaging instrument for Earth resource monitoring, planetary exploration, and military applications. SAR is an active sensor, illuminating targets with electromagnetic waves that can penetrate through cloud coverage. Consequently, it has all-weather and day/night imaging capabilities. Polarimetric synthetic aperture radar (PolSAR), also known as quad-polarization SAR, measures a target's reflectivity with quad-polarizations: horizontal transmitting and receiving (HH), horizontal transmitting and vertical receiving (HV), vertical transmitting and horizontal receiving (VH), and vertical transmitting and vertical receiving (VV). This is achieved by alternately transmitting horizontal (H) and vertical (V) polarization radar pulses and receiving both H and V polarizations of reflected pulses with sufficiently high pulse repetition frequencies. Unlike single or dual polarization SAR, PolSAR data can be used to synthesize responses from any combination of transmitting and receiving polarizations. This capability provides information to characterize scattering mechanisms of various terrain covers. Open areas typically show surface scattering characteristics, trees and bushes show volume scattering, and buildings, vehicles, and man-made objects have double bounce and specular scattering. This capability enhances the accuracy and detail of terrain characterization.

PolSAR Terrain Classification: Terrain and land-use classification are arguably the most important applications of PolSAR. Many supervised and unsupervised (automated) classification methods have been proposed. Earlier algorithms classify PolSAR images based on their statistical characteristics. Recently, the inherent characteristics of physical scattering mechanisms have been used as an additional advantage by providing information for class type identification. The deficiency of this approach is that the classification result lacks details, because of statistical properties were not used.

Current Research: A new and robust classification algorithm[1] has been developed that preserves the scattering mechanism of each class and uses the statistical properties for retaining the spatial resolution in the classification results. The first step is to divide image pixels into the three categories of surface, volume, and even bounce scattering, by applying the Freeman and Durden decomposition.[2] Pixels in each category are classified independent of pixels in the other categories to preserve purity in the scattering characteristics. A new and effective initialization scheme has also been devised to initially merge clusters by applying a criterion developed based on the Wishart distance measure. Pixels are then iteratively classified by a Wishart classifier using the initial clusters as the training sets within each scattering category. To produce an informative classification map, class color selection is important. Therefore, we have developed a procedure that automatically colors the classification map by using scattering characteristics, categorized as surface scattering, double-bounce scattering, and volume scattering.

Experiment Result: A NASA/JPL AIRSAR L-band image of San Francisco (Fig. 4) is used to show the applicability of this algorithm for general terrain classification. The spatial resolution is about 10 × 10 m. This polarimetric SAR data has 700 × 901 pixels. The radar incidence angles span from 5° to 60°. This scene contains scatterers with a variety of distinctive scattering mechanisms. Figure 4(a) shows the original POLSAR image, with |HH-VV|, |HV|, and |HH+VV|, for the three composite colors (red, green, and blue, respectively). Figure 4(b) shows the Freeman/Durden decomposition using the magnitude of double bounce $|P_{DB}|$, volume scattering $|P_V|$, and surface scattering $|P_S|$ for red, green, and blue. The classification result is shown in Fig. 5(a) with the color-coded class label shown in Fig. 5(b). We have 9 classes with surface scattering because of the large ocean area. Three volume classes detail volume scattering from trees and vegetation. The double-bounce classes clearly show the street patterns associated with city blocks, and they are also scattered throughout the park areas, associated with man-made structures and tree trunk-ground interactions. The classified image with 15 classes reveals considerably more terrain information than the original image (Fig. 4(a)).

Summary: We have developed an effective and automated terrain classification algorithm that preserves scattering characteristics in PolSAR data while still allowing terrain type identification. This algorithm has been found to be applicable to sea ice classification

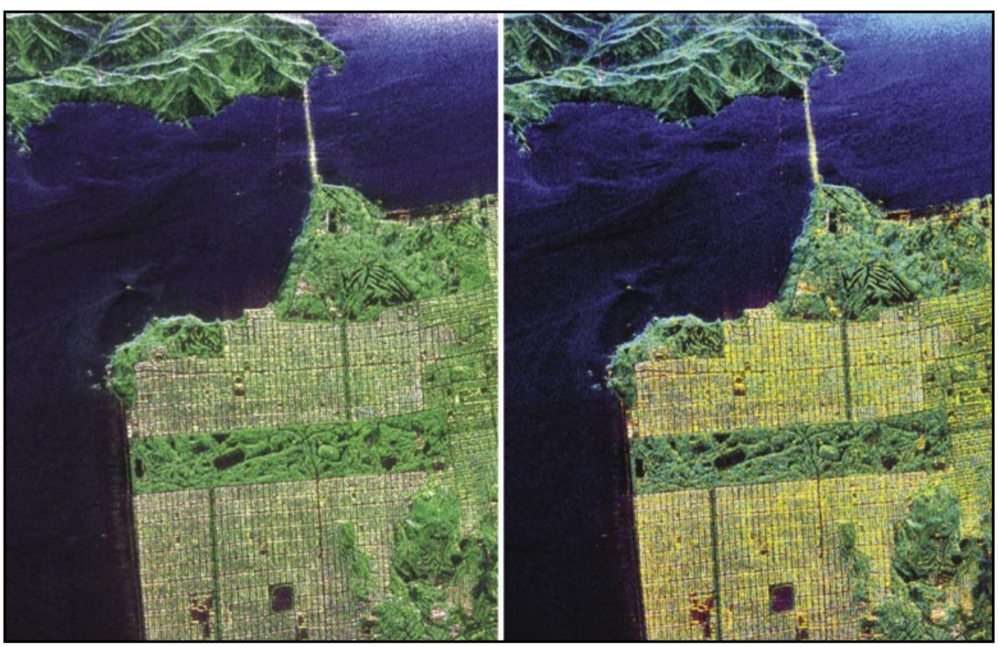

(a) (b)

FIGURE 4
(a) NASA JPL POLSAR image of San Francisco displayed with |HH-VV|, |HV|, and |HH + VV|, for red, green and blue, respectively. (b) The Freeman/Durden decomposition using $|\mathbf{P_{DB}}|$, $|\mathbf{P_V}|$, and $|\mathbf{P_S}|$ for red, green, and blue.

(a) Classification map

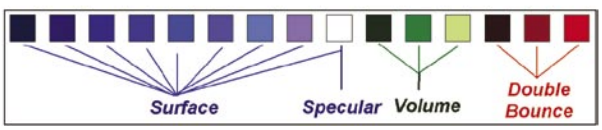

(b) Color-coded class label

FIGURE 5
(a) Final classification map of the San Francisco image into 15 classes. (b) The color-coded class label indicates scattering mechanisms.

and to rapid detection and deployment in disaster management, e.g., the detection of landslide associated with earthquake and forest fires.

Acknowledgment: DARPA has funded us through a terrain characterization study using a FOPEN (foliage penetration) UHF (233-445 MHz) polarimetric SAR. A FOPEN terrain characterization software package has been developed based on this automated classification technique and is being integrated into a FOPEN Terrain Workstation.

[Sponsored by ONR and DARPA]

References

[1] J.S. Lee, M.R. Grunes, E. Pottier, and L. Ferro-Famil, "Unsupervised Terrain Classification Preserving Scattering Characteristics," *IEEE Trans. Geoscience Remote Sens.* **42**(4), 722-731 (2004).

[2] A. Freeman and S.L. Durden, "A Three-Component Scattering Model for Polarimetric SAR Data," *IEEE Trans. Geoscience Remote Sens.* **36**(3), 963-973 (1998).

★

Comparing Ocean Prediction System Skill Using Ocean Color

H.E. Hurlburt,[1] J.F. Shriver,[1] O.M. Smedstad,[2] A.J. Wallcraft,[1] R.A. Arnone,[1] C.N. Barron,[1] E.P. Chassignet,[3] P.M. Flynn,[1] D.-S. Ko,[1] R.C. Rhodes,[1] and L.F. Smedstad[1]
[1]*Oceanography Division*
[2]*Planning Systems Inc.*
[3]*University of Miami*

Introduction: This article illustrates the value of SeaWiFS ocean color imagery in assessing the ability of five different ocean prediction systems to map the "ocean weather." Nowcast results are presented from three global systems in the northwestern Arabian Sea and from all systems in the Gulf of Mexico. Ocean weather includes warm and cold eddies, the oceanic analog of atmospheric highs and lows, and the meandering pathways of ocean currents and fronts. Ocean color imagery is a unique independent data set that is very effective in differentiating the relative skill of the different systems and in helping to diagnose specific strengths and weaknesses of the systems. Ocean color from the SeaWiFS satellite (operated by Orbital Sciences Corp.) was collected and processed at NRL using an extension of NASA algorithms.[1] Improved coupled ocean-atmosphere algorithms for coastal waters were used to uncouple the spectral color signature into the near-surface chlorophyll concentrations. These images provide unique tracers of both circulation and biological activity. Daily chlorophyll images were generated by a 7-day latest pixel composite to remove clouds and retain ocean features. The chlorophyll features are clearly associated with the location of ocean circulation features, whereas their absolute concentration is associated with the biological response. Features marked by both chlorophyll-rich and chlorophyll-poor water proved useful in comparing the ocean prediction systems. In addition, the study clearly illustrates that biological responses of the surface waters are strongly linked to physical events and processes.

Ocean Prediction Systems Compared: The five ocean prediction systems are based on three ocean models. (1) The NRL Layered Ocean Model (NLOM) has seven Lagrangian layers in the vertical (layer thickness varies in space and time), including the mixed layer. It is relatively inexpensive computationally and thus is presently run with high horizontal resolution globally (excluding the Arctic and most shallow water). Two of the systems are based on this model with 1/16° and 1/32° (~7 km and ~3.5 km mid-latitude) resolution. (2) The Navy Coastal Ocean Model (also developed at NRL) uses 40 levels in the vertical, which are at fixed depths in deep water and terrain following at depths <137 m. Two systems presented here are based on NCOM. The first uses a 1/8° fully global configuration (15-16 km midlatitude resolution)[2] and the second uses a regional 1/24° Intra-Americas Sea (Caribbean, Bahamas, Gulf of Mexico) configuration[3] nested in the global NCOM. (3) The HYbrid Coordinate Ocean Model (HYCOM) has a generalized vertical coordinate, which is typically Lagrangian isopycnic in the stratified ocean, fixed depth in the unstratified mixed layer, and terrain-following in shallow water. It makes a dynamically smooth space-time varying transition between the coordinate types via the layered continuity equation. It has been developed under the National Ocean Partnership Program as a next-generation community ocean model, with contributions from researchers at several different institutions, including NRL. Here HYCOM is used in a 1/12° Atlantic configuration (~7 km midlatitude resolution) with 26 hybrid layers in the vertical.

All of the prediction systems assimilate sea surface height (SSH) from satellite altimetry and sea surface temperature (SST) from satellite infrared radiometry. The 1/16° global NLOM system[4] (1/16° NLOM) was the world's first real-time global prediction system of the ocean weather (October 2000), and in September 2001 it became the first operational system (run at the Naval Oceanographic Office). It is slated for replacement by the 1/32° global NLOM system[5] (1/32° NLOM) in early 2005. The 1/16° and 1/32° NLOM systems are the only ocean prediction systems here that assimilate altimeter track data using the model as a first guess. All of the NCOM systems assimilate SSH indirectly via synthetic temperature and salinity profiles. In this manner, the 1/8° global NCOM system assimilates the SSH analysis from 1/16° NLOM (1/8° NCOMa) or 1/32° NLOM (1/8° NCOMb). In that sense, global NLOM and global NCOM are components of the same ocean prediction system.[6] The high horizontal resolution of NLOM is used to assimilate altimeter data and to make 30-day forecasts of the ocean weather, while NCOM extends coverage to the Arctic and shallow water and adds the capability to make 5-day forecasts of the ocean mixed layer and upper ocean with high vertical resolution and to provide boundary conditions for nested models. The 1/24° Intra-Americas Sea (IAS) NCOM (1/24° NCOM) is nested in 1/8° NCOM and assimilates model-independent SSH analyses, as does the present version of the 1/12° Atlantic HYCOM prediction system (1/12° HYCOM). The surface observations provided by satellite have a strong correlation to the subsurface ocean structure, and each system represents this correlation differently. A 1/12° global HYCOM system with improved data assimilation is planned as a replacement for the present NLOM/NCOM system in 2007.

Comparison in the NW Arabian Sea: Satellite altimetry provides the key available data type (SSH) that allows a data-assimilative, eddy-resolving ocean model to accurately map the ocean weather. This is illustrated in Fig. 6 for the northwestern Arabian Sea and the Gulf of Oman. Table 1 provides a quantitative comparison of eddy center position errors in the global ocean predictions in relation to eddy center locations in the ocean color. Clearly defined eddy centers in the ocean color (Fig. 6(a)) were used in Table 1 (with eddies listed in order of decreasing size in the table and marked by number on Fig. 6(a)). Comparison of 1/32° NLOM (with assimilation of SSH from three altimeters) and 1/32° NLOMn (no assimilation of altimeter data, atmospheric forcing only) demonstrates the effectiveness of the altimeter data assimilation. Assimilation of the altimeter data is essential because the eddies are generally nondeterministic due to flow instabilities. The table also indicates the value-added of high horizontal resolution in depicting eddies. The 1/8° NCOMa,b systems generally depict only the larger eddies, e.g., the prominent column of 4 alternating counterclockwise and clockwise eddies extending southward from the coast of Iran in the SeaWiFS ocean color imagery and all of the data-assimilative ocean prediction systems (Fig. 6).

Comparisons in the Gulf of Mexico: In Fig. 7, SSH contours from six ocean predictions are overlaid on ocean color. Chlorophyll-poor water, advected into the Gulf of Mexico from the Caribbean, depicts the Loop Current and shed eddies as dark areas. A bright high chlorophyll plume emanating from the Mississippi River outlines the eastern edge of the Loop Current and a semidetached eddy. SSH from two altimeters, GFO and JASON-1, were used for the ocean prediction system results depicted here. The 1/12° HYCOM system and the two NLOM systems have realistic northward penetration of the Loop Current and a semidetached eddy in accord with the ocean color. However, the eddy in 1/16° NLOM is extremely weak. The 1/24° IAS NCOM system and 1/8° NCOMb (with assimilation of 1/32° NLOM SSH) both depict a robust eddy, while 1/8° NCOMa

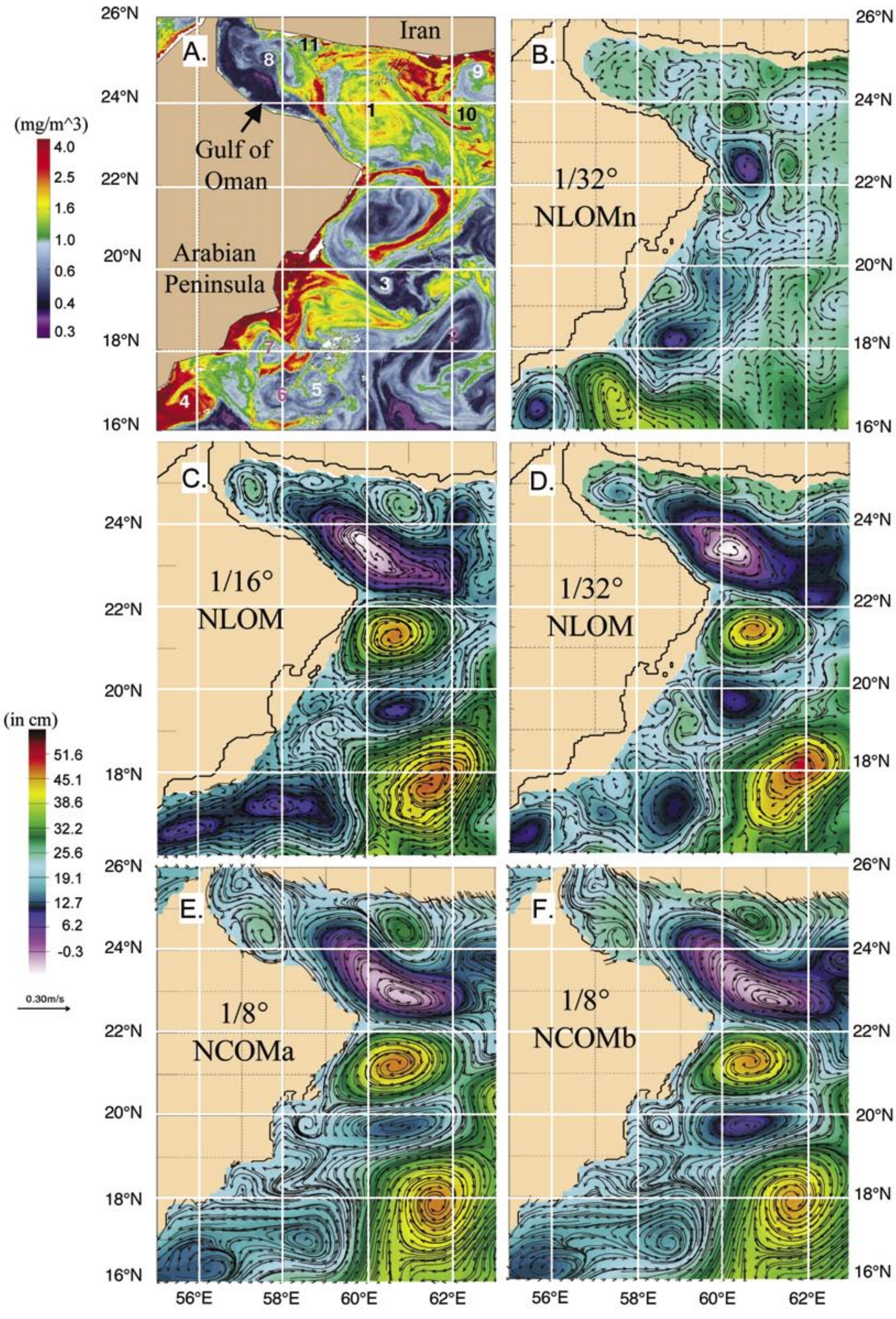

FIGURE 6
A comparison of (a) chlorophyll concentration from SeaWiFS (2-6 October 2002 latest cloud-free pixel composite with most data from 6 October) with 6 October 2002 from (b) 1/32° NLOMn with no assimilation of ocean data (atmospheric forcing only) and (c-f) nowcast results from the data-assimilative ocean prediction systems. (b-f) show surface layer currents overlaid on sea surface height (SSH). The color of the numbers plotted on (a) was varied for visual clarity only.

Table 1 — Eddy Center Position Errors in Ocean Prediction Systems Compared to Ocean Color

Ocean color eddy ID #	**1/32° NLOM**	**1/16° NLOM**	**1/8° NCOMb**	**1/8° NCOMa**	**1/32° NLOMn**
	Eddy center position error in km				
1	18	35	124	93	NP
2	28	103	58	70	NP
3	12	44	8	37	45
4	42	35	74	81	31
5	17	42	20	27	NP
6	79	53	NP	NP	NP
7	40	NP	NP	NP	NP
8	39	NP	NP	NP	NP
9	35	30	NP	NP	NP
10	22	60	46	82	42
11	33	36	NP	NP	30
Number of the ocean color eddies depicted					
11	11	9	6	6	4
Times had most accurate position					
	6	2	1	0	2

NP: eddy not present.

Notes:

The eddy ID numbers are plotted on Fig. 6(a). Eddies are listed in order of decreasing size as depicted by the ocean color. Eddy position measurement error is 10-15 km in both the ocean color and the models.

1/32° NLOM: 1/32° NLOM system with assimilation of altimeter track data from ERS-2, GFO, and JASON-1 altimeters.

1/16° NLOM: Operational 1/16° NLOM system with assimilation of real-time altimeter data from the ERS-2 and GFO altimeters (JASON-1 not in the operational data stream at that time).

1/8° NCOMb: 1/8° NCOM system with assimilation of 1/32° NLOM SSH.

1/8° NCOMa: 1/8° NCOM system with assimilation of 1/16° NLOM SSH.

Assimilation of 1/32° NLOM SSH vs 1/16° NLOM SSH improved the eddy center position accuracy for 5 of the 6 eddies 1/8° NCOMb,a depicted. With one exception 1/8° NCOMb,a only include the larger eddies depicted in the ocean color.

1/32° NLOMn: 1/32° NLOM with no assimilation of ocean data, only atmospheric forcing.

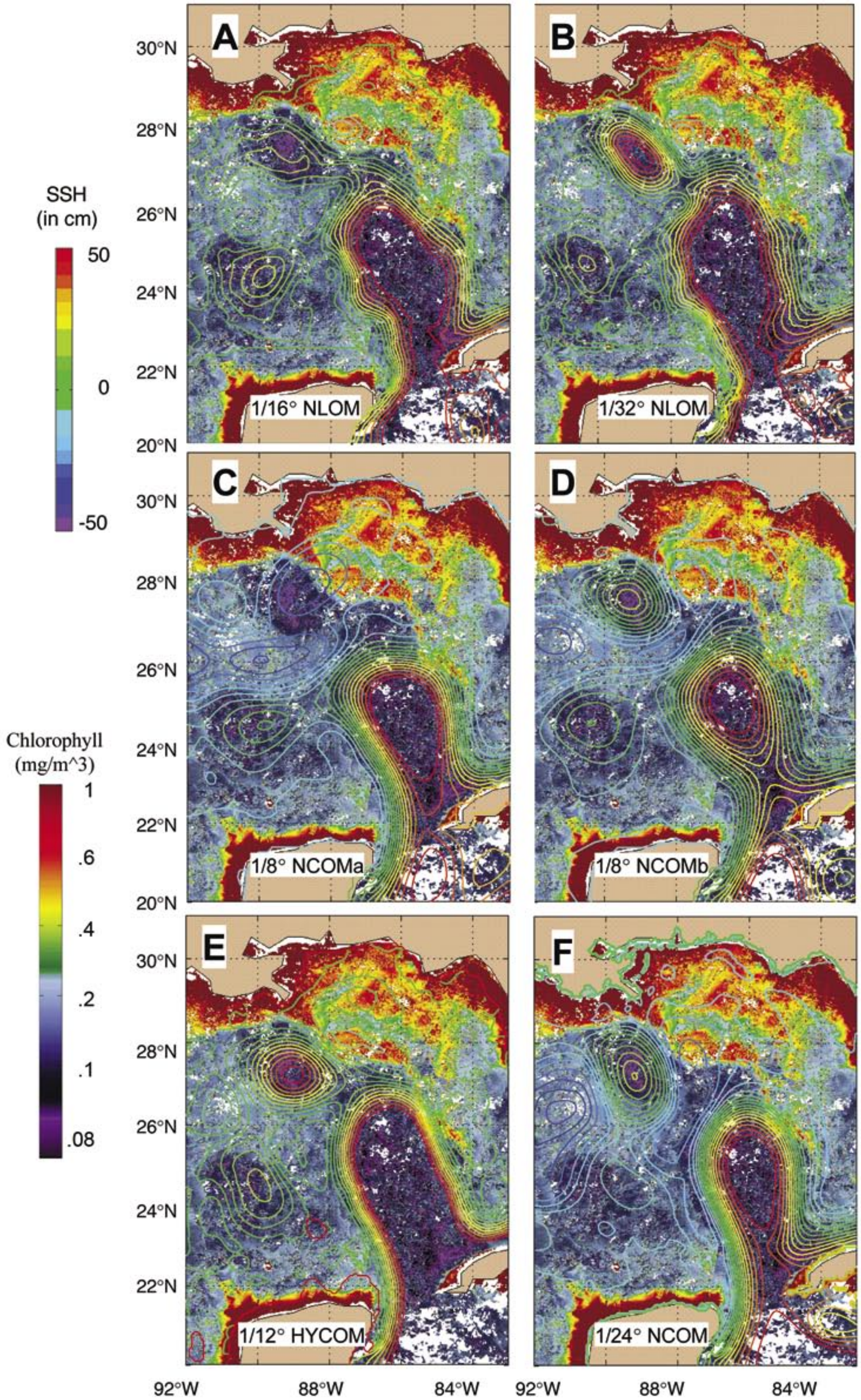

FIGURE 7

Nowcast SSH line contours from 6 ocean prediction systems or their variants on 28 August 2003 overlaid on ocean color imagery from SeaWiFS. Both the SeaWiFS imagery and the SSH contours are colored prismatically from low (violet) to high (red). The SeaWiFS chlorophyll concentration is the latest cloud-free pixel composite over 22-28 August 2003. SSH from the GFO and JASON-1 altimeters are used for assimilation. SSH contour interval is 5 cm, and contours >50 cm are omitted.

(with assimilation of 1/16° NLOM SSH) shows none. Because none of the NCOM systems have sufficient northward penetration of the Loop Current, the Loop Current eddy is fully detached in 1/8° NCOMb and 1/24° NCOM.

Since the data assimilation method is identical for 1/16° and 1/32° NLOM, and it uses the model forecast as the first guess for the altimeter data assimilation, it is obvious that the ocean model is an integral component of the data assimilation. Hence, model simulation skill (without ocean data assimilation) is an important factor in both the data assimilation phase (for dynamical interpolation skill) and the forecasting phase of ocean prediction. Loop Current penetration is sensitive to the inflow transport from the Caribbean and to having a strongly surface-trapped inflow jet hugging the western boundary (evidenced by tightly packed SSH contours hugging the western boundary at the inflow in the HYCOM and NLOM systems). These are also requirements for strong baroclinic flow instabilities within the Gulf of Mexico, which are responsible for observed contortions of the Loop Current and associated eddies. Lack of a robust semidetached eddy in 1/16° NLOM is due to spurious westward bottom inflow into the Gulf of Mexico through the Florida Strait (not present in 1/32° NLOM). By following the geostrophic contours of the bottom topography, this results in a spurious westward current below the semidetached eddy location. Since bottom currents can advect upper ocean currents,[7] there is excessively rapid westward advection of any eddy that begins to form in this location, severely damaging the dynamical interpolation skill of the model in this case. Similar comparisons in the Gulf of Mexico for other Loop Current and eddy configurations can be seen on the HYCOM and NLOM web pages (listed below), including some with severe contortions.

Impact: Finding independent data sets that are effective in evaluating and comparing the skill of ocean prediction systems is essential in developing a state-of-the-art ocean prediction capability for the Navy. Ocean color is an independent data set that is particularly effective in assessing the ability of ocean prediction systems to map the "ocean weather." The strong correlation between the ocean dynamic field (SSH) and the ocean color imagery also suggests the possibility to use the ocean color imagery within the assimilation process to better predict the ocean circulation. NRL is participating in the multinational Global Ocean Data Assimilation Experiment (GODAE), which is designed to help justify a permanent global ocean-observing system by demonstrating useful real-time global ocean products with a customer base, a major step forward in transitioning oceanography into an operational science. NRL is also participating in the GODAE-related European Marine Environment and Security for the European Area (MERSEA) multinational ocean prediction system intercomparison project. Real-time and archived results from all of the ocean prediction systems compared here can be seen on the web:

1/12° Atlantic HYCOM at
http://hycom.rsmas.miami.edu
1/8° global NCOM at
http://www.ocean.nrlssc.navy.mil/global_ncom
1/16° and 1/32° global NLOM at
http://www.ocean.nrlssc.navy.mil/global_nlom
1/24° IAS NCOM at
http://www7320.nrlssc.navy.mil/IASNFS_WWW

[Sponsored by ONR, SPAWAR, NOPP, and HPCMO]

References

[1] R.A. Arnone and A.R. Parsons, "Real-time Use of Ocean Color Remote Sensing for Coastal Monitoring," chapter 14 in *Remote Sensing of Aquatic Coastal Environments*, ed. R.L. Miller, C.E. Del Castillo, and B.A. McKee, (Kluwer Academic Publishers, Netherlands, 2004).

[2] C.N. Barron, A.B. Kara, H.E. Hurlburt, C. Rowley, and L.F. Smedstad, "Sea Surface Height Predictions from the Global Navy Coastal Ocean Model (NCOM) During 1998-2001," *J. Atmos. Oceanic Technol.* **21**,1876-1894 (2004).

[3] D.S. Ko, R.H. Preller, and P.J. Martin, "An Experimental Real-time Intra-Americas Sea Ocean Nowcast/Forecast System for Coastal Prediction," Proceedings of the American Meteorological Society's Conference on Coastal Atmospheric and Oceanic Processes and Prediction, Seattle, WA, pp. 97-103 (2003).

[4] O.M. Smedstad, H.E. Hurlburt, E.J. Metzger, R.C. Rhodes, J.F. Shriver, A.J. Wallcraft, and A.B.Kara, "An Operational Eddy Resolving 1/16° Global Ocean Nowcast/Forecast System," *J. Mar. Sys.* **40-41**, 341-361 (2003).

[5] J.F. Shriver, H.E. Hurlburt, O.M. Smedstad, A.J. Wallcraft, and R.C. Rhodes, "1/32° Real-time Global Ocean Prediction and Value-added Over 1/16° Resolution," *J. Mar. Sys.*, accepted (2004).

[6] R.C. Rhodes, H.E. Hurlburt, A.J. Wallcraft, C.N. Barron, P.J. Martin, E.J. Metzger, J.F. Shriver, D.S. Ko, O.M. Smedstad, S.L. Cross, and A.B. Kara, "Navy Real-time Global Modeling Systems," *Oceanography* **15**(1), 29-43 (2002).

[7] H.E. Hurlburt and J.D. Thompson, "A Numerical Study of Loop Current Intrusions and Eddy Shedding," *J. Phys. Oceanogr.* **10**, 1611-1651 (1980).

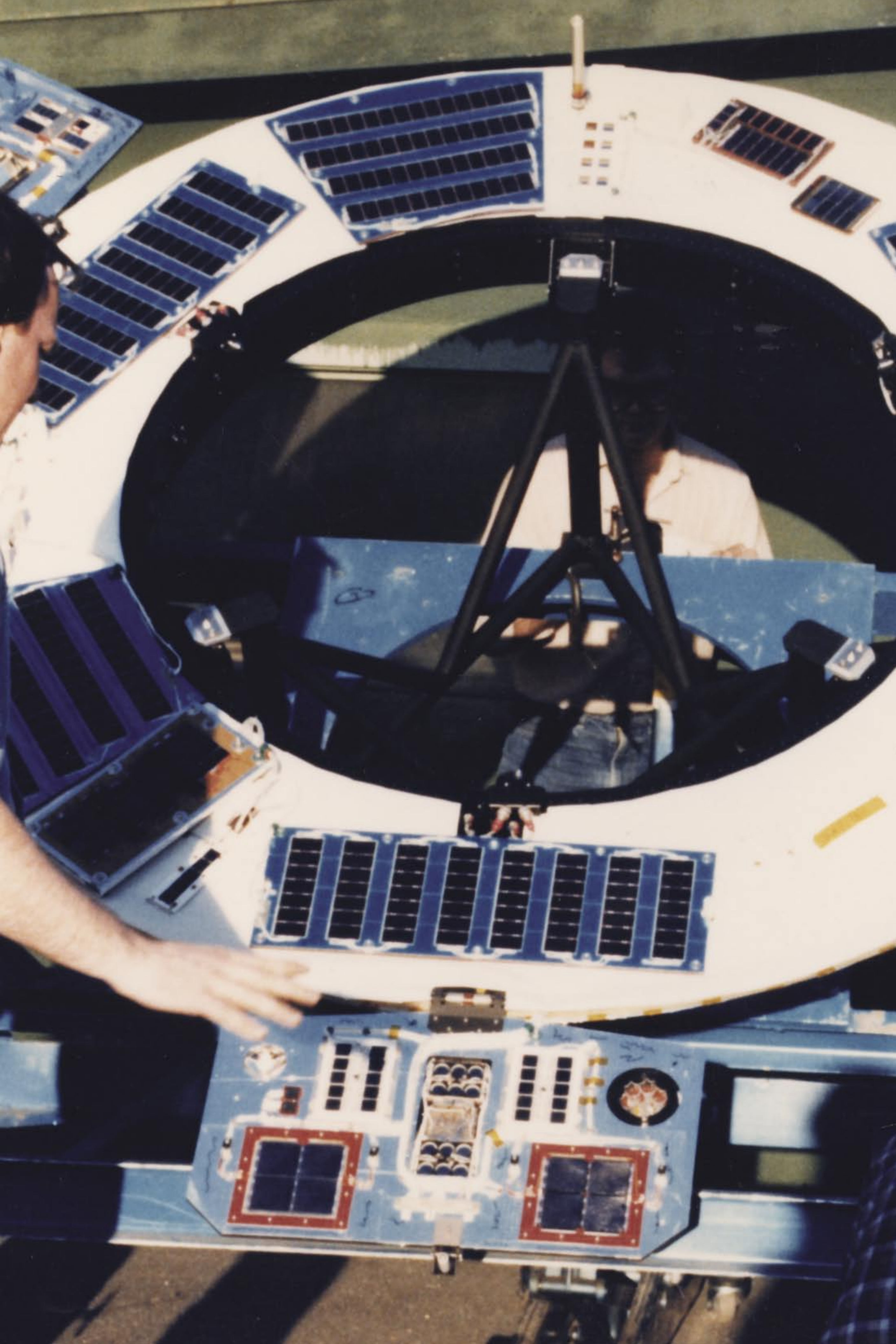

Simulation, Computing, and Modeling

Photo caption: The LIving Plume Shield (LIPS) was used first to develop and test new software radio links and on this third LIPS, to test the latest developments in solar cell technologies.

Adaptive Radar Pulse Compression

S.D. Blunt and K. Gerlach
Radar Division

Introduction: Pulse compression enables a radar to achieve the high range resolution of a short pulse without the need for high peak transmit power via the transmission of a modulated long pulse (or waveform) followed by its subsequent matched filtering upon reception. However, the matched filtering of large target returns produces sidelobes that can mask the presence of smaller nearby targets. A pertinent example of this is in landmine detection by ground-penetrating radar in which the ground return can mask the presence of a mine.

The Radar Division has recently developed an approach denoted as Adaptive Pulse Compression (APC) whereby the radar receiver matched filter is adapted to the received signal using a novel variation of Minimum Mean-Square Error (MMSE) estimation. By adapting the receiver filter to the received signal, the sidelobes resulting from large targets can be suppressed to the level of the noise, thereby greatly increasing the radar's sensitivity to smaller targets.

Adaptive Pulse Compression: The range profile illuminated by a radar can be modeled as an impulse response whereby each sample represents an individual range cell, with a range resolution that is inversely proportional to the bandwidth of the transmitted waveform. As such, the received signal is effectively a convolution of the waveform with the range profile impulse response that is to be extracted from the received signal. The application of the standard matched-filter to the received signal maximizes the SNR of a point target in white noise but is known to suffer from range sidelobes induced by large targets, which can mask the presence of smaller targets (Fig. 1).

To suppress the range sidelobes from the large targets and thereby improve the radar's sensitivity to detect smaller nearby targets, the Adaptive Pulse Compression algorithm uses Reiterative Minimum Mean-Square Error (RMMSE) estimation. RMMSE uses the range cell estimates from the matched filter as a priori knowledge to estimate the appropriate receive filter for each individual range cell. Given the knowledge of the relative locations of large scatterers within the range profile that is provided by the matched filter, the RMMSE receive filter for each particular range cell places nulls at range offsets that correspond to nearby large targets. In so doing, RMMSE suppresses the range sidelobes induced by the nearby large targets so that the true complex amplitude of the particular range cell can more accurately be estimated. Furthermore, the refined range cell estimates obtained from applying RMMSE can themselves be used as more accurate a priori knowledge with which to repeat RMMSE and further improve the estimation accuracy. It has been found via extensive numerical simulation that 3 to 4 stages of range cell estimation (inclusive of the initial matched-filtering operation) are sufficient to suppress the sidelobes into the noise and thereby unmask any small targets. The process of alternating estimation between the range cells and the receive filters is denoted as the Adaptive Pulse Compression (APC) algorithm. As an example, consider Fig. 2 in which three stages of the APC algorithm is able to uncover the small target that was previously masked by using the matched filter. Furthermore, as an example of a stressing scenario, Fig. 3 illustrates the case of several densely spaced targets with highly disparate power levels such as might occur for a convoy with a Ground Moving Target Indicator (GMTI) radar, an airborne formation, or as a result of synthetic aperture radar (SAR) clutter imaging. In this scenario the matched filter reveals only the largest targets and masks the smaller ones. In comparison, the APC algorithm enables the detection of even the very small targets by mitigating the range sidelobes from the large targets.

Summary: The Adaptive Pulse Compression algorithm using Reiterative Minimum Mean-Square Error estimation has been demonstrated via computer simulation to substantially reduce range sidelobes resulting from the matched filtering of large target returns. In so doing, APC greatly improves radar sensitivity and enables the detection of previously masked targets. Current work is involved with the test and evaluation of APC using measured radar data, preliminary results appear quite promising.

[Sponsored by ONR]

References

[1] S.D. Blunt and K. Gerlach, "A Novel Pulse Compression Scheme Based on Minimum Mean-Squared Error Reiteration," *IEEE Intl. Radar Conf.*, Adelaide, Australia, September 3-5, 2003, pp. 349-353.

[2] S.D. Blunt and K. Gerlach, "Adaptive Pulse Compression," *IEEE National Radar Conf.*, Philadelphia, Pennsylvania, April 26-29, 2004, pp. 271-276.

[3] S.D. Blunt and K. Gerlach, "Robust Predictive Deconvolution System and Method," U.S. Patent Application, September 30, 2003, Navy Case # 84,597.

★

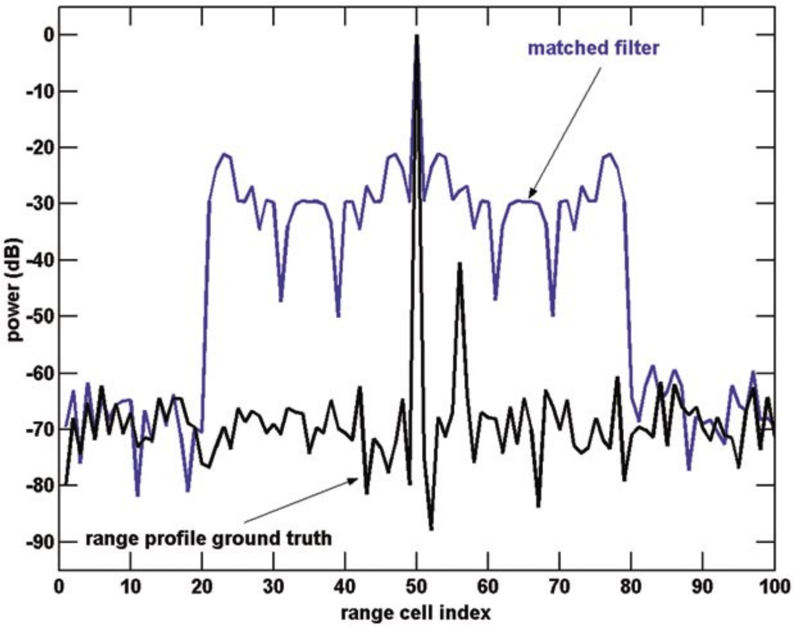

FIGURE 1
Matched-filter output vs ground truth.

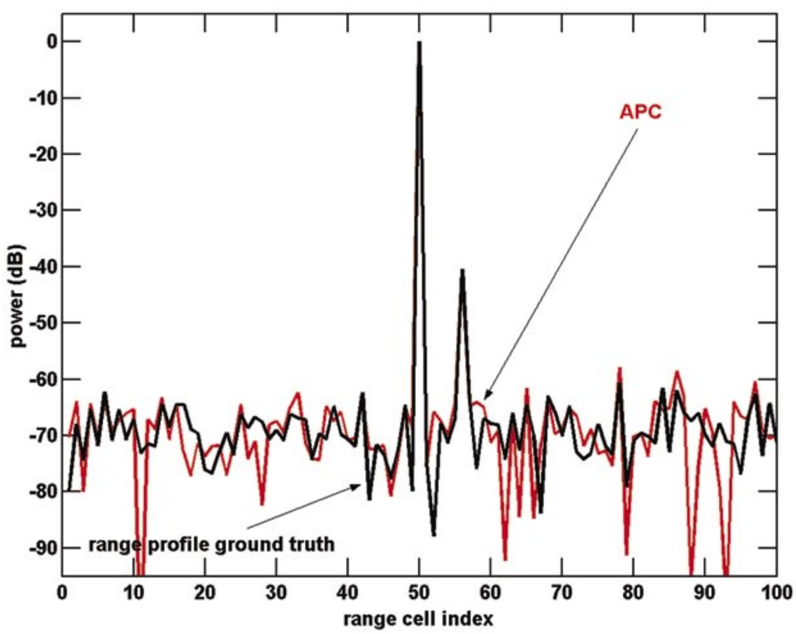

FIGURE 2
APC output vs ground truth.

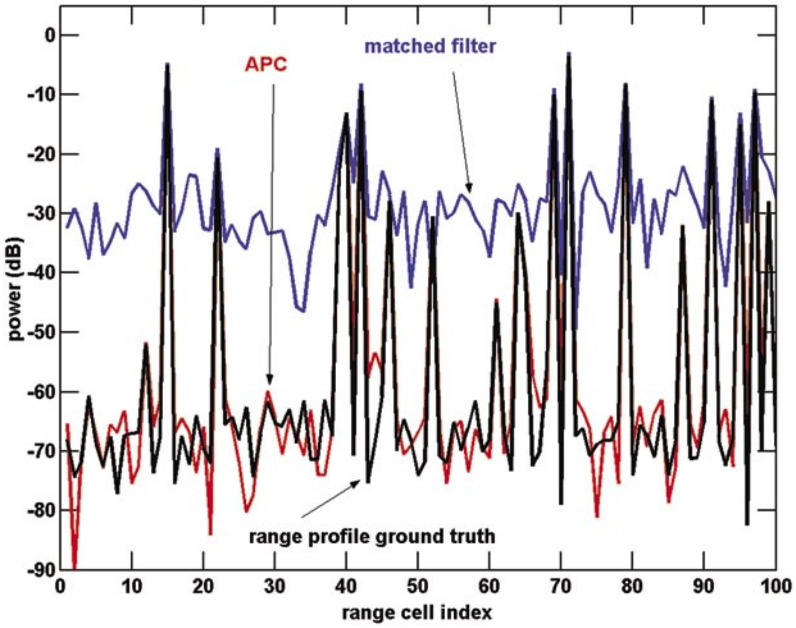

FIGURE 3
Comparison of matched-filter and APC for a dense target environment.

Detonation Initiators for Propulsion Systems

K. Kailasanath and C. Li
Laboratory for Computational Physics and Fluid Dynamics

Introduction: Detonations are an extremely efficient means of burning a fuel-air mixture and converting its chemical energy content into mechanical energy. Air-breathing and rocket engines based on pulsed detonations have the potential to provide the Navy with increased range and speed while reducing fuel consumption and system costs.[1] Over the past few years, we have conducted computational studies of the pulsed detonation engine concept. The results of these simulations have been invaluable in assessing the performance of these engines and isolating factors that may hinder the realization of their full potential. Reliable and repeated low-energy initiation of detonations in the high-speed flow of fuel-air mixtures is one of the challenging problems hindering the practical development of these engines.

Methods to Initiate Detonations: One of the approaches currently adopted is to use a more detonable fuel-oxygen mixture to initiate a detonation wave and then transition the detonation wave into the desired fuel-air mixture. However, for this approach to be practically feasible, additional oxygen must be carried or generated onboard, thereby increasing the weight and complexity of the propulsion system. Other techniques involving hot turbulent jets and radical species; physical obstacles to generate flow turbulence and enhance the transition from a flame to a detonation; and the use of geometrical devices to focus shock waves have also been investigated.[1] We have used our fundamental studies of detonation initiation to develop an innovative initiator concept that does not require any additional oxygen or geometrical obstacles for initiating detonations in fuel-air mixtures.[2] In this concept, shown schematically in Fig. 4, air is introduced along the circumference of a tube in the form of an annular jet. The high temperatures and pressures generated by the implosion of the shock waves generated by these impulsive jets are sufficient to ignite most fuel-air mixtures of practical interest.

Concept Validation using Numerical Simulations: We have extensively validated the detonation initiation concept using multidimensional, time-accu-

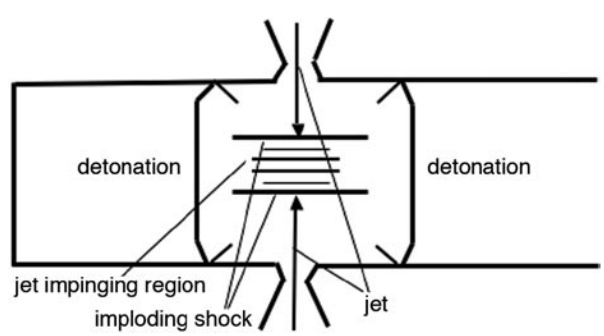

FIGURE 4
Schematic of the new detonation initiation concept involving jet-induced imploding shocks.

rate numerical simulations based on the Flux-Corrected Transport (FCT) algorithm and the Virtual-Cell Embedding (VCE) technique developed at NRL. Figure 5 shows results from a typical simulation. Both pressure and water concentration (typical product of combustion) are shown at a sequence of times. The jet impinges onto itself near the tube centerline around 112 μs and a high-temperature-pressure kernel begins to form. However, there is no water production until 140 μs. At 140 μs, a high-temperature-pressure kernel of elliptical shape is observed. At the edge of the kernel, the pressure is very high and a detonation front begins to form. At 160 μs, the kernel expands and the pressure at the edge of the kernel reduces somewhat to a level corresponding to a slightly overdriven detonation in the chosen mixture. At 178 μs, the kernel further expands. However, at this time, the detonation is observed only at either end of the kernel, and two detonation fronts propagate mainly along the longitudinal direction of the tube toward the tube ends. The part of the detonation front on the side of the kernel is quenched by the air brought in by the jet and becomes a nonreactive shock. Beyond 178 μs, the jet air is entrained and mixed with the combustion products from the detonation process, reducing the water concentration level around the side of the kernel. At 195 μs, the detonation fronts at the two ends of the kernel reach the sidewall of the tube. From this time on, the two detonation fronts further propagate in opposite directions, consuming the combustible material along their way to the tube ends. At 229 μs, reflected shocks from the sidewall can be observed, which further raise the pressure. These reflected shocks might serve as an additional initiation source at marginal conditions where the original annular jet-induced cylindrically imploding shock is not strong enough to initiate detonation directly. After about 230 μs, both detonation fronts are fully established.

Further simulations show that the concept is robust. Depending on the jet parameters, detonation initiation may occur from the implosion of the initial shocks or after subsequent reflections of these shocks from the walls of the confining chamber.

Conclusions: We have developed a method for initiating detonations using annular jet-induced cylindrically imploding shocks. Our numerical simulations have shown that detonation can be initiated by a single, annular jet at modest jet pressures and temperatures that can be readily provided by practical engineering means. The jet material can be the same fuel used in the engine or air, which is particularly beneficial for air-breathing propulsion applications.

[Sponsored by ONR]

References

[1] K. Kailasanath, "Recent Developments in the Research on Pulse Detonation Engines," *AIAA J.* **41**, 1698-1708 (2003).
[2] C. Li and K. Kailasanath, "Detonation Initiation by Annular Jet-Induced Imploding Shocks," accepted for publication, *J. Propul. Power*, September 2004.

★

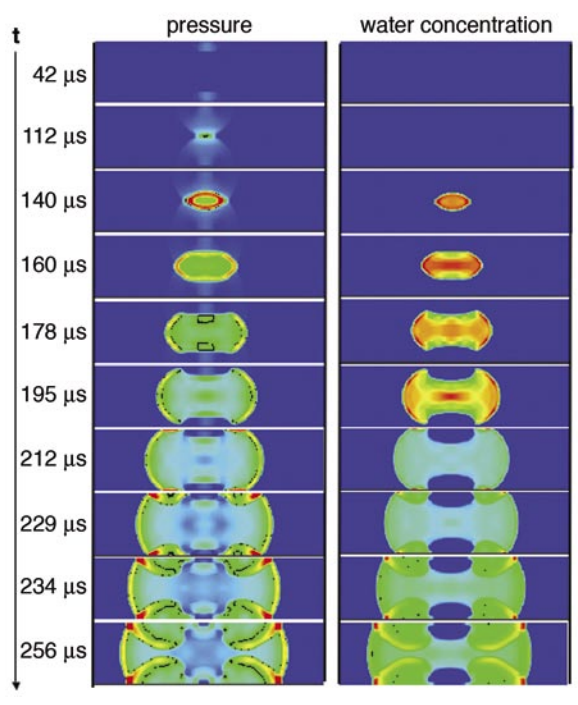

FIGURE 5
Series of snapshots showing the time evolution of the pressure and water concentration distributions during the detonation initiation process.

Computations of Chaotic Flows In Micromixers

C.R. Kaplan, E.S. Oran, and D.R. Mott
Laboratory for Computational Physics and Fluid Dynamics
J. Liu
Berkeley Research Associates

Introduction: Microfluidic devices are important components of chemical and biological sensors proposed for many Naval and civilian applications. The problem of controlling fluid mixing in microdevices is often critical to their successful operation. This is especially true for cases involving chemical reaction, in which the reactants and products must be delivered to selected target locations within a specified concentration range. Flows in these devices are laminar (low Reynolds number), and mixing is controlled by the relatively slow process of molecular diffusion. An important practical issue is how to modify the flow to speed up the mixing process.

One method used to enhance mixing is surface patterning, in which structures are placed along one or more surfaces of a channel. Stroock et al.[1] have shown that repeating sequences of bas-relief herringbone-shaped structures on the floor of a microchannel create flow patterns that increase the interface area between the fluids to be mixed. The geometrical arrangement of obstacles stretches and folds the fluid, so that surface area between fluids is increased and mixing is enhanced. This phenomenon is called chaotic advection.

We are working on a joint computational and experimental effort to design and build microreactors with enhanced and controlled mixing and surface delivery capabilities. In the work described here, we have used numerical simulations to study chaotic advection and focus on the Stroock et al.[1] mixer. The numerical model[2] solves the three-dimensional incompressible Navier-Stokes equations coupled with an equation that describes the advection of a passive scalar, such as a marker dye.

Staggered Herringbone Mixer: Figure 6 shows the staggered herringbone configuration. This micromixer contains two full sequences of herringbone structures. Each sequence consists of six herringbones with the short segment on the left and the long segment on the right, followed by six more herringbones with the short segment on the right and the long segment on the left. At the inflow boundary, water enters at 1 cm/s, while the outflow boundary is set at a fixed pressure of 1 atm.

The major effect of the herringbone structures is to deflect the flow in such a way that the interface area between the fluids increases, and therefore mixing is enhanced. This flow pattern results in convective rolls in the cross section of the microchannel, as shown by the velocity vectors in Fig 6. For the first six herringbones, the larger convective roll is located on the right-hand side (the side with the longer segment), while the smaller convective roll is on the left-hand side (the side with the shorter segment). The flow is reversed for the second set of six herringbones, when the long and short segments of the herringbone structure have been switched.

Advection of Passive Scalars: To evaluate mixing effectiveness, two passive scalars, “red” and “purple,” are introduced at the inflow. The passive scalars follow the streamlines of the flow but have no interaction with the fluid, similar to a dye. Figure 7 shows images of the two passive scalars, at the indicated cross sec-

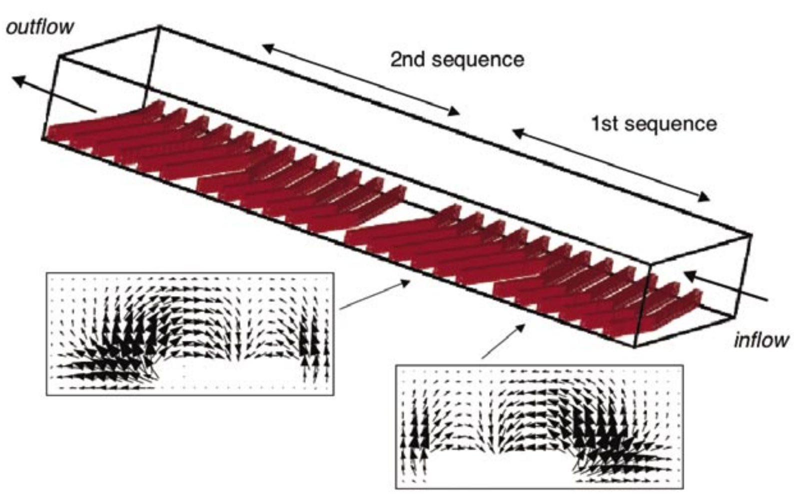

FIGURE 6
Schematic of staggered herringbone mixer. Dimensions are 90 × 200 μm in the cross section, and 4000 μm in length. Individual herringbones are 20 μm high. Velocity vectors show the convective rolls that are formed due to the herringbone structures.

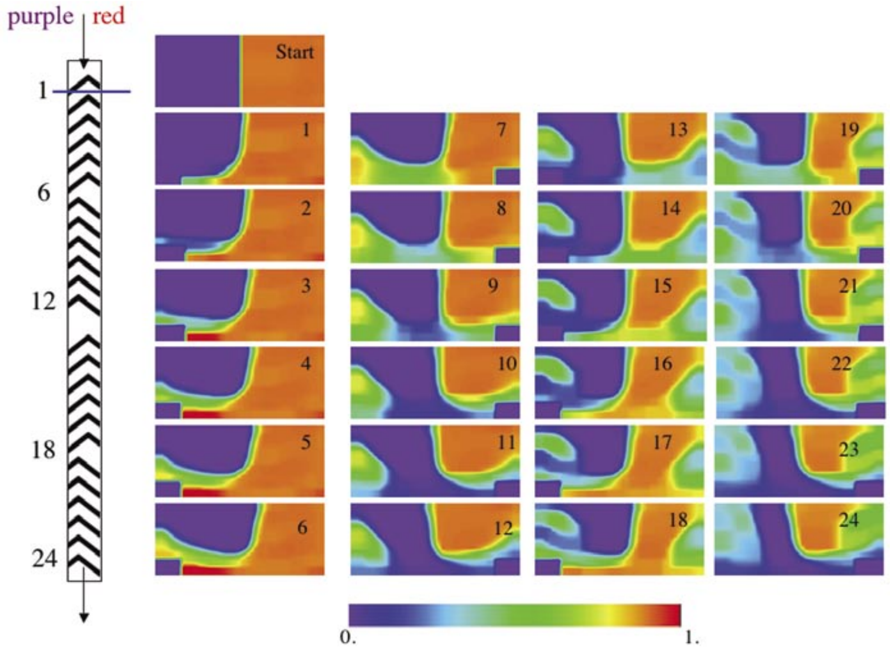

FIGURE 7
Mixing of two passive scalars in the staggered herringbone mixer.

tional planes. That is, "1" corresponds to the plane immediately after the first herringbone. Initially, at time zero, "red" fluid is on the right and "purple" fluid is on the left. For the first six herringbones, the larger convective roll forms on the left side. Therefore, purple fluid is pushed toward the right, near the top of the microchannel, while red fluid is pulled toward the left, near the bottom. When the herringbone pattern is reversed (structures 7 through 12), the red fluid is pushed upward and over to the left at the top, while purple fluid is pulled toward the right near the bottom. At the end of the first sequence of herringbones (after structure 12), some of the red fluid has travelled to the left side and some of the purple fluid has travelled to the right side, resulting in green fluid, which corresponds to well-mixed fluid. This flow pattern repeats itself during the second full cycle of structures, herringbones 13 through 24.

Chaotic Flow: Figure 7 shows that the resulting passive scalar concentrations become more complex after the second set of herringbones, compared to the first. In fact, in Stroock's mixer, which contains 15 full sequences of herringbones, the striations in the flow become finer with each successive herringbone sequence. To capture the finer scales of mixing that are indicative of chaotic advection, the resolution of the calculations must be increased. Figure 8 shows results for a high-resolution calculation containing four complete sequences of herringbone structures. This calculation shows how the flow becomes more complex and the striations become finer as the number of sequences increase.

Discussion: The term *chaotic advection* is used to describe a type of complex behavior that a passive scalar can show under specific conditions. It is an important phenomenon to understand and be able to use for controlling microflows. For a fluid to exhibit chaotic advection, it must be driven, folded, and stretched. In the flows shown here, the bending and stretching is accomplished passively, due to the herringbone structures. This leads to the formation of striations in the passive scalars, which become finer and finer as the flow develops. The result is an exponential increase in the surface area between the different fluids.

Acknowledgments: Drs. F. Ligler and P. Howell and Mr. J. Golden are acknowledged for insightful discussions on microfluidics.
[Sponsored by ONR and HPCMO]

References
[1] A.D. Stroock, S.K.W. Dertinger, A. Ajdari, I. Mezic, H.A. Stone, and G.M. Whitesides, "Chaotic Mixer for Microchannels," *Science* **295**, 647-651 (2002).
[2] D.R. Mott, C.R. Kaplan, and E.S. Oran, "Development of a Robust Incompressible Solver for Cartesian Grids with Colocated Variable Arrangement," AIAA Paper No. 2004-0248, American Institute of Aeronautics and Astronautics, Reston, VA, 2004. ★

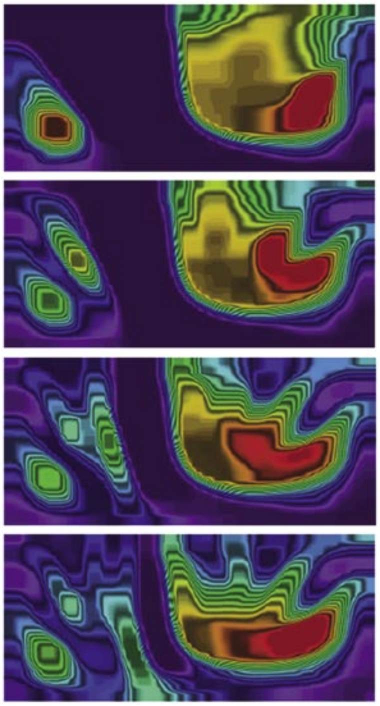

FIGURE 9
Calculations on a 3200 × 36 × 80 grid, using computational cells of 2.5 μm, that show stretching and folding indicative of chaotic advection after four sequences in the herring-bone mixer.

Three-Dimensional Hall Magnetic Reconnection

J.D. Huba
Plasma Physics Division
L.I. Rudakov
Berkeley Research Scholars, Inc.

Introduction: One of the most important and intriguing processes in space and laboratory plasmas is magnetic field line reconnection: it provides a mechanism to rapidly convert magnetic field energy into particle energy. For example, magnetic reconnection is considered to be a key factor in the onset and evolution of solar flares and magnetic storms. These two phenomena play a critical role in the dynamics of the near-Earth space environment, and are an integral part of "space weather" that can adversely impact communication and navigation systems.

The standard picture of magnetic reconnection is shown in Fig. 9, which depicts the evolution of a reconnecting, reversed field current layer, i.e., the magnetic field $\mathbf{B} = B_x \hat{e}_x$ reverses direction along $y = 0$. There is an inflow of plasma and magnetic field in the $\pm y$ direction with a velocity V_{in}, and an outflow in the $\pm x$ direction with a velocity V_{out}. The magnetic topology changes at the X-point where the red and blue field become interconnected. This region is often referred to as the "diffusion region" (the shaded box in Fig. 9). The release of magnetic tension associated with the strong curvature in the reconnected magnetic field lines leads to the acceleration of the plasma in the $\pm x$ direction. Typically, for fast reconnection $V_{in} \simeq 0.1\ V_A$ and $V_{out} \simeq V_A$, where V_A is the Alfvén velocity in the inflow region.

One of the major issues in reconnection physics is to understand the mechanism(s) for "fast reconnection" in collisionless plasmas. Conventional resistive magnetohydrodynamic (MHD) analysis leads to very slow reconnection rates in collisionless systems such as the solar corona and the Earth's magnetosphere. However, it has become evident that Hall physics can playa critical role in collisionless magnetic reconnection. The National Science Foundation Global Envi-

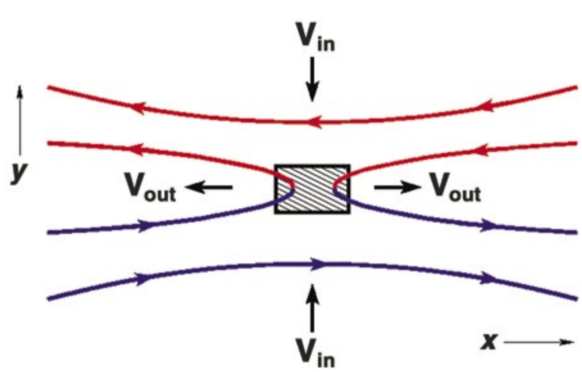

FIGURE 9
Standard, two-dimensional concept of magnetic field line reconnection.

ronment Modeling (GEM) challenge on reconnection physics concluded that Hall physics is the minimum physics needed to achieve fast reconnection—regardless of the mechanism that decouples the electrons from the magnetic field, i.e., allows the magnetic field lines to reconnect.[1] Physically, the Hall term decouples the ion and electron motion on length scales comparable to the ion inertial length. In essence, the electrons remain magnetized while the ions become unmagnetized. In recent years, NRL has carried out a number of studies to better understand the Hall dynamics of magnetic reconnection.

3D Simulation Results: We have carried out the first three-dimensional (3D) study of Hall magnetic reconnection[2] using the NRL Hall MHD code VooDoo.[3] Figure 10 illustrates the key findings. Figure 2(a) shows the initial configuration of the system. The color-coded slabs are in the x-y plane (same as Fig. 9) and denote the density:red indicates $n = 5n_0$ and blue indicates $n = n_0$, where n_0 is the density at the $\pm y$ boundary at $t = 0$. The white lines at $z = 0$ represent magnetic field lines. Lastly, the simulation is initiated with a magnetic perturbation localized in the z direction ($-20 > z > -30$). This perturbation is shown by the red and yellow isosurfaces of the magnetic field in the y direction and are indicative of magnetic reconnection.

Figure 10(b) shows the system at the end of the simulation run. A number of interesting features are observed. First, the magnetic perturbation induces a magneticwave structure that propagates in the direction of the electron drift (i.e., $-z$ direction). This wave is a Hall phenomenon associated with the curvature in the magnetic field (i.e., the curved field lines in the diffusion region shown in Fig. 9). Second, as this wave propagates, it leads to the thinning of the plasma current layer and the triggering of fast reconnection. In Fig. 10(b) magnetic reconnection is occurring in the region $20 > z > -20$, as evidenced by the elongated isosurfaces of B_y and is not isolated to a thin region in the z direction. Third, as reconnection proceeds, the magnetic field lines are "bent" in the $-z$ direction leading to the quadrupole magnetic field structure in B_z that has been observed in 2D simulation studies. This field line bending can be seen in the vicinity of the origin in Fig. 10(b) ($x = y = z = 0$). Finally, after magnetic reconnection occurs, the release of magnetic tension also leads to plasma acceleration in the $+z$ direction, not just in the x direction as shown in Fig. 9. We find that $V_z \simeq 0.5\ V_A$.

Conclusion: A major new finding in this research is that a localized magnetic perturbation along the current in a reversed-field plasma system dominated by Hall physics initiates a shock-like "reconnection wave" that propagates asymmetrically along the current channel and leads to an extended region of reconnection. Laboratory experiments using the Space Chamber in the Plasma Physics Division are now being designed to test this result. In addition, these results are relevant to the dynamics of the Earth's magnetosphere; specifically, at the magnetopause and in the magnetotail where thin current layers exist and Hall magnetic reconnection processes can reconfigure the magnetic topology and energize the plasma.

[Sponsored by ONR and NASA]

References

[1] J. Birn, J.F. Drake, M.A. Shay, B.N. Rogers, R.E. Denton, M. Hesse, M. Kuznetsova, Z.W. Ma, A. Bhattacharjee, A. Otto, and P.L. Pritchett, *J. Geophys. Res.* **106**, 3715-3720 (2001).

[2] J.D. Huba and L.I. Rudakov, *Phys. Plasmas* **9**, 4435-4438 (2002).

[3] J.D. Huba, "A Tutorial on Hall Magnetohydrodynamics," in *Space Plasma Simulation*, ed. J. Buchner, C.T. Dum, and M. Scholer (Springer, New York, 2003), p. 166-192.

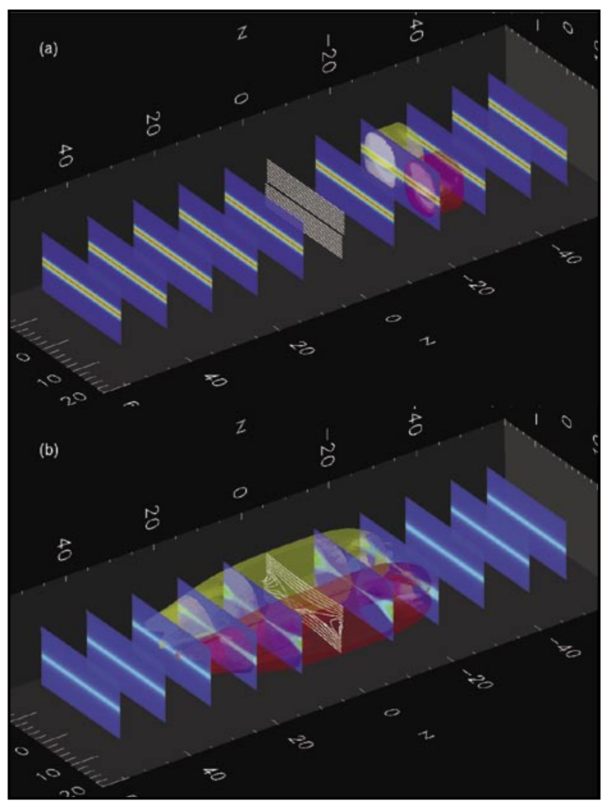

FIGURE 10
Three-dimensional simulation study of magnetic field line reconnection using the NRL Hall MHD code VooDoo.

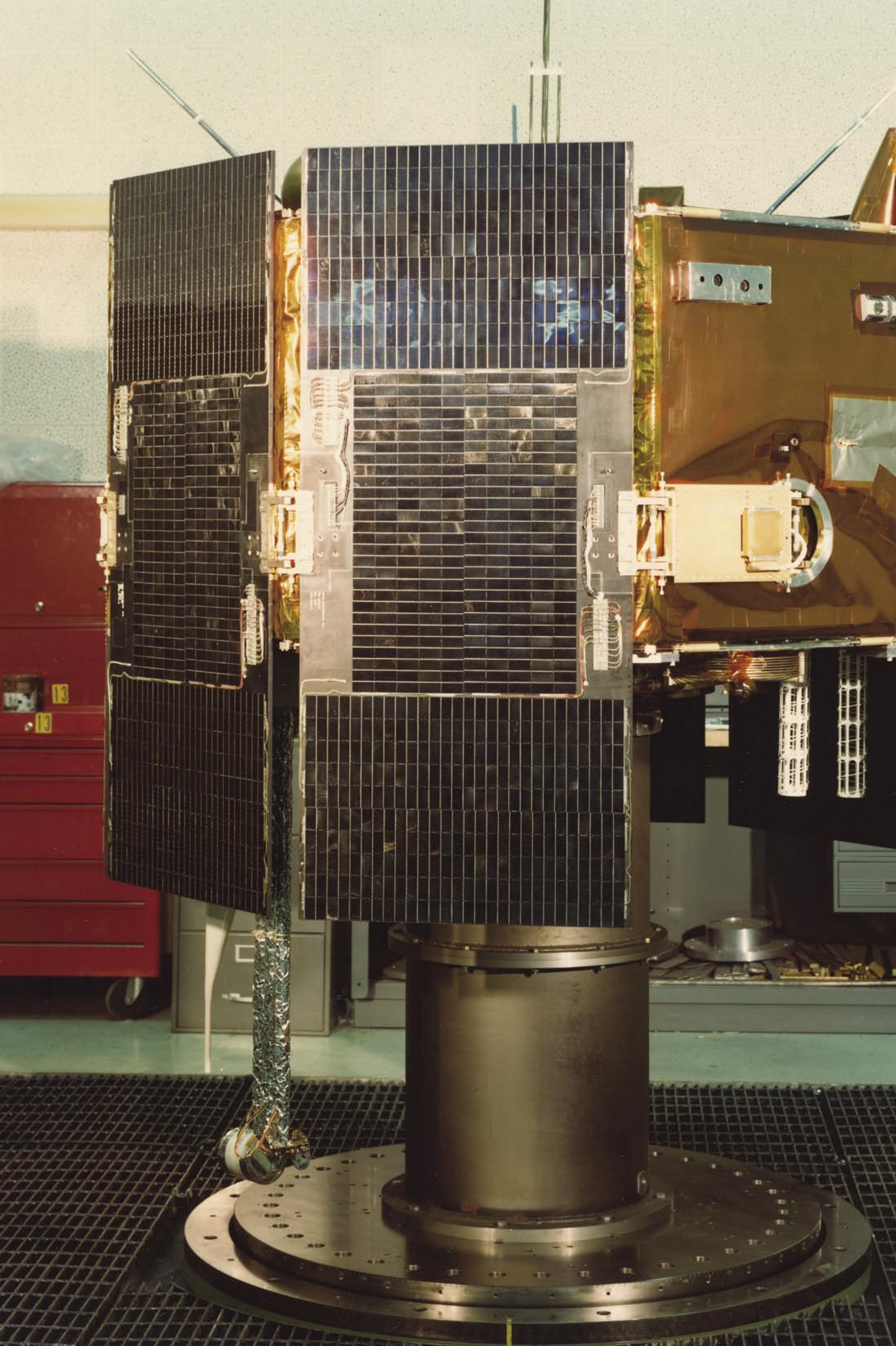

Space Research and Satellite Technology

Photo caption: The last in the Timation series of four satellites, it also became known as Navigation Technology Satellite 2, since it was now part of the Joint Program Office. We consider it the first of the GPS satellites since it is the first to fly in the GPS orbit, the first to fly the GPS cesium clocks, and the first to fly the GPS unique waveforms.

Global Change in the Thermosphere: Compelling Evidence of a Secular Decrease in Density

J.M. Picone and J.L. Lean
E.O. Hulburt Center for Space Research
J.T. Emmert
NRL/NRC Postdoctoral Research Associate

Introduction: The Naval Research Laboratory has pioneered a fast and accurate method of processing standard data on spacecraft orbits ("two-line element sets" or TLEs) to determine the total mass density of the highest layer of the Earth's atmosphere, known as the thermosphere.[1] Although the atmosphere is extremely thin in this region (the air at the Earth's surface is a trillion times thicker), it is enough to exert a drag force on satellites, causing their orbits to decay slowly and ultimately resulting in a fiery disintegration at lower altitudes. The Naval Space Surveillance System (NAVSPASUR) radar fence, operated from the Naval Surface Warfare Center in Dahlgren, Virginia, provides key observation sets from which the trajectories of Earth-orbiting objects are reduced to TLEs. The resulting Space Object Catalog presently allows the U.S. Space Command to track and predict the locations of more than 12,000 objects, most of which are in low-Earth orbit (LEO). This archive extends back 40 years and represents an unexploited source of global information on the thermosphere. The thermosphere exerts drag on LEO objects, reducing their useful lifetimes, orbital predictability, and safety.

Starshine Satellites: The power of the new method became clear when the NRL group retrieved density values from orbits of the Starshine satellites (1, 2, and 3) that flew during the years 1999-2003, the maximum of the 11-year solar cycle.[2] NRL's Spacecraft Engineering Department (Code 8200) built the Starshine spacecraft, which were covered with hundreds of mirrors polished by students around the world. The spherical shape of these objects made them invaluable as drag and radar calibration objects. The thermospheric mass density values derived from the Starshine orbits agree well with NRL's empirical atmospheric model, NRLMSISE-00, the space research community standard for estimating the properties of the thermosphere (Fig. 1). This accord across three different orbits and distinct levels of solar activity verifies the new method. The orbits and the model both show density fluctuations that are driven mainly by changes in the Sun's extreme ultraviolet radiation. More importantly, the TLE-based densities represent the true thermospheric state for a given day and year—superior to the model.

Armed with this new tool and with TLEs of spacecraft remaining in orbit over several decades, NRL attacked one of the central issues of modern-day geophysics—long-term, global atmospheric change. The study shows that the highest layers of the Earth's atmosphere are cooling and contracting, most likely in response to increasing levels of greenhouse gases.[3] The average density of the thermosphere has decreased by about 10% during the past 35 years, a contraction that could cause longer orbital lifetimes for both satellites and the hazardous space debris that threatens them.

Figure 2 shows the trends derived from orbital tracking data on 25 long-lived objects whose closest approach to the Earth lies within 200 to 800 km (124 to 497 miles). For comparison, the Space Shuttle typically orbits at 300 to 450 km (186 to 279 miles), and the International Space Station maintains an altitude of about 400 km (248 miles). By analyzing changes in the orbits of the selected objects, the NRL team derived the yearly average density encountered by each object over the period 1966-2001. After adjusting for the larger-amplitude 11-year density cycles driven by solar activity and for other factors, the data from every object indicated a long-term decline in the density of the thermosphere.

Density Changes: Such a density decrease had been predicted by theoretical simulations of the upper atmosphere's response to increasing carbon dioxide and other greenhouse gases. In the troposphere (the lowest layer of the atmosphere), greenhouse gases trap infrared radiation, causing the well-known "global warming" effect. In contrast, higher up (above 12 km, or 7.5 miles), these gases enhance the ability of the atmosphere to radiate heat to space, tending toward cooling. As the amount of carbon dioxide increases, the upper atmosphere becomes cooler and contracts, bringing lower-density gas to lower heights. Consequently, the average density at a given height decreases. Because each layer of the atmosphere rests on the layers below it, small changes at lower altitudes become amplified at higher altitudes. According to Fig. 2, the observed decrease in density depends on height in the same way as predicted by the theoretical simulations. This suggests that greenhouse gases are a likely source of the change. An extreme example of the greenhouse gas effect can be found on Venus, whose atmosphere is 96% carbon dioxide (compared to trace amounts in the Earth's atmosphere), resulting in a very

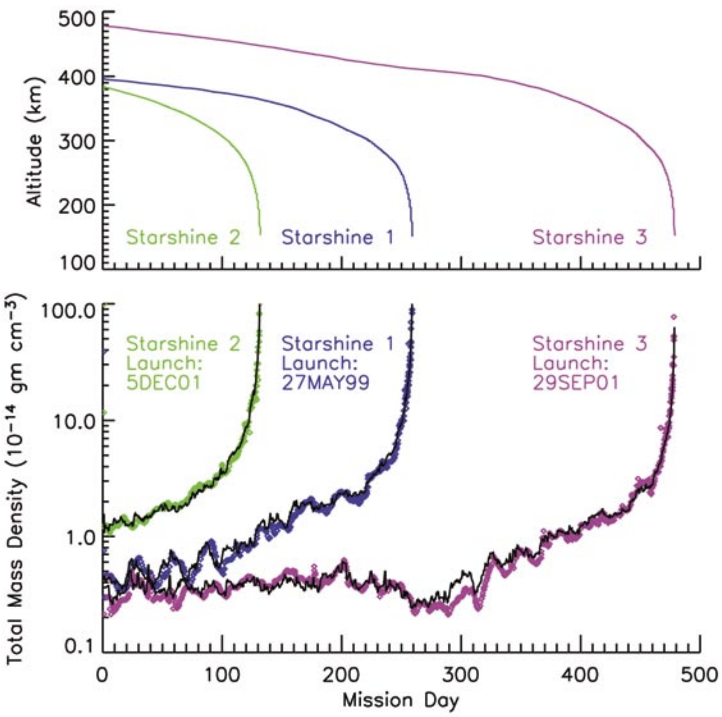

FIGURE 1

Shown throughout each Starshine mission are (top) the altitude of the satellite vs mission day and (bottom) corresponding total mass density values. In the latter, the colored symbols show the TLE-based density values; the black lines show the corresponding values from NRLMSISE-00.

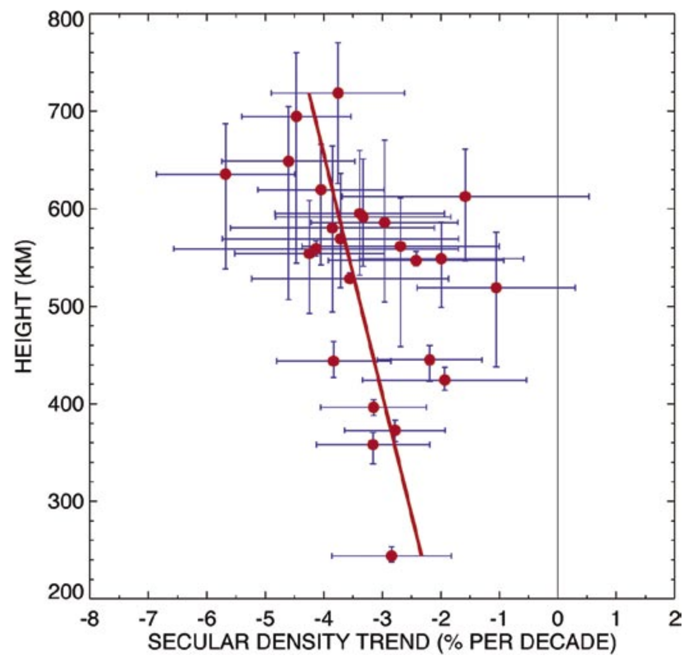

FIGURE 2

Summary of secular density trends derived from 25 objects, as a function of drag-weighted average height (near perigee). The horizontal bars indicate the 1σ uncertainty in the trends, and the vertical bars denote the range of heights covered by each object.

hot lower atmosphere (800 °F, 427 °C) and a very cold and compact upper atmosphere.

Conclusions: Based on the NRL analysis and projections of carbon dioxide levels in the atmosphere, the density at thermospheric heights may be halved by the year 2100. This change may have mixed impacts: while satellites will stay in orbit longer, saving fuel, so will damaging spacecraft debris, potentially increasing the frequency of collisions.

Acknowledgments: The authors are grateful for helpful discussions with Dr. S.L. Coffey, Code 8233, and Mr. W.R. Braun, Code 8222. Dr. S.H. Knowles, now of SAIC, and Dr. R.R. Meier, now of George Mason University, provided invaluable assistance in acquiring two-line element sets from the U.S. Space Command for this study.

[Sponsored by ONR and NASA]

References

[1] J.M. Picone, J.T. Emmert, and J.L. Lean, "Thermospheric Densities Derived from Spacecraft Orbits I. Accurate Processing of Two-Line Element Sets," *J. Geophys. Res.* 2004JA010585, in press, 2004.

[2] J.L. Lean, J.M. Picone, and J.T. Emmert, "Thermospheric Densities Derived from Spacecraft Orbits II. Application to the Starshine Satellites," *J. Geophys. Res.* in preparation, 2004.

[3] J.T. Emmert, J.M. Picone, J.L. Lean, and S.H. Knowles, "Global Change in the Thermosphere: Compelling Evidence of a Secular Decrease in Density," *J. Geophys. Res.* **109**(A02301), doi:10.1029/2003JA010176 (2004).

★

Operationally Responsive Tactical Microsatellites

T.M. Duffey and M.S. Hurley
Naval Center for Space Technology

Introduction: The Secretary of Defense's Office of Force Transformation (OFT) and the Naval Research Laboratory, in concert with the Air Force Research Laboratory (AFRL), are expanding their development of and experimentation with operationally responsive tactical microsatellite systems. Key elements of this system include: modular payloads, a highly automated satellite bus, common payload and launcher interfaces, launch on demand, and direct tasking and data dissemination using the Secret Internet Protocol Routing Network (SIPRNET). This system ultimately integrates space assets into the forces so that the Joint Task Force (JTF) Commander can call up assets by deciding the payload capability required, the area of interest, the area for direct downlink, and the date the assets must be operational. This article provides an overview of this experimentation, and a roadmap for where operationally responsive space is going.

Background: The Naval Research Laboratory (NRL), in concert with OFT, developed a tactical space system concept that makes space an organic part of the JTF. Three enabling elements of this system are capable microsatellites, low cost and rapid launch systems, and tactical networks, primarily the SIPRNET. Based on this work, OFT started the Operationally Responsive Space Initiative consisting of a series of experiments. TacSat-1 was the first experiment in this initiative.

During the second half of 2003 and the first half of 2004, NRL designed, assembled, integrated, and tested the TacSat-1 spacecraft. The entire spacecraft was completed in less than one year, from go-ahead to the end of system-level testing, for less than $10M. This spacecraft (Fig. 3) is currently awaiting launch on the maiden flight of the Space Exploration Technologies (SpaceX) Falcon I launch vehicle. The second experiment in this initiative, TacSat-2 (Fig. 4), aims to build on this achievement, and continue to develop near-term paths for the tactical exploitation of space. These efforts have helped to create and institutionalize a joint TacSat experimentation program with the objective of testing key elements needed to realize a fully operationally system. TacSat-3 was the first experiment selected under this joint process. TacSat-4 is already in the planning stages, with a possible selection in February 2005.

Objectives: The overall objective of the TacSat experiments is to test the key elements needed to realize an operationally responsive space system. Integral to the TacSat approach is operational experimentation, which closely couples the science and technol-

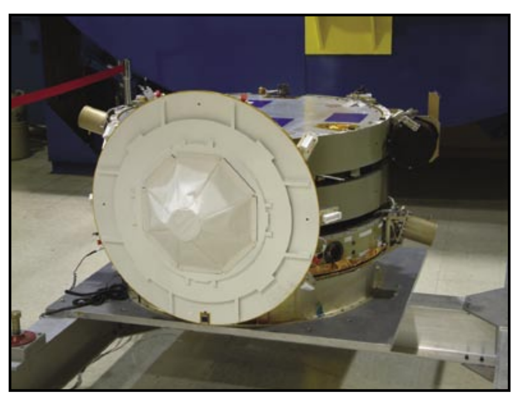

FIGURE 3
Tac-Sat-1 spacecraft after vibration testing.

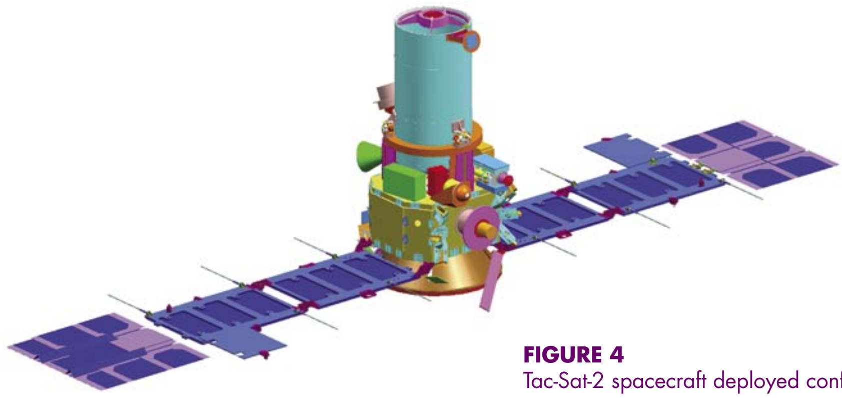

FIGURE 4
Tac-Sat-2 spacecraft deployed configuration.

ogy (S&T) and research and development (R&D) work with realistic field evaluations and concept of operations (CONOP) development.

TacSat-1: The primary objectives of TacSat-1 are: to provide an operationally relevant 100 kg class microsatellite with electronic intelligence (ELINT), specific emitter identifier (SEI), and cross-platform capability; demonstrate launch within one year (which was not met), while supporting a new low-cost commercial launch vehicle; make the space asset an organic part of the forces; and develop lessons learned and process to begin a repeatable cycle. Spacecraft development and launch are to be completed for less than $15M. The success to date of this experiment has helped OFT successfully excite the broader DoD and industry in the responsive space area. With an eye toward an operational system, TacSat-1 contributes SIPRNET-based networking using the Virtual Mission Operation Center (VMOC) software, support for a new low-cost launch vehicle, and an iterative operational experimentation approach led by PACOM.

TacSat-2: TacSat-2 begins a spiral development cycle. One objective of the TacSat-2 experiment is to develop an understanding of the requirements for and limitations of rapid deployment. This includes launch vehicle integration, launch, and on-orbit checkout of the satellite. A second objective is to understand the requirements and limitations for the rapid development of new spacecraft and payloads. From an operational standpoint, the program seeks to obtain high-resolution images of tactical significance using the VMOC operational network to task the satellite and disseminate the resulting data. Another objective is to develop and test a CONOP for the geolocation and cued imaging of a target during the same pass. TacSat-2 also will experiment with autonomous flight software to perform on-orbit checkout of the spacecraft, and autonomous tasking of the various payloads carried by the spacecraft. The most important contribution of TacSat-2 is the use of a space-based common data link (CDL) tactical communications link. Flying a CDL transponder requires ground-breaking work in frequency allocations and communications security (COMSEC) approaches.

TacSat-2 Payload Capabilities: The TacSat-2 spacecraft carries a large number of experimental payloads. The payloads that primarily address operationally relevant tactical capabilities include the Target Indicator Experiment (TIE) supplied by NRL and the imaging system supplied by Nova Biomimetics and SAIC. The TIE payload is an improved version of the primary payload carried by TacSat-1. The TIE payload performs real-time signal geolocation and SEI of radio frequency (RF) signals using space and air-based collection platforms. It is also capable of collecting the Automated Identification System (AIS) signal now required on large ships for port safety and homeland defense. The TIE payload is also reprogrammable on-orbit for acquiring new targets.

The TacSat-2 imaging system has panchromatic, red, green, and blue sensors with a ground sample distance (GSD) of approximately 1 meter. This imager uses a Fairchild Imaging CCD 583 TDI Line Scan array, sampling at approximately 9600 lines per second. The high ground scan speeds of TacSat-2 that result from its low Earth orbit (~7.5 km/s satellite ground trace speed) are an ideal application for a time-delay integration (TDI) approach. The TDI process is essentially noise-free, allows charge accumulation to take place over the number of TDI stages, and preserves the ground resolution capability of the very high rates that the TDI lines are "scanned" off the array.

TacSat-3, -4 and Beyond: While efforts on TacSat-3 and TacSat-4 have just begun, the primary objective of both of these experiments will be to identify and mature the standards (interfaces, performance levels, etc.) necessary to develop a standard spacecraft bus in the near term. A successful standard bus has been elusive in the past. However, by coupling elegant and discipline standards for system interfaces with realistic acquisition goals, a standard microsatellite class bus is achievable. This prototype work is focused on transitioning the design to the Space and Missile Systems Center (SMC) for acquisition. Combining SMC operationally responsive space procurements of a standard bus with SMC procurements for STP will provide the necessary incentive for payload developers to keep their payloads within the limits of the standard bus' capabilities.

Key Partnerships: Many successful partnerships made TacSat-1 possible. As the TacSat series progresses, many more partnerships will develop. The primary programmatic partners for TacSat-1 are OFT, NRL, SpaceX, and SMC. For TacSat-2, NRL and AFRL have teamed up with an AFRL lead industry team. Both TacSat-1 and TacSat-2 payload capabilities have been possible because of the diverse capabilities within NRL. Code 8100 has provided an ELINT payload with cross-platform (spacecraft to aircraft) capability, Code 5700 provided the SEI capability and IR camera, Code 7200 provided imaging expertise and radiometric calibration of two commercial cameras, and Code 8200 provided the spacecraft engineering for integration and testing; Code 8100's Blossom Point facility will be the ground station for flight operations. As the TacSat experimentation process formalizes, partnerships are expected to grow with Air Force Space Command, Space and Missile Systems Center, Air Force Research Laboratory, Army Space and Missile Command, and the Marine Corps space requirements representative. ★

Heating of the Polar Ionosphere

S.P. Slinker and J.D. Huba
Plasma Physics Division
J.A. Fedder and G. Joyce
George Mason University

Introduction: As technology advances, modern society and especially the military rely on space-based assets. Sensitive systems include communications, surveillance, and navigation. Consequently, understanding and predicting "space weather"—the state of the environment in near-Earth regions—has become increasingly critical.

Recently, geomagnetic storms have come to the public's attention through the popular press. For example, the great storms that occurred around Halloween in 2003 were widely reported in the news. Adverse effects resulting from the impact of geomagnetic storms include the loss of satellite services because of electronic disruption and outages in the electric power grids from surges. In this article, we discuss research on another consequence of geomagnetic activity, namely, the large amount of energy deposited in the polar ionosphere. During geomagnetic storms, the heated ionosphere and neutral atmosphere expand, increasing density at high altitudes so that satellites experience enhanced drag. As a direct result, orbits are altered, communications to other satellites or to the ground can be disrupted, and the spacecraft may require a "boost" to continue its mission.

Background: The source of the energy responsible for heating the ionosphere and atmosphere is the Sun. Normally, solar radiation is the primary contributor. However, during solar disturbances, the solar wind plays an increasingly important role. The solar wind is a plasma that continually streams radially away from the Sun. The solar wind also carries a magnetic field called the Interplanetary Magnetic Field (IMF). During solar storms, the solar wind is greatly enhanced, with the density and IMF strength many times the nominal values. These solar storm events can last more than a day and are often associated with the occurrence of a coronal mass ejection (CME) on the Sun. This was the case for the 2003 Halloween storms. When the direction of the disturbed IMF as it reaches the Earth is opposite to the direction of the Earth's magnetic field, a geomagnetic storm occurs, and the solar wind energy flowing into the magnetosphere and downward to the ionosphere is greatly enhanced. In recent years, considerable effort at NRL and other research institutions has been devoted to studying and predicting these conditions and their effects.

Two main processes deposit solar wind energy in the polar ionosphere: resistive heating and energetic particle precipitation. Electric currents are driven by the solar wind-magnetosphere interaction. They flow along geomagnetic field lines into the ionosphere in the polar regions, where they flow across the magnetic field at altitudes around 100 km and then return to the magnetosphere. During geomagnetic storms, these currents can exceed 10 million amperes. In a manner similar to a wire heating from resistance to current, the ionosphere is heated. The total resistive heating rate can exceed 1 trillion watts during the peak of a geomagnetic storm.

The electromagnetic forces from the solar wind-magnetosphere interaction also accelerate plasma in the outer magnetospheric regions. A well-known consequence of energetic particle precipitation is the aurora. High-energy electrons and ions travel down the geomagnetic field and, as they encounter the dense atmosphere, excite the atoms and molecules that emit the light we see. During geomagnetic storms, the precipitating particles are greatly enhanced, and the power entering the ionosphere can be several 100 GW.

Model Description: Our research uses numerical simulation models to study polar capionosphere heating. The Lyon-Fedder-Mobarry (LFM) global magnetosphere model was developed at NRL in the early 1990s. It is a three-dimensional (3D) ideal magnetohydrodynamics representation of the Earth's magnetosphere, which is driven by solar wind data as input and is coupled to the ionosphere in the polar regions. The LFM model is also used at several universities and is the flagship magnetosphere model at the Center for Integrated Space Weather Modelling, (CISM), a National Science Foundation Science and Technology Center headquartered at Boston University.

Two types of studies are involved in this research. In one, we specify the solar wind and other conditions, such as the solar radiation output or the season of the year, to see how the polar cap heating responds. Secondly, we use measured conditions to simulate real events. Figure 5 is an example from the simulation of the effect of a shock front in the solar wind that hit Earth on 04 November 2003 during the Halloween geomagnetic storm period. The top row shows contours of the resistive and precipitation heating rates in the southern polar cap at 0651 UT. The polar plots are centered on the magnetic pole, and the circles are drawn every 10 deg of latitude. The shock front arrived at about 6 min later. The bottom row of the plot gives the heating rates after another 6 min. We see that both rates have more than doubled.

The ionospheric results from the LFM simulation can be used as input to the NRL ionosphere model, SAMI3. This is a 3D simulation that resolves the ionosphere from the polar regions to the equator. SAMI3 can predict the "swelling" of the ionosphere from the heating and the resulting winds.

Summary: Geomagnetic storms can deposit sufficient energy in the polar ionospheres to cause the atmosphere to expand upward. The increased atmospheric density enhances atmospheric drag on low-altitude spacecraft and causes their orbits to decay. We are performing simulation studies to understand this and other processes to predict their impacts on space weather conditions and on space-based systems.

[Sponsored by ONR and NASA] ★

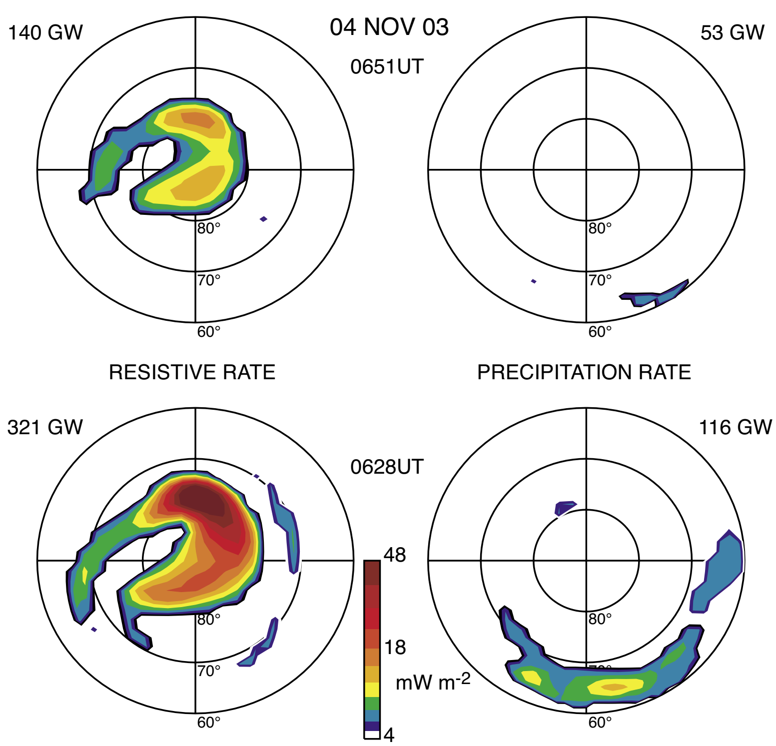

FIGURE 5
Polar plots of contours of resistive and precipitation heating for the southern hemisphere on 04 November 2003. The top row shows heating approximately 6 min before a solar wind shock wave arrives. The bottom row is taken about 6 min after arrival.

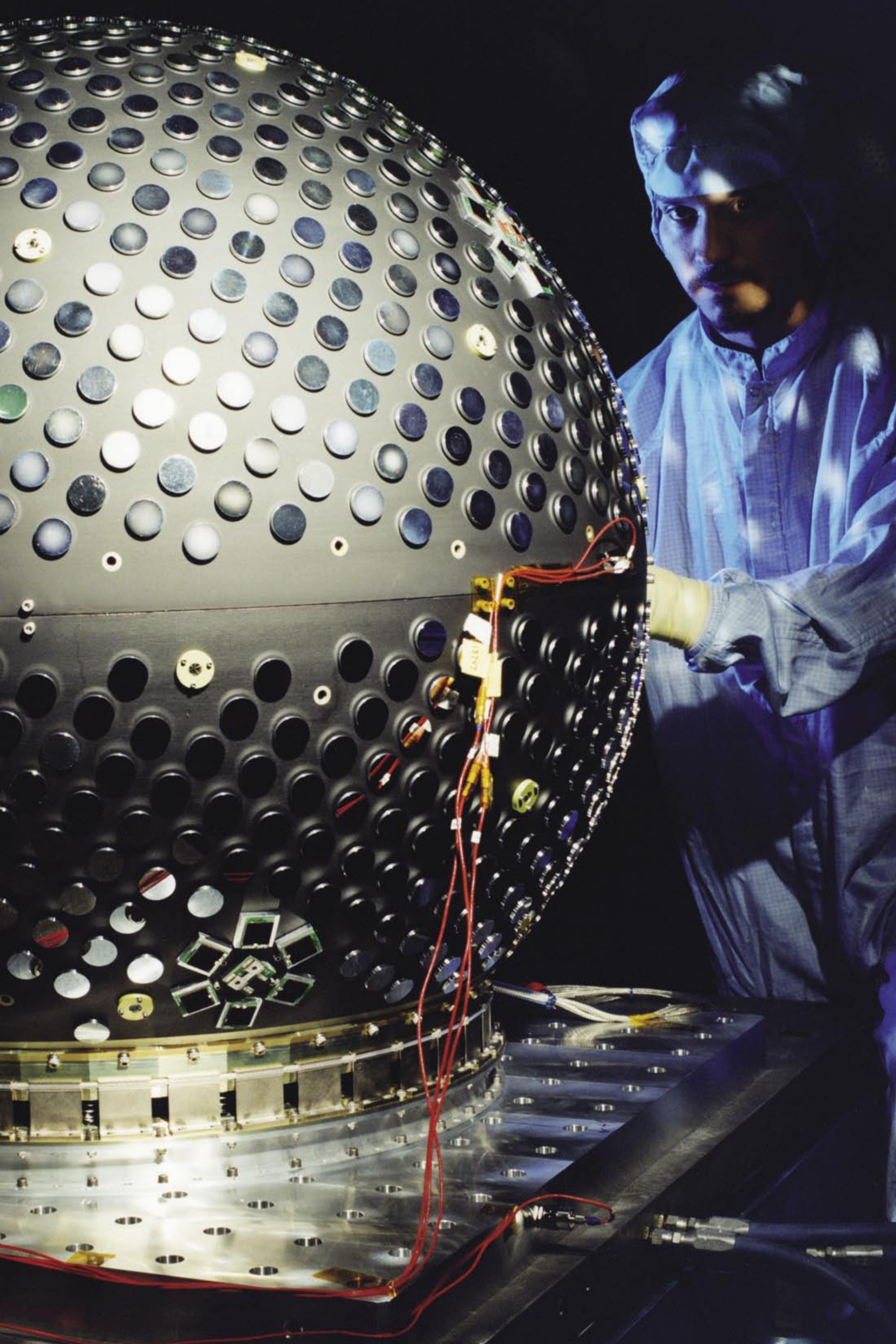

Programs for Professional Development

Photo caption: The Starshine satellites were the idea of Gil Moore, whose relationship with NRL goes back to the 1950s. The satellites are spheres with highly reflective polished mirrors on their surface. Students as young as grade school levels polished the mirrors and can spot this satellite at dawn and dusk against a star background and try to predict the time and place of reentry to win a prize.

PROGRAMS FOR NRL EMPLOYEES

The Human Resources Office, Personnel Operations Branch, continues to support and provide traditional and alternative methods of training for employees. During 2004, NRL employees were encouraged to develop their skills by attending training to enhance their job performance in order to continue to meet the future needs of NRL as well as their own goals for growth.

One common study procedure is for employees to work full time at the Laboratory while taking job-related scientific courses at universities and schools in the Washington area. The training ranges from a single course to full graduate and postgraduate programs. Tuition for training is paid by NRL. The formal programs offered by NRL are described here.

GRADUATE PROGRAMS

• The **Advanced Graduate Research Program** (formerly the Sabbatical Study Program, which began in 1964) enables selected professional employees to devote full time to research or pursue work in their own or a related field for one year at an institution or research facility of their choice without the loss of regular salary, leave, or fringe benefits. NRL pays all travel and moving expenses for the employee and dependents. Criteria for eligibility include professional stature consistent with the applicant's opportunities and experience, a satisfactory program of study, and acceptance by the facility selected by the applicant. The program is open to employees in Career Track NP Levels III and IV; NO Levels III, IV, and V; and NR Level IV who have completed 6 years of Federal Service, 4 of which have been at NRL.

• The **Edison Memorial Graduate Training Program** enables employees to pursue advanced studies in their fields at local universities. Participants in this program work 24 hours each workweek and pursue their studies during the other 16 hours. The criteria for eligibility include a minimum of one year of service at NRL, a bachelor's or master's degree in an appropriate field, and professional standing in keeping with the candidate's opportunities and experience.

• To be eligible for the **Select Graduate Training Program**, employees must have a college degree in an appropriate field and must have demonstrated ability and aptitude for advanced training. Students accepted into this program devote a full academic year to graduate study. While attending school, they receive one-half of their salary, and NRL pays for tuition and laboratory expenses.

• The **Naval Postgraduate School (NPS)**, located in Monterey, California, provides graduate programs to enhance the technical preparation of Naval officers and civilian employees who serve the Navy in the fields of science, engineering, operations analysis, and management. It awards a master of arts degree in national security affairs and a master of science degree in many technical disciplines.

NRL employees desiring to pursue graduate studies at NPS may apply for a maximum of six quarters away from NRL, with thesis work accomplished at NRL. Specific programs are described in the NPS catalog. Participants will continue to receive full pay and benefits during the period of study.

• In addition to NRL and university offerings, application may be made to a number of noteworthy programs and fellowships. Examples of such opportunities are the **Capitol Hill Workshops**, the **Legislative Fellowship (LEGIS) program**, the **Federal Executive Institute (FEI)**, the **Fellowship in Congressional Operations**, and the **Executive Leadership Program for Mid-Level Employees**. These and other programs are announced from time to time, as schedules are published.

• Research conducted at NRL may be used as **thesis material for an advanced degree**. This original research is supervised by a qualified employee of NRL who is approved by the graduate school. The candidate should have completed the required course work and should have satisfied the language, residence, and other requirements of the graduate school from which the degree is sought. NRL provides space, research facilities, and supervision but leaves decisions on academic policy to the cooperating schools.

CONTINUING EDUCATION

• **Undergraduate and graduate courses** offered at local colleges and universities are subsidized by NRL for employees interested in improving their skills and keeping abreast of current developments in their fields. These courses are also available at a number of DoD installations in the Washington, DC, area.

• NRL offers **short courses** to all employees in a number of fields of interest including technical subjects, computer operation, and supervisory and management techniques. Laboratory employees may attend these courses at nongovernment facilities as well. Interagency courses in management, personnel, finance, supervisory development, and clerical skills are also available.

For further information on any of the above programs, contact the Employee Relations and Development Branch (Code 1850) at (202) 767-2365.

• The **Scientist-to-Sea Program (STSP)** provides increased opportunities for Navy R&D laboratory/center personnel to go to sea to gain first-hand insight into operational factors affecting system design, performance, and operations on a variety of ships. NRL is a participant of this Office of Naval Research (ONR) program. For further information contact (202) 767-0851.

PROFESSIONAL DEVELOPMENT

NRL has several programs, professional society chapters, and informal clubs that enhance the professional growth of employees. Some of these are listed below.

• The **Counseling Referral Service (C/RS)** helps employees to achieve optimal job performance through counseling and resolution of problems such as family, stress and anxiety, behavioral, emotional, and alcohol- or drug-related problems that may adversely impact job performance.

C/RS provides confidential assessments and short-term counseling, training workshops, and referrals to additional resources in the community. (Contact (202) 767-6857.)

• The NRL **Women in Science and Engineering (WISE) Network** was formed in 1997 through the merger of the NRL chapter of WISE and the Women in Science and Technology Network. Luncheon meetings and seminars are held to discuss scientific research areas, career opportunities, and career-building strategies. The group also sponsors projects to promote the professional success of the NRL S&T community and improve the NRL working environment. Membership is open to all S&T professionals. (Contact (202) 404-4143 or (202) 404-6052.)

• **Sigma Xi**, the scientific research society, encourages and acknowledges original investigation in pure and applied science. As an honor society for research scientists, individuals who have demonstrated the ability to perform original research are elected to membership in local chapters. The NRL Edison Chapter, comprising approximately 400 members, recognizes original research by presenting awards annually in pure and applied science to outstanding NRL staff members. The chapter also sponsors lectures at NRL on a wide range of scientific topics for the entire NRL community. These lectures are delivered by scientists from all over the nation and the world. The highlight of the Sigma Xi lecture series is the Edison Memorial Lecture, traditionally featuring a distinguished scientist. (Contact (202) 767-3934.)

• The **NRL Mentor Program** was established to provide an innovative approach to professional and career training and an environment for personal and professional growth. It is open to permanent NRL employees in all job series and at all sites. Mentorees are matched with successful, experienced colleagues having more technical and/or managerial experience who can provide them with the knowledge and skills needed to maximize their contribution to the success of their immediate organization, to NRL, to the Navy, and to their chosen career fields. The ultimate goal of the program is to increase job productivity, creativity, and satisfaction through better communication, understanding, and training. NRL Instruction 12400.1A provides policy and procedures for the program. (Contact (202) 767-2957.)

• Employees interested in developing effective self-expression, listening, thinking, and leadership potential are invited to join either of two NRL chapters of **Toastmasters International**. Members of these clubs, who possess diverse career backgrounds and talents, meet two to four times a month in an effort to learn to communicate not by rules but by practice in an atmosphere of understanding and helpful fellowship. NRL's Commanding Officer and Director of Research endorse Toastmasters as an official training medium

Children of NRLers get the opportunity to visit the Laboratory at the annual "Take Our Children to Work" program. This years program included a tree-planting ceremony to recognize "Earth Day."

at NRL. (Contact (202) 404-4963 for more information.)

EQUAL EMPLOYMENT OPPORTUNITY (EEO) PROGRAMS

Equal employment opportunity is a fundamental NRL policy for all employees regardless of race, color, national origin, sex, religion, age, or disability. The NRL EEO Office is a service organization whose major functions include counseling employees in an effort to resolve employee/management conflicts, processing formal discrimination complaints, providing EEO training, and managing NRL's affirmative employment recruitment program. The NRL EEO Office is also responsible for sponsoring special-emphasis programs to promote awareness and increase sensitivity and appreciation of the issues or the history relating to females, individuals with disabilities, and minorities. (Contact the NRL Deputy EEO Officer at (202) 767-5264 for additional information on any of their programs or services.)

OTHER ACTIVITIES

• The **Community Outreach Program** traditionally has used its extensive resources to foster programs that provide benefits to students and other community citizens. Volunteer employees assist with and judge science fairs, give lectures, tutor, mentor, coach, and serve as classroom resource teachers. The program also sponsors African American History Month art and essay contests for local schools, student tours of NRL, an annual holiday party for neighborhood children, and other programs that support the local community. Also through this program, NRL has active partnerships with four District of Columbia public schools. (Contact (202) 767-2541.)

• Other programs that enhance the development of NRL employees include four computer user groups (**IBM PC**, **Mac**, **NeXT**, and **Sun**) and the **Amateur Radio Club**. The **Recreation Club** encourages wide interest in sports for employees with its many facilities and programs, such as a heated indoor pool; basketball and volleyball court; weight room; table tennis; hot tub; five martial arts disciplines; aerobics classes; and water walking and exercise. Sportswear and NRL and seasonal paraphernalia are available at the Rec Club office. The **Showboaters** theater group has been "in the dark" for a number of years. Regrouping has been unsuccessful. Showboaters was looking for dedicated persons with all sorts of talent for membership. Traditionally, the NRL Showboaters performed two major productions each year (in Building 222) in addition to occasional performances at Laboratory functions and benefits for local charities. (Contact (202) 404-4998 or visit our website at www.nrl.navy.mil/showboaters/Past_Productions.html.)

CAPT Schubert and neighborhood children enjoy the spirit of the holiday season filled with stories, sing-alongs, and treats with Santa and Mrs. Claus.

PROGRAMS FOR NON-NRL EMPLOYEES

Several programs have been established for non- NRL professionals. These programs encourage and support the participation of visiting scientists and engineers in research of interest to the Laboratory. Some of the programs may serve as stepping-stones to federal careers in science and technology. Their objective is to enhance the quality of the Laboratory's research activities through working associations and interchanges with highly capable scientists and engineers and to provide opportunities for outside scientists and engineers to work in the Navy laboratory environment. Along with enhancing the Laboratory's research, these programs acquaint participants with Navy capabilities and concerns and provide a path to full-time employment.

RECENT PH.D., FACULTY MEMBER, AND COLLEGE GRADUATE PROGRAMS

• The **National Research Council (NRC) Cooperative Research Associateship Program** selects associates who conduct research at NRL in their chosen fields in collaboration with NRL scientists and engineers. The tenure period is two years (renewable for a possible third year).

• The **NRL/ASEE Postdoctoral Fellowship Program**, administered by the American Society for Engineering Education (ASEE), aims to increase the involvement of highly trained scientists and engineers in disciplines necessary to meet the evolving needs of naval technology. Appointments are for one year (renewable for a second and possible third year).

• The **Naval Research Enterprise Intern Program (NREIP)** program has been initiated as a two-year demonstration effort involving 69 NROTC colleges and universities. The Office of Naval Research (ONR) is offering summer appointments at Navy laboratories to current sophomores, juniors, seniors, and graduate students from participating schools. Academia Research Management (ARM) is handling the administration of the application process through a website. Electronic applications are sent for evaluation to the point of contact at the Navy laboratory identified by the applicant. ONR will provide directly to the student a stipend of $5,500 to undergraduates and $6,500 to graduate students.

• The American Society for Engineering Education also administers the **Navy/ASEE Summer Faculty Research and Sabbatical Leave Program** for university faculty members to work for 10 weeks (or longer, for those eligible for sabbatical leave) with professional peers in participating Navy laboratories on research of mutual interest.

• The **NRL/United States Naval Academy (USNA) Cooperative Program for Scientific Interchange** allows faculty members of the U.S. Naval Academy to participate in NRL research. This collaboration benefits the Academy by providing the opportunity for USNA faculty members to work on research of a more practical or applied nature. In turn, NRL's research program is strengthened by the available scientific and engineering expertise of the USNA faculty.

• The **National Defense Science and Engineering Graduate Fellowship Program** helps U.S. citizens obtain advanced training in disciplines of science and engineering critical to the U.S. Navy. The three-year program awards fellowships to recent outstanding graduates to support their study and research leading to doctoral degrees in specified disciplines such as electrical engineering, computer sciences, material sciences, applied physics, and ocean engineering. Award recipients are encouraged to continue their study and research in a Navy laboratory during the summer.

For further information about the above six programs, contact (202) 404-7450.

PROFESSIONAL APPOINTMENTS

• **Faculty Member Appointments** use the special skills and abilities of faculty members for short periods to fill positions of a scientific, engineering, professional, or analytical nature.

• **Consultants and experts** are employed because they are outstanding in their fields of specialization or because they possess ability of a rare nature and could not normally be employed as regular civil servants.

• **Intergovernmental Personnel Act Appointments** temporarily assign personnel from state or local governments or educational institutions to the Federal Government (or vice versa) to improve public services rendered by all levels of government.

COLLEGE STUDENT PROGRAMS

The student programs are tailored to undergraduate and graduate students to provide employment opportunities and work experience in naval research. These programs are designed to attract applicants for student and full professional employment in fields such as engineering, physics, mathematics, and computer sciences. The student employment programs are designed to help students and educational institutions gain a better understanding of NRL's research, its challenges, and its opportunities. Employment programs for college students include the following:

• The **Student Career Experience Program** (formerly known as the Cooperative Education Program) employs students in study-related occupations. The program is conducted in accordance with a planned schedule and a working agreement among NRL, the educational institution, and the student. Primary focus is on the pursuit of bachelors degrees in engineering, computer science, or the physical sciences.

• The **Student Temporary Employment Program (STEP)** enables students to earn a salary while continuing their studies and offers them valuable work experience.

• The **Summer Employment Program** employs students for the summer in paraprofessional and technician positions in engineering, physical sciences, computer sciences, and mathematics.

• The **Student Volunteer Program** helps students gain valuable experience by allowing them to voluntarily perform educationally related work at NRL.

For additional information on these undergraduate and graduate college student programs, contact Code 1810 at (202) 767-8313.

HIGH SCHOOL STUDENT PROGRAMS

• The **DoD Science & Engineering Apprentice Program (SEAP)** offers high school students, grades 9 to 12, the opportunity to serve for eight weeks as junior research associates. Under the direction of a mentor, students gain a better understanding of research, its challenges, and its opportunities through participation in scientific programs. Criteria for eligibility are based on science and mathematics courses completed and grades achieved; scientific motivation, curiosity, and capacity for sustained hard work; a desire for a technical career; teacher recommendations; and achievement test scores. The NRL Program is the lead program and the largest in DoD.

For additional information, contact Code 1850 at (202) 767-2957.

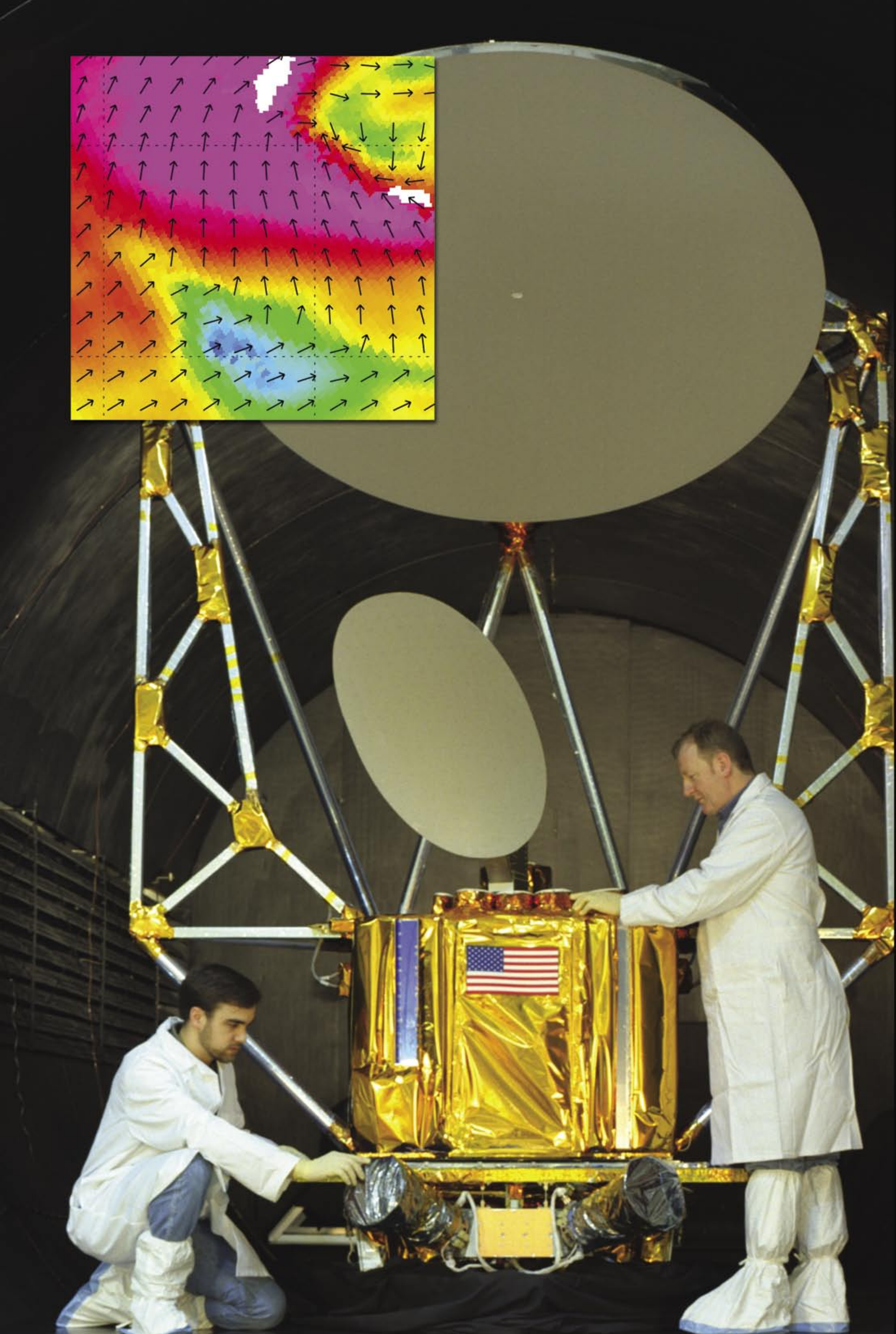

Photo caption: The Windsat payload is shown in our thermal vacuum chamber. It has a 2-m antenna that rotates at 30 rpm. The smaller antenna is used to calibrate the big antenna. The inset picture shows the data that Windsat measures. The different colors are different ocean temperatures and the arrows are the wind speed and direction at the ocean surface.

TECHNICAL OUTPUT

The Navy continues to be a pioneer in initiating new developments and a leader in applying these advancements to military requirements. The primary method of informing the scientific and engineering community of the advances made at NRL is through the Laboratory's technical output—reports, articles in scientific journals, contributions to books, papers presented to scientific societies and topical conferences, patents, and inventions.

The figures for calendar year 2004 presented below represent the output of NRL facilities in Washington, D.C.; Bay St. Louis, Mississippi; and Monterey, California.

In addition to the output listed, NRL scientists made more than 900 oral presentations during 2004.

Type of Contribution	Unclassified	Classified	Total
Articles in periodicals, chapters in books, and papers in published proceedings	1182	0	1182*
NRL Formal Reports	21	5	26
NRL Memorandum Reports	76	6	82
Books	3	0	3
Patents granted			83
Statutory Invention Registrations (SIRs)			0

*This is a provisional total based on information available to the Ruth H. Hooker Research Library on February 3, 2005. Additional publications carrying a 2004 publication date are anticipated.

CONTRIBUTIONS BY DIVISIONS, LABORATORIES, AND DEPARTMENTS

SUBJECT INDEX

AUTHOR INDEX

EMPLOYMENT NRL OPPORTUNITIES

NRL offers a wide variety of challenging positions that involve the full range of work, from basic and applied research to equipment development. The nature of the research and development conducted at NRL requires professionals with experience. Typically there is a continuing need for electronics, mechanical, aerospace, materials engineers, metallurgists, computer scientists, and oceanographers with bachelor's and/or advanced degrees and physical and computer scientists with Ph.D. degrees.

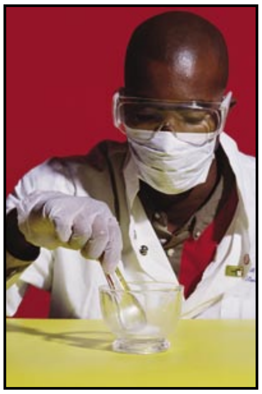

Chemists. Chemists are recruited to work in the areas of combustion, polymer science, bioengineering and molecular engineering, surface science, materials, synthesis, nanostructures, corrosion, fiber optics, electro-optics, microelectronics, electron-device technology, and laser physics.

Biologists. Biologists conduct research in areas that include biosensor development, tissue engineering, molecular biology, genetic engineering, proteomics, and environmental monitoring.

Physicists. Physics graduates may concentrate on such fields as materials, solid-state physics, fiber optics, electro-optics, microelectronics, vacuum science, plasma physics, fluid mechanics, signal processing, ocean acoustics, information processing, artificial intelligence, electron-device technology, radio-wave propagation, laser physics, ultraviolet/X-ray/gamma-ray technology, electronic warfare, electromagnetic interaction, communications systems, radio frequency/microwave/millimeter wave/infrared technology, computational physics, radio and high energy astronomy, solar physics, and space physics.

Oceanographers, Meteorologists, and Marine Geophysicists. These employees work in the areas of ocean and atmospheric dynamics, air-sea interaction, upper-ocean dynamics, oceanographic bio-optical modeling, oceanic and atmospheric numerical modeling and prediction, data assimilation and data fusion, retrieval and application of remote sensing data, benthic processes, aerogeophysics, marine sedimentary processes, advanced mapping techniques, atmospheric physics, and remote sensing. Oceanographers and marine geophysicists are located in Washington, D.C., and the Stennis Space Center, Bay St. Louis, Mississippi. Meteorologists are located in Washington, D.C., and Monterey, California.

for Highly Innovative, Motivated, *and* Creative Personnel

Electronics Engineers and Computer Scientists. These employees may work in the areas of communications systems, electromagnetic scattering, electronics instrumentation, electronic warfare systems, radio frequency/microwave/millimeter wave/infrared technology, radar systems, laser physics technology, radio-wave propagation, electron device technology, spacecraft design, artificial intelligence, information processing, signal processing, plasma physics, vacuum science, microelectronics, electro-optics, fiber optics, solid state, software engineering, computer design/architecture, ocean acoustics, stress analysis, and expert systems.

Materials Scientists/Engineers. These employees are recruited to work on materials, microstructure characterization, electronic ceramics, solid-state physics, fiber optics, electro-optics, microelectronics, fracture mechanics, vacuum science, laser physics and joining technology, and radio frequency/microwave/millimeter wave/infrared technology.

Mechanical and Aerospace Engineers. These employees may work in areas of spacecraft design, remote sensing, propulsion, experimental and computational fluid mechanics, experimental structural mechanics, solid mechanics, elastic/plastic fracture mechanics, materials, finite-element methods, nondestructive evaluation, characterization of fracture resistance of structural alloys, combustion, CAD/CAM, and multi-functional material response.

For more information on current vacancy listings, visit http://hroffice.nrl.navy.mil/

NAVAL RESEARCH LABORATORY

4555 Overlook Ave., SW ◆ Washington, DC 20375-5320

LOCATION OF NRL IN THE CAPITAL AREA

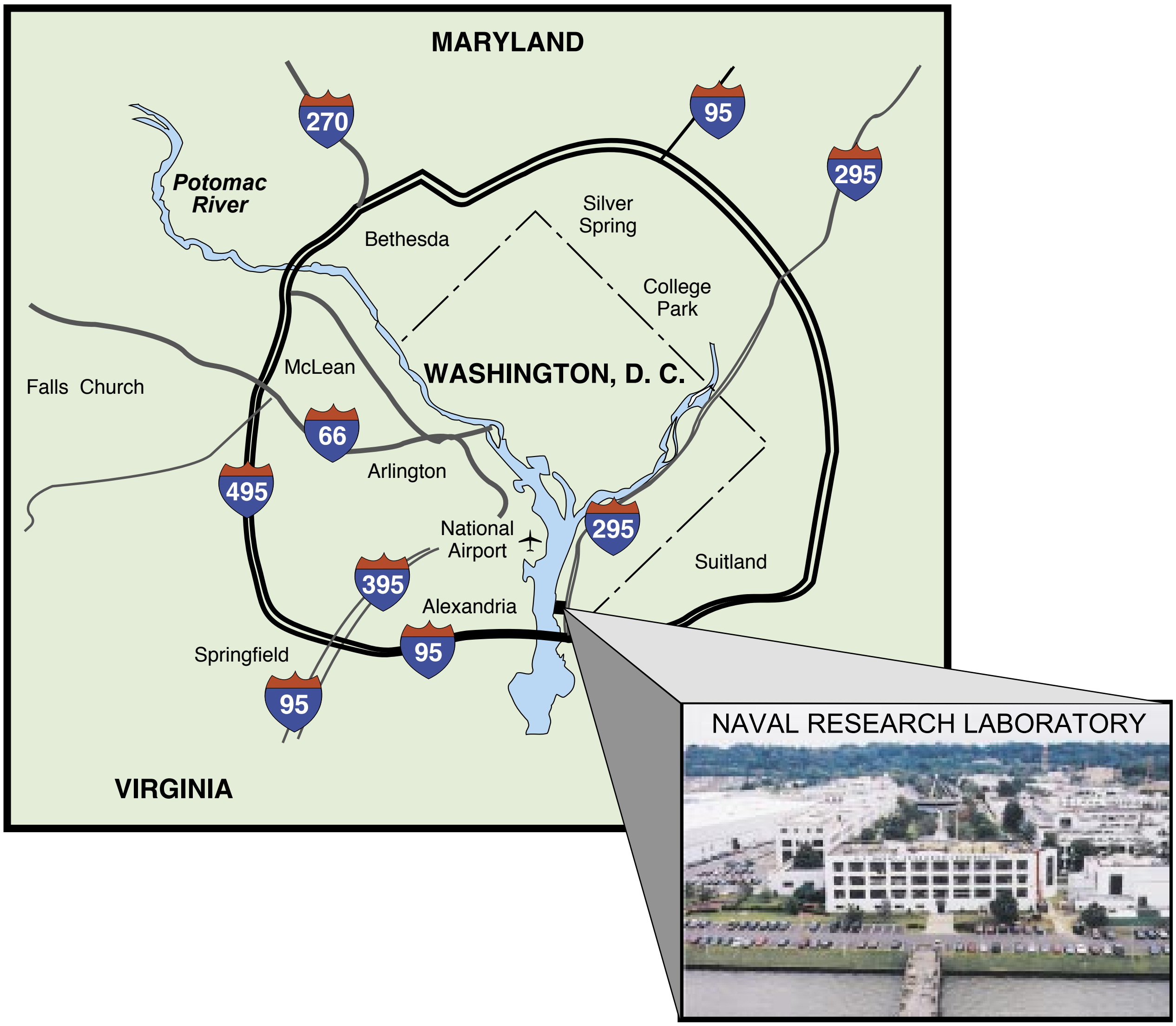

Quick Reference Telephone Numbers

	NRL Washington	NRL-SSC	NRL-Monterey	NRL CBD	NRL VXS-1 Patuxent River
Hotline	(202) 767-6543	(202) 767-6543	(202) 767-6543	(202) 767-6543	(202) 767-6543
Personnel Locator	(202) 767-3200	(228) 688-3390	(831) 656-4316	(410) 257-4000	(301) 342-3751
DSN	297- or 754-	828	878	—	342
Direct-in-Dialing	767- or 404-	688	656	257	342
Public Affairs	(202) 767-2541	(228) 688-5328	(202) 767-2541	—	(202) 767-2541

Additional telephone numbers are listed on page 260.

Featuring one of the most experienced space system engineers in the world today...

MR. PETER G. WILHELM

For 45 years, Mr. Wilhelm's engineering leadership and exceptional vision have provided the Nation with timely, effective, and cost-efficient solutions to DoD and National space support needs. The consistent theme in all of his work has been the introduction of new designs and technology to enable new and improved capabilities for users and reduced system costs. From his initial appointment at the Naval Research Laboratory in 1959 through his present position as Director of NRL's Naval Center for Space Technology, Mr. Wilhelm has contributed to the design and deployment of 87 scientific and defense satellites. He personally is credited with primary responsibility for leading the design, development, and deployment of 48 of these satellites, making him one of the most experienced space system engineers in the world today. Mr. Wilhelm and his team have established a truly remarkable record of performance and reliability in all satellite deployments. This is validated by operational results in the full range of his space activities from short-duration experiments to complex, long-life, multiple-satellite systems operating in a real-time integrated, worldwide network of national and military users. He is unique in his ability to blend and fulfill the needs of customers that span the space community, including military and non-military components. The results of his efforts have been praised by frontline tactical echelons in the military, countless representatives of industry and government, and by two Presidents.

www.nrl.navy.mil